Process-Structure-Property Relationships in Closed-Loop Temperature-Controlled Additive Friction Stir Deposition of Ti-6Al-4V

A Dissertation Presented for the

Doctor of Philosophy

Degree

The University of Tennessee, Knoxville

Eric Michael Heikkenen

December 2024

Copyright © 2024 by Eric Michael Heikkenen

All rights reserved.

ACKNOWLEDGEMENTS

Thank you to Dr. Dayakar Penumadu's research group, including Zach Arwood, and REUs William Outhier, Brennan Hume, Jack Christian, and Ethan Barnhill for helping me with tensile testing of my samples. I would also like to extend a thank you to Dr. Peter Metz for assisting me with X-ray diffraction as well as being a great springboard to bounce ideas off. Thank you as well to Rob Patterson and Josh Kincaid for assisting me with printing my titanium samples. Thanks to Jose Nazario and Dave Roberson for teaching me to use the EDM. Thank you to Michael Haines and Kevin Sisco for suffering through dealing with metal powder with me. Thank you to Sarah Graham for tolerating thousands of questions in the metallography lab. And thank you to Andres Marquez Rossy and Julio Ortega Rojas for helping me constantly troubleshoot the SEM. Finally, I need to extend another thank you to the countless other people at UTK, ORNL, and elsewhere not directly mentioned in this acknowledgement that have helped me over the course of my PhD. I could not have done it without your help.

ABSTRACT

Closed-loop temperature-controlled AFSD of Ti-6Al-4V was conducted at a series of temperature setpoints including 700 ºC, 750 ºC, 800 ºC, and 850 ºC. Oxygen pickup in the bulk material did not exceed ASTM standards for the material. The resulting deposits were sectioned and characterized. Based on the temperature setpoint, it was found that the resulting microstructure morphologies in the stir zone varied from equiaxed, as in the 700 ºC temperature setpoint, to lamellar, as in the 850 ºC temperature setpoint. The intermediate 750 ºC and 800 ºC temperature setpoints exhibited mixed microstructures with a mix of both equiaxed and lamellar characteristics. It was also found that microstructure morphology and microhardness varied as a function of the build height for all deposition conditions. These variations were attributable to the processing conditions with the order of the variation linked to both process stoppages for material reloads as well as the individual layers during deposition.

Subsize tensile bars were extracted from the deposits in the weld, transverse, and normal directions before being quasi-statically tensile tested. Despite drastic differences in microstructure morphology, all tensile samples exhibited similar mechanical properties with only slight differences among the temperature setpoint conditions and orientations. An additional set of normal direction tensile bars was polished and etched to investigate the effects of microstructure morphology on resulting mechanical properties. It was found that samples from all temperature setpoint conditions exhibited multiple-yielding behavior with initial yielding observed in lamellar regions, though failure was sometimes observed in equiaxed regions. Tungsten contamination was observed in some tensile

samples that exhibited lowered ductility, especially in samples near the periphery of the deposits. This shows the potential for poor bonding in the flash regions of the deposit.

TABLE OF CONTENTS

Chapter 1 Introduction and Motivation 1

Introduction 1

Current State and Research Gaps 2

Research Objective 4

Chapter 2 Literature Review 5

Titanium 5

Crystallography and Titanium Alloys 5

Deformation in Titanium 9

A Brief Review on Recrystallization 10

Friction Stir Welding 11

Microstructure Development in FSW Titanium 12

Microstructure Characterization in FSW Titanium 15

A Review of Solid-State Additive Manufacturing Techniques 17

Additive Friction Stir Deposition 19

Comparisons to FSW 19

AFSD of Ti-6Al-4V 20

Tooling and Tool Wear in FSW and AFSD 23

Characterization and Classification of Titanium Microstructures 25

EBSD and EDS 25

Prior Beta Reconstruction 26

Manual Classification Methods 27

Semi-Automated Image Analysis Methods 28

Machine Learning Classification Methods 29
Modeling and Simulation 30
Simulation of Other Additive Manufacturing Processes 30
Physical Simulation of FSW/FSP 31
FSW and AFSD 32
Chapter 3 Materials and Methods 35
Additive Friction Stir Deposition 35
In-Situ Data Collection 40
Machine Data Logging 40
Infrared Thermography 40
Metallography 42
Identification of Microstructures 44
Electron Backscatter Diffraction 45
Prior Beta Reconstruction 47
X-Ray Diffraction 47
Mechanical Testing 49
Microhardness 49
Quasi-Static Tensile Testing 51
Chemical Analysis 55
Bulk Chemical Analysis 55
Energy Dispersive X-Ray Spectroscopy 55
Electron Microprobe Analysis 56
Chapter 4 Experimental Results 57

Closed Loop AFSD Builds 57
In-Situ Data Collection 57
Machine Data Logging 57
Infrared Thermography 59
Metallography 62
Closed-Loop Temperature-Controlled Builds 62
Identification of Microstructures 68
Agglomerative Clustering Approach 68
Electron Backscatter Diffraction 71
Closed-Loop Builds 71
Prior Beta Reconstruction 75
X-Ray Diffraction 77
Mechanical Testing 85
Microhardness Testing 85
Quasi-Static Tensile Testing 91
Fractography 106
Chemical Analysis 106
Bulk Chemical Analysis 121
Electron Microprobe Analysis 123
Chapter 5 Analysis and Discussion 128
Temperature Setpoint and Microstructure 128
Impact on Processing 128
Sub-Transus to Intermediate to Super-Transus Processing 134

Heterogenous Microstructure Development 139
Differences Compared to Traditional FSW/FSP 144
Mechanical Properties 145
Temperature Setpoint and Mechanical Properties 145
Microstructure and Mechanical Properties 148
Defects in AFSD Ti-6Al-4V 149
Oxygen/Nitrogen Pickup 149
Equiaxed Alpha Banding 151
Tungsten Inclusions 161
Flash/Kissing Bonds 170
Chapter 6 Future Work 174
Texture Development and Effect on Mechanical Properties 174
Fatigue Testing 174
Tool Development 175
Residual Stress 175
Process Monitoring / PID Tuning 176
In-Situ Process Modification 176
Increase Deposition Rates Using Hydrogen 176
AFSD Modeling 177
Chapter 7 Summary and Conclusions 178
Summary 178
Conclusions 179
Significance of Current Work 183

References 185

Appendix 212

Vita 230

LIST OF TABLES

Table 1: Material certification sheet information 36

Table 2: PID Temperature Control Process Parameters 38

Table 3: Closed-loop temperature control setpoint, mean, and standard deviation..... 58

Table 4: Measured oxygen content in the enclosure during AFSD 60

Table 5: Microstructure characterization of polished and etched tensile bars..... 73

Table 6: XRD alpha/beta wt. % fraction..... 81

Table 7: Microhardness testing mean, standard deviation, 95% confidence interval, minimum, and maximum..... 87

Table 8: Tensile testing compiled results..... 100

Table 9: Tensile testing data for ND-LD polished and etched tensile samples (*Note: sample 800S13 was tested to plasticity, stopping before failure)..... 102

Table 10: Measured bulk oxygen and nitrogen content..... 122

Table 11: EMPA line scan average values..... 126

Table 12: AFSD processing conditions and energy metrics..... 131

Table 13: LD-TD 700 ºC Tensile Testing Data 212

Table 14: LD-TD 750 ºC Tensile Testing Data 213

Table 15: LD-TD 800 ºC Tensile Testing Data 214

Table 16: LD-TD 850 ºC Tensile Testing Data 215

Table 17: TD-LD 700 ºC Tensile Testing Data 216

Table 18: TD-LD 750 ºC Tensile Testing Data 217

Table 19: TD-LD 800 ºC Tensile Testing Data 218

Table 20: TD-LD 850 ºC Tensile Testing Data 219

Table 21: ND-LD 700 ºC Tensile Testing Data..... 220

Table 22: ND-LD 750 ºC Tensile Testing Data..... 221

Table 23: ND-LD 800 ºC Tensile Testing Data..... 222

Table 24: ND-LD 850 ºC Tensile Testing Data..... 223

LIST OF FIGURES

Figure 1: Alpha/Beta phase fraction in Ti-6Al-4V at temperatures approaching the beta transus temperature 15

Figure 2: Build plate thermocouple locations 38

Figure 3: Inert Environment Enclosure 39

Figure 4: IR Thermography Setup 41

Figure 5: GLCM for microstructure classification 46

Figure 6: Oxidized (#2) and Unoxidized (#1) Samples 48

Figure 7: XRD experimental setup 50

Figure 8: Subscale Tensile Bar Geometry 52

Figure 9: Tensile Bar and Microscopy Sample Extraction Locations 54

Figure 10: Closed-Loop Temperature Controlled Builds 58

Figure 11: Measured (a) tool thermocouple and (b) build plate thermocouples for all temperature setpoints 60

Figure 12: Tool temperature as a function of (a) spindle power and (b) spindle velocity60

Figure 13: Tool temperature vs. material feed actuator force 61

Figure 14: IR vs. tool thermocouple for 700 ºC build, feed bar #1 63

Figure 15: Closed Loop AFSD Ti-6Al-4V Builds at a) 700 ºC, b) 750 ºC, c) 800 ºC, and d) 850 ºC 64

Figure 16: 700 ºC sample final layer center stir zone 66

Figure 17: 750 ºC sample final layer center stir zone 67

Figure 18: 800 ºC sample final layer center stir zone 69

Figure 19: 850 ºC sample final layer center stir zone 69

Figure 20: Agglomerative clustering results on polished and etched tensile bar 500x montage image for (a) 700 ºC, (a) 750 ºC, (a) 800 ºC, (a) 850 ºC temperature setpoints 70

Figure 21: 800 ºC polished and etched tensile bar selected area (axes are given in pixels) 72

Figure 22: Final layer center stir zone alpha Ti IPFs for (a) 700 ºC, (b) 750 ºC, (c) 800 ºC, and (d) 850 ºC temperature setpoint builds 74

Figure 23: 700 ºC center top layer stir zone grain area as a function of total area 76

Figure 24: Disorientation histogram between transformed grain misorientations and the Burgers OR 76

Figure 25: XRD of as printed unoxidized and oxidized top surfaces 78

Figure 26: XRD Rietveld refinement for the Ti-6Al-4V feedstoclk 78

Figure 27: XRD Rietveld refinement for the 700 ºC build 79

Figure 28: XRD Rietveld refinement for the 750 ºC build 79

Figure 29: XRD Rietveld refinement for the 800 ºC build 80

Figure 30: XRD Rietveld refinement for the 850 ºC build 80

Figure 31: Phase fractions in wt. % for the (a) alpha and (b) beta phases as a function of deposition temperature. The feedstock is plotted in red 81

Figure 32: Cell volume for the (a) alpha and (b) beta phases as a function of deposition temperature. The feedstock is plotted in red 83

Figure 34: Microstrain for the (a) alpha and (b) beta phases as a function of deposition temperature. The feedstock is plotted in red 83

Figure 35: Texture index for the (a) alpha and (b) beta phases as a function of deposition temperature. The feedstock is plotted in red 84

Figure 36: Combined microhardness plots (scaled to 320 HV 0.2 to 380 HV 0.2)..... 86

Figure 37: Feedstock microhardness plot (scaled to 320 HV 0.2 to 380 HV 0.2)..... 87

Figure 38: Microhardness violin plot 89

Figure 39: Anomalous high-hardness indent (a) BSE image with inset and (b) EDS element map for W 90

Figure 40: Stress-strain plots for 700 ºC samples 93

Figure 41: Stress-strain plots for 750 ºC samples 94

Figure 42: Stress-strain plots for 800 ºC samples 95

Figure 43: Stress-strain plots for 850 ºC samples 96

Figure 44: Stress-strain curves for LD-TD samples 97

Figure 45: Stress-strain curves for TD-LD samples 98

Figure 46: Stress-strain curves for ND-LD samples 99

Figure 47: 20x images of polished and etched tensile bars from (a) 700 ºC, (b) 750 ºC, (c) 800 ºC, and 850 ºC temperature setpoints 101

Figure 48: Polished and etched ND-LD tensile bar stress-strain curves for (a) 700S13, (b) 750S13, (c) 800S13, and (d) 850S13 103

Figure 49: 700 ºC ND-LD polished and etched tensile bar (a) initial characterized microstructure, (b) tested sample micrograph and (c) surface height profile 104

Figure 50: 750 ºC ND-LD polished and etched tensile bar (a) initial characterized microstructure, (b) tested sample micrograph and (c) surface height profile 104

Figure 51: 800 ºC ND-LD polished and etched tensile bar (a) initial characterized microstructure, (b) tested sample micrograph and (c) surface height profile 105

Figure 52: 850 ºC ND-LD polished and etched tensile bar (a) initial characterized microstructure, (b) tested sample micrograph and (c) surface height profile 105

Figure 53: 850 ºC ND-LD polished and etched tensile bar showing failure in the lamellar region adjacent to equiaxed microstructure 107

Figure 54: BSE image of ND-LD 700S14 fracture surface 108

Figure 55: High-magnification BSE image of ND-LD 700S14 fracture surface 109

Figure 56: BSE image of ND-LD 750S14 fracture surface 110

Figure 57: High-magnification BSE image of ND-LD 750S14 fracture surface 111

Figure 58: BSE image of ND-LD 800S14 fracture surface 112

Figure 59: High-magnification BSE image of ND-LD 800S14 fracture surface 113

Figure 60: BSE image of ND-LD 850S14 fracture surface 114

Figure 61: High-magnification BSE image of ND-LD 850S14 fracture surface 115

Figure 62: BSE image of ND-LD 750S22 fracture surface 116

Figure 63: High-magnification BSE image of ND-LD 750S22 fracture surface 117

Figure 64: BSE image of ND-LD 800S2 fracture surface 118

Figure 65: High-magnification BSE image of ND-LD 800S2 fracture surface 119

Figure 66: Equiaxed alpha band seen near top of 850 ºC temperature setpoint 120

Figure 67: BSE image of 200-micron EMPA line scan across tungsten band 124

Figure 68: EMPA line scan data for Ti, Al, V, W, O, and N 125

Figure 69: Top region stir zone microstructure for 850 ºC and 700 ºC conditions as well as feedstock 129

Figure 70: Pseudo-heat index (a) (ΩV) and (b) ($\Omega 2V$) for this study 133

Figure 71: Etched microstructure and alpha Ti IPF for each temperature setpoint..... 135

Figure 72: Alpha Ti IPFs and alpha textures for each temperature setpoint 138

Figure 73: Microstructure heterogeneity in the 850 ºC sample 140

Figure 74: FFT analysis results: (a) microhardness plots, (b) FFT results in reciprocal space, (c) 1D vertical slice of the FFT data 142

Figure 75: Mean tensile properties as a function of temperature setpoint..... 146

Figure 76: Mean elongations as a function of temperature setpoint..... 147

Figure 77: Strain hardening exponent as a function of temperature setpoint and tensile bar orientation 147

Figure 78: Etching Band of Equiaxed Alpha in the 850 ºC Sample..... 152

Figure 79: a) Ti-O Phase Diagram and b) WDS Location for Electron Microprobe Analysis..... 153

Figure 80: Ti-N phase diagram 155

Figure 81: Equiaxed alpha banding in tungsten contaminated region surrounded by lamellar alpha (a) CLAHE filtered BSE image and (b) W particle spatial distribution 157

Figure 82: Histogram of W particle size from Figure 81 (b)..... 158

Figure 83: BSE image of W contaminated equiaxed region at 3k magnification 159

Figure 84: BSE image of W contaminated equiaxed region at 7.18k magnification 160

Figure 85: Quantitative EDS line scan location and elemental map 162

Figure 86: Quantitative EDS line scan location..... 163

Figure 87: Quantitative EDS line scan wt. % results..... 164

Figure 88: Diffusive tungsten tool wear in an AFSD Ti-6Al-4V build (process parameters unknown) 165

Figure 89: A large tungsten inclusion in the 800 ºC AFSD sample 166

Figure 90: A very large tungsten inclusion in the 850 ºC temperature setpoint build... 167

Figure 91: BSE montage image of tungsten inclusions in (a) 700 ºC and (b) 850 ºC temperature setpoint builds 169

Figure 92: Apparent kissing bond in the 700 ºC sample originating at the flash (a) optical (b) Keyence Optical Shadow Effect Mode 171

Figure 93: Flash region of 700 ºC temperature setpoint exhibiting partial bonding 172

Figure 94: ND-LD 700ºC Tensile Specimens at Failure (a) s2, (b) s6, (c) s10, (d) s14, (e) s18, (f) s22, (g) s26 224

Figure 95: ND-LD 750ºC Tensile Specimens at Failure (a) s2, (b) s6, (c) s10, (d) s14, (e) s18, (f) s22, (g) s26 225

Figure 96: ND-LD 800ºC Tensile Specimens at Failure (a) s2, (b) s6, (c) s10, (d) s14, (e) s18, (f) s22, (g) s26 226

Figure 97: ND-LD 850ºC Tensile Specimens at Failure (a) s2, (b) s6, (c) s10, (d) s14, (e) s18, (f) s22 227

Figure 98: 700 ºC pair plot..... 228

Figure 99: 750 ºC pair plot..... 228

Figure 100: 800 ºC pair plot..... 229

Figure 101: 850 ºC pair plot..... 229

CHAPTER 1

INTRODUCTION AND MOTIVATION

Introduction

Additive manufacturing (AM) has revolutionized the production of metallic components with its ability to fabricate near-net-shape parts. Among the myriad techniques available, solid-state additive manufacturing is gaining significant attention. Additive friction stir deposition (AFSD) is one such recently developed solid-state AM process (1–4).

This research focuses on AFSD of Ti-6Al-4V, also known as ASTM Grade 5 and UNS56400. Building upon the prior work of friction stir welding (FSW) and friction stir processing (FSP), AFSD uses a rotating, non-consumable tool to generate frictional heating at the tool's shoulder. The significant difference between FSW/FSP and AFSD, is that the latter is characterized by a hollow tool that allows for the deposition of feed material through the center of the tool. Through friction, the heated material becomes softened, allowing it to be stirred and consolidated into a layer below the tool. This softened material undergoes massive plastic deformation via a stirring action driven by the rotating tool, breaking up any prior oxide layer coating the feed material and substrate. With the breakup and dispersion of the oxide layer, this contact results in metallic bonding. Adiabatic heating also contributes to the material softening and the subsequent deposition process.

A primary advantage of AFSD lies in its inherent solid-state nature ensuring the absence of melt-related issues such as solidification and liquation cracking, a type of cracking that occurs in the mushy zone of a weld during solidification. Lower

temperatures also mean reduced residual stress gradients and the associated part distortion as compared to processes that involve local melting solidification. Moreover, because processing takes place at temperatures below the melting temperature, the solid-state nature means AFSD has the potential to be more energy-efficient than fusion based processes. The feedstock is acquired in the form of bar stock that is obtained from extrusion, casting, or cutting from easily sourced metal sheets and does not require wire drawing or powder atomization. This leads to easier sourcing of feed material and contributes to an additional source of cost and energy savings as compared to beam and arc-based metal additive manufacturing techniques. As an additional advantage, AFSD is a free-form process that does not necessitate a rigid enclosure or powder bed. These benefits enable this process to be scaled to large build volumes with high material deposition rates.

The AFSD process is often compared to FSW, as both are linked thermo-mechanical processes. Both temperature and deformation directly affect microstructure and resulting mechanical properties. However, as an additive manufacturing process, AFSD differs from traditional FSW as it is a layer-by-layer process. This results in significant volumes of previously deposited material being repeatedly reheated and deformed again before cooling. Over the course of many layers, this will produce thermo-mechanical cycling that may influence the resulting mechanical properties.

Current State and Research Gaps

Currently, all theses (5,6) and peer-reviewed publications (7–10) regarding AFSD of titanium have focused on Ti-6Al-4V. In order of publication, Miller (6) first demonstrated AFSD of Ti-6Al-4V. Agrawal et at. (7) then demonstrated the deposition of

Ti-6Al-4V using compacted recycled chips derived from a machining process. Next, Farabi et al. (8) deposited Ti-6Al-4V at fixed spindle speeds from 400 rpm to 500 rpm and the resulting influence of processing conditions on microstructure and mechanical properties. As the AFSD process has matured, Yoder et al. (9) used closed-loop temperature and force control to demonstrate mechanical properties exceeding forging standards. Most recently, Metz et al. (10) point out the possibility of microstructural heterogeneities leading to a non-uniform mechanical response under loading. Considering this observation of heterogeneity, it is apparent that there is a need to further investigate the process-structure-property relationships in AFSD Ti-6Al-4V.

Beyond the observations of heterogeneity, based on current publications, it can be observed that the processing window for AFSD titanium has not been fully explored. While it has been demonstrated multiple times that the AFSD process can be successfully used to deposit Ti-6Al-4V, only super beta transus deposition has been consistently demonstrated, where the beta transus is the temperature at which a titanium alloy undergoes an allotropic phase change with increasing temperature from the alpha phase to the beta phase. Yoder et al. claim a homogenous microstructure yet also point out the existence of a band of equiaxed alpha microstructure, suggesting otherwise. Metz et al. report non-uniform plastic deformation in an AFSD Ti-6Al-4V tensile sample which also supports the potential for heterogeneity in AFSD titanium. Modeling efforts to support these experimental studies are limited. Beyond one master's thesis (5), there are no peer reviewed publications to date that focus on process modeling of AFSD titanium.

Research Objective

AFSD of Ti-6Al-4V is relevant to the naval, aerospace, defense, automotive, and chemical sectors. However, the complex interplay between operating parameters, as-deposited microstructure, and subsequent mechanical properties have not been fully established. The research objective of this study is to increase this understanding by investigating the process-structure-property relationships in closed-loop temperature-controlled AFSD of Ti-6Al-4V at a variety of processing conditions, both above and below the beta transus temperature. The outcome will be to improve parameter selection for commercial production of AFSD Ti-6Al-4V components.

CHAPTER 2

LITERATURE REVIEW

While the available literature on AFSD of Ti-6Al-4V is limited, there is an abundance of studies describing the conventional processing of titanium, including FSW and FSP.

Titanium

While titanium is one of the most abundant metals in the Earth's crust, its difficulty in production and processing has meant that it is a relatively recent addition to available structural materials. It did not become a commercially viable metal until the invention of the Kroll process roughly in the mid 20th century. Accordingly, much of the early developmental work in titanium alloys took place in the years following World War II. Titanium production drastically increased since this early work.

Titanium provides a combination of high strength and low density as well as high corrosion resistance. However, these advantages are offset by its high cost and difficulty in machining. Additionally, titanium presents difficulties in processing due to its high reactivity with oxygen and nitrogen. Therefore, processing at high temperatures must be performed in an inert environment or vacuum (11). Despite these difficulties, titanium is increasingly being used in a variety of industries, including aerospace, defense, chemical, power, biomedical, civil, and consumer goods.

Crystallography and Titanium Alloys

Titanium has two major crystallographic phases. The first is the hexagonal close packed (HCP) alpha phase. The second is the high temperature body centered cubic

(BCC) beta phase. The HCP unit cell is not as symmetric as the BCC unit cell, yielding some unique properties to the alpha phase in titanium. Notably, this reduced symmetry leads to anisotropic properties for the alpha phase depending on the alignment of the c-axis, which is the long axis of the HCP unit cell. This results in the modulus of elasticity of an alpha titanium single crystal varying with orientation from a minimum of 100 GPa, when the stress is perpendicular to the c-axis, to a maximum of 145 GPa, when the stress is parallel to the crystal c-axis (11). BCC beta titanium, while not anisotropic, has a lower modulus comparatively (11,12). The effects of crystal anisotropy extend to other physical properties as well. Textured titanium alloys can yield large variations in yield strength, Poisson's ratio, stress corrosion cracking, and fracture toughness depending on texture strength and orientation (13).

Beyond the anisotropy of the HCP crystal structure, the alpha and beta phases in titanium also have different slip systems, where slip is the sliding of crystals along certain crystallographic planes. In titanium, as with most crystal systems, the easiest slip occurs along the close-packed planes (14). HCP crystal structures, however, have limited slip systems (14,15). In HCP titanium, there are three close packed planes of the form $\langle 11\bar{2}0\rangle$. Older literature states that there are three slip systems for HCP titanium that all occur in the close-packed $\langle 11\bar{2}0\rangle$ family of directions (13). More recent literature states that there is an additional slip system of the $\{11\bar{2}2\}$ plane in the $\langle 11\bar{2}3\rangle$ direction, though it is noted that this system is unlikely to be activated in polycrystalline titanium that is not strongly textured (11). In addition to slip systems, titanium can also accommodate deformation through twinning. Twinning is the result of a portion of a crystal deforming about a plane in such a way as to produce a symmetric structure to the undeformed

portion. There are multiple modes of twinning (13); however, the addition of atoms into solution such as Al and O limit the likelihood of twinning in alloys other than pure titanium (11). Twinning is more likely seen in alloys with large additions of beta stabilizing elements (13).

Because of the anisotropic slip systems in alpha titanium, slip systems in the material may not be aligned with the direction the material is stressed. Thus, the critical resolved shear stress (CRSS) is often used in the context of titanium to refer to the critical value of shear stress under which slip occurs. The equation describing CRSS is also known as Schmid's Law. A crystal will deform when one of the possible slip systems is loaded beyond its CRSS.

Unlike FCC and HCP structures, BCC beta titanium does not have true close packed planes, but it does have an abundance of slip systems, allowing easy deformation compared to HCP alpha titanium. The slip systems in beta titanium consist of the $\{110\}$, $\{112\}$, and $\{123\}$ planes, all in the $\langle 111 \rangle$ direction resulting in a total of 48 possible slip systems (11,14). These differences in slip systems play a large role in the deformation response of titanium under physical processing.

Titanium alloys can be divided into categories based on their room temperature crystallographic structures. These categories are alpha, alpha + beta, and beta titanium alloys. These alloy classifications are largely based on how the added alloying elements change the beta transus temperature as compared to pure titanium. These alloying additions can also be categorized based on the effects of these additions on the relative stability of the alpha and beta phases.

Alpha alloys are characterized by a predominantly alpha phase crystal structure at room temperature, though some small amount of the beta phase is often present. Another characteristic of alpha alloys is that they are not heat treatable for increased mechanical properties (11). Alpha alloys, such as commercially pure (CP) titanium, are commonly strengthened using oxygen as solid solution strengthener; however, Al, N, and C are also effective alpha phase stabilizers. Alpha phase stabilizing elements reduce the beta transus temperature.

With increasing additions of beta stabilizers, both the alpha and beta phases remain stable at room temperature. This category of titanium alloys is known as the alpha + beta alloys. Within this category, Ti-6Al-4V first appeared in 1954 and remains the most widely used alloy (11). Titanium alloys with a small addition of beta stabilizers but not enough to make a true alpha + beta alloy are referred to as near-alpha alloys.

Beta titanium alloys have sufficient beta stabilizers to prevent the formation of martensite on fast cooling. Beta stabilizers include V, Mo, Nb, Cr, Fe, and Si. Commercial beta titanium alloys are typically metastable alloys. Beta titanium alloys have seen their most usage in high strength applications such as aircraft landing gear components, though there are some developments in the biomedical field due to the low modulus of beta titanium alloy implants better matching that of bone (12).

When considering the phase change between the high temperature beta phase and the low temperature alpha phase, the orientation relationships between the phases must be considered. Burgers first noted the $(110)_\beta||(0001)_\alpha$, $\langle 111\rangle_\beta||\langle 11\bar{2}0\rangle_\alpha$ orientation relation between the BCC and HCP phases in zirconium (16). The Burgers OR is active

for both diffusive (nucleation and growth) and displacive (martensitic) transformations (11).

Deformation in Titanium

Crystalline materials exhibit repeating patterns of their constituent atoms over large distances. Due to these repeating patterns, crystals are anisotropic. Metallic engineering materials are typically made up of an arrangement of many crystals of varying sizes, shapes, and orientations, making up a polycrystalline material. The statistical measure of these crystalline orientations is referred to as "texture" (15).

Crystalline materials deform on slip planes via shear. These slip planes are typically the close packed planes which most easily allow dislocation movement. As a polycrystalline material undergoes deformation, individual crystals in the aggregate experience strain and deformation. For each strained grain, there is a critical resolved shear stress that much be exceeded to initiate slip. The shear stress on an individual slip plane can be calculated by Equation 1, where ϕ is the angle from the direction of the force to the slip plane normal and λ is the angle between the tensile and slip directions. Breaking the equation apart, $A/\cos\ \phi$ is the area of the slip plane and $F\cos\lambda$ is the force on the slip plane. Due to geometric constraints, particularly the Schmid factor ($\cos\phi\cos\lambda$), the individual crystals must rotate to accommodate the strain of their deformation along the slip plane. During deformation of a polycrystalline material, some deformation pathways are more favorable than others, resulting in preferred deformation textures. Thus, there is a relation between the deformation of a single crystal and the deformation of a polycrystalline material.

Equation 1: Shear stress on the slip plane in the slip direction

$$\tau = \frac{F}{A}\cos\phi\cos\lambda$$

Deformation texture analysis of materials was expanded in the 1980s with severe plastic deformation torsion experiments to better understand the relation between deformation of grains and deformation of a bulk material. These works resulted in a better understanding of deformation textures that was then applied to other severe plastic deformation methods such as equal channel angular extrusion and later, friction stir welding.

A Brief Review on Recrystallization

Recrystallization is a way for a deformed material to lower its stored energy by forming a new grain structure (17). The stored energy results in the creation of and movement of high angle grain boundaries, lowering the material's stored energy. High angle grain boundaries (HAGB) are typically defined as boundaries with a misorientation greater than 10º to 15º, where misorientation is defined as the difference in crystallographic orientation between grains in a crystalline material. HAGBs correspond to low angle grain boundaries (LAGB) below 10º to 15º.

Stored energy in a material can specifically be lowered through the processes of recovery, recrystallization and grain growth. Recovery refers to the movement of dislocations within a material with little overall change to the microstructure, such as in an annealing process. Recrystallization is the result of the formation of new strain-free grains. Grain growth is the result of continued recrystallization where large grains continue growing at the expense of smaller grains. While these processes have been

thought of as distinct, they have also been described by one framework depending on grain size, orientation, second phase particles, and boundary mobility of single grains relative to the matrix (18,19). It should be noted that second phase particles should not be considered solely such but more generally as any particle or grain that is harder than the surrounding matrix to provide a Zener pinning pressure and limit dislocation movement.

Recrystallization can be divided into two major categories: continuous and discontinuous. Continuous processes occur homogeneously throughout a material such that no specific nucleation and growth can be identified, while discontinuous ones occur heterogeneously throughout a material in a way that can be described through nucleation and growth. Together, there are a total of six phenomena consisting of three continuous processes: continuous subgrain growth, continuous recrystallization, and normal grain growth, and three discontinuous processes: discontinuous subgrain growth, primary recrystallization, and abnormal grain growth (18). When recrystallization occurs concurrently with the application of strain, the resulting process can be referred to as dynamic recrystallization, which can occur either continuously or discontinuously (20).

Friction Stir Welding

Friction stir welding is a process developed in 1991 at The Welding Institute (TWI) in Cambridge, UK (21). It is a solid-state, non-fusion based welding process characterized by massive plastic deformation induced by a rotating, non-consumable tool with a protruding pin to aid in weld penetration. As opposed to fusion welding, there is no melting of the material in the friction stir process. Instead, peak temperatures are typically in the range of 60% to 90% of the melting temperature in Kelvin. The lack of melting assists in the joining of difficult to weld materials, such as some aluminum alloys

that are prone to solidification cracking or form brittle intermetallic compounds when remelted. Frictional heating from the rotating shoulder and pin, as well as viscous heat generation, provides the process heat which enables massive plastic deformation by thermal softening. When the material is plastically deformed, the existing oxide layer on the base material is broken apart, allowing solid-state metallic bonding to occur. FSW is an autogenous process, meaning there is no addition of material.

Because FSW is fully thermo-mechanically coupled, the process is also known to be self-regulating. When the material gets excessively hot during welding, it flows more easily, reducing viscous heating. Conversely, if the process becomes too cold, the effective viscosity increases, which restores the equilibrium through additional viscous heating. It should be noted that material flow is well constrained in FSW. The material is constrained on the bottom by a backing plate or, in the case of reactionless FSW, a bobbin. The material is also constrained on the top by the tool shoulder. Finally, the material is constrained on the sides by the base material. Due to these constraints, the plasticized material must flow around the pin.

Microstructure Development in FSW Titanium

As noted, titanium alloys can roughly be divided into three categories based on their microstructures at room temperature: alpha, alpha + beta, and beta alloys. The room temperature microstructures are a function of chemistry, with certain elements stabilizing either the alpha or beta phases. Ti-6Al-4V is considered an alpha + beta alloy, as it does not completely transform into the alpha phase after cooling from the high temperature beta phase. This results in some amount of the beta phase being retained at room temperature.

Like steel, titanium undergoes an allotropic (fixed composition) phase change at high temperatures. Titanium can exist at low temperature as an HCP α [alpha] phase and at high temperature as a BCC β [beta] phase. As a result, titanium alloys can undergo complex phase transformations during processing depending on welding conditions and cooling rates, as well as post-processing heat treatments. This provides the potential for control of the resulting microstructures in FSW of titanium alloys (22).

Due to titanium's high temperature phase change, FSW parameters can be exploited to tailor microstructures for desired mechanical properties. It has been found that resulting microstructures are primarily controlled by two things: peak temperature and cooling rate (22). In FSW, peak temperature is most influenced by tool rotation speed, while the cooling rate is most influenced by tool travel speed (23).

Upon heating above the beta transus temperature, titanium transforms into the high temperature BCC beta phase. The size of the BCC grains formed are most dependent on the maximum temperature. Depending on the chemistry, when beta titanium cools to room temperature it undergoes a phase change to alpha titanium. At slow cooling rates, the result is colony alpha, where alpha variants grow in distinct colonies into the prior beta grain, meeting at the center. At moderate cooling rates, Widmanstätten microstructures can result, characterized by patterned, needle-like features, where multiple alpha variants chaotically grow into the same prior beta grain resulting in interlinked alpha laths. The Widmanstätten and basketweave terminologies are often used interchangeably. In Ti-6Al-4V, the result is typically a lamellar structure where the lath spacing is based on the cooling rate. In general, higher cooling rates result

in a smaller lath spacing and higher strength. At the highest cooling rates, martensitic transformations can occur (24).

For processing below the beta transus temperature, the alloy does not completely transform into the beta phase. Friction welding of titanium below the beta transus temperature has been demonstrated in the FSW literature (25). It has been noted that alpha processed Ti-6Al-4V has a higher strength than the rolled plate base material (22). At temperatures approaching the beta transus temperature, mixed microstructures can be produced, resulting from some areas transforming to the beta phase while other areas remain in the alpha phase during deformation. For high travel speeds and, therefore, high cooling rates, titanium can also undergo a martensitic transformation upon cooling, resulting in some martensite in the stir zone (26).

Kitamura et al. (22) suggested that strain induced by the FSW process may stabilize the beta phase and therefore decrease the beta transus temperature. However, Kitamura et al. also cite a paper which refers to the stabilization of austenite in stainless steels in which highly strained FCC crystals prevent the movement of the glissile martensitic transformation front (27). While strain may stabilize the beta phase, the phase transformation will typically be diffusive instead of displacive based on the cooling rates typical to titanium FSW, ranging from 10 ºC/s to 100 ºC/s (22). The alternative hypothesis is that the local elastic stress field contributes to the molar free energy of the alpha phase, stabilizing the beta phase (28,29). Another possibility is much simpler: there could be a temperature offset between the temperature measured at the thermocouple and the temperature in the stir zone depending on the location of the thermocouple, as has

been noted elsewhere in literature (30). Additionally, the beta transus temperature does not provide a binary effect. As shown by equilibrium simulation in Thermo-Calc (

Figure 1), as the temperature increases in the alpha phase, the beta phase increasingly becomes stable over a temperature range of almost 200 degrees under equilibrium conditions.

Microstructure Characterization in FSW Titanium

For characterizing welds resulting from FSW and FSP titanium, the resulting microstructures are typically divided into separate regions, in order, consisting of the base metal (BM), heat affected zone (HAZ), thermomechanical affected zone (TMAZ), and stir zone (SZ). The BM, sometimes also referred to as the baseplate (BP) is the original material unaffected by either heating or deformation. The HAZ is the next region at the extremities of the weld that consists of the material that is affected by heating and subsequent cooling of the BM. Next, the TMAZ consists of the BM where the microstructure has been changed by the simultaneous heating and deformation resulting

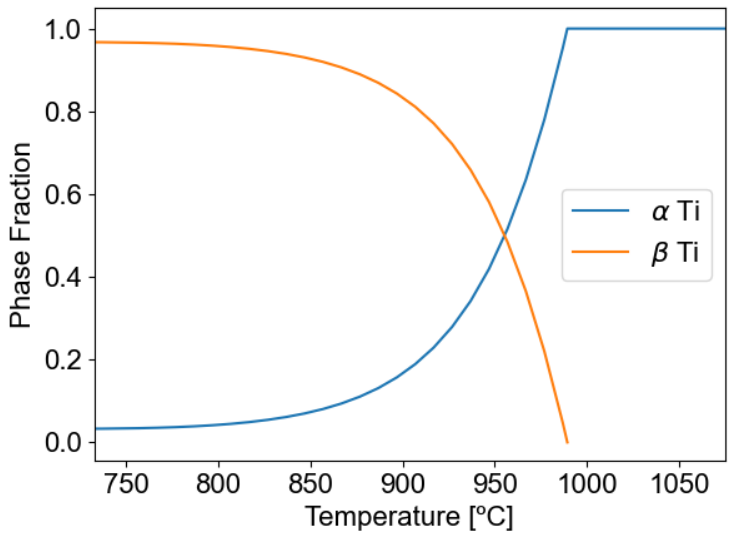


Figure 1: Alpha/Beta phase fraction in Ti-6Al-4V at temperatures approaching the beta transus temperature

from processing. This is the region that is only partially affected by the deformation resulting from the process. Finally, the SZ is the region where massive plastic deformation takes place to the point that the originating microstructure is completely recrystallized.

The most extreme extent of the affected material is the HAZ. Knipling and Fonda report the existence of a HAZ and separate the HAZ into two regions consisting of an inner HAZ and an outer HAZ in the near-alpha Ti-5111 alloy (31). These regions are identified by a coarsening of the interlath beta titanium from 100 nm to 150 nm in the base metal to 150 nm to 350 nm in the outer HAZ with the inner HAZ experiencing even greater coarsening to the point that small 30 nm to 90 nm secondary alpha platelets could be observed nucleating in the coarsened beta. It was additionally noted that the BM and HAZ were indistinguishable at low magnifications.

There is some controversy or disagreement on terms regarding the existence of the TMAZ in friction stir welding of titanium. Zhou et al. and others claim that there is no distinguishable TMAZ in titanium FSW studies (25,32–34), whereas others do report the existence of a TMAZ (30,35,36). Knipling and Fonda go further, dividing the TMAZ into an inner TMAZ and outer TMAZ (31). Other literature instead uses the term transition zone (TZ) (20,37–39). It is suggested that, in certain alloys with a highly temperature dependent flow stress, a TMAZ may not always be evident, and instead, only a small TZ between the HAZ and SZ may be present (30). It is the author's opinion that the TMAZ and TZ are equivalent, and TMAZ will be the preferred term henceforth. The

TMAZ is like the HAZ in that there is some coarsening of the interlath prior beta, but there is also a plastic deformation component that partially breaks up the BM structure resulting in features such as partially recrystallized microstructures and deformed BM lamella. The TMAZ can exhibit unique behaviors: In a study of FSP of a near-alpha alloy, the TMAZ was noted to have periodic banding of sub-transus and super-transus microstructures (31).

It is important to note that FSW and FSP titanium typically exhibit a narrow HAZ and TMAZ as compared to aluminum. This disparity can be primarily attributed to the low thermal conductivity of titanium (on the order of 15 W/m/k at 1,000 ºC) (40,41), as compared to that of aluminum alloys (250 W/m/K) (36). This difference means that FSW and FSP titanium will have significantly sharper thermal gradients as compared to aluminum.

The SZ, sometimes also referred to as the weld nugget, lies at the center of the weld. SZ microstructures do not retain any of the previous characteristics of the BM. Instead, the microstructure has been completely transformed and recrystallized. Depending on the processing temperature, the SZ microstructure may be lamellar resulting from super-transus processing, equiaxed alpha from sub-transus processing, or a mixture of equiaxed and lamellar resulting from processing around the beta transus temperature.

A Review of Solid-State Additive Manufacturing Techniques

While the following review is not exhaustive, it attempts to give a broad overview of solid-state additive manufacturing techniques. The first method uses FSW/FSP as a sheet lamination type method to build up layers of material. While the terminology is not

consistent, the method is typically referred to as friction stir additive manufacturing (FSAM). There are many examples in literature of this process (42–46). Additive friction stir processing (AFSP) modifies the process, eliminating the pin and feeding metal powder in front of the tool to make an additive manufacturing process (47).

Dispensing with the non-consumable tool completely, another method of solid-state additive manufacturing is friction surfacing, in which a rotating bar of feed material is pushed into and translated across a substrate. The process has been demonstrated with aluminum, steel, titanium, and other alloys (48–51). When used as an additive manufacturing technique, the process is referred to as friction surfacing additive manufacturing (also FSAM).

A particularly unique solid-state additive manufacturing technique is friction rolling additive manufacturing (FRAM) (52,53). The process uses a horizontally rotating tool that rotates away from the travel direction. Material is added to the process using wire fed into the front of the roller.

Another category of solid-state additive manufacturing techniques resembles material extrusion techniques. Hybrid metal extrusion and bonding (HYB) is a process that looks like FSW/FSP but uses a fluted pin that allows for the addition of feed material using a wire (54). There are also other processes of this type that do not employ a protruding tool. Friction screw extrusion additive manufacturing (FSEAM) extrudes a feedstock using a tapered screw (55). Another similar technology is solid stir additive manufacturing (SSAM) (56). Similar still is wire-based friction stir additive manufacturing (WFSAM) (57). The process has also been mounted on an industrial robot arm, with the authors noting the low normal forces required for the process (58). An

additional technique is additive friction extrusion deposition (AFED) which feeds a non-rotating feedstock into a rotating die (59). Finally, there is the AFSD process.

Additive Friction Stir Deposition

AFSD is a nascent metal additive manufacturing technique (1–4). It applies the fundamentals of FSW to an additive manufacturing process. A proprietary version of the process was originally patented and developed by the Aeroprobe Corporation, now MELD Manufacturing, located in Christiansburg, VA (60). Like FSW, AFSD is also a solid-state, non-fusion welding process characterized by massive plastic deformation induced by a rotating, non-consumable tool. However, instead of a protruding pin, AFSD uses a hollow tool to add feed material in the form of square cross-section bar stock.

Previously studied deposition materials have included aluminum (61–63), magnesium (64–66), copper (63,67,68), steel (69–71), nickel (72,73), titanium (6–9), metal matrix composites (MMCs) (74), a high entropy alloy (75), and even a tantalum-tungsten refractory alloy (76). Other research interests have included repair and cladding (77–79), cladding (80), effect of alloy temper (81), effect of layer thickness (82), fatigue behavior (83), residual stress (84), miniaturization (71), process modeling (85–88), and force/temperature control (9,89).

Comparisons to FSW

AFSD is often compared to FSW and FSP due to the similarities in how the technologies function, mainly through the input of heat via frictional heating from a rotating shoulder. Like FSW, there is no melting of the deposited material, allowing deposition of difficult to weld materials such as 7000 series aluminums. Heating is similarly accomplished via frictional heating and viscous heat dissipation. As the material

is deposited, massive amounts of plastic deformation break apart the natural surface oxide layers on the build plate, previously deposited material, as well as on the feed material, allowing metallic bonding to occur.

The additive nature of the process, however, is a differentiating point that is not present in traditional FSW. The addition of feed material through the tool complicates the material flow characteristics and has been noted to create a curved interface between the former and latter deposited layers (90). This mean that, as compared to traditional FSW, the AFSD process is not as well constrained. There is a top constraint from the tool shoulder and a bottom constraint from the baseplate or previously deposited material; however, side constraints are only present in the case of parallel deposits.

AFSD of Ti-6Al-4V

Due to the relatively new nature of AFSD, there are few published research papers regarding the deposition of titanium (6–10). Miller (6) first demonstrated the solid-state deposition of Ti-6Al-4V using proprietary parameters with a W-La tool at a rate of 533 cm^3/hr. It was found that the as-built titanium exhibited a fine grain size on the order of 1 μm resulting in a hardness of 384 HV 0.3, a YS of 1066 MPa, and a UTS of 1157 MPa (average values). Percent elongation was not reported. No tungsten contamination was found; however, Fe and Cr were reported as contamination from a previous stainless-steel build.

Agrawal et al. (7) investigated the deposition of titanium using recycled metal chips from machining processes. The chips were compacted into a rod and used for the deposition process using a tungsten carbide tool resulting in a maximum deposition rate of 243 cm^3/hr. The processing resulted in a lamellar microstructure typical of processing

above the beta transus temperature. The reported YS, UTS, and elongation were 1050 MPa, 1140 MPa, and 7%, respectively. The hardness was reported to range from 325 HV 0.5 to 335 HV 0.5 depending on the processing conditions. Additionally, tungsten contamination was noted in the sample with the highest traverse rate attributed to wear of the tool material into the build.

Farabi et al. (8) described the deposition of wrought titanium rods for a series of deposition parameters. It was found that lowering the deposition temperature by changing the input parameters resulted in improved mechanical properties due to grain refinement in the high temperature beta phase. The reported microstructures were lamellar indicating processing above the beta transus temperature. The depositions resulted in maximum properties of 1010 MPa YS, 1233 MPa UTS and up to 18% elongation. The maximum deposition rate was 487 cm^3/hr. Tungsten contamination was not reported for a lanthanated tungsten tool as compared to the earlier Agrawal et al. study using a tungsten carbide tool. However, two of the included SEM images appear to contain brightly contrasting particles that could potentially be high density tungsten particles. This conjecture is dependent on the images being taken using a backscatter detector, with the caveat that not enough information is given in the paper to come to a definitive conclusion.

More recently, Yoder et al. (9) investigates the use of closed-loop temperature control for the deposition of Ti-6Al-4V using a lanthanated tungsten tool. Despite the emphasis of closed-loop temperature control in the publication, no temperature setpoints are provided, having been considered proprietary information. It was reported that the deposited material was fully dense and exceeded ASTM standards for forged materials as

given by ASTM B381 (91).The maximum properties in the build direction were given as 948 MPa YS, 1024 MPa UTS, and 16% elongation. The maximum deposition rate achieved was 627 cm^3/hr, and the hardness was reported to vary from 325 HV 1 to 350 HV 1 in the deposited material. It was reported that all the deposited material exhibited a lamellar microstructure indicating deposition above the beta transus temperature; however, a band of equiaxed alpha was noted as arising from a process stoppage. It was theorized that deposition of titanium alloys below the beta transus may be possible. No tungsten contamination was reported.

Metz et al. (10) investigated the stress-strain response in an AFSD sample of Ti-6Al-4V printed with unknown process parameters. The samples exhibited a basketweave structure typical of titanium processed above the beta transus temperature. Under quasi-static, uniaxial tensile testing, samples exhibited heterogenous stress-strain responses over the area of the sample as observed by digital image correlation. These differences were investigated using X-ray diffraction and were found to arise from preferential loading of the $\{0\ 0\ 0\ 1\}_\alpha$ preferred orientation. This suggests that texture from thermomechanical processing conditions may contribute to heterogenous mechanical properties in AFSD builds.

Raihan (5) modeled AFSD of Ti-6Al-4V using Ansys Fluent. It was found that the deposition temperature was most strongly linked to the rotation rate of the tool, mirroring prior findings in FSW and AFSD literature. Additionally, it was found that material flow played a large role on heat transfer in the material, contributing to an asymmetric temperature profile. Simulation results were not compared to experiments.

Tooling and Tool Wear in FSW and AFSD

FSW, FSP, and AFSD all rely on tooling that must endure the hostile environments inherent to plastically flowing and deforming metal without being themselves consumed. The tool environment concerns are intensified in the case of high-temperature materials such as titanium. There are several concerns for FSW tooling (36,92). Strength must be considered at both ambient and processing temperatures. Because welding may take place over extended times at elevated temperatures, stability of the tool material at temperature must also be considered. The tool must be chemically unreactive with the workpiece material. The tool must also be damage tolerant to survive potential transient high stresses and strains, meaning a high fracture toughness is desirable. These considerations often lead to the requirements of exotic tool materials for usage with high-temperature materials. AFSD presents an additional challenge as compared to FSW in that the tool also experiences tensile stresses as material is plasticized and pushed out of the end (76).

Unlike FSW of steel alloys, polycrystalline cubic boron nitride (pcBN) is typically avoided for the use with titanium alloys due to the material's low fracture toughness and concerns with titanium's high reactivity with nitrogen. Accordingly, pcBN tools used for FSW of titanium result in severe tool wear (34,93). Nickel alloys have been used for FSW of titanium, though contamination is an issue due to intermetallic compounds forming in the weld resulting from an interaction between titanium and nickel (94–96). Cobalt alloys have also been used for FSW of titanium but exhibited high tool wear (97,98). Tungsten carbide (WC-Co) has also been used for FSW (99–103) and AFSD (7) of titanium, but again show significant tool wear. Another more exotic tool

material for FSW of titanium in literature was sintered titanium carbide; however, tool wear was not commented upon (33). Finally, iridium-based alloys have been suggested for FSW of titanium (104–107) despite the high cost of the element.

For FSW of titanium and other high strength alloys such as steel, tungsten alloys are typically used (30,32,92,100,108–116). Tungsten-rhenium alloys are specifically known for their high temperature strength and low ductile to brittle transition temperature, but have the caveat that rhenium is an extremely expensive element addition (92). They have seen limited use as an AFSD tool material for an attempt at AFSD of a tungsten alloy (76) and a miniaturized AFSD study depositing 4140 steel (71). Lanthanated tungsten (W-La_2O_3) has been reported as a tool material of choice for FSW of titanium due to its resistance to adhesive/diffusive wear (109,114). It is also a preferred tool material for AFSD of titanium (8,9). The addition of lanthanum oxide creates an oxide dispersion strengthening effect that, due to the high stability of the oxide, is maintained at elevated temperatures. Tungsten contamination is nonetheless a possibility in FSW of titanium (37,111,117) and has also been noted in AFSD of Ti-6Al-4V (7). In titanium alloys, tungsten acts as a beta phase stabilizer. When tool wear occurs, the local chemistry of the alloys may be changed, potentially affecting the local microstructural evolution and the resulting phase fraction, again potentially affecting mechanical properties. This may be a particular concern, especially if fatigue loading is to be expected. Under fatigue loading, tungsten contaminated areas may experience possible strain localizations. Due to beta titanium having a lower modulus and flow stress, areas with an increased beta phase fraction may locally experience a greater share of the loading conditions and contribute to premature failure (117).

While the usage of tool coatings is almost ubiquitous in machining, the use of tool coatings for friction stir welding has not been as prevalent. Efficacy of tool coatings for FSW of aluminum alloys has been mixed with some authors noting improvements (118), while others note no significant improvements (119). Tool coating has been attempted for FSW of titanium; however, the use of a coating was not found to reduce tool wear (36,120).

Characterization and Classification of Titanium Microstructures

EBSD and EDS

Two common microscopy tools for microstructure analysis are electron backscatter diffraction (EBSD) and energy-dispersive X-ray spectroscopy (EDS). EBSD is a characterization technique using backscattered electrons from a scanning electron microscope to determine crystallographic information in observed materials. EDS uses characteristic X-rays emitted from a material excited by an electron beam to determine the elemental composition of an analyzed material. Both EBSD and EDS can be used as complimentary analysis techniques to reveal information about microstructural orientations and features.

EBSD has been noted to provide a pathway to characterize residual strains and dislocation structures in analyzed materials (121). One method is to use the pattern/image quality (IQ) metric from the Hough indexing process. For the Hough indexed patterns, the IQ metric is given based on the quality of the diffraction pattern. Kikuchi patterns from EBSD analysis of strained materials show a diminished pattern quality resulting from the crystalline lattice being deformed by dislocations or other defects. These defects result in a broadening of the Braggs scattering angles. For each indexed point in an EBSD

scan, an IQ is calculated and can be constructed into an IQ map that can be used to better see grain boundaries and strain in a material (122). The technique, however, is sensitive to grain orientations, surface topography, and even imaging conditions (121).

Another method to characterize the dislocations and strain in a material using EBSD is to investigate the density of low angle (<15º) misorientations, with the idea being that, while individual dislocations cannot be resolved, the trends and systemic effects from defects can be observed in the material (121). One technique to investigate these trends is through the kernel average misorientation (KAM). KAM correlated well with geometrically necessary dislocations (GND); however, it does not fully capture statistically stored dislocations (SSD). This discrepancy can lead to disagreement between IQ and KAM measures (123).

More recently, a sharpness index resulting from spherical indexing of Kikuchi patterns has been demonstrated to reveal the strain and dislocations in a material while being unaffected by grain orientations (124). The sharpness index is calculated based on the results of the spherical cross correlation indexing process. Significant advantage of the technique are that it is not affected by orientation, and it can capture both SSDs and GNDs, enabling the method to see defects in microstructures resulting from processing.

Prior Beta Reconstruction

Since titanium alloys have a body centered cubic high temperature phase, special care must be taken when interpreting the mostly hexagonal close packed room temperature microstructures in Ti-6Al-4V. Because there are multiple possible prior beta grain orientation variants due to crystal symmetry for any given transformed alpha grain, the prior beta orientation cannot be determined from any individual alpha grain. Instead,

statistical methods using orientation information from many transformed alpha grain orientations must be employed. Prior beta reconstruction is based on the Burgers orientation relation mentioned earlier.

Prior beta reconstruction, along with general parent grain reconstruction, has been documented in literature abundantly (125–130). There are two main approaches: nucleation algorithms and graph clustering algorithms. Nucleation and growth algorithms begin the reconstruction process on the grain scale then iteratively repeat the process of incorporating new pixels based on an acceptance criterion to grow parent grains over the entire grain map. A graph clustering algorithm, on the other hand, considers the orientation relationships for every grain in the map. First, every grain is represented as a node in a graph with the connections to adjacent grains represented as edges. The connections are weighted based on the probability of fitting the expected Burger's orientation relation. This probability is determined by comparing the misorientation between adjacent grains to the potential expected Burger's orientation relation variants. A graph clustering algorithm groups grains that have a high likelihood of originating from a common parent grain and a parent orientation is fit to each cluster. The resulting grouped grains with a common parent grain are the prior beta grains.

Manual Classification Methods

Makiewicz (131,132) and Tiley (133) separately demonstrated that manual point counting can be used to characterize the microstructure using the method defined by ASTM E562 (134). In this method, a 10 x 10 grid is overlaid over an optical micrograph, giving 100 intersection points that can be manually characterized. This process is then repeated over all the images that will be characterized. However, the method may be time

consuming for analyzing large areas. As an example, for stitched images taken at 100x over the entire surface of an AFSD sample, the stitched image is made of a 13 x 15 grid of images. Using the 10 x 10 grid, for example, this results in a total of 19,500 points per each stitched image to be manually characterized for each of the deposition conditions. As an additional disadvantage, the method relies on the subjectivity of the user when analyzing microstructures. Tiley (133) also used a similar method to determine other information from microstructural features such as mean alpha lath thickness and Colony Scale Factor by using Photoshop to draw random lines on a binarized backscatter SEM image.

Semi-Automated Image Analysis Methods

Kelly (135) applied a semi-automated thresholding technique using backscattered SEM images to determine the alpha/beta phase fraction over the final layers of a laser directed energy deposition (L-DED) process. The process relies on a backscatter detector's sensitivity to Z-contrast (atomic number contrast) along with the fact that aluminum and vanadium partition into the alpha and beta phases, respectively. In this method, a grayscale image was binarized into a black and white image based on a user-chosen threshold value. Afterwards, the number of white pixels was divided by the total number of pixels to get an estimated phase fraction for the processed image. This technique is repeated for each image to be processed. A primary disadvantage to this method is that the thresholding value is manually chosen by the user, optimally for each image, introducing subjectivity into the method. Other disadvantages include the need for enough elemental partitioning present to provide imaging contrast as well as the fact that there may be contrast differences arising from electron channeling due to preferred

crystallographic orientations. Due to these issues, it was concluded that this method of image analysis was not sufficient to prove differences in phase fraction.

Machine Learning Classification Methods

Ducato et al. (136) used a Support Vector Machine (SVM) to automatically characterize titanium microstructures in an FSW sample. An SVM is a machine learning algorithm well suited to binary classification. In the paper, the SVM is used to distinguish the alpha and beta microstructure of the rolled plate from the alpha + beta microstructure resulting from FSW. For the method, each image was split into patches where, for each patch, texture features were extracted. The features included statistical, wavelet, Tamura, and edge histogram descriptors. The SVM was then trained on patches from 10 representative images for each morphology and then tested a larger set of images. The SVM technique was claimed to achieve approximately 95% precision when identifying lamellar morphologies, however, the system was less precise in identifying rolled microstructures from the base metal, achieving only a claimed maximum precision of 83% to 84%. The paper did not show the results for application to the full dataset of 150 images. A disadvantage to the technique include potential lack of definite separation between microstructure morphologies. Other disadvantages include that the model required some amount of fine tuning to yield satisfactory results, and the model can be limited by the magnification of the input images.

Additionally, the commercial software package MIPAR (137) advertises machine learning techniques to automatically characterize titanium microstructures and phase fractions. An additional potential disadvantage inherent to all machine learning models is the issue of overfitting, whereby a model learns on unintentional details and noise in the

training data set to the point that the model is limited in its ability to generalize beyond the training data set (138).

Modeling and Simulation

Modeling of engineering processes can be an important tool for better understanding complex real-world phenomena such as material flow and temperature evolution during friction stir welding of metals. Considering the opaque nature of metals and the harsh environment resulting from the plastic flow of metal, modeling techniques are necessary to make predictions within the stir zone. Of the various techniques for modeling FSW, physical models using tracers or material analogues, analytical models, and numerical methods are some techniques that have been presented.

Simulation of Other Additive Manufacturing Processes

Metal additive manufacturing processes deposit material in a layer-by-layer approach, resulting in inhomogeneous application of heat and material depending on the geometry and scan strategies that can result in variation of properties across a build (139–141). Understanding of thermal and thermo-mechanical history resulting from processing during additive manufacturing is critical for understanding residual stress, microstructures, phase changes, and distortions (28,142–146).

Plotkowski et. al. developed a semi-analytical heat transfer model that that can be applied to powder bed processes (147). Stump et al. further developed the code into an open-source simulation software, 3DThesis (148). The model was applied to a stochastic scan strategy to predict solidification cooling rates in a nickel alloy, successfully predicting differences in texture and solidification microstructure (139).

For larger scale metal additive manufacturing processes, Kelly and Kampe developed an implicit finite-difference method to model the thermal history during laser directed energy deposition Ti-6Al-4V (L-DED) builds (144). It was found that thermal cycling resulting from subsequently printed layers resulted in a characteristically repeating microstructure through the Z-height of the build, where heating from the most recently deposited layer results in microstructural changes to the previously deposited layer (141).

Physical Simulation of FSW/FSP

The conceptually simplest modeling technique for FSW is to use physical modeling techniques with material analogues or to input tracer particles or wires into the material for later observation. The first method of physical modeling is to substitute the deposition material with a lower strength, lower temperature material analogue such as plasticine, an oil-based modeling clay. Plasticine has been noted to accurately approximate FSW flow of metallic materials (149–151). Different colors of plasticine can be used to observe the material flow and the amount of mixing for various welding parameters. A disadvantage of the use of a material analogue is that an experiment for each test case must be run, usually on the same equipment used for welding of metallic samples.

The second method of physical modeling is to use a physical tracer material placed or embedded into the weld. This tracer material may be in the form of wires, powder, or other markers. After welding, the displaced markers can be observed by x-ray or traditional metallographic techniques and the final position can be compared to the initial starting position. This technique has the advantage of using the same material that

is used in an actual weld. Using physical tracers, however, has the same disadvantage as material analogues in that a physical experiment must be run for each test case.

A final method of physical simulation involves the use of a thermomechanical simulator such as a Gleeble (Dynamic Systems Inc., Poestenkill, NY). These machines can apply various heating and cooling cycles as well as stresses and strains while monitoring and measuring temperatures, stresses, strains, and phases changes. Thermomechanical simulators can be used to simulate processes such as casting, forging, welding, or heat treatments in a repeatable, controlled environment. Studies comparing FSP and hot torsion simulation of Ti-6Al-4V showed good agreement, matching resulting microstructures (30,152).

FSW and AFSD

To predict FSW and AFSD behavior, analytical methods may be applied to predict heat transfer and/or material flow (153–162). Due to the fully constrained nature of traditional FSW, analytical models are well suited for prediction of nominal welding conditions. Analytical methods are computationally efficient but may not fully capture the underlying physics due to simplifying assumptions.

Numerical methods may also be applied. A common numerical method used for modeling of FSW is the finite volume method. The finite volume method divides the computational domain into discrete volumes and then applies conservation laws to each volume. Fluxes into and out of each volume are determined to evaluate flow properties at each point. Because fixed position volumes are used, the finite volume method is considered an Eulerian simulation technique. Eulerian techniques evaluate fluid flow at fixed points in space over time. This stands in contrast to Lagrangian techniques, which

evaluate the flow by tracking individual particles over time through a computation domain. Numerical methods can incorporate many physical considerations, but each addition tends to increase computational complexity.

As compared to traditional FSW, the reduced physical constraints on material flow and the addition of feed material make AFSD modeling more difficult. Prior AFSD modeling efforts can be divided into two methods: the smoothed-particle hydrodynamics (SPH) method and the finite volume (FV) method.

SPH is a Lagrangian numerical method typically used for solving CFD problems, where the fluid is represented as a discrete number of particles, each representing a volume of fluid, and tracks the motion of each particle over time and space. Properties and flow characteristics are determined by the summation of the properties of each particle around a particular location. “Smoothed” refers to the use of a smoothing kernel to interpolate properties from a discreet number of particles.

In a series of papers by Stubblefield et. al., SPH is used to describe temperatures during the AFSD process (85,86,88). While these papers investigate strain rates and temperature distributions during AFSD of aluminum, they do not consider the material flow path during deposition. The SPH method is well-suited to parallelization on graphics processing units (GPUs), but typically suffers from high computational complexity. Another disadvantage of the SPH method is that many of the programs and software tools are proprietary, limiting the use of the method as compared to more accessible tools.

The FV method is traditionally applied to numerical simulation of fluid dynamics problems. It offers conservation of properties, making it particularly well suited to CFD problems. It has the advantages of having a large body of prior work and many well-

established software programs. Parallelization can be accomplished using domain decomposition. The FV method is typically implemented as an Eulerian simulation technique.

Currently, there are several approaches describing FV modeling of the AFSD process. Kincaid used the open source FV solver OpenFOAM (87,163). Kincaid's results show that, for multilayer depositions on the tested geometry, the material reaches a steady state by the end of the 5^{th} layer. Raihan used ANSYS Fluent to model AFSD of titanium; however, limited results were shown, and the material flow path was not described (5). More recently, an FV model was implemented in MATLAB to investigate flow paths in AFSD of aluminum (164). It was found that temperatures were 75% to 80% of the material's melting temperature and strain rates were on the order of 10 1/s to 100 1/s.

Alternatively, there has been continued interest in the application of machine learning based methods and surrogate models to materials science problems (138). Neural network-based machine learning methods have previously been applied to predict properties in FSW aluminum and titanium (165,166). Recently, Shi et al. developed a physics-informed machine learning approach to predict tool and build temperature profiles for AFSD aluminum (167). It was found that the model was successfully able to predict tool and build temperatures for a new spindle speed outside of the original training data.

CHAPTER 3

MATERIALS AND METHODS

Additive Friction Stir Deposition

Ti-6Al-4V (Ti: bal., Al: 6.24-6.31%, V: 3.91-4.01%, O: 0.17-0.18%, N: 0.14%, C: 0.024-0.026%, Fe: 0.15-0.19%, Si: 0.017-0.021%, wt. %) in the annealed condition was acquired as 9.45 mm (0.372 in) square rod in approximately 50.8 cm (20 in) lengths to be used as AFSD Feedstock (Perryman Company, USA via MELD Manufacturing, USA). The mill certificate compositions are given in **Table 1**. Both materials arrived in the rolled, mill-annealed condition with only slight differences in the annealing process. The feedstock was annealed at 760 ºC for 1 hour, while the build plates were annealed at 780 ºC for 50 minutes. The square rod feedstock was coated with a sparse layer of spray graphite lubricant to assist in feeding during deposition. Additional 9.525 mm (3/8 in) thick Ti-6Al-4V (Ti: bal., Al: 6.30-6.33%, V: 4.00-4.11%, O: 0.165-0.171%, N: 0.004%, C: 0.021-0.023%, Fe: 0.15-0.19%, wt. %) rolled plate was acquired to be used as build plates (VSMP, Russia via TMS Titanium, USA). Initial build plates were cut to various sizes before being standardized to approximately a 250 mm x 100 mm (10 in x 4 in) size.

AFSD builds were performed using a discreet-feed MELD L3 (MELD Manufacturing, USA) with a flat, featureless lanthanated tungsten (W-La_2O_3) tool with a diameter of 38.1 mm (1.5 in). The lanthanum oxide loading percentage is not known. All deposits were made using a 1.016 mm (0.040 in) layer height other than the first layer of each feed bar which was deposited using half the nominal layer height (0.508 mm / 0.020

Table 1: Material certification sheet information

	Build Plates			Feedstock		
Element	Top	Bottom	Avg.	Top	Bottom	Avg.
Al	6.3	6.33	6.315	6.24	6.31	6.275
V	4.11	4	4.055	4.01	3.91	3.96
Fe	0.19	0.15	0.17	0.19	0.15	0.17
C	0.023	0.021	0.022	0.026	0.024	0.025
N	0.004	0.004	0.004	0.014	0.014	0.014
O	0.165	0.171	0.168	0.17	0.18	0.175
H	0.0038	0.0038	0.0038	0.0003	0.0003	0.0003
Si	-	-	-	0.021	0.017	0.019
Cu	-	-	-	<0.008	<0.008	-
Pd	-	-	-	<0.002	<0.002	-
Y	-	-	-	<0.002	<0.002	-
B	-	-	-	<0.002	<0.002	-
Ru	-	-	-	<0.003	<0.003	-
Other	0.078	0.072	0.075	-	-	-

in) and a 50% traverse and material feed rate override. Initial proof of concept builds used a set, open-loop, fixed tool spin velocity targeting approximately 300 rpm with a traverse feed rate of 4.23 mm/s (10 in/min) and a material feed rate of 1.86 mm/s (4.4 in/min).

Later tools came equipped with an internally embedded type K thermocouple. The tool-embedded thermocouple enabled the use of closed loop temperature control via modulating the spindle speed. A series of four builds were completed using closed loop temperature control with temperature setpoints of 700 ºC, 750 ºC, 800 ºC, and 850 º C for 24 layers deposited as 4 bars with 6 layers each and a commanded deposit length of 152.4 mm (6 in). This resulted in a wall approximately 38 mm (1.5 in) wide and 184 mm (7.25 in) long with a height of (0.98 in). The process parameters used for each build are given in **Table 2.** All deposits were made using a back-and-forth raster pattern.

For the closed-loop temperature-controlled builds, four type K thermocouples were placed in machined channels in the build plates spaced 50.8 mm (2 in) apart approximately in line with the longitudinal direction of the deposit and 6 mm (0.236 in) from the top surface of the build plate (**Figure 2**). The thermocouple readings were recorded by the machine and logged at a 1 Hz rate. The thermocouple wires were routed through a sealing plate mounted on the enclosure to maintain an inert build environment.

Due to the reactivity of titanium, all builds took place in a custom fabricated enclosure (Figure 3) made of Stretchlon 800 vacuum bagging film backfilled with welding-grade argon (Airgas, USA). All materials needed for each build were pre-staged

Table 2: PID Temperature Control Process Parameters

Tool Temperature Setpoint	Traverse Feed Rate		Material Feed Rate	
°C	mm/s	in/min	mm/s	in/min
700	2.12	5.00	0.93	2.20
750	2.54	6.00	1.12	2.64
800	3.39	8.00	1.49	3.52
850	4.23	10.00	1.86	4.40

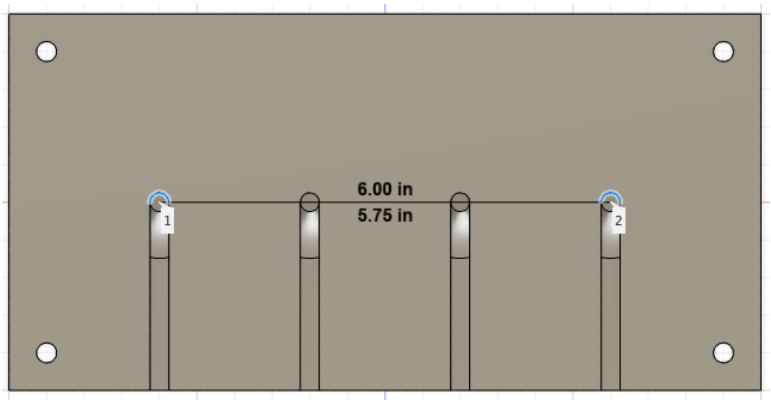


Figure 2: Build plate thermocouple locations

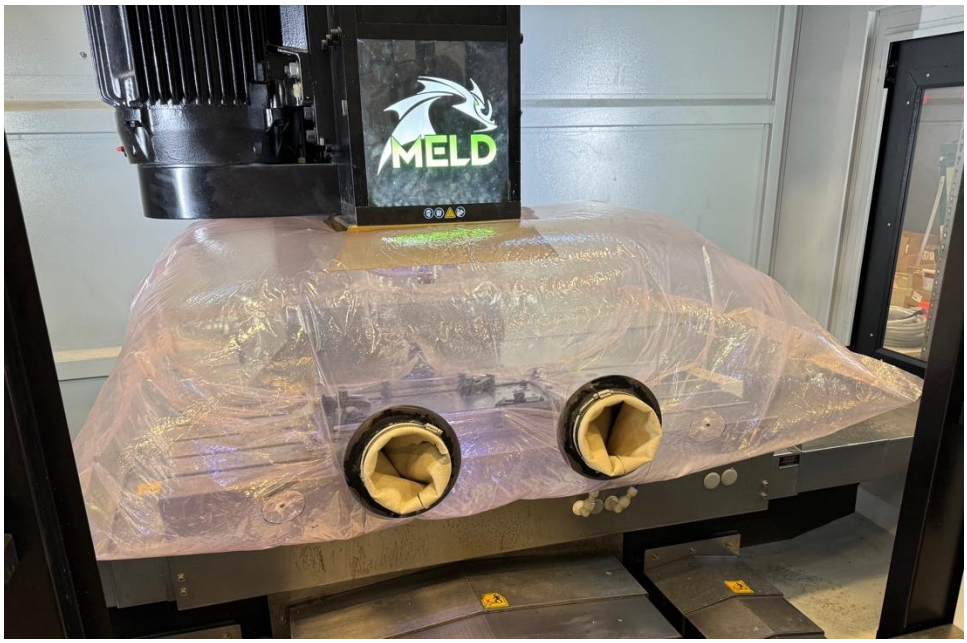


Figure 3: Inert Environment Enclosure

in the enclosure to eliminate the need to open the enclosure during bar reloads. Material feed reloads were accomplished using gloves built into the enclosure in a glovebox type arrangement. Therefore, an inert environment was maintained over the course of the build, including during cooling.

In-Situ Data Collection

Machine Data Logging

The MELD L3 machine logged information during deposition and saved the resulting data in a .csv file. The .csv file logged the date, time, spin velocity, spin torque, spin power, feed velocity, feed position, feed torque, actuator force, feed rate override multiplier, path velocity, XYZ position, XYZ velocity, XYZ torque, oxygen content in the build chamber, tool thermocouple temperature, and the four build plate type-K thermocouple inputs at a 1 Hz logging rate. The resulting data was plotted using Matplotlib (168) and Python.

Infrared Thermography

A FLIR A70 thermal camera was used to collect infrared thermography during each build. The camera was placed approximately 0.2 m (8 in) from the build, perpendicular to the tool travel direction, allowing the camera to monitor the entire side profile of the build as well as the tool temperature. The placement is detailed in **Figure 4.** The data was logged at a 30 Hz rate. The spectral sensitivity range of the camera is listed as 7.5-14-microns, meaning it is a long-wave infrared camera. The temperature vs time

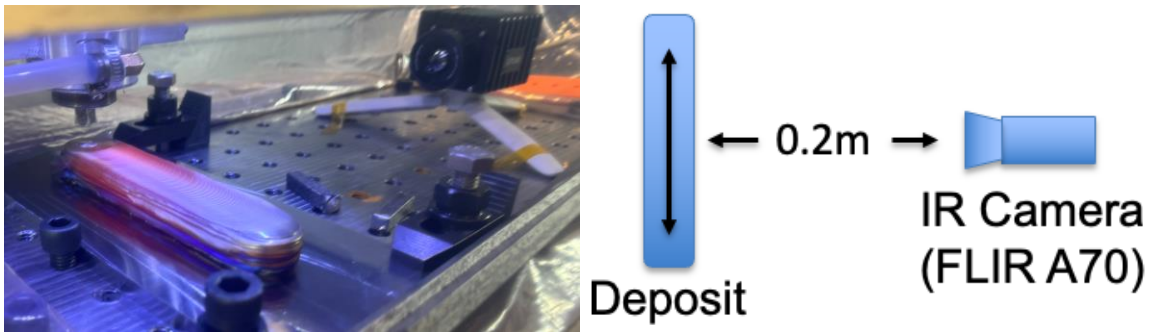


Figure 4: IR Thermography Setup

data during deposition was recorded using the factory calibration assuming an emissivity of 0.95.

Metallography

Samples were sectioned normal to the travel direction using a wire EDM. The sectioned samples were mounted in a 50mm puck using Buehler KonductoMet, a conductive, hot mount phenolic resin, in a Buehler SimpliMet 3000 Automatic Mounting Press. Care was taken to ensure the samples were mounted with respect to the final layer traverse direction being into the sample. The samples were then ground on a Buehler AutoMet 300 Pro with progressively finer grits of Struer's SiC grinding foil from FEPA P #320 until plane and the EDM recast layer was removed. Then ground further up to at least a #2,000 grit for one minute per step at 20N individual force. Samples were visually inspected and touched up via hand polishing as needed at each step to ensure planeness across the entire surface and that no deep scratches remained from previous grinding steps. Following this, the samples underwent attack polishing using a chemical/mechanical polish mixture (96% 0.05-micron colloidal silica, 2% hydrogen peroxide (30%), 2% ammonium hydroxide (25%)) for at least 30 minutes until no visible scratches remained at 40N individual force using a Struer's MD-Chem polishing pad. Optionally for EBSD, some samples underwent a final polish using 0.05-micron colloidal silica on a VibraMet2 for at least 6 hours to minimize surface deformation, however, this step was later found to be unnecessary after the chemical/mechanical polishing step. All samples were rinsed in tap water and cleaned with a neutral detergent on a cotton ball and additional tap water. The cleaning steps were followed by an ethanol rinse before being gently dried with compressed air to prevent the formation of water spots.

Etching to reveal the microstructure for optical microscopy was conducted on freshly polished samples in a PTFE beaker using a solution of Kroll's reagent (ES Laboratory, LLC, USA) as defined by ASTM E407 #192 (169) for approximately 5-10 seconds until the microstructure was revealed. This step was immediately followed by immersion in DI water. Afterwards, the samples were rinsed with tap water and again with methanol then gently dried with compressed air.

Optical microscopy was performed on the etched samples using a Keyence VHX 7000. Images were taken up to 1,000x magnification. To create the large area micrographs, the microscope was commanded to take tiled grid images across the entire surface of the sample. Individual images were stitched into mosaics for each build condition using FIJI's image stitching plugin (170,171) after undergoing a pseudo-flat field de-vignetting procedure (172). Additional images were taken using the Keyence Optical Shadow Effect Mode to provide enhanced contrast via compositing multiple images taken with varying light angles.

Backscattered scanning electron microscope images were taken using a Zeiss Gemini 450 FE-SEM. The use of the BSE detector allowed for imaging by element Z-contrast to reveal compositional differences. Additional, large-scale BSE montage imaging scans were conducted on the 700 ºC and 850 ºC temperature setpoints to gather information on the tungsten contamination distribution for the lowest and highest temperature deposition conditions. The montage images were CLAHE filtered and denoised to better see the tungsten contamination distributions.

Identification of Microstructures

Image analysis was performed on the 500x magnification montage optical images of a tensile bar from each temperature setpoint condition in the polished and etched condition to characterize the microstructure over the area of the tensile bars. An approach was developed to characterize the microstructures in an automated fashion over the entire montaged optical images. An unsupervised machine learning approach was developed using Python and Scikit-learn (173). Multiple methods, including Gaussian mixture modeling and K-means clustering among others, were tested; however, the best results, based on a manual characterization of selected areas, resulted from an agglomerative clustering approach to group analyzed areas of the microstructure based on a set of selected image features.

The montage input images were converted to grayscale and normalized using the OpenCV library in Python. For image features, a gray level co-occurrence matrix (GLCM) was calculated in patches for the montage images using the scikit-image library. A GLCM measures an image's texture, where texture, in this case, refers to the spatial arrangement of grayscale values in the image and not crystallographic texture. For a given pixel, statistics are calculated for adjacent grayscale pixels horizontally, vertically, and diagonally. It was found that the GLCM Correlation and Dissimilarity/Homogeneity measures produced distinct groupings between the equiaxed and lamellar microstructure morphologies for a test image, as seen in **Figure 5**. Correlation in the context of a GLCM is a measure of the linear dependency of gray levels. Dissimilarity is a measure of the variation of gray levels between pixel pairs. Homogeneity measures the distribution of elements in the GLCM to the GLCM diagonal. The GLCM matrix was calculated for

500x magnification montage images of the ND-LD tensile bars in a 150 pixel by 150 pixel kernel. The 150 pixel by 150 pixel kernel was chosen as a good compromise among RAM usage, processing time, and accurate unsupervised labeling. The image feature matrix was then used as an input for the agglomerative clustering algorithm from the scikit-learn library with a user defined 3 clusters. The results were plotted using Python and matplotlib.

Electron Backscatter Diffraction

Orientation Imaging Microscopy (OIM) was performed on cross sectioned samples in the transverse-normal plane using Electron Backscatter Diffraction (EBSD). A Thermo Scientific Helios 5 DualBeam FE-SEM was paired with an EDAX Velocity Pro EBSD detector to capture orientation information in the as deposited microstructure. The data was collected at an accelerating voltage of 20 kV and a probe current of 52 nA to 100 nA at a 70º sample tilt, a 10º detector tilt, and approximately a 10 mm working distance. The open-loop EBSD patterns were Hough indexed in EDAX APEX software. The closed-loop AFSD EBSD patterns was spherically indexed using EmSphInx at a bandwidth of 158 (174). Both the HCP alpha phase and BCC beta phase were indexed for each method. Note that Hough indexed EBSD pattern quality maps use the image quality metric, while the spherically indexed EBSD pattern quality maps use the sharpness index.

The acquisition of simultaneous EDS data was attempted; however, high X-Ray counts resulting from using high probe currents exceeded the maximum count rate limits of the detector, resulting in the detector being automatically retracted by the software.

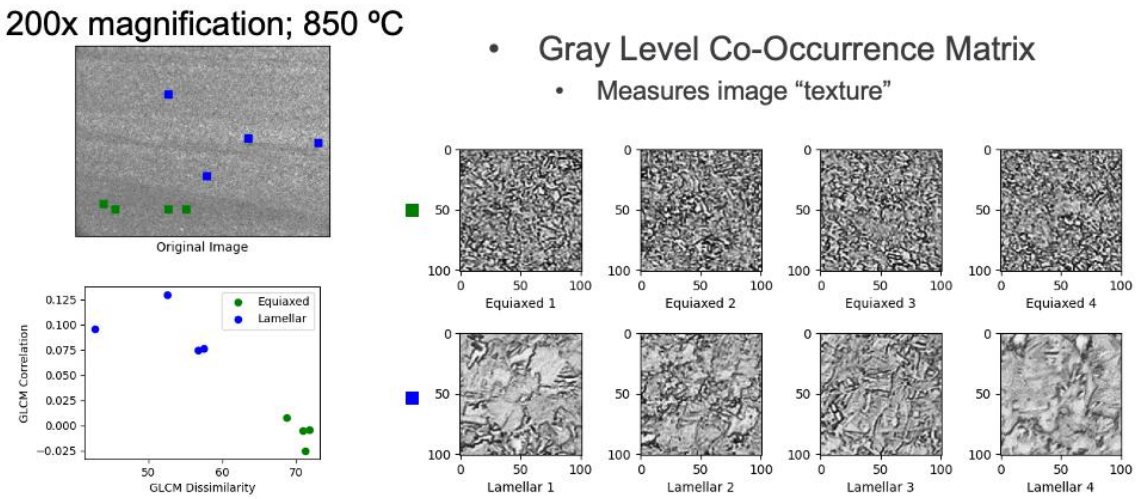


Figure 5: GLCM for microstructure classification

Prior Beta Reconstruction

A graph clustering algorithm implemented in the MATLAB toolbox MTEX was employed for prior beta reconstruction (127). First, alpha grain boundaries were calculated using a 1.5-degree threshold to limit the chance of alpha grains that originate from different prior beta grains being erroneously grouped into the same grain. A graph was then calculated for the entire map with a misorientation threshold of 1.4 degrees and a tolerance of 2 degrees. The clustering algorithm was then applied with three iterations to maximize the quality of the reconstruction and the number of successfully reconstructed grains. Finally, parent grains were calculated based on the likelihood of sharing a common parent beta grain with a minimum probability criterion of 50%.

X-Ray Diffraction

X-ray diffraction (XRD) was conducted with a Malvern Panalytical Empyrean with a 240 mm goniometer using a $CuK\alpha_1$ X-ray source at 45 kV / 40 mA to investigate the effects of oxidation resulting from deposition in an imperfect inert environment. Two samples were measured, with one exhibiting a shiny, metallic gray surface finish, while the second sample showed a blue/purple color, indicating surface oxidation (**Figure 6**). XRD was used to determine the resulting phase fractions at the top surface of the deposited material for both samples. Due to issues with collecting data on the as-built onion-skin surface finish, parallel beam optics XRD analysis was employed using a Xe proportional detector to mitigate errors associated with sample alignment and surface finish.



Figure 6: Oxidized (#2) and Unoxidized (#1) Samples

Additional XRD was conducted on polished cross-sections in the transverse-normal plane (TD-ND) as well as a polished cross section sample of the feedstock. The experimental setup is shown in **Figure 7**. Due to the use of a polished cross-section, parallel beam XRD was not required, and a PIXcel3D detector was used. The measurement area was 4 mm in the transverse direction (TD) of the sample/equatorial axis of the diffractometer by 20 mm in the normal direction (ND) of the sample/axial direction of the diffractometer. The measurements were centered in the middle of sample and oriented to capture diffraction data over multiple layers and deposited bars of the build. The goniometer was scanned over the range of approximately 30 degrees to 140 degrees 2-theta. The instrument resolution function was determined from NIST SRM 640e (Si) using the fundamental parameters approach. Rietveld refinements were performed in TOPAS v7. The results were plotted using Matplotlib (168) and Python.

Mechanical Testing

Microhardness

Microhardness testing was performed on the mounted and polished samples using a LECO AMH55 Automatic Hardness Tester with a LM110 Series Vickers indenter as according to ASTM E384 (175). A total of 10,000 indents for each sample were made in a 100 x 100 grid with a 250-micron spacing, a 1.961 N (200 gf) force, and a 10 second dwell time. Average indent diagonals were on the order of 30 microns, meaning the spacing exceeds the 2.5x indent diagonal requirement to ensure data quality. The microhardness measurements for the feedstock were made in a 25 x 40 grid while maintaining the same 250-micron spacing, 1.961 N (200 gf) force, and 10 second dwell

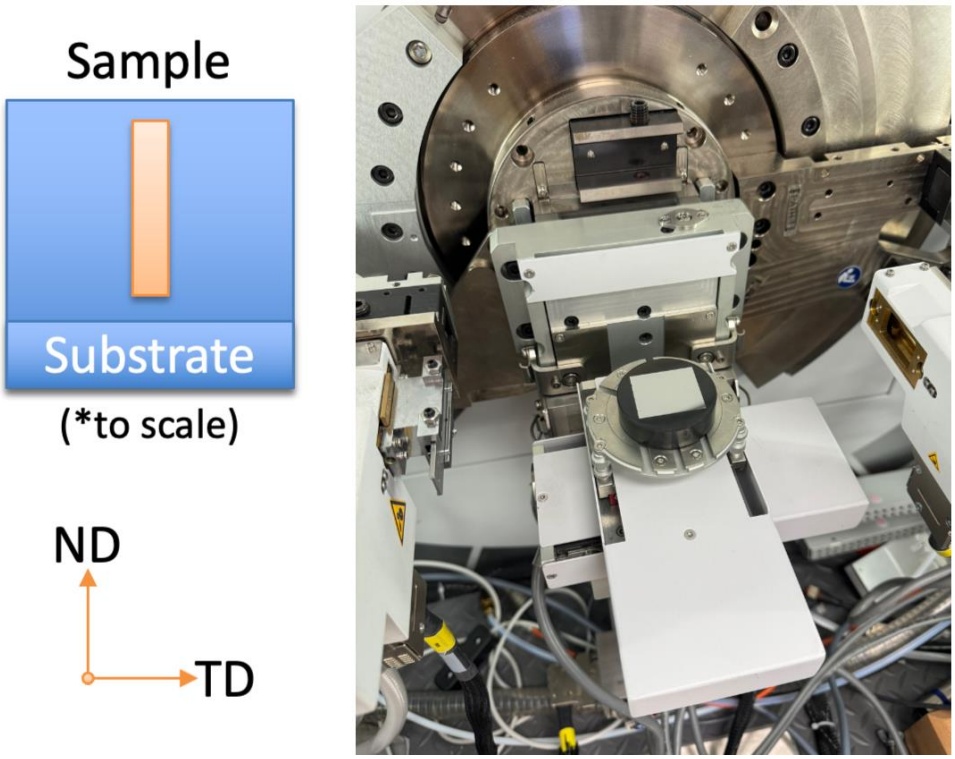


Figure 7: XRD experimental setup

time. For all samples, the resulting indents were automatically measured with a 50x objective, refocusing at every indent, because it was found that periodic refocusing introduced measurement artifacts. The resulting hardness data was plotted using Matplotlib (168) and Python.

Quasi-Static Tensile Testing

Tensile bars were extracted using electric discharge machining on a Mitsubishi MV2400 EDM using the steel machining setting as recommended by the user manual. A sub-size tensile bar geometry (**Figure 8**) was chosen to ensure that the gage section would consist entirely of deposited material for the Z-direction samples. Note that this tensile geometry is smaller than the ASTM E8 defined sub-size tensile geometry. Additional material was included on one end of the tensile bar to facilitate EDM cutting. Samples were extracted in the weld (travel/longitudinal) direction (LD-TD), transverse direction (TD-LD), and normal (build) directions (ND-LD). The naming convention is that the first direction represents the long axis of the tensile bar, and the second direction is the second axis making the plane of the flat surface of the tensile bar.

For the in-plane samples (LD-TD and TD-LD), the sample are numbered starting from the top of the build height, i.e. the top extracted sample is numbered one. For the normal direction samples (LD-TD), the samples are numbered starting from the final layer retreating side. The normal direction samples were extracted in locations including the flash, meaning that some of the samples did not have full bonding in the flash regions.

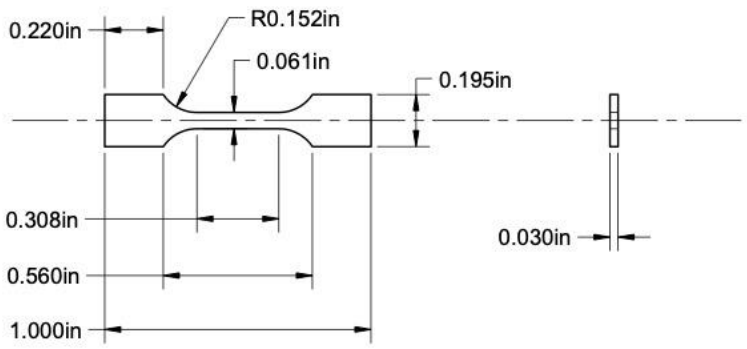


Figure 8: Subscale Tensile Bar Geometry

Sample numbering for these samples started and ended at the first and last samples that remained whole after the EDM extraction process. In the build direction, a total of 27 tensile bars were extracted from the 700 ºC temperature setpoint while 26 tensile bars were extracted from the 750 ºC, 800 ºC, and 850 ºC temperature setpoints.

The layout of the sample extraction was planned so that the gage volumes would not be near the turnaround locations and would instead be closer to the center of the deposit to avoid the effects of thermo-mechanical transients at the extremes of the deposit. The sample layout is given in **Figure 9**. The samples were extracted using only a single pass of the EDM with no finishing passes. Sample width, thickness, and total length were measured with calipers for each sample. A matte black speckle pattern was then applied over a matte white base coat using an airbrush. Samples were tested in the as-built condition. No other surface preparation was performed.

Quasi-static, room-temperature tensile testing was performed on a servo-hydraulic MTS 858 Table Top System with a calibrated 25 kN load cell using a constant crosshead speed (displacement control) of 0.1238 mm/min (0.004875 in/min) to achieve a 0.0158 /min strain rate as according to ASTM E8 (176). The samples were tested until fracture at a sampling rate of 10 Hz. The samples were placed into an aligned shoulder grip fixture. The fixture was gripped by hydraulic wedge grips. Sample preload was manually zeroed as needed by moving the crosshead. A black speckle pattern was applied over a white base coat using an airbrush to facilitate 3D digital image correlation (3D-DIC) using a two-camera setup. Images of the speckle pattern were acquired at a frequency of 5 Hz, and the resulting images were processed using *VIC-3D v8* (Correlated Solutions, USA).

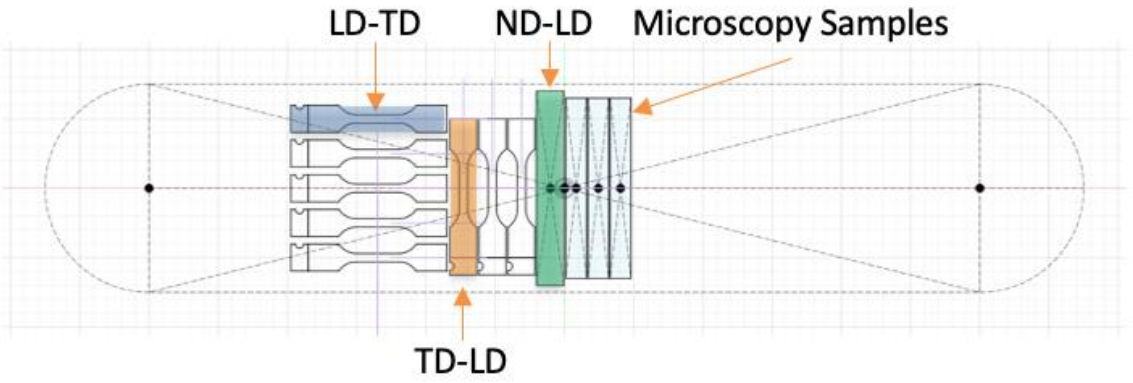


Figure 9: Tensile Bar and Microscopy Sample Extraction Locations

Prior to testing, the DIC software was calibrated using a calibration target. Strain was measured both locally at the failure location using 3D-DIC and over the full gage section using a virtual extensometer. Stress data was correlated to DIC data via timestamp and interpolation with a MATLAB script.

Chemical Analysis

Bulk Chemical Analysis

EAG Laboratories (Liverpool, NY) was used to analyze the bulk oxygen and nitrogen content in the samples. The testing was conducted in accordance with ASTM E1409 (177). The oxygen content was measured using the inert gas fusion non-dispersive infrared detection method. The nitrogen content was measured by inert gas fusion thermal conductivity detection. A total of five samples were analyzed at 700 ºC, 750 ºC, 800 ºC, 850 ºC, and feedstock. The submitted sample size was on the order of 2 g of material, corresponding to the equivalent of approximately a 5 mm – 7.5 mm cube. It was reported by EAG that the samples were run in replicates of 3-5 and reported as the average to two significant figures. These samples were extracted via EDM at the same time as the tensile specimens to ensure the measurements are being taken at the same place in all the builds and each sample consisted of multiple layers worth of deposited material. This bulk analysis was intended to show how much oxygen and nitrogen was taken into the sample as an average across multiple layers.

Energy Dispersive X-Ray Spectroscopy

Energy dispersive X-ray spectrometry (EDS) is a chemical analysis technique that uses excited X-rays from the interaction of an electron beam on a material inside an SEM. A Zeiss Gemini 400 FE-SEM was used with a Bruker XFlash 6|60 ex EDS detector

to perform both qualitative and standardless Phi(Rho-Z) quantitative EDS with an accelerating voltage of 15 kV and a probe current of 20 nA. The results were processed in the Bruker Espirit software.

Electron Microprobe Analysis

Wavelength dispersive spectrometry (WDS) is a similar method to EDS that has an improved peak-to-background ratio better enabling detection of low atomic weight and trace elements. It is hypothesized that WDS can be used to investigate the dark etching bands of equiaxed alpha near the top surface of the titanium samples to determine if the change in microstructure can be attributed to oxygen contamination. An attempt at WDS was undertaken using a Zeiss EVO SEM equipped with a EDAX WDS detector; however, the tungsten filament microscope had difficulty achieving the required resolution to discern microstructural features. Instead, WDS was done using a JEOL 8200/8500 electron microprobe equipped with five tunable WDS detectors at Oak Ridge National Lab. For this experiment, a 200-micron line scan was conducted across a band of equiaxed alpha. The line scan was conducted with a 1 micron spacing between sampled points.

The microprobe data was collected at an accelerating voltage of 15 keV and a beam current of 50 nA. The take-off angle for the instrument was 40 degrees. The elements investigated were Al, Ti, V, W, O, C, and N. Detection limits ranged from 0.007 wt. % for V to 0.680 wt. % for O. An additional 12 randomly distributed measurements were taken in a reference sample of sectioned and polished feedstock.

CHAPTER 4

EXPERIMENTAL RESULTS

Closed Loop AFSD Builds

Using a type-K thermocouple equipped, lanthanated tungsten tool, a series of temperature-controlled depositions were conducted. These depositions were conducted at temperature setpoints of 700º C, 750º C, 800º C, and 850º C. All depositions were made using the same tool in order of decreasing temperature. It was observed that as the deposition temperature decreased, the visual appearance of the as-built samples progressively transitioned from a dull light straw color to a shiny metallic silver **(Figure 10**).

In-Situ Data Collection

Machine Data Logging

For the closed-loop temperature-controlled samples, the mean tool temperature as measured by the tool thermocouple very closely matched the commanded temperature setpoint. The mean tool temperature and standard deviation are given in **Table 3**. There is a slight trend of increasing tool temperature standard deviation with increasing temperature setpoint, however, this is likely explained by the difference in traverse speed for the different build conditions. The lower temperature setpoint conditions, having a lower traverse velocity, give more time for the PID loop to maintain temperature after the disruptions induced by layer changes.

The oxygen content inside the enclosure was measured using an oxygen sensor build into the machine located near the tool. The mean and accompanying standard



Figure 10: Closed-Loop Temperature Controlled Builds

Table 3: Closed-loop temperature control setpoint, mean, and standard deviation

PID Temperature Setpoint [ºC]	700	750	800	850
Mean Tool Temperature [ºC]	700.22	750.57	801.36	851.72
Tool Temperature Std. Dev. [ºC]	14.492	17.401	20.938	19.713

deviation for the oxygen content in the chamber are given in **Table 4.** While the enclosure remained sealed during deposition and material reload events there was some residual oxygen in the enclosure during the AFSD process. Average oxygen concentrations during all builds was 0.6% though there was some variation in the standard deviation of the oxygen content during the different builds. Particularly, the 850 ºC temperature setpoint had the highest standard deviation in the oxygen measurements at 0.3 %.

The measured tool and build plate thermocouple temperatures are shown in **Figure 11.** It can be again seen that the PID temperature control loop was able to maintain the desired temperatures during deposition. There are peaks that correspond to the start of each of the 6 layers per bar that then settle back towards the temperature setpoint with some ringing. Note that the build times for each deposited bar increase with decreasing temperature due to the differences in build parameters.

A look at the spindle power in **Figure 12** (a) shows that the spindle power converges about a single point for each of the deposition temperatures. A similar trend is seen in **Figure 12** (b) for the spindle velocity. Interestingly, it was found that actuator force was not strongly correlated to the tool temperature as seen in **Figure 13**. This may indicate that deformation in the bar inside the tool and deformation in the stir zone below.

Infrared Thermography

Analysis of machine log files and infrared thermography for the closed-loop temperature-controlled builds was performed to measure the tool temperatures and to

Table 4: Measured oxygen content in the enclosure during AFSD

PID Temperature Setpoint [ºC]	700	750	800	850
Mean O_2 [%]	0.6	0.6	0.6	0.6
O_2 Std. Dev. [%]	0.2	0.1	0.2	0.3

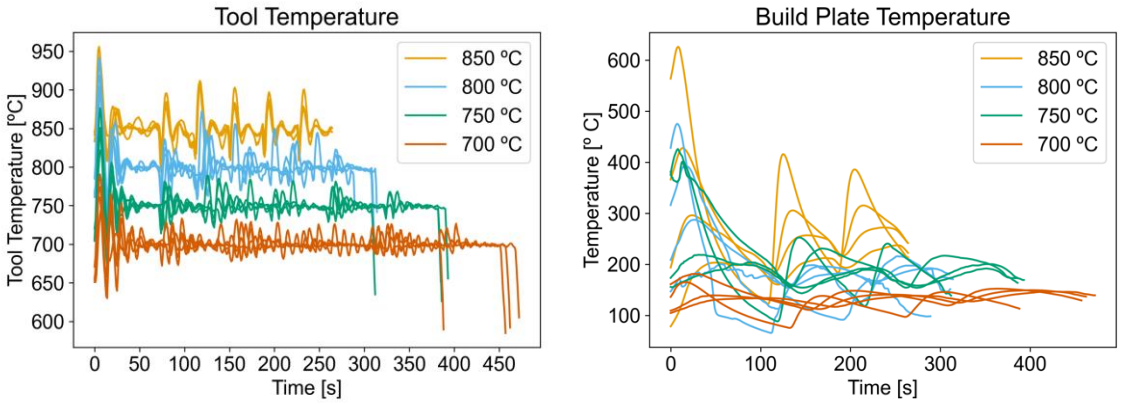


Figure 11: Measured (a) tool thermocouple and (b) build plate thermocouples for all temperature setpoints

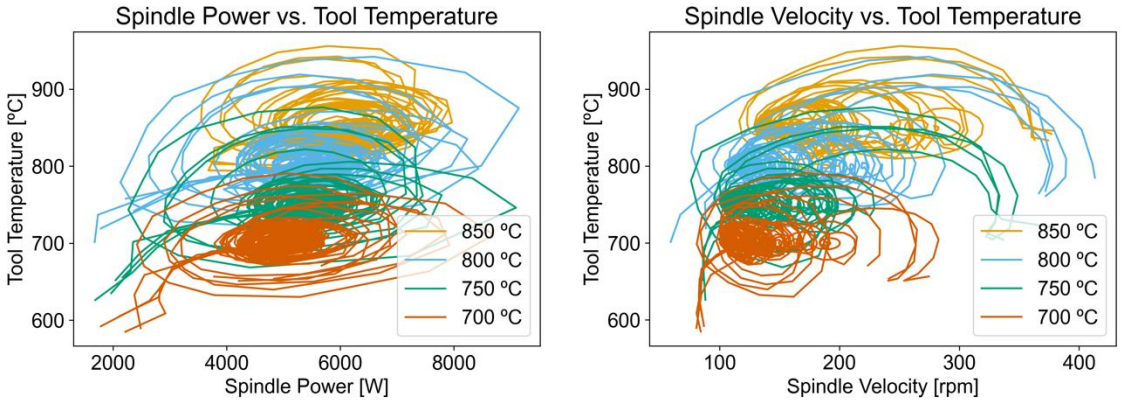


Figure 12: Tool temperature as a function of (a) spindle power and (b) spindle velocity

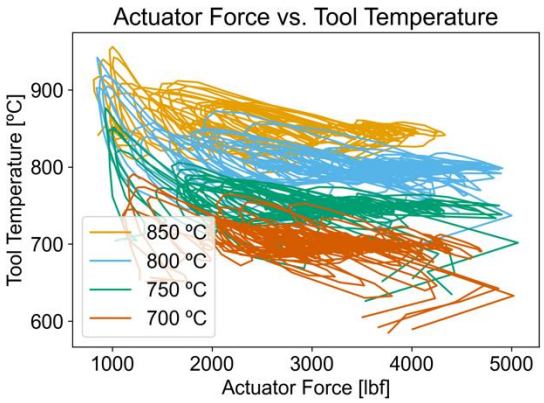


Figure 13: Tool temperature vs. material feed actuator force

investigate thermal cycling in the material over the deposition of multiple layers. For the investigation of the temperatures recorded by the tool-embedded thermocouple, the measured temperatures were compared to the temperatures as monitored by IR thermography. The results for the 700 ºC AFSD build for the first deposited bar of material are given in **Figure 14**. While the trends align, there is an increasing temperature mismatch between the two readings as the build progresses through the six printed layers. By the end of the sixth printed layer, the maximum measured temperature by the IR camera is approaching 750 ºC, a full 50 ºC higher than the temperature as measured by the tool thermocouple. This finding may be of particular significance for comparing results of different methods of closed-loop temperature control of AFSD titanium, such as in Yoder et al. (9).

Metallography

Closed-Loop Temperature-Controlled Builds

A montage image of the Kroll's reagent etched cross-section for the closed-loop temperature-controlled builds is presented in **Figure 15**. Observation of the micrographs shows contrasting light and dark etching regions that appear to be in a layered pattern. This pattern is consistent with many additive manufacturing processes. A comparison of the montage images for each temperature setpoint reveals some differences between the processing conditions. The highest temperature setpoints, 850 ºC, appears to have larger areas of light and dark etching with some smaller variation in the dark etching regions. The 800 ºC temperature setpoint also has some of the same large areas of light and dark

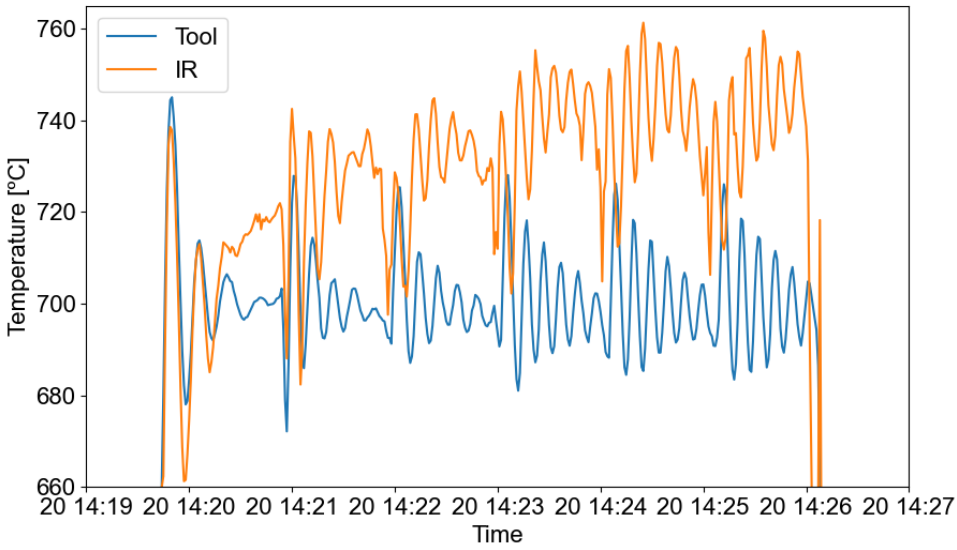


Figure 14: IR vs. tool thermocouple for 700 ºC build, feed bar #1

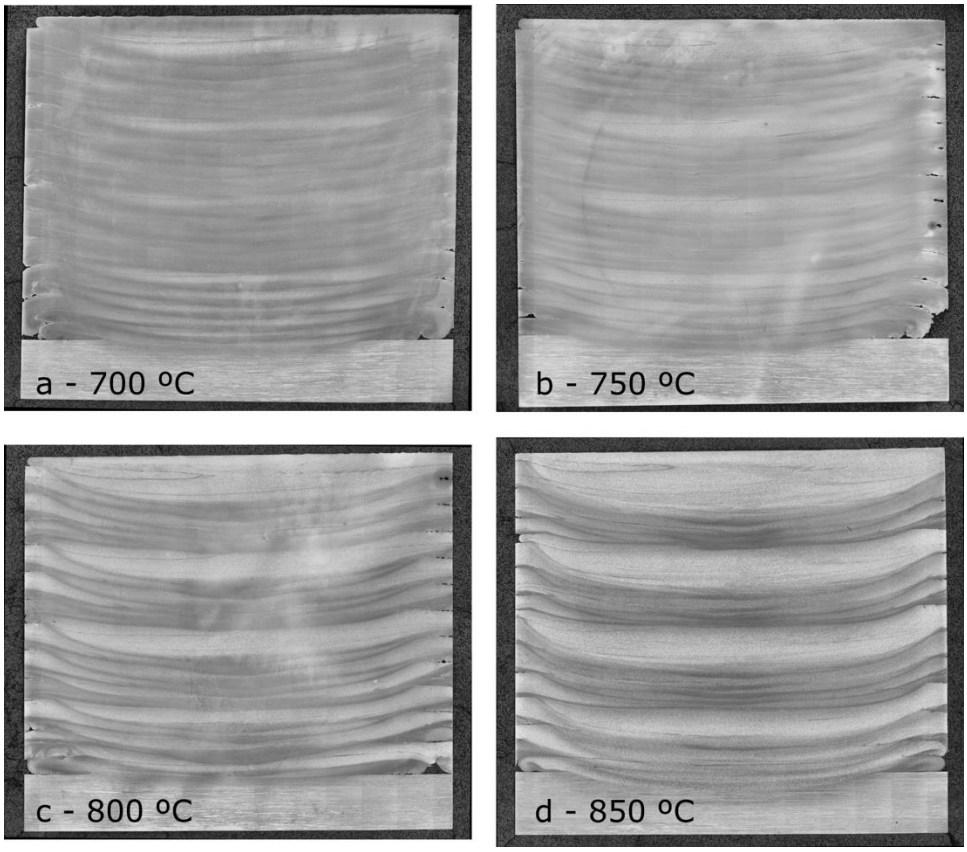


Figure 15: Closed Loop AFSD Ti-6Al-4V Builds at a) 700 ºC, b) 750 ºC, c) 800 ºC, and d) 850 ºC

etching however, they are smaller as compared to the 850 ºC build. While the 700 ºC and 750 ºC temperature setpoints show some light etching areas, they are predominantly darker etching.

In the case of the 850 ºC temperature setpoint, the microstructure can be divided into four distinct regions in a characteristic repeating pattern of etching contrast. It is worth noting that all the builds were completed using four bars of material with cooling of the builds between reloads. The 800 ºC build also exhibits a similar repeating pattern of etching, however, it is less pronounced that the 850 ºC case. Upon close observation, there is a darkly etching swirl visible in the final deposited layers of each sample. The build plate of all the deposition conditions shows a rolled, mill annealed microstructure.

Beyond the large-scale etched montages, the AFSD Ti-6Al-4V builds were examined optically at high resolution. In the 700 ºC temperature setpoint, the microstructure in the stir zone is completely equiaxed alpha as seen in **Figure 16**. There are no other microstructure morphologies seen in the top region of the final layer stir zone. The diameter of the equiaxed alpha grains are on the order of 1 micron. Increasing to the 750 ºC temperature setpoint, the microstructure is a mixture of lamellar and equiaxed alpha. The final layer center stir zone microstructure is shown in **Figure 17**. From the visible grain boundary alpha, the prior beta grain boundaries are small, on the order of 10 microns diameter. It was also observed that different areas of the lamellar microstructure exhibited different etching characteristics.

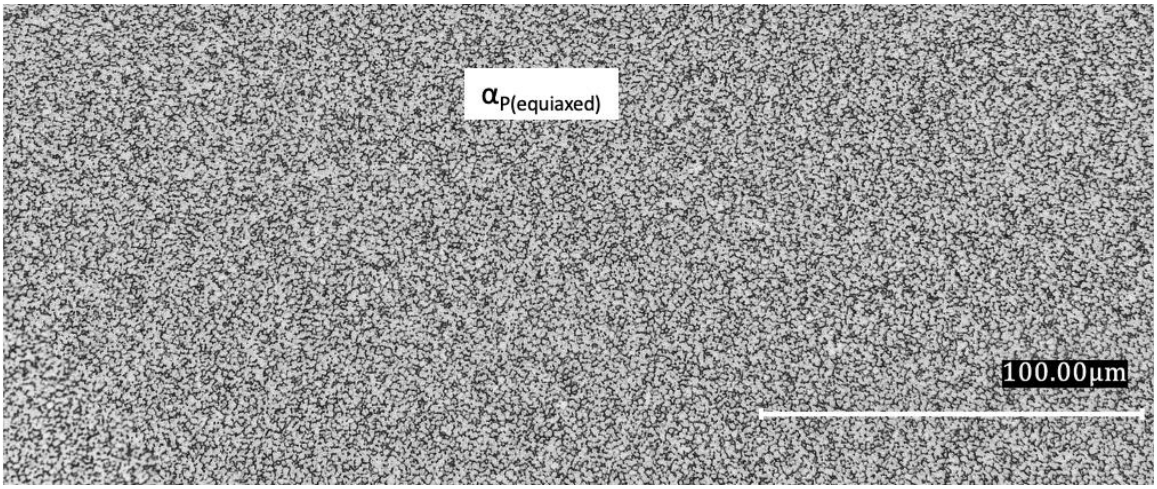


Figure 16: 700 ºC sample final layer center stir zone

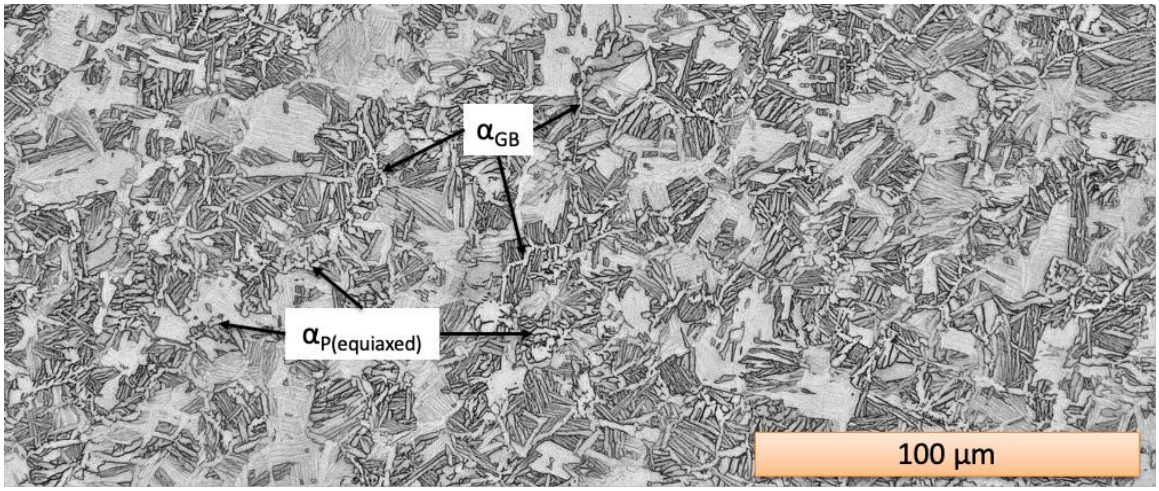


Figure 17: 750 ºC sample final layer center stir zone

The 800 ºC temperature setpoint yields a mixed microstructure also consisting of lamellar and equiaxed alpha. The 800 ºC temperature setpoint final layer stir zone microstructure is given in **Figure 18**. Additionally, the lamellar areas show morphologies of both basketweave and colony alpha. The prior beta grain size is slightly larger than the 750 ºC temperature setpoint. The different etching characteristics visible in the 750 ºC sample are not as strongly observed. Like the 750 ºC temperature setpoint, both equiaxed and lamellar morphologies are present. The microstructure appears to have a greater fraction of lamellar morphologies as compared to equiaxed alpha.

The 850 ºC temperature setpoint exhibits a fully lamellar microstructure consisting of grain boundary alpha decorating the prior beta grain boundaries, as seen in **Figure 19.** There are some regions with distinct colonies of alpha laths, however, most of the prior beta grains display interweaving alpha laths characteristic of a basketweave microstructure. The prior beta grain size is again larger than both the 750 ºC and 800 ºC temperature setpoints. This microstructure does not show any equiaxed alpha.

Identification of Microstructures

Agglomerative Clustering Approach

An unsupervised machine learning approach using agglomerative clustering of GLCM image texture features was used to characterize the microstructures in the polished and etched ND-LD tensile bars using 500x montage images. The results of this approach can be seen in **Figure 20.** The agglomerative clustering approach can distinguish the lamellar microstructure morphology from the equiaxed alpha morphology as well as from the image background.

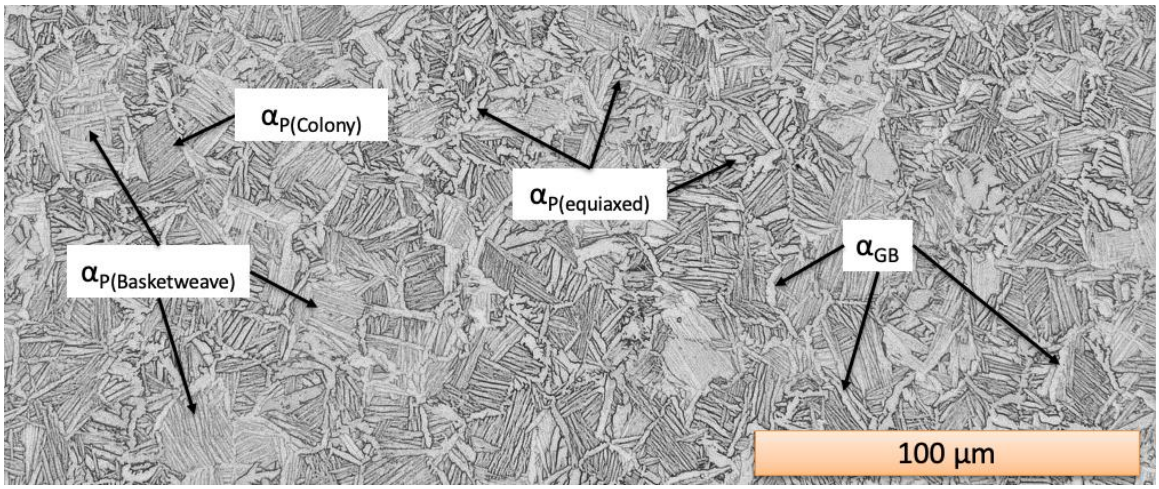


Figure 18: 800 ºC sample final layer center stir zone

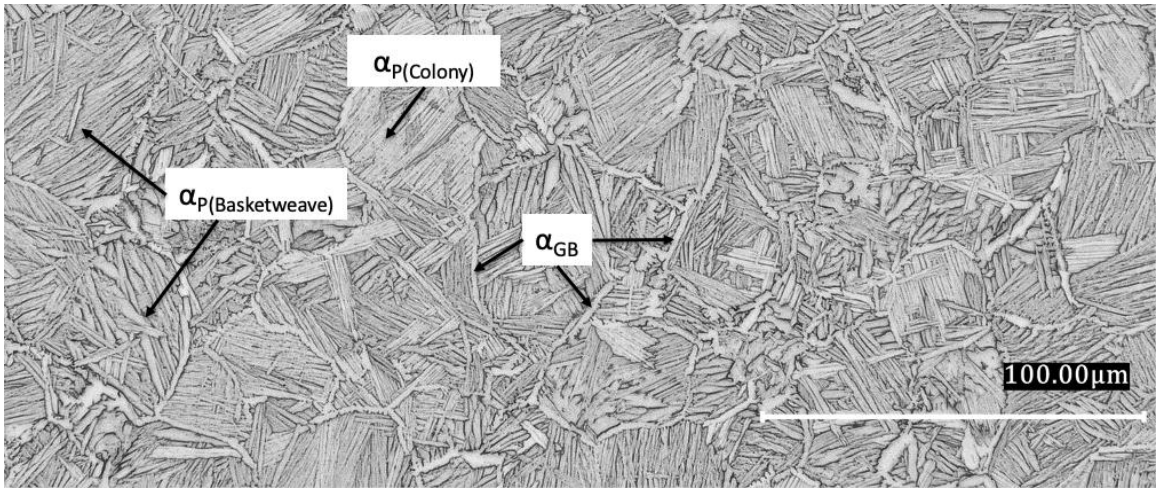


Figure 19: 850 ºC sample final layer center stir zone

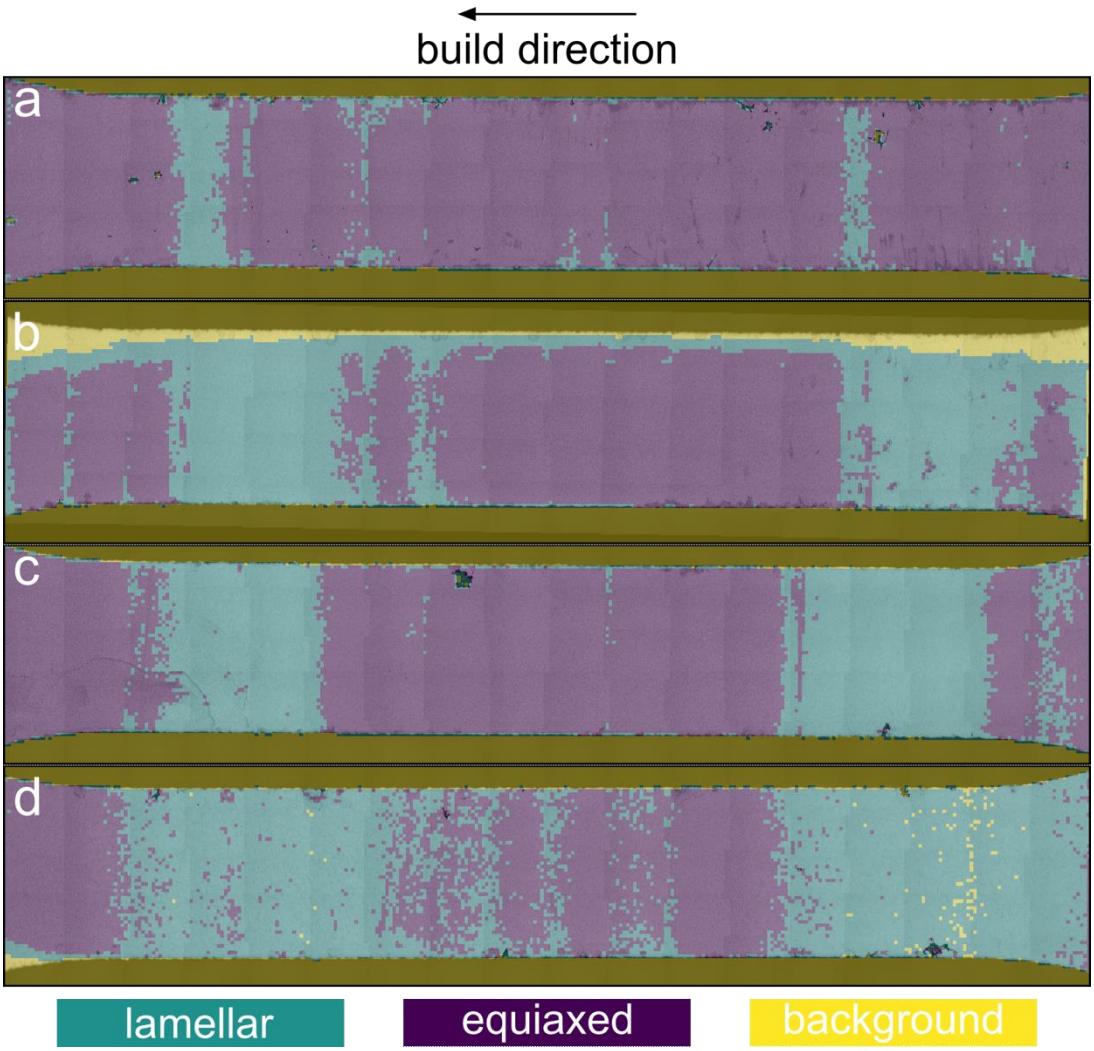


Figure 20: Agglomerative clustering results on polished and etched tensile bar 500x montage image for (a) 700 ºC, (a) 750 ºC, (a) 800 ºC, (a) 850 ºC temperature setpoints

In all the polished and etched tensile bar images, it can be observed that there are microstructural banding between equiaxed and lamellar morphologies. In some of the tensile bars, there are additionally smaller bands of equiaxed microstructure as seen in **Figure 21**.

While the agglomerative clustering approach does capture most of the microstructure morphology changes in the polished and etched tensile bars, there are some incorrectly identified areas. In the 750 ºC tensile bar montage images, the top row of images was slightly out of focus, causing those areas to be incorrectly identified as the background. Additionally, in the 850 ºC tensile bar, portions of the lamellar region were also incorrectly identified as the background. Image stitching artifacts also appears to affect the microstructure characterization in some cases like the 750 ºC tensile bar montage image.

The percentages of the microstructure morphology between lamellar and equiaxed derived from the agglomerative clustering approach are given in **Table 5**. Based on these results, there is a roughly increasing trend in the percentage of lamellar microstructure morphology with increasing temperature setpoint ranging from 10.8 % for the 700 ºC temperature setpoint to 58.6% for the 850 ºC temperature setpoint, though the 750 º and 800 ºC intermediate temperature setpoints have roughly similar lamellar fractions of 43.1 % and 36.9 %.

Electron Backscatter Diffraction

Closed-Loop Builds

EBSD results for the top layer center stir zones are shown in **Figure 22**. The EBSD scans were taken in similar areas. The 700 ºC deposition temperature shows a completely

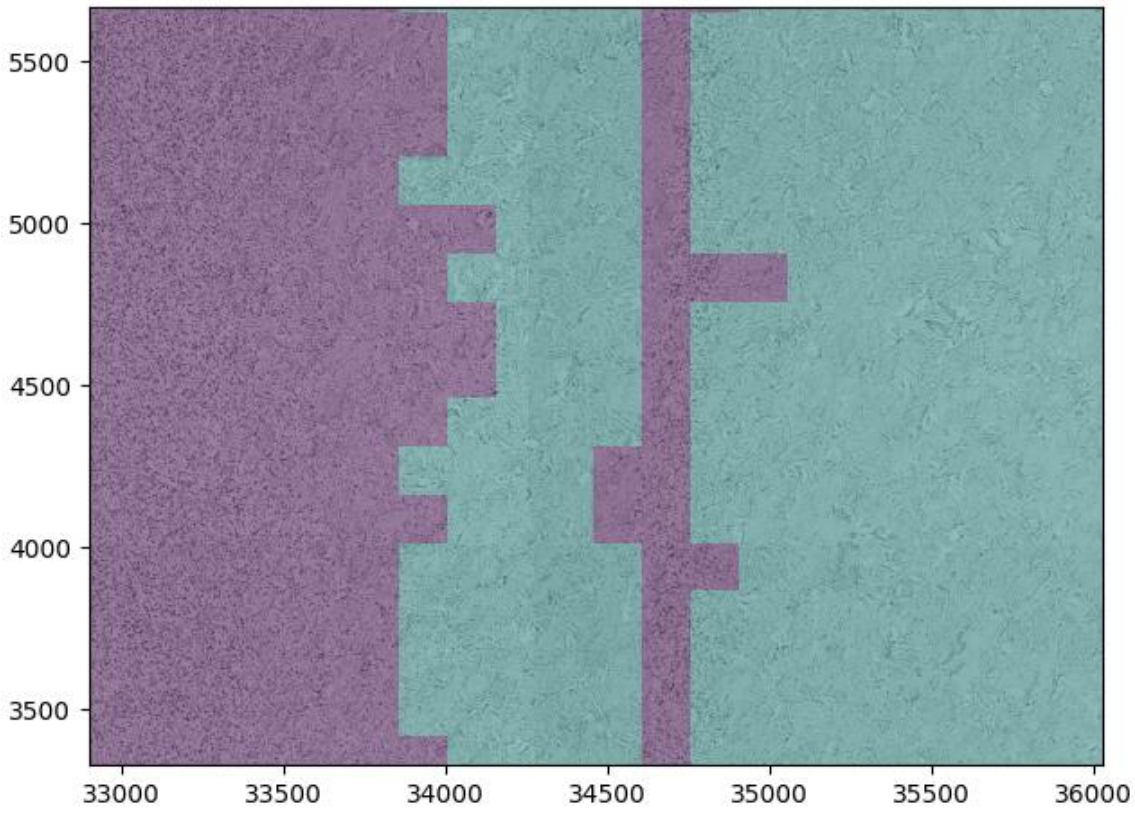


Figure 21: 800 ºC polished and etched tensile bar selected area (axes are given in pixels)

Table 5: Microstructure characterization of polished and etched tensile bars

	700 ºC		750 ºC		800 ºC		850 ºC	
	# Patches	%	# Patches	%	# Patches	%	# Patches	%
Lamellar	1698	10.8%	6231	43.1%	5883	36.9%	9130	58.6%
Equiaxed	14008	89.2%	8210	56.9%	10076	63.1%	6446	41.4%
Background	4326	-	6880	-	4265	-	4684	-

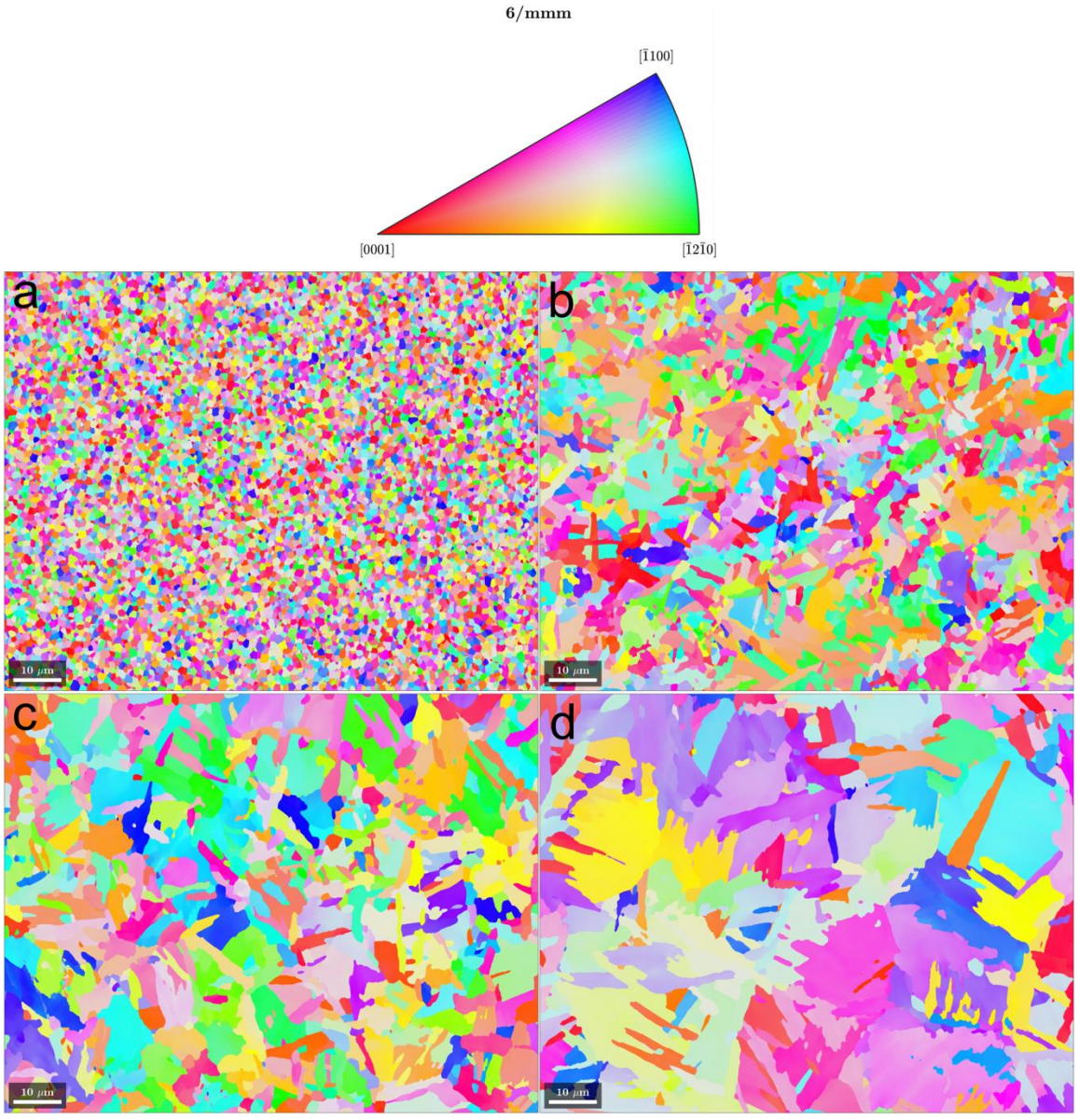


Figure 22: Final layer center stir zone alpha Ti IPFs for (a) 700 ºC, (b) 750 ºC, (c) 800 ºC, and (d) 850 ºC temperature setpoint builds

equiaxed microstructure. The grain size is on the order of 1 μm as shown in **Figure 23**. The 750 ºC and 800 ºC show a mixture of alpha colonies with some spheroidization. The 850 ºC temperature setpoint shows a lamellar microstructure with different alpha variants intersecting. It appears that the scale of the microstructure is increasing with increasing deposition temperature setpoint.

Prior Beta Reconstruction

Most of the transformed alpha grains are within a few degrees of the expected Burgers orientation relation (**Figure 24**). While the disorientation distribution is likely skewed due to local plastic deformation during the phase transformation, the sharp concentration of disorientations around the Burgers orientation relation shows that the Burgers orientation relation holds during cooling following AFSD of alpha-beta titanium. While most of the transformed grains match the expected Burgers orientation relation (**Figure 24**), there are some grains that have large misorientations. There are two sources for these grains with large misorientations from the expected relation: the grains could be grain boundary alpha that was outcompeted in the growth phase by other nucleation sites, or the grains could also be equiaxed alpha that did not completely transform to the beta phase during processing, leaving behind alpha grains that do not have the expected orientation relation to the other transformed alpha grains. It is hypothesized that, among the grains not mapped to a parent beta grain, the unmapped alpha grains correspond to spheroidized alpha resulting from deformation in the alpha + beta phase field.

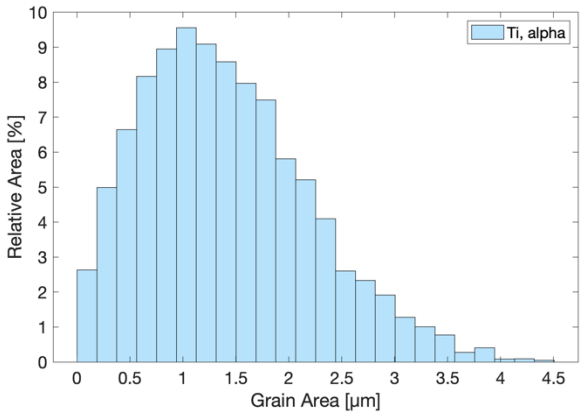


Figure 23: 700 ºC center top layer stir zone grain area as a function of total area

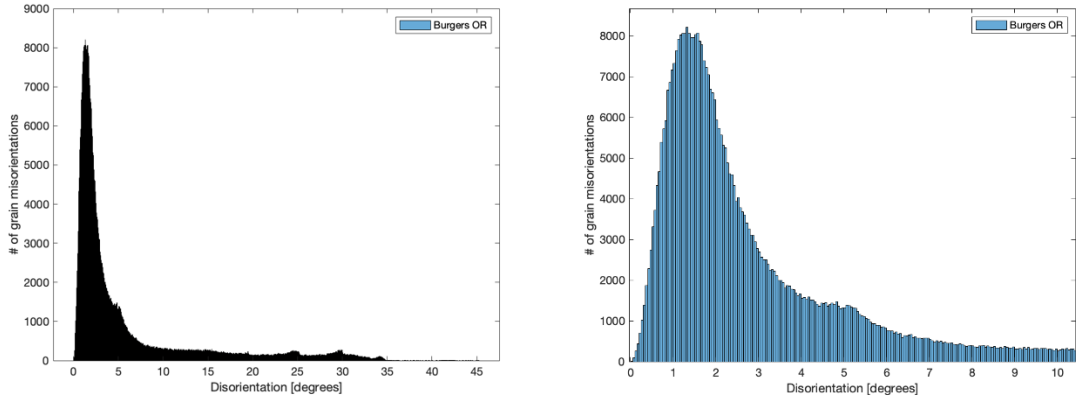


Figure 24: Disorientation histogram between transformed grain misorientations and the Burgers OR

X-Ray Diffraction

Based on EBSD results that indicate some amount of equiaxed alpha at layer boundaries, it was hypothesized that oxygen contamination may be locally stabilizing the alpha phase. X-ray diffraction analysis was used to investigate the effects of oxidation on the alpha/beta phase fractions at the surface of the deposit. Two as-printed samples were analyzed to investigate this oxidation. The first sample displayed a unoxidized metallic gray surface while the second sample showed a blue and purple surface characteristic of oxidation The initial results have been difficult to analyze due to systemic error introduced from surface effects. This experiment was therefore repeated using parallel-beam X-ray diffraction analysis to limit sources of error arising from surface finish and sample displacement issues. The results are given in **Figure 25**. It was shown that the rutile and anatase phases were present in the oxidized surfaces.

In addition to the oxidized and unoxidized top surfaces, XRD analysis of the polished cross sections was used to yield information for the bulk printed samples as averaged over approximately 20 layers. The Rietveld refinements are given in **Figure 26 through Figure 30**.

It was found that the alpha/beta fraction is similar in all process conditions, with the as-printed material having a higher beta fraction than the annealed feedstock. The values are given in **Table 6** and are plotted as a function of deposition temperature in **Figure 31**.

The change in cell volume suggests possible differences in solute segregation in alpha and beta Ti processed at different temperature setpoints. Particularly the increase in cell volume in the intermediate temperature setpoints of 750 ºC and 800 ºC may suggest

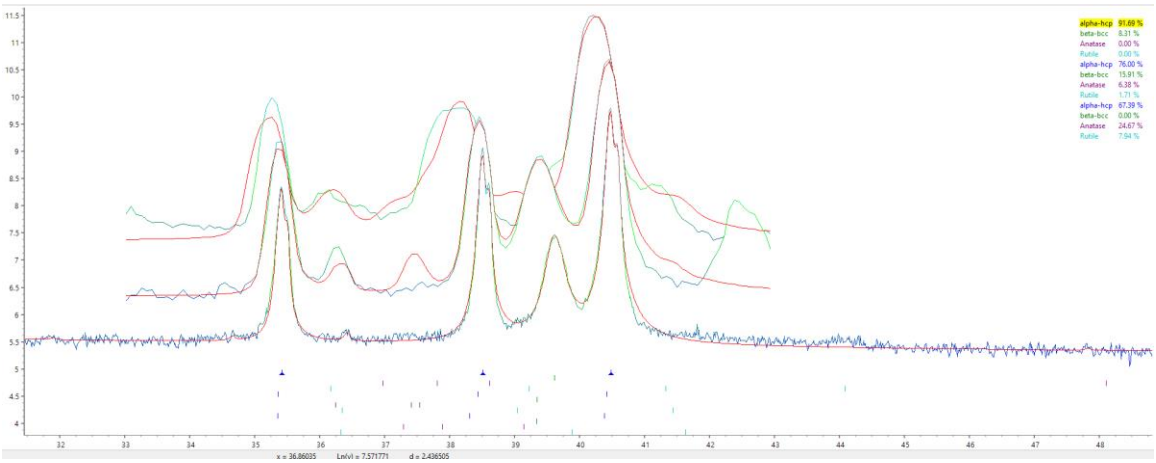


Figure 25: XRD of as printed unoxidized and oxidized top surfaces

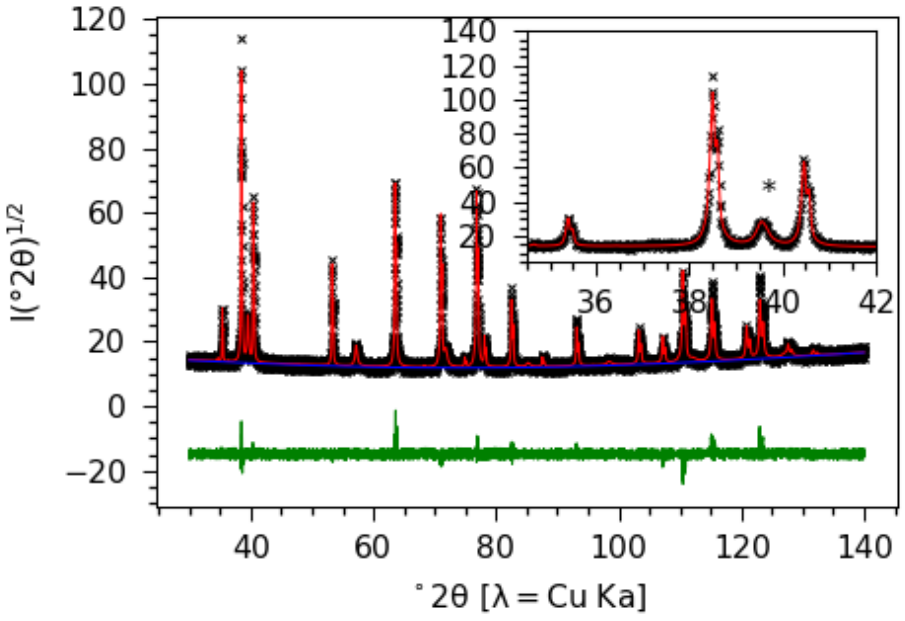


Figure 26: XRD Rietveld refinement for the Ti-6Al-4V feedstoclk

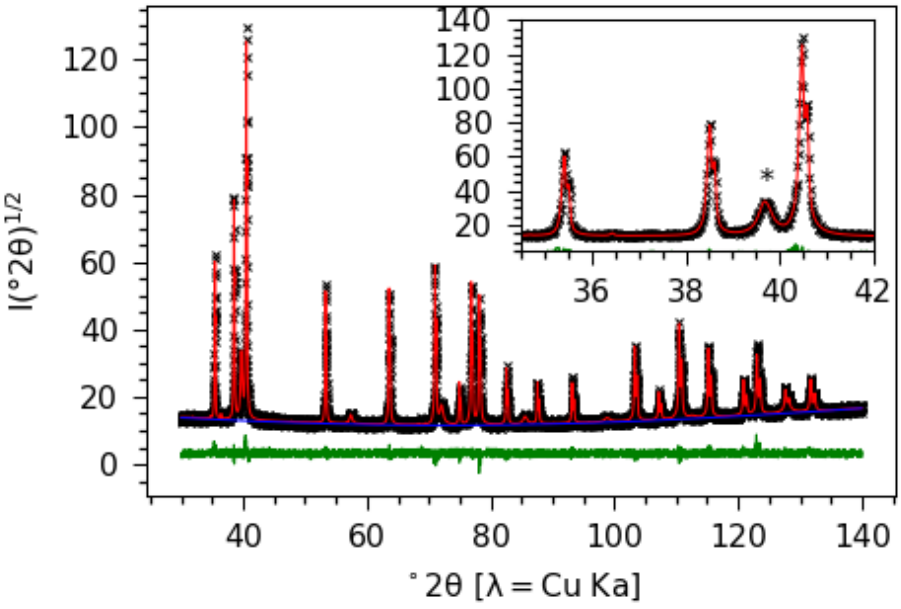


Figure 27: XRD Rietveld refinement for the 700 ºC build

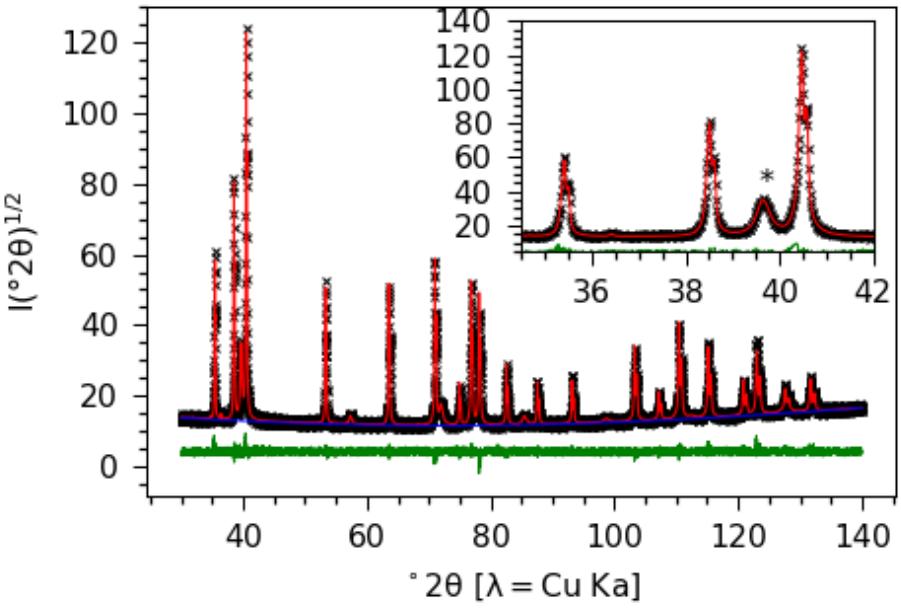


Figure 28: XRD Rietveld refinement for the 750 ºC build

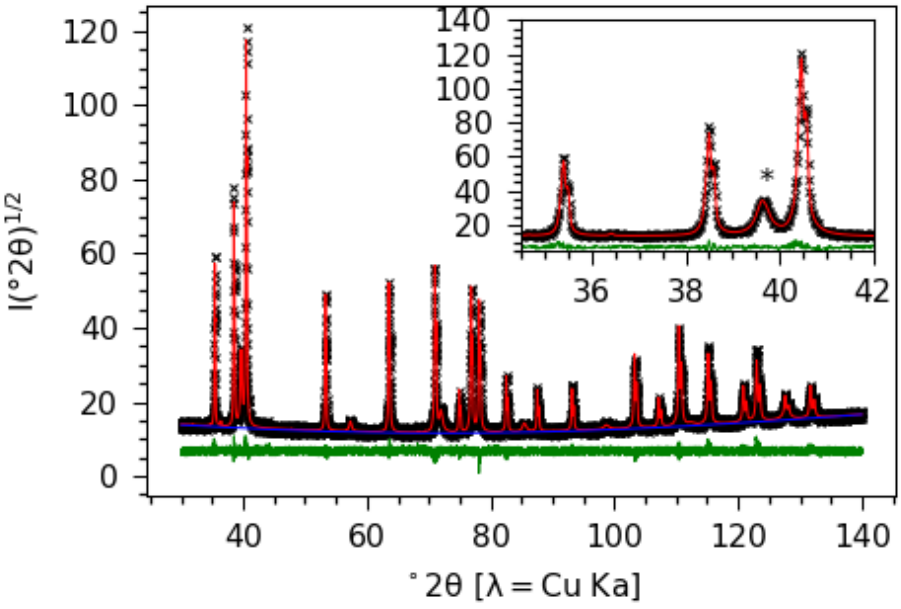


Figure 29: XRD Rietveld refinement for the 800 ºC build

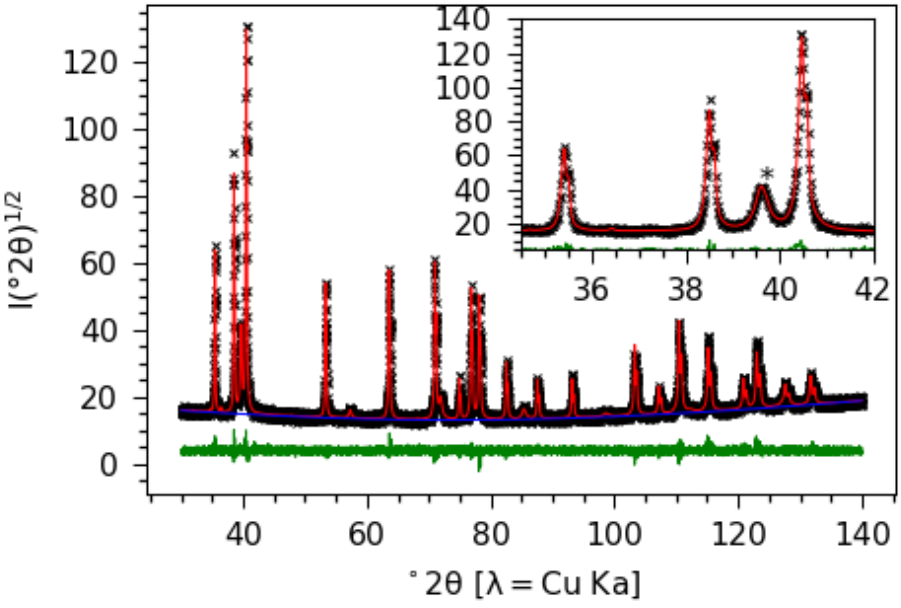


Figure 30: XRD Rietveld refinement for the 850 ºC build

Table 6: XRD alpha/beta wt. % fraction

	Alpha [wt. %]	Beta [wt. %]
Feedstock	93.75 +/- 0.34	6.25 +/- 0.34
700 ºC	92.13 +/- 0.20	7.87 +/- 0.20
750 ºC	91.85 +/- 0.24	8.15 +/- 0.24
800 ºC	92.20 +/- 0.17	7.80 +/- 0.17
850 ºC	92.27 +/- 0.22	7.73 +/- 0.22

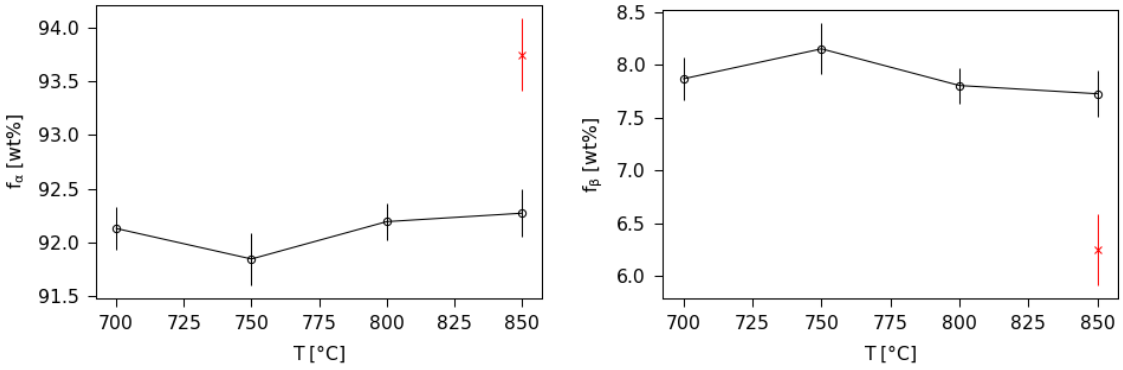


Figure 31: Phase fractions in wt. % for the (a) alpha and (b) beta phases as a function of deposition temperature. The feedstock is plotted in red

that other forms of recrystallization may be at play as compared to the more extreme temperature settings. Cell volume for the alpha and beta phases as a function of temperature are plotted in **Figure 32**. The microstrain broadening, shown in **Figure 33**, in the two phases varies inversely, suggesting that plasticity and recovery of the two phases differs under the different target AFSD temperatures. It should be noted, however, that there are many different factors that can influence peak broadening, making definite interpretation of the XRD results difficult (178).

The texture index for both the alpha and beta phase are shown as a function of deposition temperature in **Figure 34**. XRD reveals that the alpha texture index for the as printed samples is low as 1.0147+/-0.0007 compared to the rolled feedstock value of 1.172+/-0.005. The beta texture index is similarly lower than the feedstock, having a minimum value of 1.059+/-0.008 as compared to 1.159+/-0.028. A random orientation distribution is expressed as a value of J=1, whereas a single crystal would have a texture index of infinity. These values indicate that, over a measurement of multiple layers, the as-printed microstructure is less textured than the rolled, mill annealed feedstock.

While tungsten inclusions have been observed in all deposition temperatures, the presence of BCC tungsten peaks in the XRD was not apparent. Additionally, though trace oxide phases were observed in the XRD of the discolored oxidized top surface, trace oxide phases were also not visible in the XRD study of the polished cross-sections encompassing multiple printed layers.

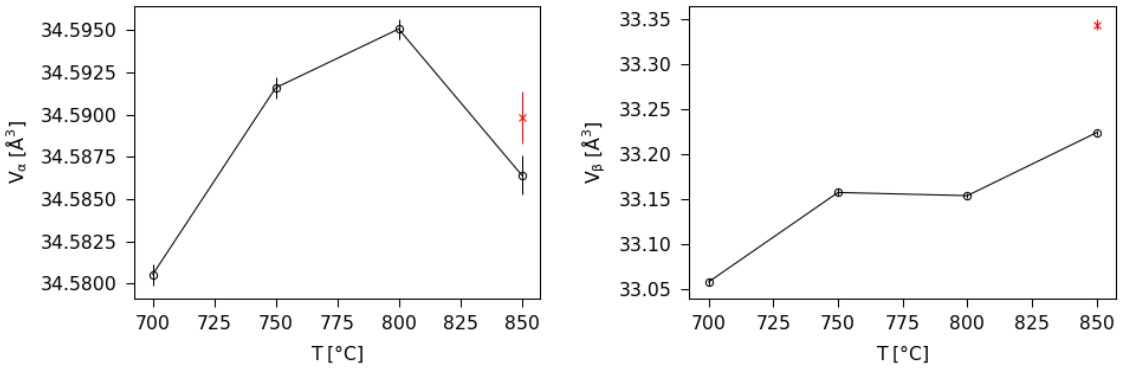


Figure 32: Cell volume for the (a) alpha and (b) beta phases as a function of deposition temperature. The feedstock is plotted in red

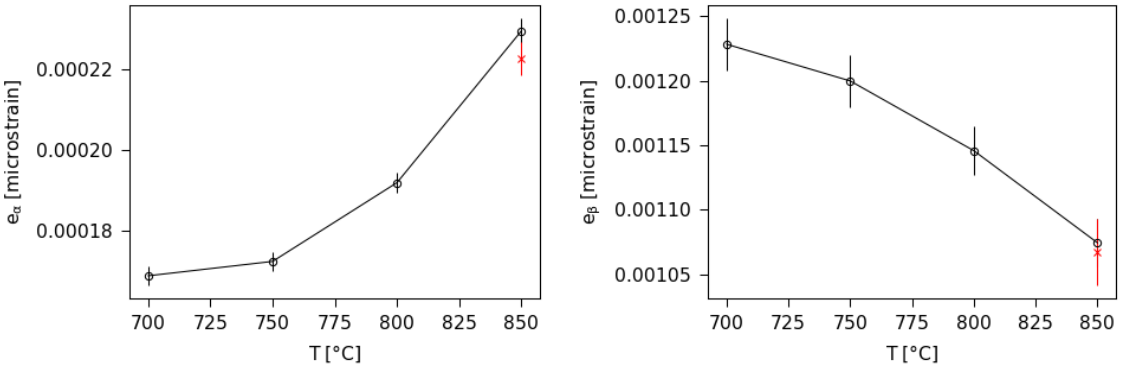


Figure 33: Microstrain for the (a) alpha and (b) beta phases as a function of deposition temperature. The feedstock is plotted in red

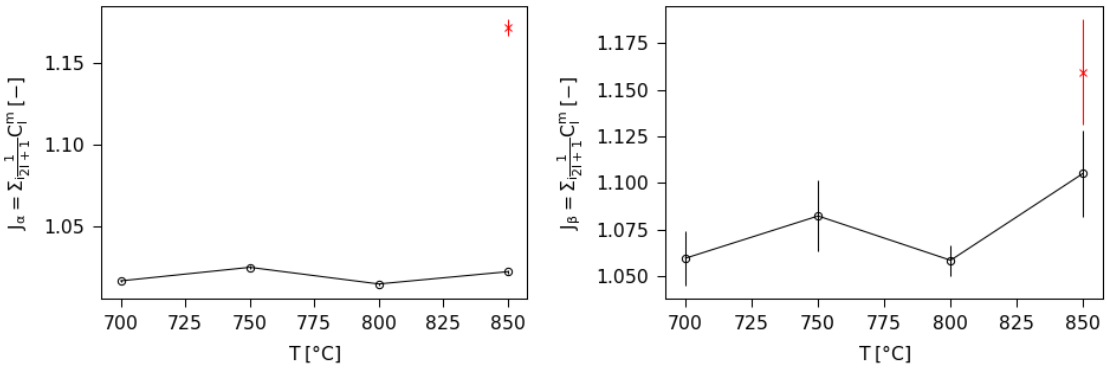


Figure 34: Texture index for the (a) alpha and (b) beta phases as a function of deposition temperature. The feedstock is plotted in red

Mechanical Testing

Microhardness Testing

Microhardness testing reveals heterogenous hardness properties in all the tested build conditions, as apparent by a clearly visible banded structure. These results are plotted in **Figure 35**. It appears that there are hardness variations at the layer scale (1mm) for the 700 ºC, 750 ºC, and 800 ºC parameter sets. Additionally, this layer scale variation appears to become less distinct as the temperature setpoint increases, to the point that layer scale variation is not apparent for the 850 ºC build. In effect, the hardness plots become "noisier" as the temperature setpoint increases. There is also a longer-range heterogeneity on the order of 5mm. This longer-range heterogeneity is on roughly the same scale as the number of layers printed for each discrete feed bar of material. This suggests that there are heterogeneities that may result from the layer-by-layer printing process as well as from bar reload events.

The feedstock hardness plot is given in **Figure 36** with the same scaling factor as the AFSD samples. There are vertical striations in the plot that appear to be related to the rolled mill-annealed microstructure of the feedstock.

As according to ASTM E384, the mean, standard deviation, 95% confidence interval, minimum, and maximum values are reported in **Table 7** (175). Interestingly, the mean hardness for every build parameter set inclusive of the feedstock is within 2 HV 0.2. This shows that, despite the drastic variation in microstructures from equiaxed alpha to lamellar, on average, there appears to be very little effect from the morphology of the microstructure on microhardness.

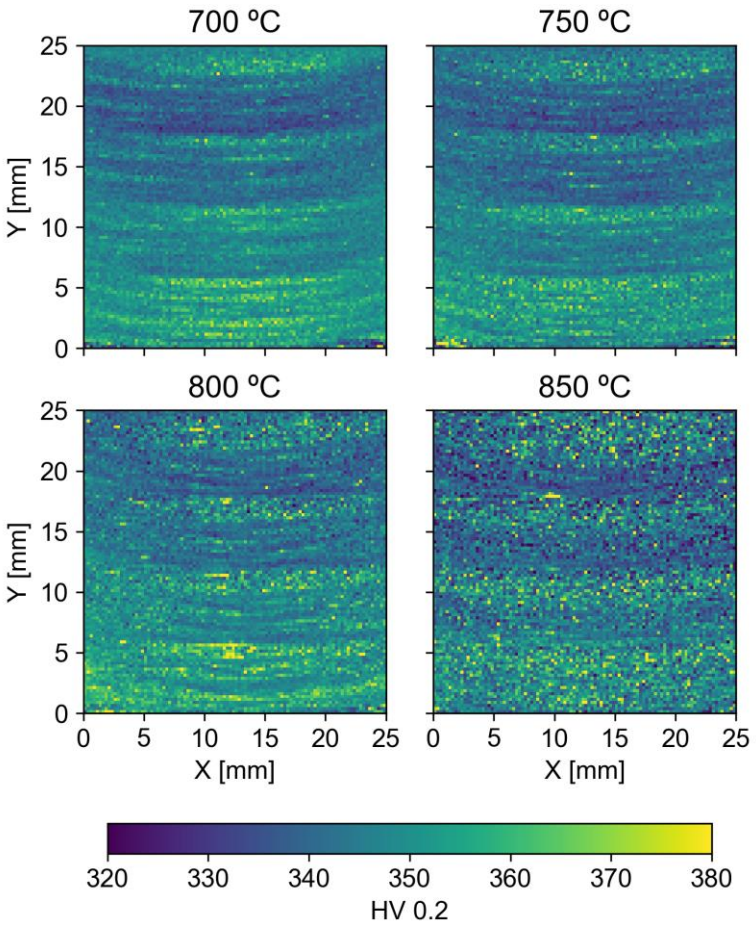


Figure 35: Combined microhardness plots (scaled to 320 HV 0.2 to 380 HV 0.2)

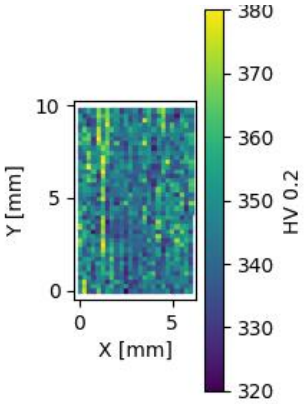


Figure 36: Feedstock microhardness plot (scaled to 320 HV 0.2 to 380 HV 0.2)

Table 7: Microhardness testing mean, standard deviation, 95% confidence interval, minimum, and maximum

Condition	Mean (HV 0.2)	Std. Dev. (HV 0.2)	95% C.I. (HV 0.2)	Min. (HV 0.2)	Max. (HV 0.2)
Feedstock	346.3	10.83	345.6, 347.0	319	387
700 ºC	347.1	7.65	346.9, 347.2	316	391
750 ºC	345.8	7.89	345.7, 346.0	312	404
800 ºC	347.7	9.23	347.6, 347.9	319	454
850 ºC	344.7	11.23	344.5, 344.9	311	400

The distribution of the hardness values can be visualized in a violin plot in **Figure 37** along with the mean, interquartile range, skewness, and kurtosis. Note that the Pearson's definition for kurtosis is used in this work, meaning that a kurtosis of 3 matches a normal/Gaussian distribution. It can be observed that the higher temperature setpoint condition have a very slightly increased spread in the hardness as shown by the increasing interquartile ranges. Additionally, all the tested samples are slightly skewed to the lower end of the hardness ranges as evidenced by the positive skewness values. This means that the samples all have more outlier hardness indents that are greater than the mean hardness. Looking at the kurtosis for each sample, all values except the 800 ºC sample have a kurtosis below 3, indicating that they are platykurtic and have a flatter curve than a Gaussian distribution. The 800 ºC case has a kurtosis greater than 3, making it leptokurtic with a sharper peak than a Gaussian distribution; however, this may be only an effect of the anomalously high hardness indent expanding the upper tail of the distribution.

The measured minimum hardness values are consistent, ranging from 311-319 HV 0.2, however, the 800 ºC sample has an anomalously high maximum hardness value of 454 HV 0.2. This indent was found to be more than 100 HV harder than the next hardest indent in the same sample, meriting a more thorough investigation. After a closer look at the anomalous indent, it was found that the high hardness was not a measurement error. The measured diagonals match the measured high hardness. Therefor the indent was investigated via SEM and EDS. It was found that the indent was centered on a band of sub-micron scale light contrasting particles as seen in the BSE image in **Figure 38** (a).

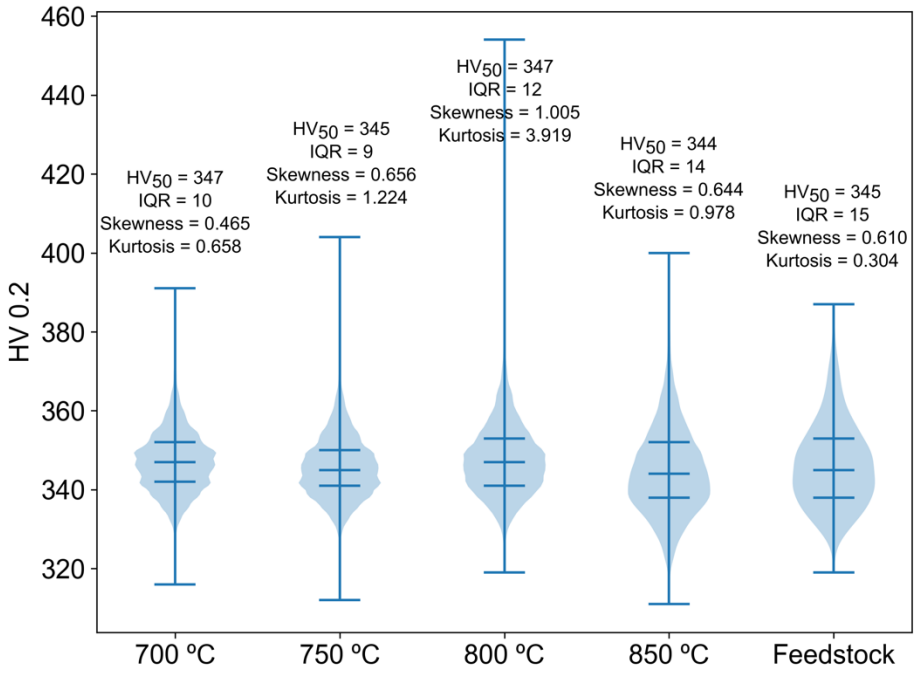


Figure 37: Microhardness violin plot

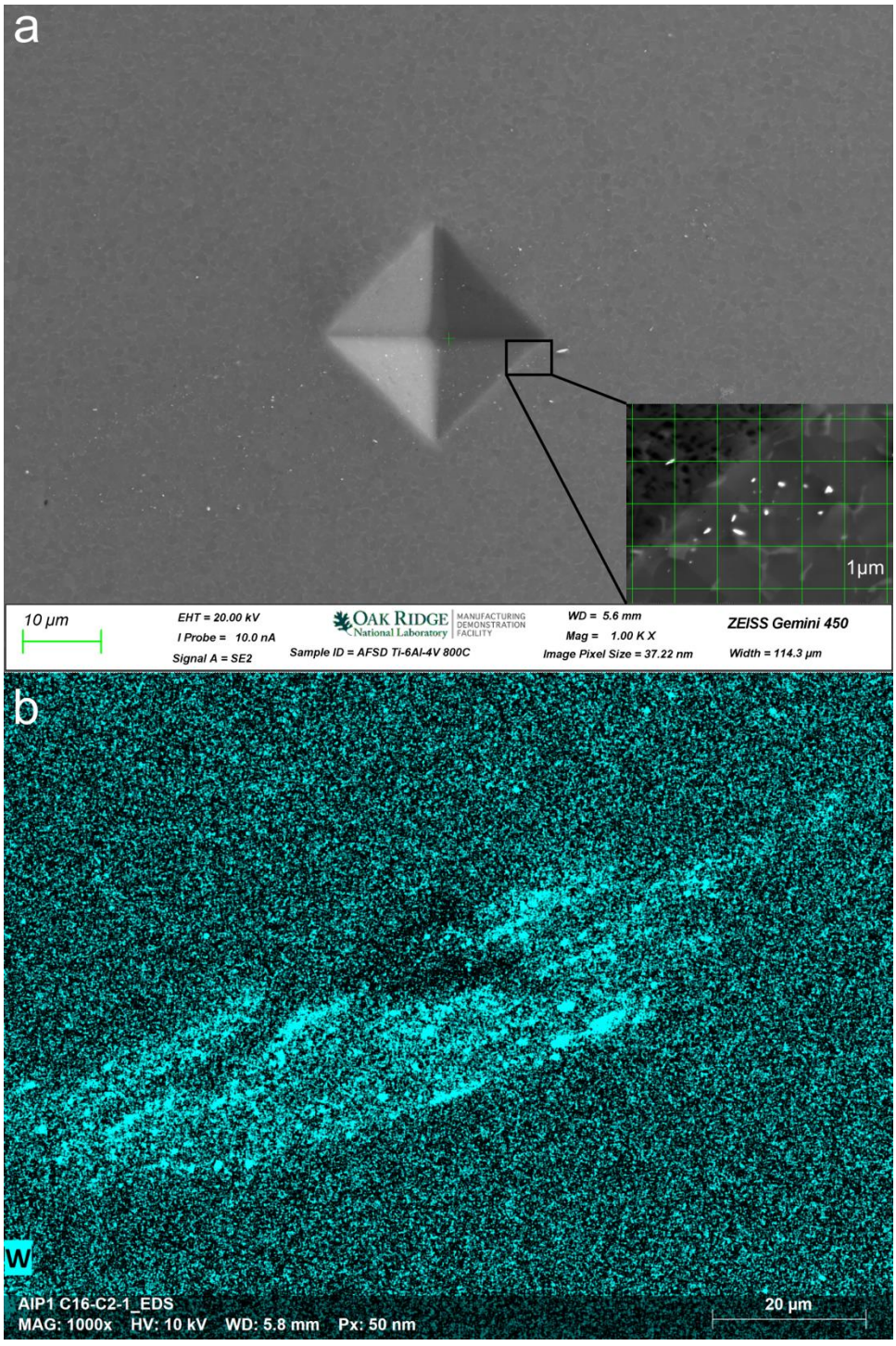


Figure 38: Anomalous high-hardness indent (a) BSE image with inset and (b) EDS element map for W

Despite the mean hardness being within 2 HV, observation of the microhardness maps in **Figure 35** reveals some significant differences. In each of the microhardness maps for the four different processing conditions, there is a repeated pattern of hardness variation spanning multiple layer heights. This can be attributed to the four bars used for each build as built in a discreet feed system. There is also interlayer variation visible in the 700 ºC, 750 ºC, and 800 ºC build. This interlayer hardness variation, however, is not readily apparent in the 850 ºC sample. The fractography results are shown

In the 800 ºC sample, there was an anomalous high hardness indent that was greater than 100 HV 0.2 harder than the next hardest indent. Upon closer examination of the anomalous indent with an SEM using a backscatter detector, there appear to be many sub-micron, brightly contrasting particles in a band that goes through the region of the indentation. Based on EDS analysis, it was determined that these particles are tungsten resulting from tool wear. Therefore, this indent landed in the middle of a band of fine, sub-micron tungsten particles. These particles act as an accidental metal matrix composite, strengthening the material in the location of the particles. This result shows that tungsten contamination will influence the resulting mechanical properties of the build. The tungsten particles do not appear to have significantly dissolved into the titanium matrix, indicating that abrasive tool wear is the likely mechanism.

Quasi-Static Tensile Testing

Tensile bars from the closed-loop temperature-controlled depositions were extracted via EDM. It is hypothesized that differences in microstructure, texture, and hardness can be correlated to resulting mechanical properties. For all tested samples, the modulus, yield strength (YS), ultimate tensile strength (UTS), extensometer strain at

UTS, strain at yield, extensometer strain at rupture, and the strain hardening exponent are given in the Appendix. Additionally, the mean, standard deviation, minimum, maximum, coefficient of variation, and range are included.

There were some testing anomalies for the LD-TD samples. Some of the ND-LD samples, ND-LD 750S22 and 800S26, failed prior to plasticity at 572 MPa (83 ksi) and 117 MPa (17 ksi), respectively. ND-LDS26 failed outside of the reduced area, yielding an invalid test. LD-TD 850S18 was not tested. These data points are not included.

The stress-strain curves are shown for the tested samples **in Figure 39 through Figure 45**. The curves are organized by temperature setpoint in **Figure 39 through Figure 42** and by tensile bar orientation in **Figure 43 through Figure 45**. The mean and standard deviation values for yield strength, ultimate tensile strength, and elongation for each tensile bar orientation and temperature setpoint are given in **Table 8**.

In addition to the aforementioned tensile bars, an additional four tensile bars from the ND-LD orientation, 700S13, 750S13, 800S13, and 850S13, or, one from each temperature setpoint, were polished and etched. This set of tensile bars was imaged at 10x, 20x, 100x, and 500x magnification. The 20x images are shown in **Figure 46**. Samples 700S13, 750S13, and 850S13 were tested to failure, while sample 800S13 was tested to high plasticity and then unloaded. Due to the differences in surface preparation, the tensile curves and data for these tensile samples are given separately in **Figure 47** and **Table 9** respectively. After mechanical testing, a surface profile was taken for each of the polished and etched tensile bars. The results are given in **Figure 48 through Figure 51** and are compared to the initial microstructure morphology. An additional profile was taken of the 850 ºC temperature setpoint next to the failure location. The results are given

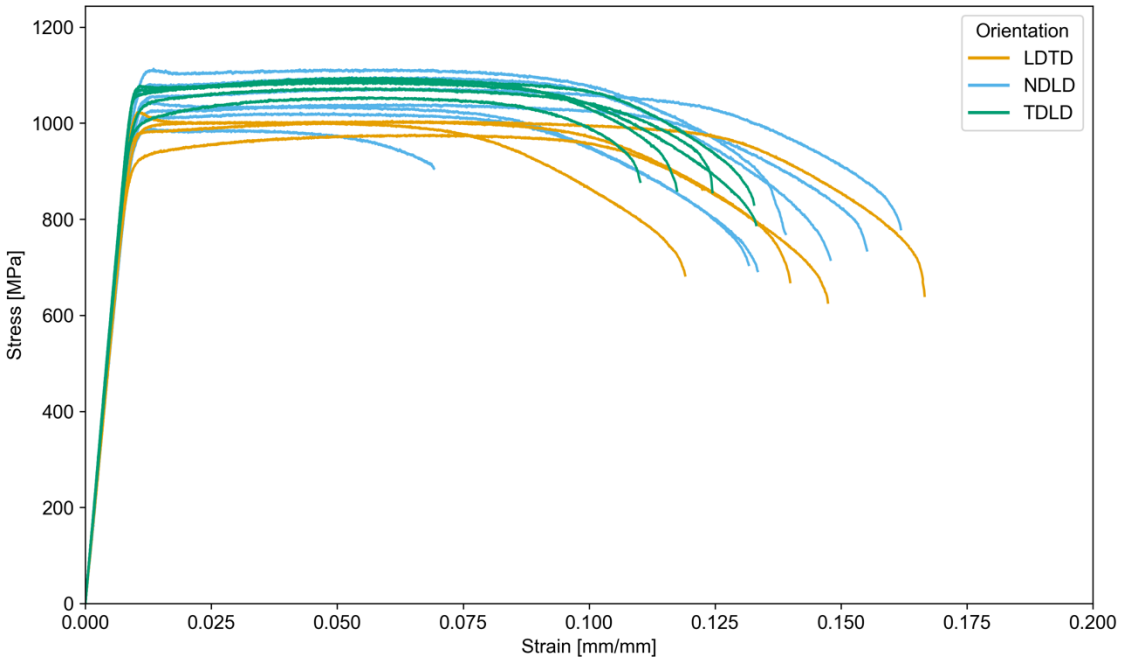


Figure 39: Stress-strain plots for 700 ºC samples

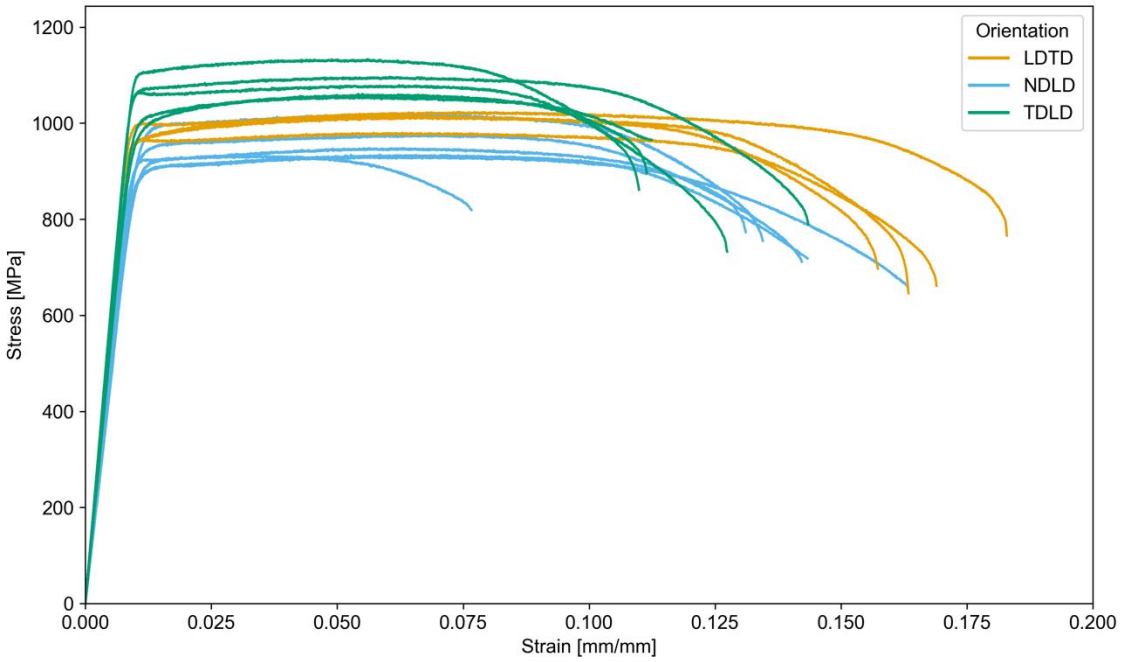


Figure 40: Stress-strain plots for 750 ºC samples

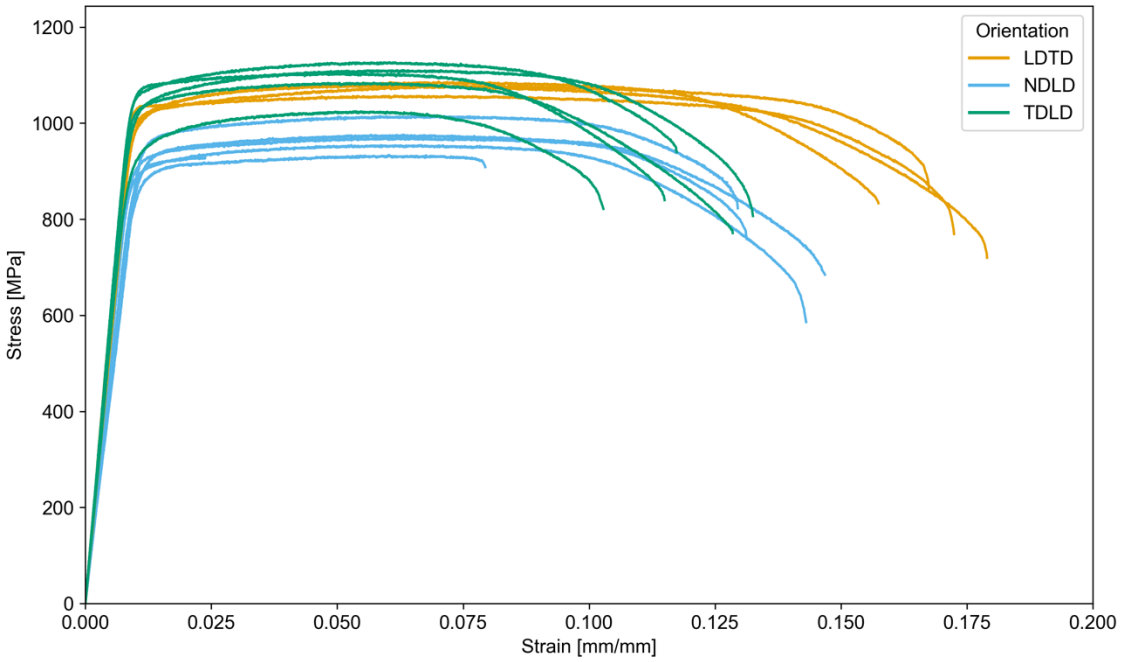


Figure 41: Stress-strain plots for 800 ºC samples

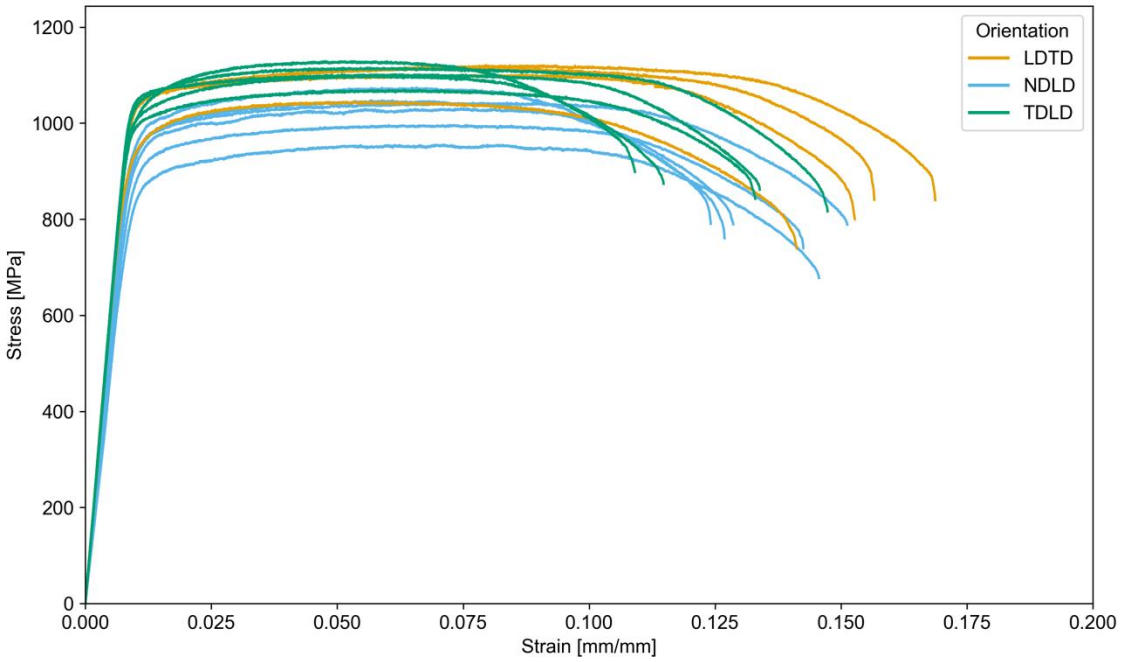


Figure 42: Stress-strain plots for 850 ºC samples

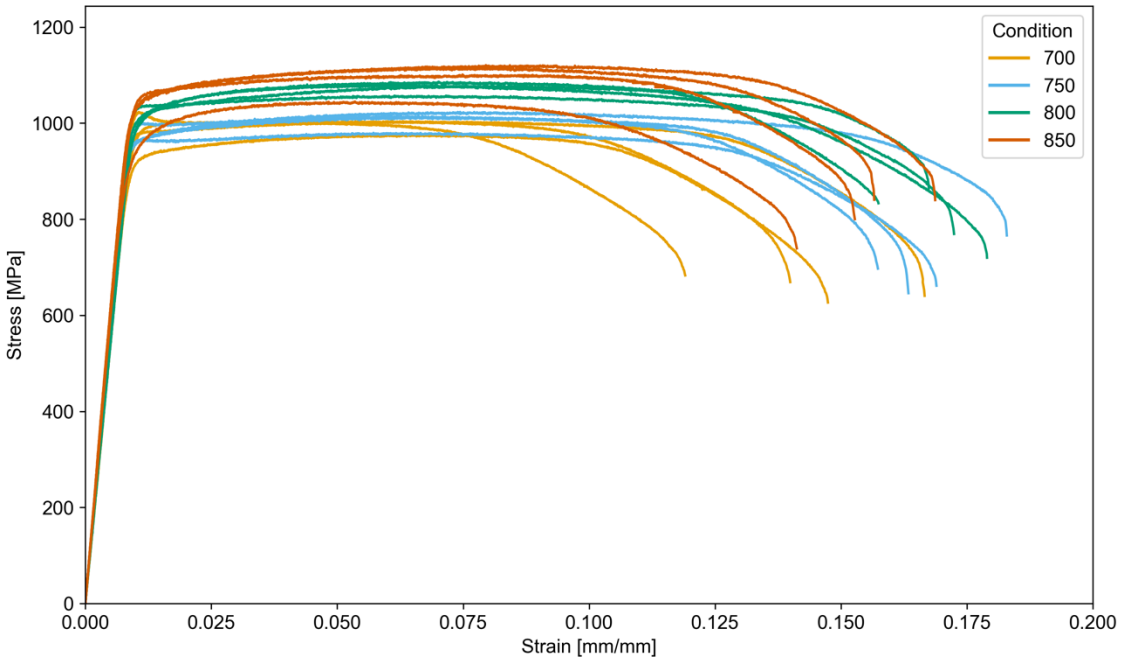


Figure 43: Stress-strain curves for LD-TD samples

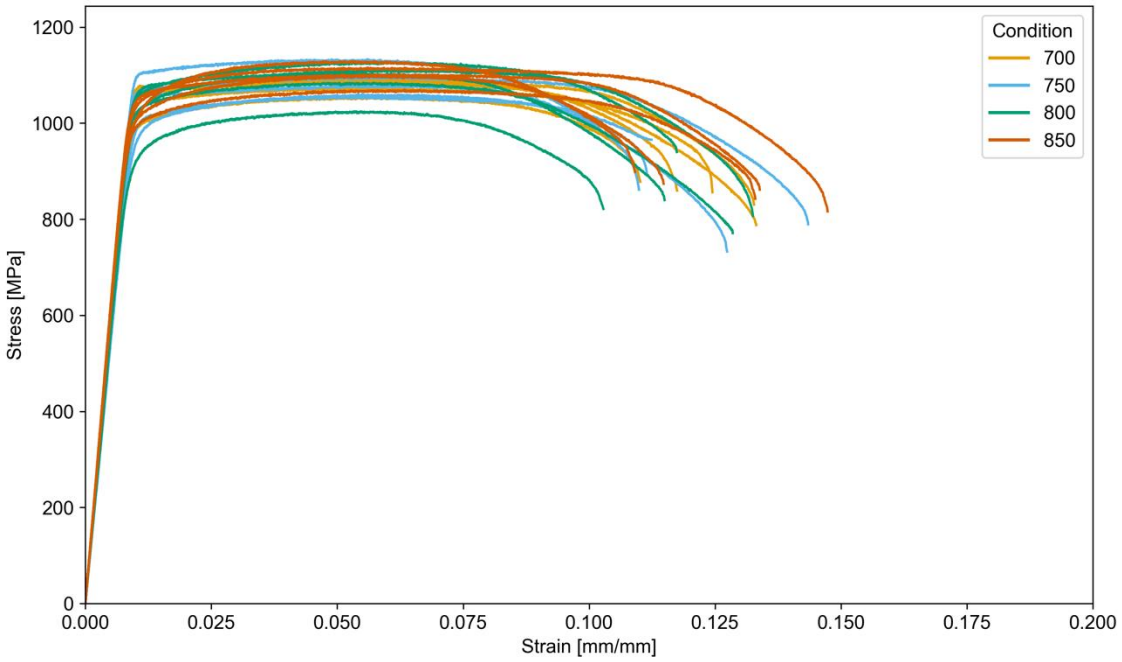


Figure 44: Stress-strain curves for TD-LD samples

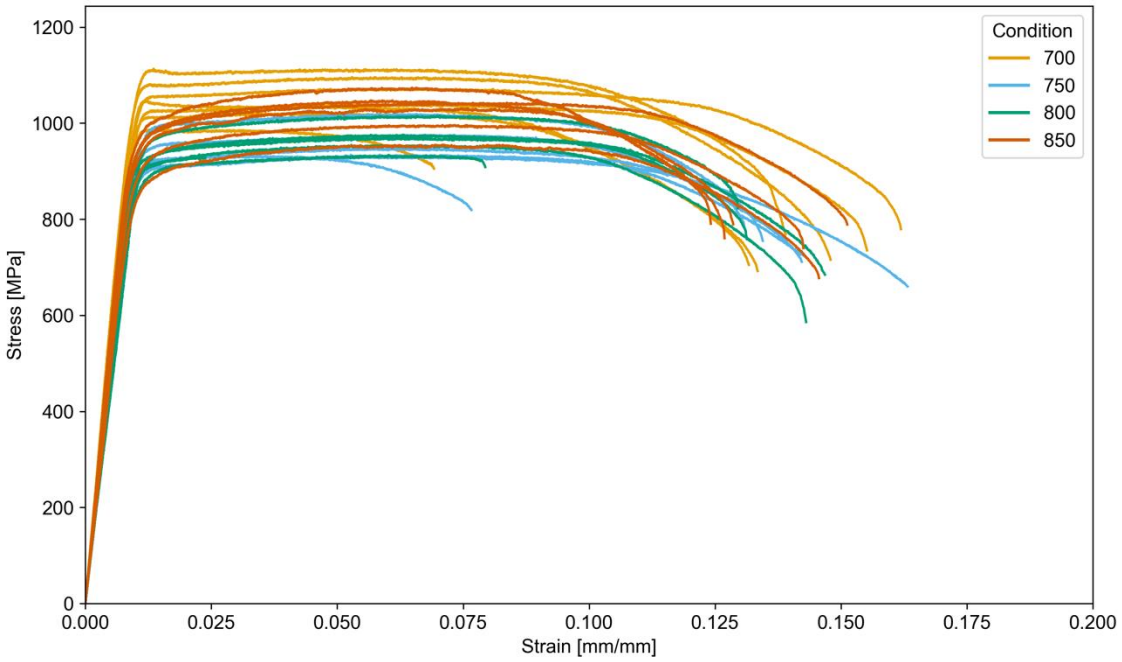


Figure 45: Stress-strain curves for ND-LD samples

Table 8: Tensile testing compiled results

Temperature	Measurement	Statistic	LD-TD	TD-LD	ND-TD
700 ºC	YS [MPa]	Mean	976	1045	1037
		Std. Dev.	39.6	33.3	41.5
	UTS [MPa]	Mean	1001	1081	1053
		Std. Dev.	17.2	16.5	43.0
	Elongation [mm/mm]	Mean	0.143	0.124	0.134
		Std. Dev.	0.020	0.010	0.031
750 ºC	YS [MPa]	Mean	970	1045	922
		Std. Dev.	19.8	47.9	35.9
	UTS [MPa]	Mean	1006.7	1083.9	956.1
		Std. Dev.	18.7	30.6	36.7
	Elongation [mm/mm]	Mean	0.168	0.121	0.132
		Std. Dev.	0.011	0.014	0.030
800 ºC	YS [MPa]	Mean	1014	1023	912
		Std. Dev.	16.9	55.1	28.5
	UTS [MPa]	Mean	1076	1089	963
		Std. Dev.	14.9	37.8	31.9
	Elongation [mm/mm]	Mean	0.169	0.119	0.109
		Std. Dev.	0.009	0.012	0.048
850 ºC	YS [MPa]	Mean	1017	1025	930
		Std. Dev.	53.6	23.2	37.4
	UTS [MPa]	Mean	1098	1103	1024
		Std. Dev.	34.4	23.4	42.0
	Elongation [mm/mm]	Mean	0.155	0.128	0.137
		Std. Dev.	0.012	0.016	0.011



Figure 46: 20x images of polished and etched tensile bars from (a) 700 ºC, (b) 750 ºC, (c) 800 ºC, and 850 ºC temperature setpoints

Table 9: Tensile testing data for ND-LD polished and etched tensile samples (*Note: sample 800S13 was tested to plasticity, stopping before failure)

Sample ID	YS (ksi)	UTS (ksi)	Modulus (ksi)	Yield Strain (in/in)	DIC Ext Strain @ UTS (in/in)	DIC Ext Strain @ Rupture (in/in)	Strain Hardening Exponent	DIC Extensometer Length (mm)
700_S13	150	153	15500	0.0118	0.056	0.15	0.035	0.311
750_S13	154	160	16700	0.0114	0.062	0.152	0.044	0.308
800_S13*	151	162*	17600	0.0107	0.059	0.101*	0.053	0.308
850_S13	140	153	15600	0.0111	0.074	0.145	0.071	0.312

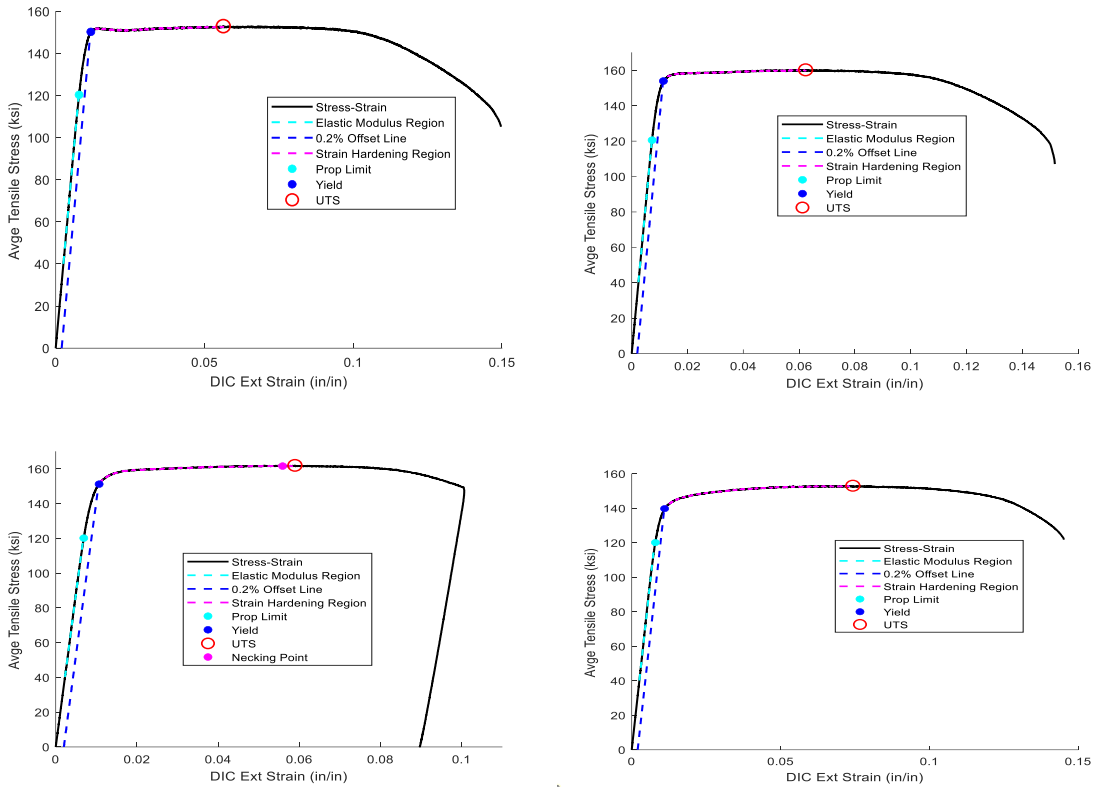


Figure 47: Polished and etched ND-LD tensile bar stress-strain curves for (a) 700S13, (b) 750S13, (c) 800S13, and (d) 850S13

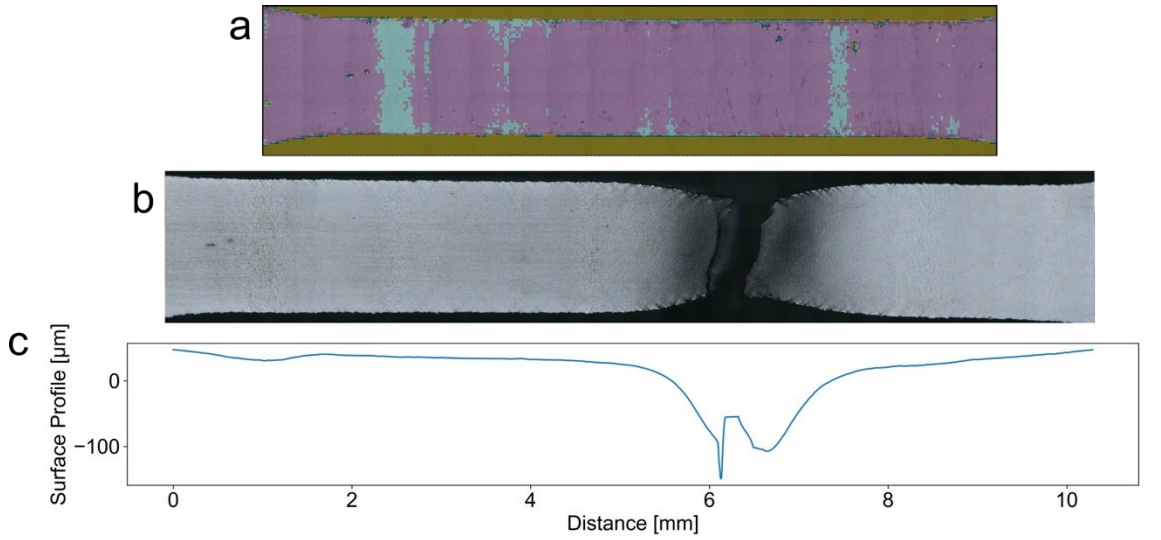


Figure 48: 700 ºC ND-LD polished and etched tensile bar (a) initial characterized microstructure, (b) tested sample micrograph and (c) surface height profile

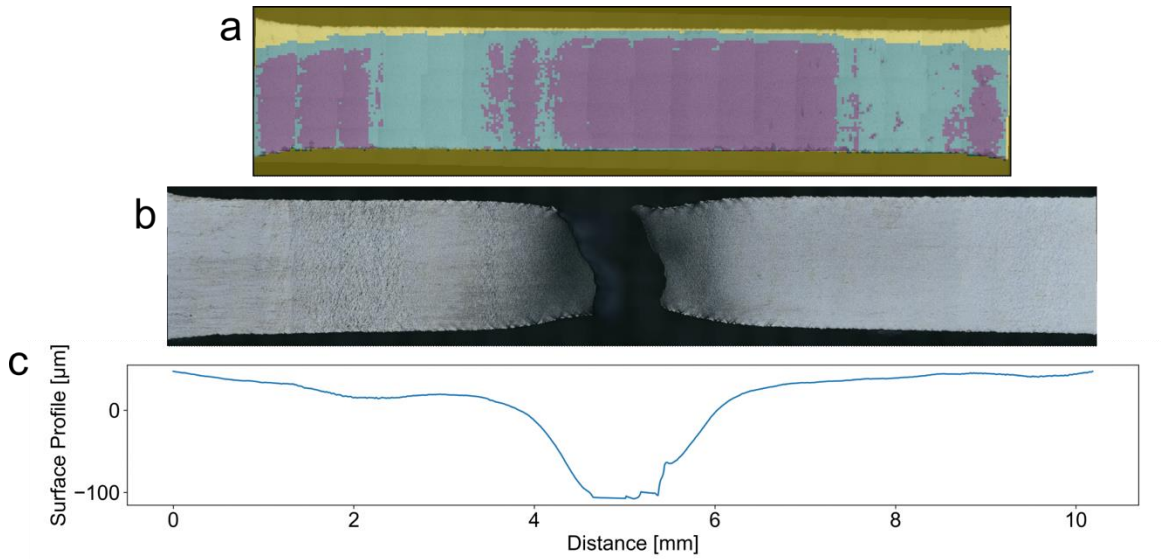


Figure 49: 750 ºC ND-LD polished and etched tensile bar (a) initial characterized microstructure, (b) tested sample micrograph and (c) surface height profile

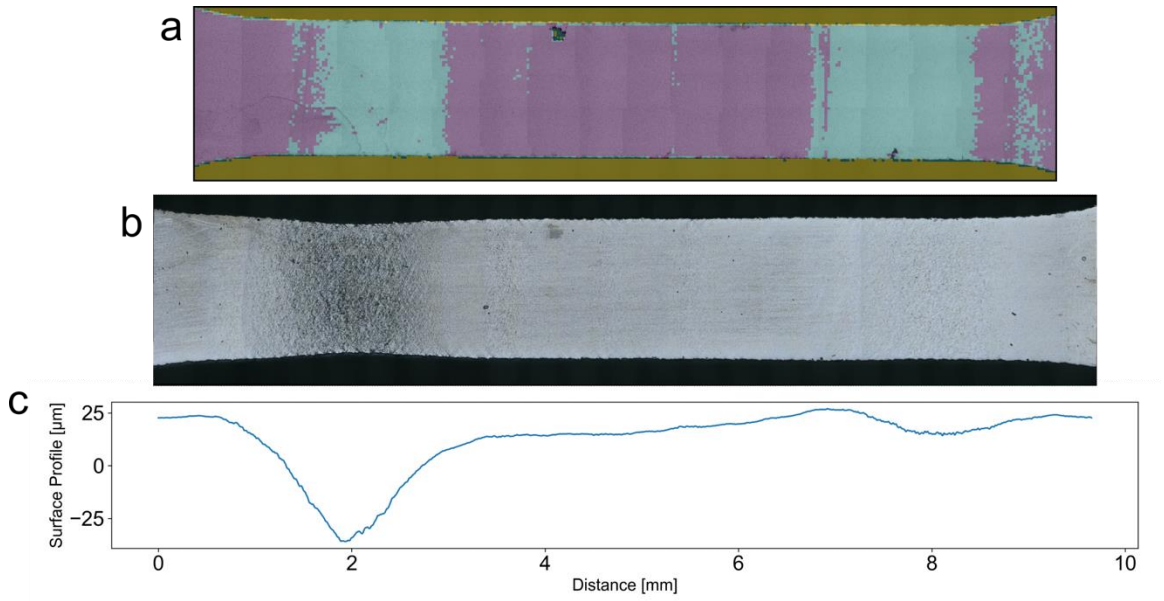


Figure 50: 800 ºC ND-LD polished and etched tensile bar (a) initial characterized microstructure, (b) tested sample micrograph and (c) surface height profile

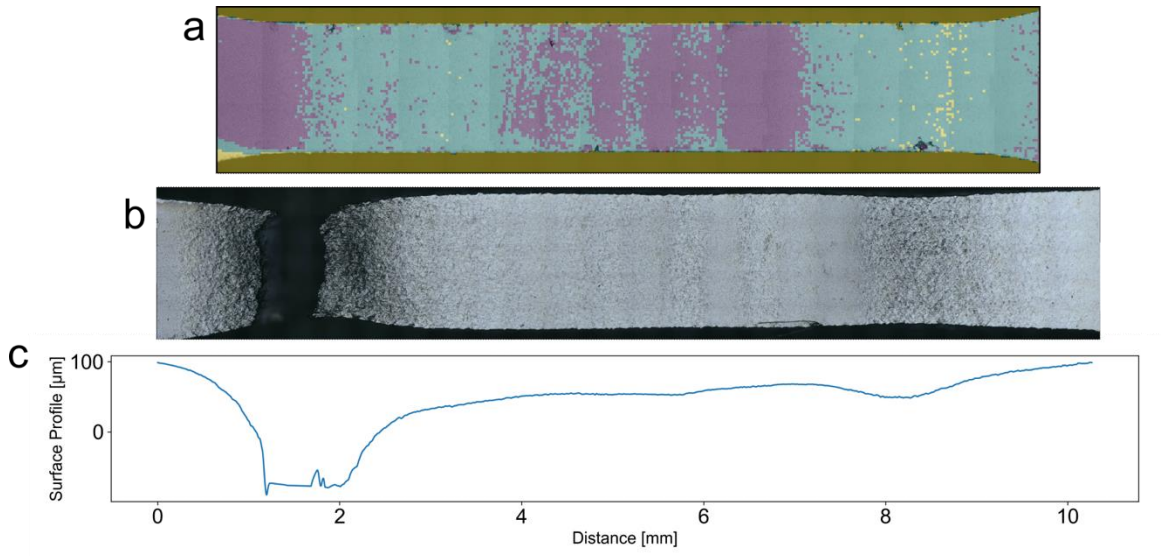


Figure 51: 850 ºC ND-LD polished and etched tensile bar (a) initial characterized microstructure, (b) tested sample micrograph and (c) surface height profile

in **Figure 52** where it is seen that increasing deformation takes place as the microstructure increasingly becomes a lamellar morphology.

Fractography

Fractography was conducted using BSE SEM images on the middle ND-LD orientation samples, 700S14, 750S14, 800S14, and 850S14, to gain insights into the fracture mechanism of the tested tensile samples in **Figure 53 through Figure 64**. In addition to the middle samples, fractography was additionally conducted on two low ductility samples from the side regions of the deposit, 750S22 and 800S2. For 700S14 and 750S14, only small amounts of tungsten are visible in the fracture surface, observed as small high-density inclusions in the SEM image. The 800S14 sample, however, shows a large amount of tungsten inclusions. 850S14 does not show any high-density inclusions.

Sample 700S22 appears to show the characteristic “onion skin” pattern typically observed on traditional FSW and AFSD top surfaces. There are also large high-density inclusions visible. At higher magnifications, the fracture surface shows a large amount of tungsten inclusions. Sample 800S2 similarly shows a large amount of both large and small high-density inclusions.

Chemical Analysis

In titanium alloys, oxygen is a strong alpha phase stabilizer. Based on observation of etched micrographs, a band of darkly etching equiaxed alpha can be seen in the final layers of the sample as shown in **Figure 65**. It was initially hypothesized that this band of equiaxed alpha is the result of local oxygen contamination from the top surface of the previously deposited layer. This hypothesis of oxygen contamination was tested via

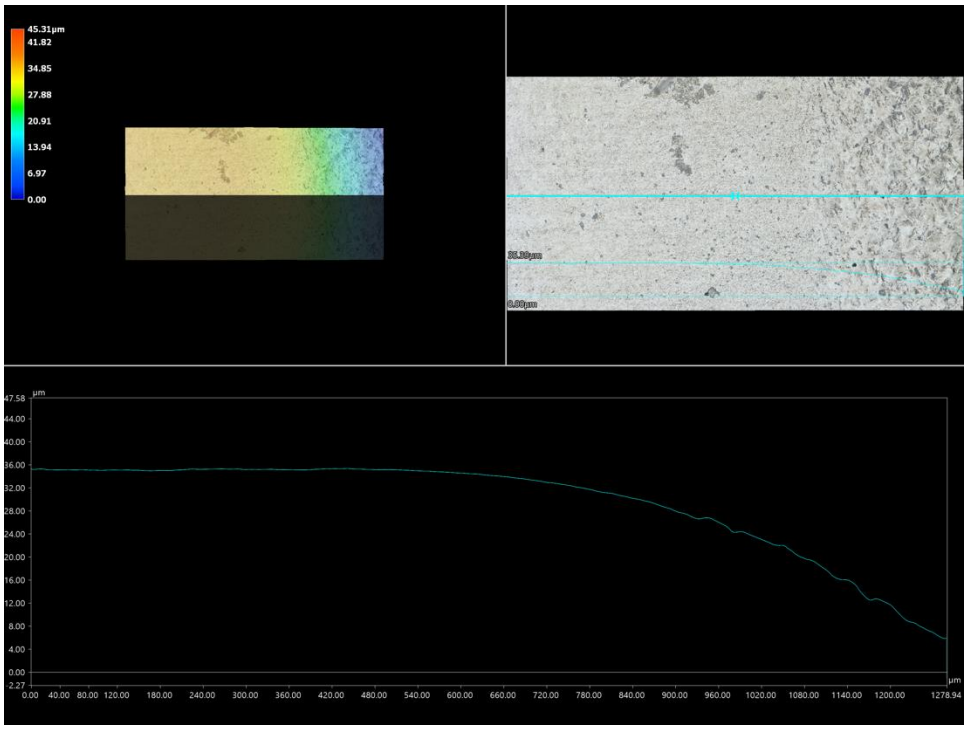


Figure 52: 850 ºC ND-LD polished and etched tensile bar showing failure in the lamellar region adjacent to equiaxed microstructure

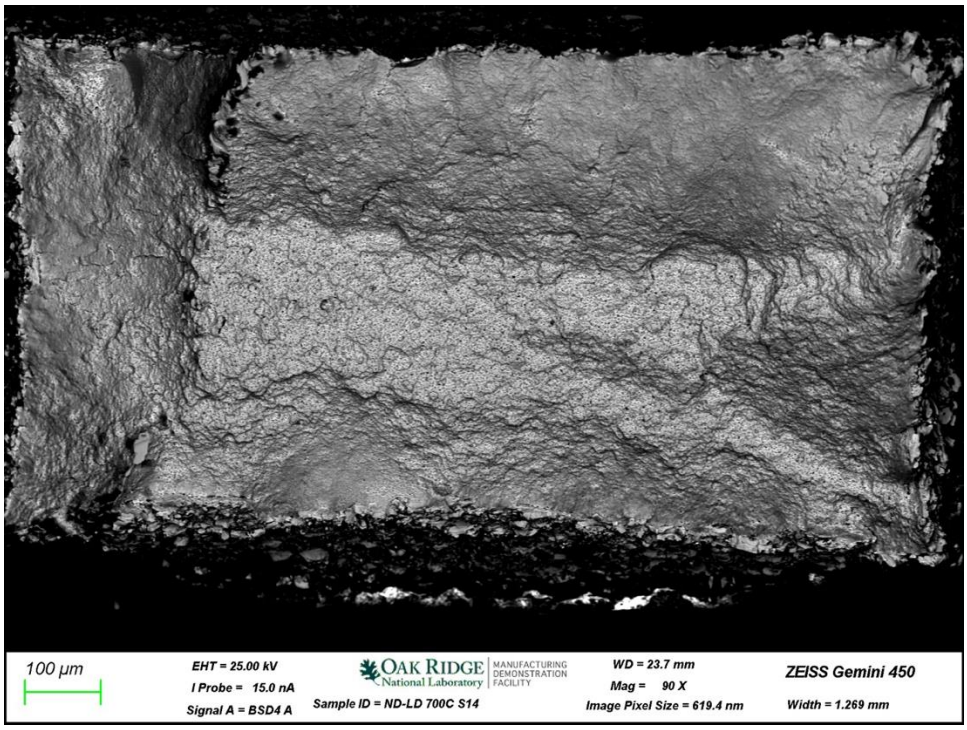


Figure 53: BSE image of ND-LD 700S14 fracture surface

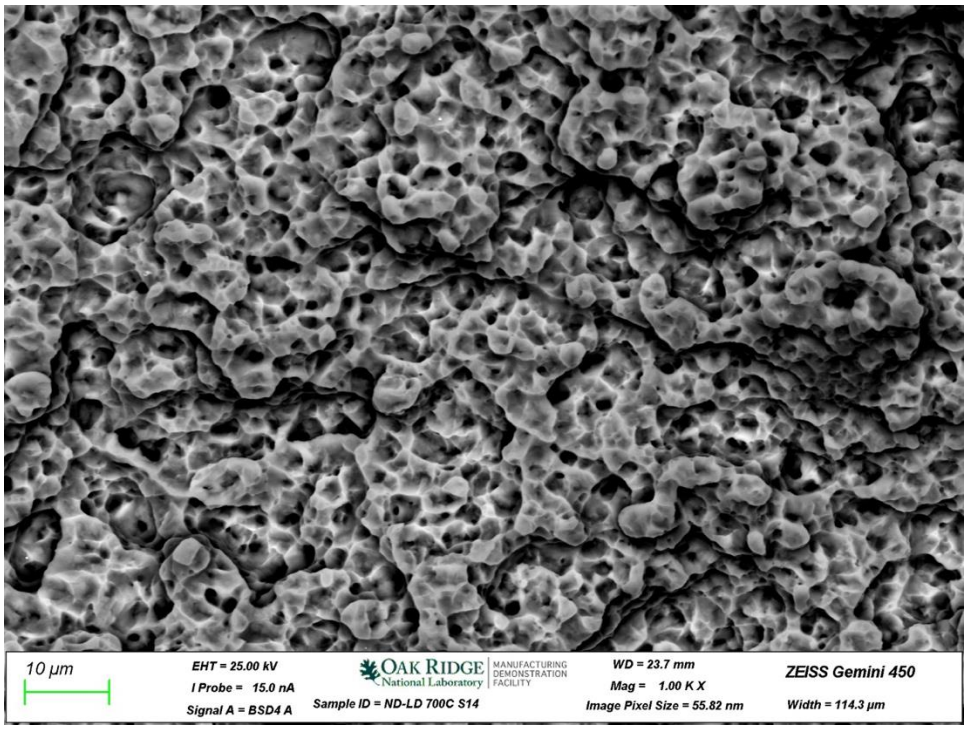


Figure 54: High-magnification BSE image of ND-LD 700S14 fracture surface

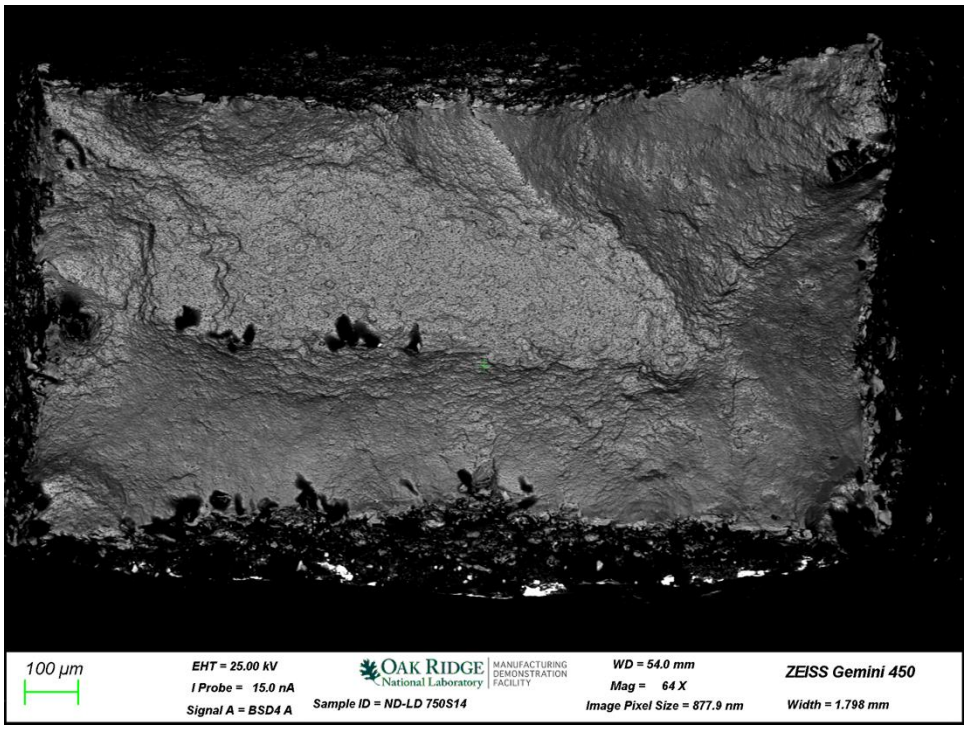


Figure 55: BSE image of ND-LD 750S14 fracture surface

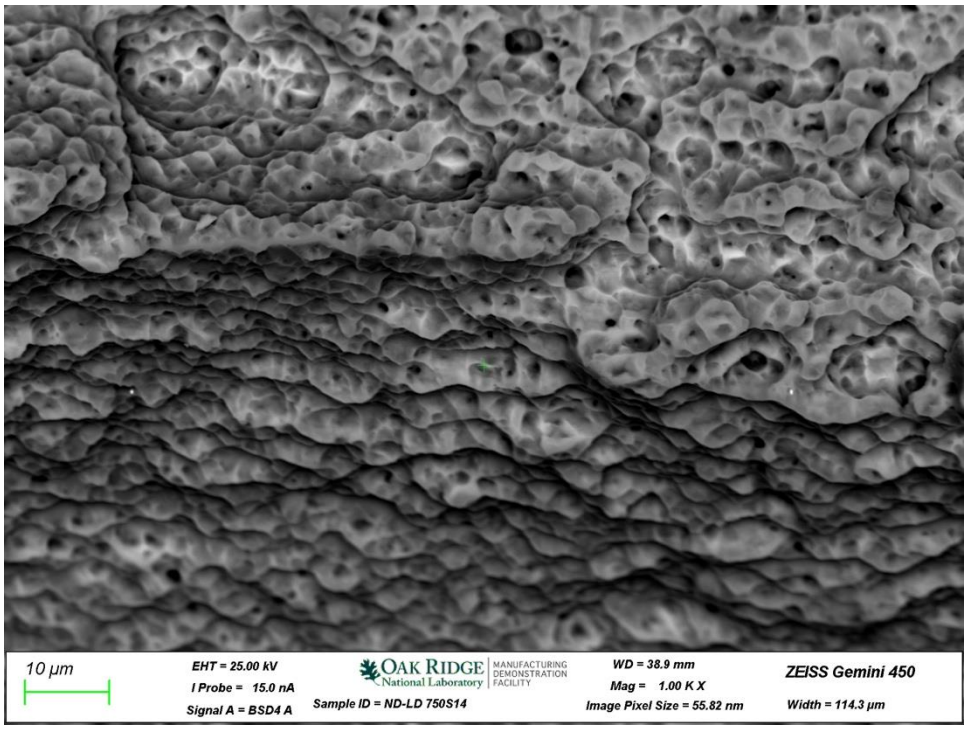


Figure 56: High-magnification BSE image of ND-LD 750S14 fracture surface

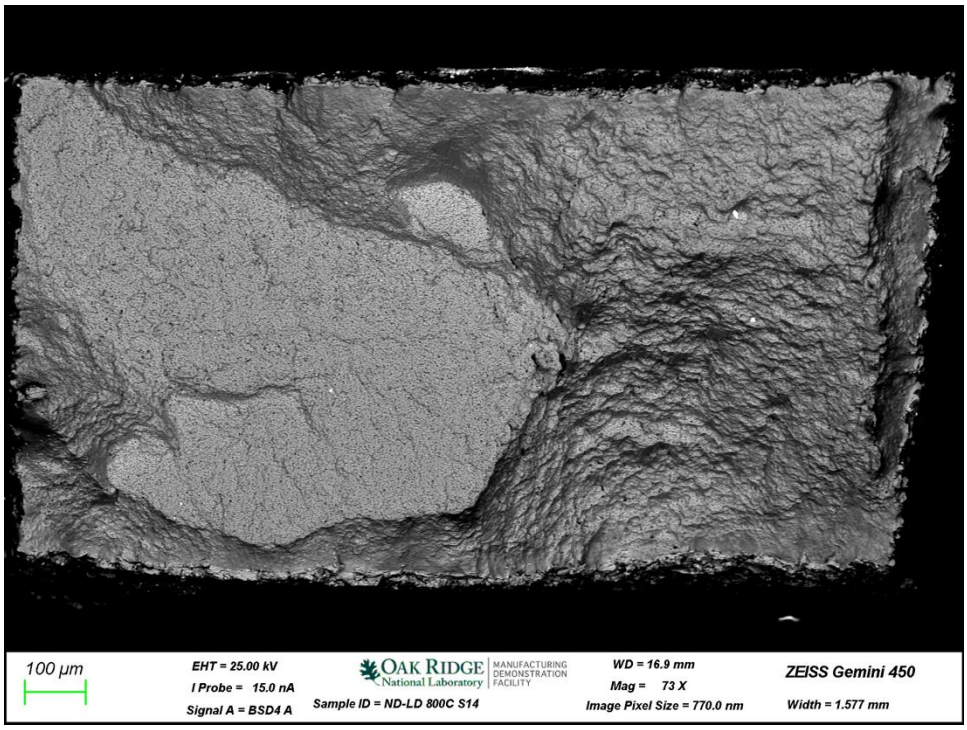


Figure 57: BSE image of ND-LD 800S14 fracture surface

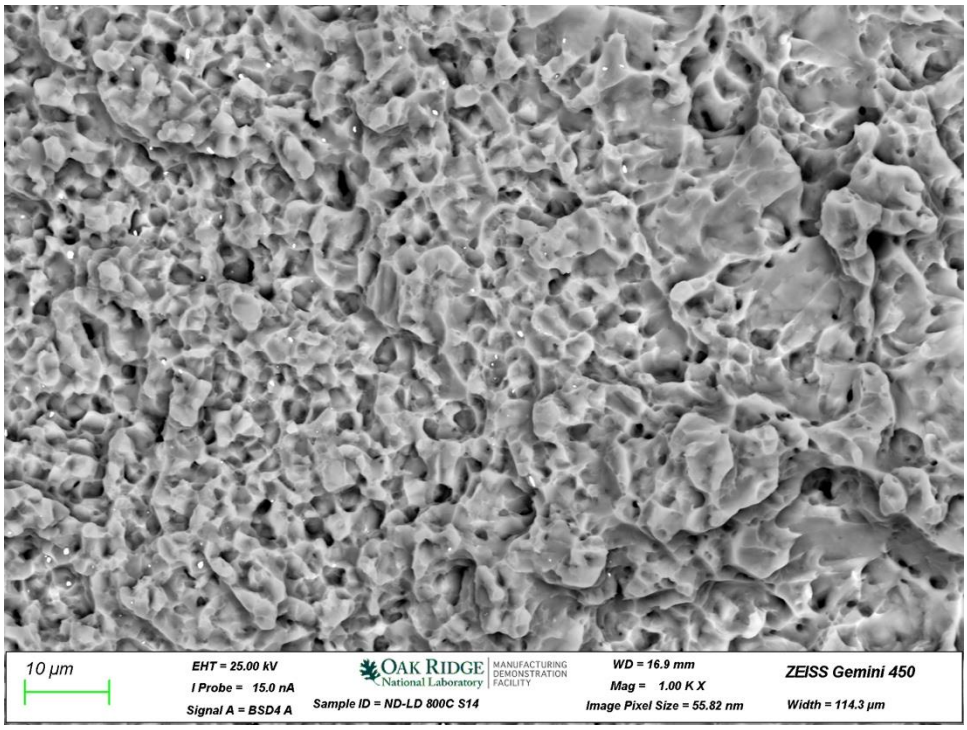


Figure 58: High-magnification BSE image of ND-LD 800S14 fracture surface

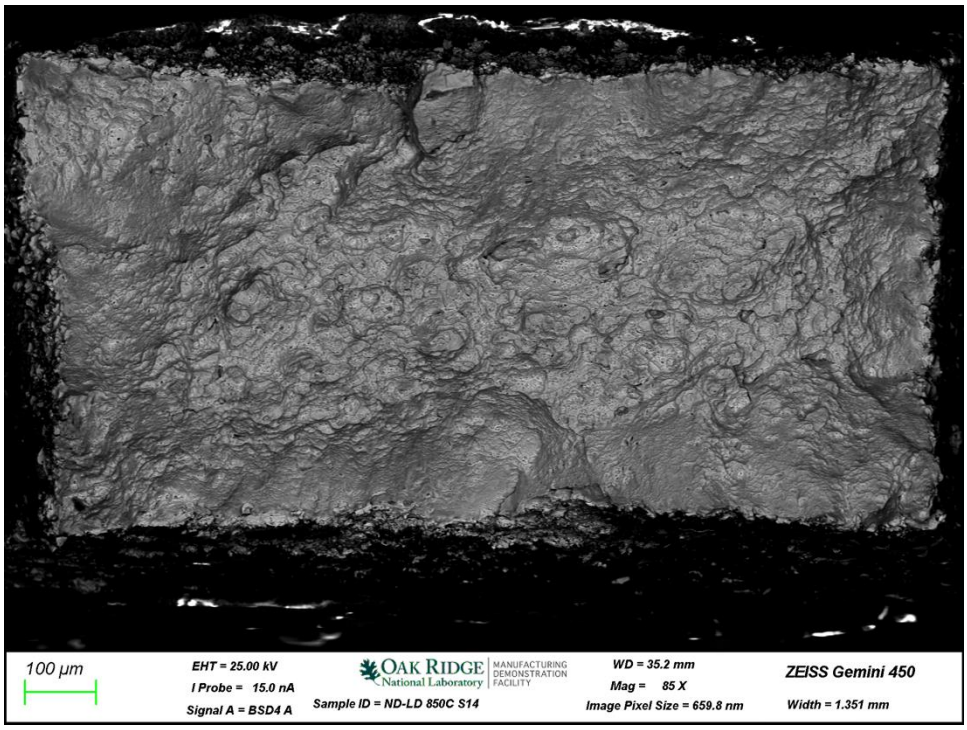


Figure 59: BSE image of ND-LD 850S14 fracture surface

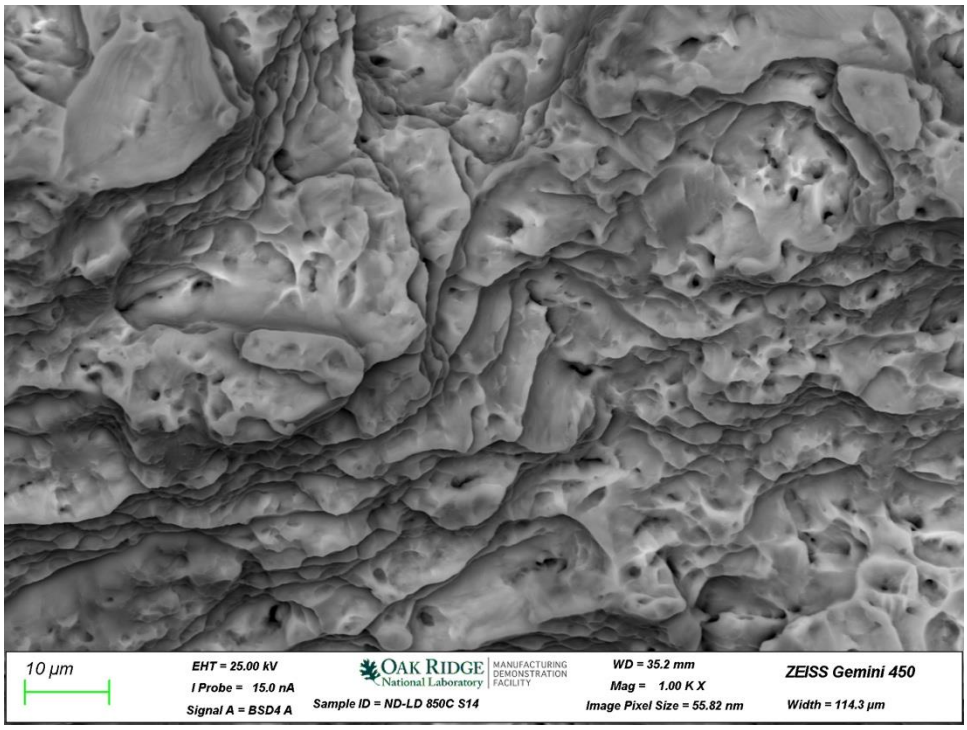


Figure 60: High-magnification BSE image of ND-LD 850S14 fracture surface

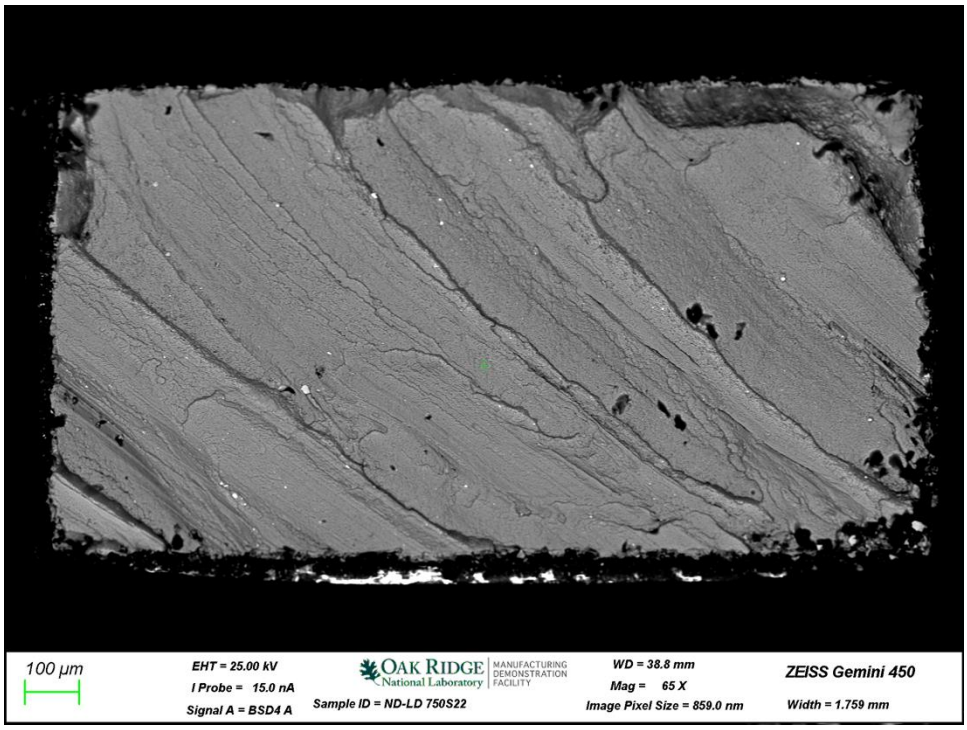


Figure 61: BSE image of ND-LD 750S22 fracture surface

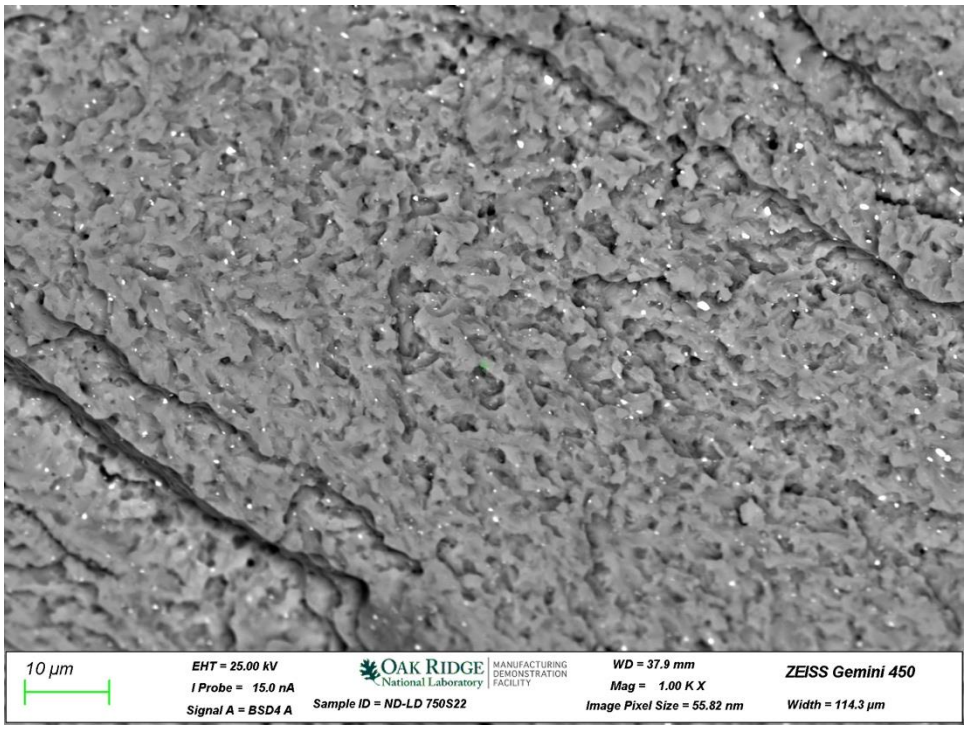


Figure 62: High-magnification BSE image of ND-LD 750S22 fracture surface

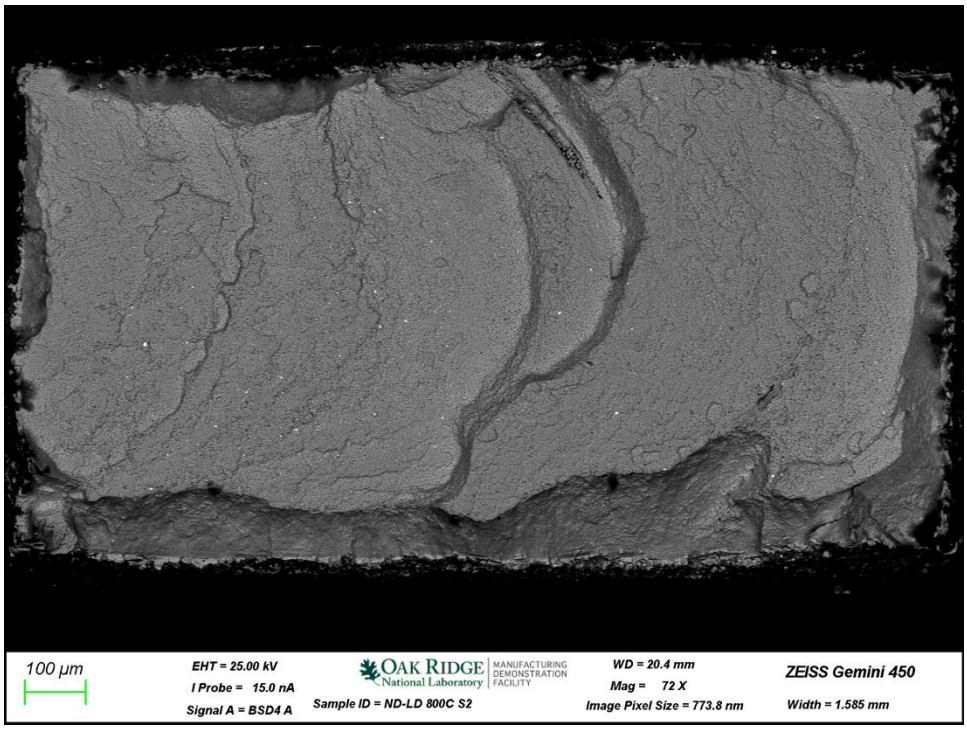


Figure 63: BSE image of ND-LD 800S2 fracture surface

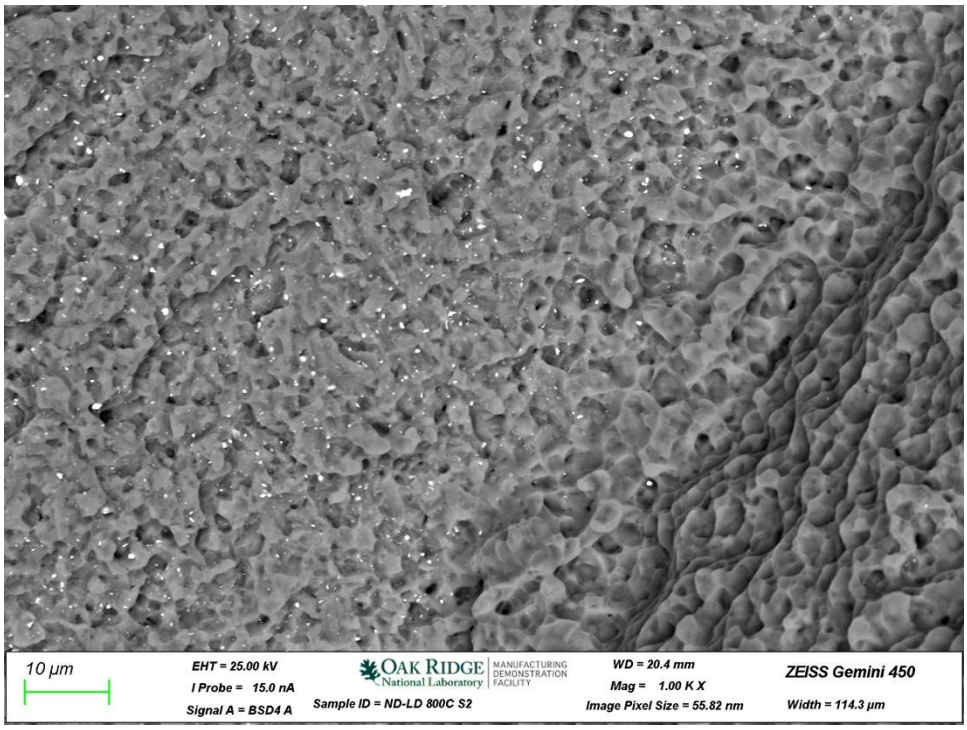


Figure 64: High-magnification BSE image of ND-LD 800S2 fracture surface

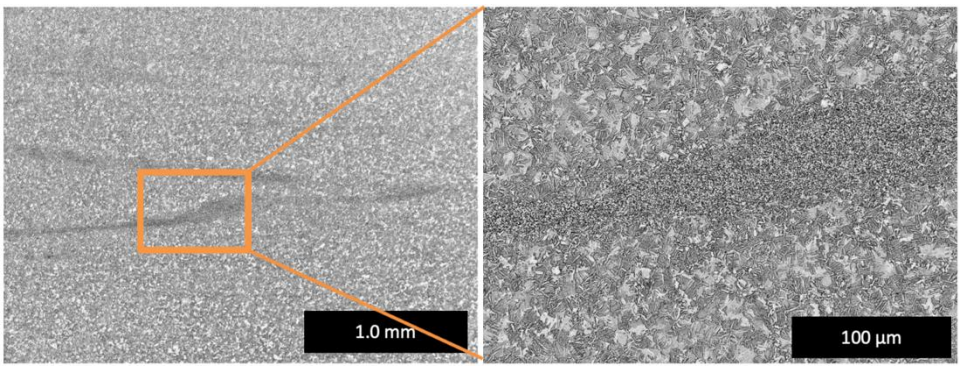


Figure 65: Equiaxed alpha band seen near top of 850 ºC temperature setpoint

chemical analysis at the bulk scale and through a more localized method to determine if the change in microstructure can be attributed to oxygen contamination.

Bulk Chemical Analysis

Bulk chemical analysis via the inert gas fusion method (**Table 10**) revealed that the feedstock had a higher oxygen content (0.19 wt. %) than indicated by the material certification for the originating initial ingot (0.18 wt. % bottom – 0.17 wt. % top). Since the material certification chemistry measurements were taken from the ingot, there may have been some oxygen pickup during the rolling process or subsequent processing to account for the increase in oxygen content. The nitrogen content in the feedstock was measured at 0.013 wt. % as compared to 0.014 wt. % in the ingot measurement.

The chemistry measurements for oxygen in the as-built condition show a slight pickup of 0.01 wt. % during the deposition process. Despite the increase in measured oxygen content, however, the as-built samples did not exceed the maximum allowable concentration of 0.20 wt. % for T-6Al-4V as given by ASTM B381 (91); however, the measurements did match the maximum allowable content for oxygen. Comparatively, there was no measured nitrogen pickup as measured in the bulk chemical analysis and the nitrogen content was well underneath the maximum allowable nitrogen content of 0.05 wt. %. Interestingly, some of the as-deposited samples were measured with a lower nitrogen content (as low as 0.010 wt. %) than the feedstock measurement. The preferential pickup of oxygen as compared to nitrogen can be explained in that the titanium has a higher attraction for oxygen than nitrogen (11). The apparent decrease in nitrogen content in the feedstock and builds may instead potentially arise from

Table 10: Measured bulk oxygen and nitrogen content

Sample	Feedstock	700 ºC	750 ºC	800 ºC	850 ºC
O [wt. %]	0.19	0.20	0.20	0.20	0.20
N [wt. %]	0.013	0.011	0.012	0.010	0.013

inhomogeneous concentrations of nitrogen in the ingot and subsequent feedstock or differences in measurement.

Electron Microprobe Analysis

While there was some difficulty in finding a tungsten band using the microprobe due to the inherently limited resolution of a tungsten filament microscope, a band of tungsten was found, and a line scan was conducted across the band. A BSE image is given in Figure 66 where the light contrasting particles are tungsten, as confirmed by EDS. The EMPA chemical analysis was conducted with a 200-micron line scan with a 1-micron spacing. For plotting of the resulting EMPA data, the zero distance corresponds to the top of the line scan in **Figure 66**, i.e. the line scan starts at the top of the sample and goes down through the Z-height.

In the EMPA data, as shown in **Figure 67**, there are low spikes in the measured wt. % titanium that correspond to low spikes in Al and elevated levels of V. Interestingly, these spikes are separated by roughly 50 microns of distance. Furthermore, these spikes are located outside of the tungsten banding area, and so the spikes are not caused by increased concentrations of tungsten. In the location of the tungsten banding, there are three distinct spikes in W concentration near the center of the line scan that indicate that the EMPA analysis location did scan across a tungsten band. There does not appear to be any spatial variation of oxygen content. There is, however, a spike in nitrogen content that correlate to the same locations that contain tungsten.

The average values from the EMPA analysis are given in **Table 11**. The major alloying elements Al and V had an average of 6.18 wt. % and 4.04 wt. % respectively, matching up well with the feed material certification values of (Al) 6.28 wt. % and (V)



Figure 66: BSE image of 200-micron EMPA line scan across tungsten band

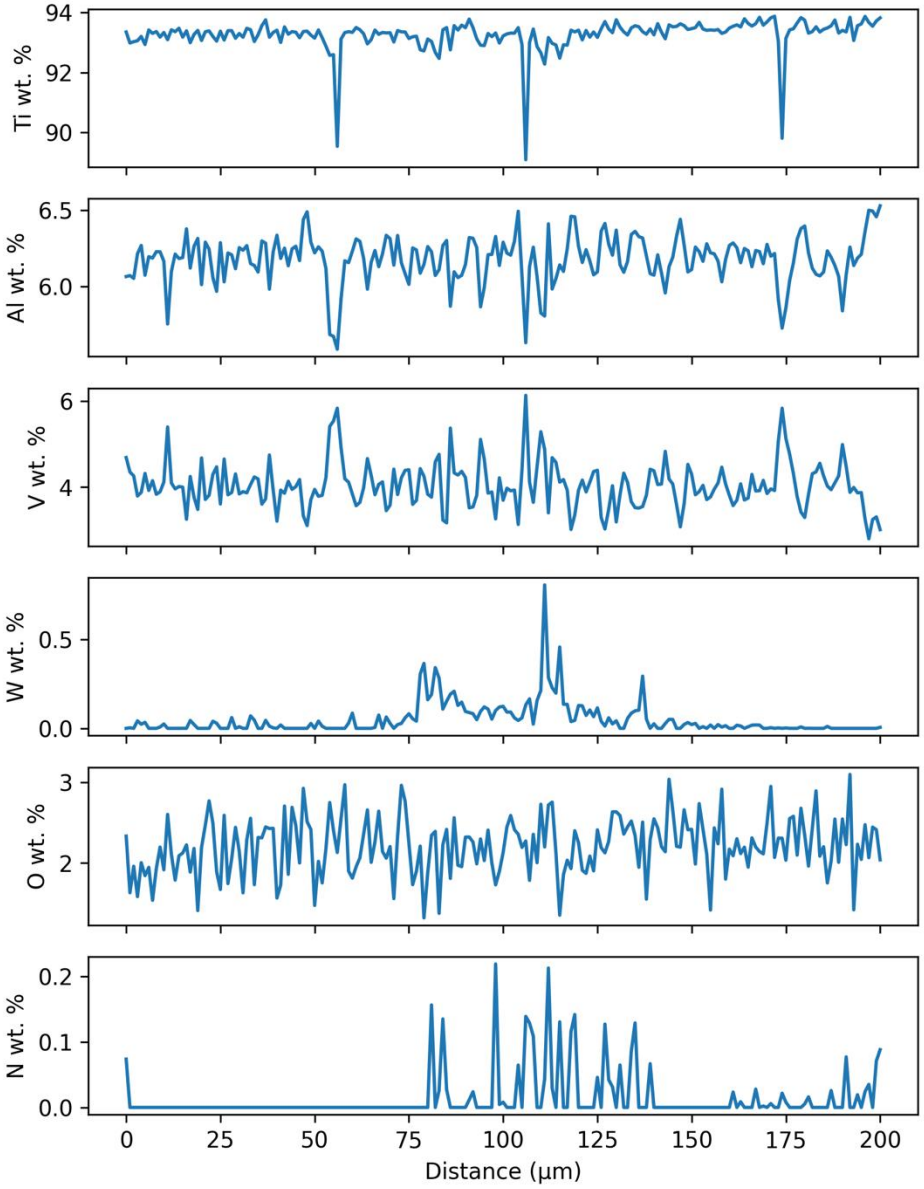


Figure 67: EMPA line scan data for Ti, Al, V, W, O, and N

Table 11: EMPA line scan average values

Elements [wt. %]					
Ti	Al	V	W	O	N
93.26	6.18	4.04	0.05	2.21	0.01

3.96 wt. %. The O measurement of 2.21 wt. %, however, seems high in the context of the bulk chemical analysis measurement.

CHAPTER 5

ANALYSIS AND DISCUSSION

Temperature Setpoint and Microstructure

All temperature conditions display a completely transformed microstructure as compared with the initial rolled mill annealed feedstock. Additionally, there is a large difference in the achievable microstructures for the different temperature setpoints. These insights can be most readily seen in **Figure 68**, where all micrographs are given at the same magnification. In traditional friction stir welding literature, the ability to achieve different microstructures by processing above or below the beta transus temperature in titanium has been well studied (22,152). It is additionally known that the resulting microstructures in FSW/FSP titanium are largely a product of peak temperatures reached during processing (179). Accordingly, differences in temperature during AFSD of Ti-6Al-4V can result in drastically different microstructures.

Impact on Processing

In a traditional FSW study of Ti-6Al-4V, it was found that sub-transus welding conditions resulted in a 300% increase in path force as compared to super-transus welding conditions (30). AFSD should not see the same path forces because the tool is not being forced through the material as in traditional FSW; however, there should still be some differences in the processing conditions for each parameter set due to the differences in flow stress by temperature.

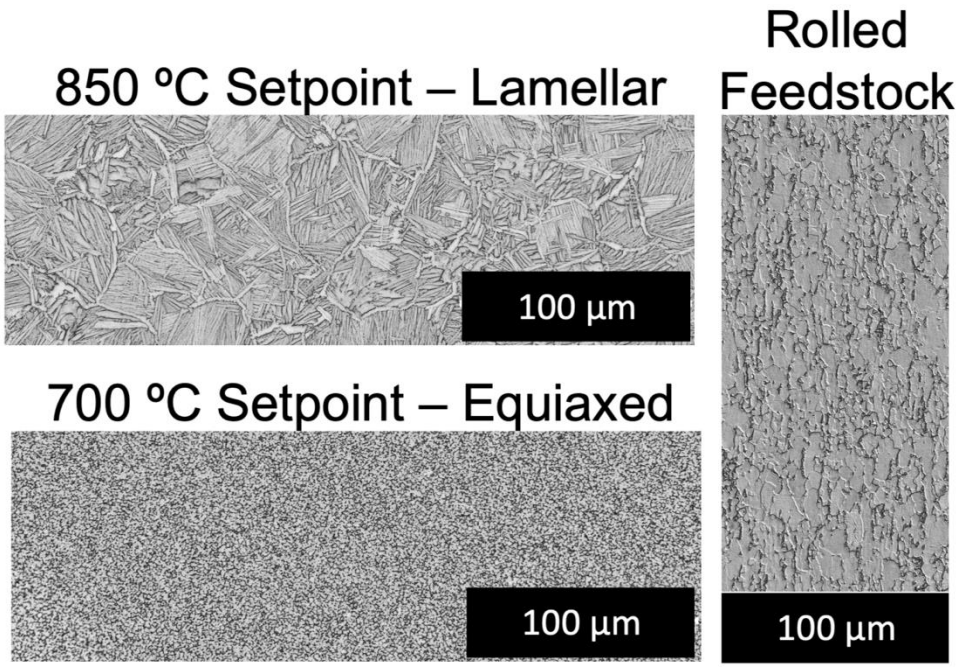


Figure 68: Top region stir zone microstructure for 850 ºC and 700 ºC conditions as well as feedstock

With an analysis of the build log files, the average motor power during deposition of the samples was 4972 W, 5391 W, 5389 W, and 5956 W for the 700 ºC, 750 ºC, 800 ºC, and 850 ºC deposition temperatures; however, it should be noted that the traverse and material feed rates decreased for the lower temperature setpoint conditions to account for increased forces. To better determine the effect of temperature setpoint on processing conditions, the feed rates must be considered in as well.

Volumetric energy density is sometimes given as a simplified energy input metric for metal additive manufacturing processes, though with some caveats that different combinations of energy input can yield different results (180,181). Nonetheless, the metric can still give a comparison of the energy input required for different deposition conditions in AFSD. The equation is given in Equation 2, where P is the input power, v is the travel speed, and t is the layer thickness.

Equation 2: Volumetric Energy Density

$$E_V = \frac{P}{v \cdot h \cdot t}$$

For the AFSD process, Sharma et al. used a specific linear energy density for AFSD of a magnesium alloy (66). This equation is given in Equation 3, with inputs (M) tool torque, (ω) tool rotational speed, and (V) tool travel speed.

Equation 3: Specific Linear Energy Density

$$E_S \approx M \frac{\omega}{V}$$

The volumetric energy density and specific linear energy density for this study of AFSD of Ti-6Al-4V are given in **Table 12**. While the mean tool power decreased for

Table 12: AFSD processing conditions and energy metrics

PID Temperature Setpoint [ºC]	700	750	800	850
Traverse Velocity [mm/s]	2.12	2.54	3.39	4.23
Mean Tool Power [W]	4972	5391	5389	5956
Mean Tool Torque [N-m]	6741	7309	7307	8075
Volumetric Energy Density [J/mm^3]	61.7	55.7	41.8	36.9
Specific Linear Energy Density [J/mm]	352	324	249	224

decreasing tool temperature setpoints, the volumetric energy density required increased significantly. The 700 ºC and 750 ºC temperature setpoints required a 67% and 51% greater volumetric energy density than the 850 ºC case. The 800 ºC condition required only a more modest 13% increase in volumetric energy density.

An additional pseudo-heat index derived from traditional FSW literature has been proposed for AFSD by Garcia et al. that is based on the spindle rotational rate and the traverse velocity (63). The pseudo-heat index is given by the equation $\frac{\Omega}{V}$ or $\frac{\Omega^2}{V}$, where omega represents the tool rotation speed and V represents the traverse feed rate. Yoder et. al later applied this pseudo-heat index to AFSD of Ti-6Al-4V, finding a correlation between the $\frac{\Omega^2}{V}$ index and prior beta grain size.

The $\frac{\Omega}{V}$ and $\frac{\Omega^2}{V}$ pseudo-heat indexes for this study is plotted in **Figure 69** based on the peak temperature being the temperature setpoint. It is observed that there is no trend for the $\frac{\Omega^2}{V}$ pseudo-heat index and peak temperature as a fraction of the melting temperature and there was a negative correlation for the and $\frac{\Omega}{V}$ index; however, it should be noted that there is a significant difference in heat input in this study as compared to previous AFSD Ti-6Al-4V publications. This study's pseudo heat index was on the order of 7,000 $RPM^2/(mm/s)$. Under the Farabi et al. study, the pseudo-heat index ranged from 47,000 $RPM^2/(mm/s)$ to 98,000 $RPM^2/(mm/s)$. The Yoder et al. study pseudo heat index ranged from 21,000 $RPM^2/(mm/s)$ to 124,000 $RPM^2/(mm/s)$. Nonetheless, extrapolating

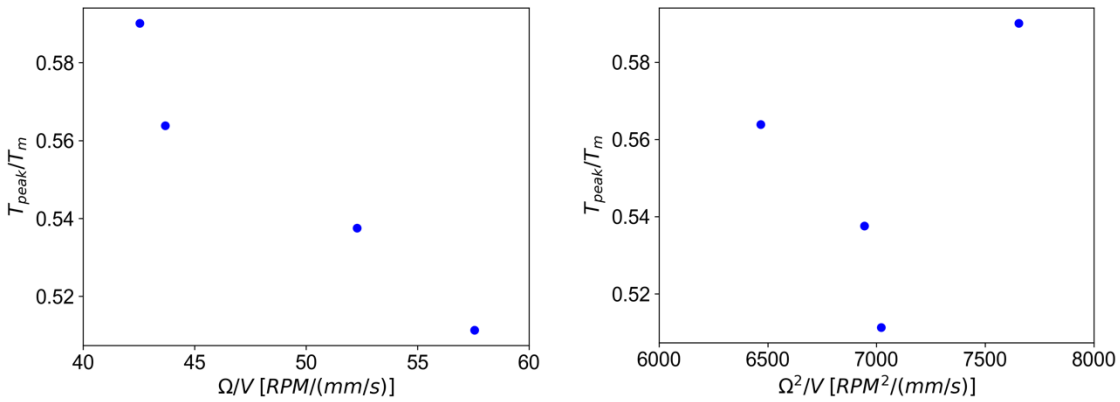


Figure 69: Pseudo-heat index (a) $(\frac{\Omega}{V})$ and (b) $(\frac{\Omega^2}{V})$ for this study

on Yoder et al.'s correlation to prior beta grain size, this study should expect a prior beta grain size on the order of 5 microns.

The pseudo-heat index was first applied to the single-phase materials copper and aluminum. In the case of Ti-6Al-4V, there is a phase change with corresponding differences in properties between the high-temperature beta phase and the low temperature alpha phase. As observed in the as-printed microstructures, the print conditions in this study are near the beta transus temperature. Therefore, it can be surmised that, while the pseudo-heat index may be descriptive for AFSD in the single beta phase field above the beta transus temperature, the index fails to explain heat generation in the material near the beta transus temperature.

It is also worth noting that, due to the use of closed-loop temperature control, geometry may play a significant role in the resulting PID controlled spindle speed due to the low thermal conductivity of titanium. Further study will be required to untangle the complex relationships between build geometry, heat generation, and microstructures.

Sub-Transus to Intermediate to Super-Transus Processing

Etched microstructures with accompanying EBSD at the same scale are given in **Figure 70**. The fully lamellar microstructure of the 850 ºC temperature setpoint build is characteristic of processing fully above the beta transus temperature. In this case, the material is deformed and heated above the beta transus temperature in the stir zone by frictional and adiabatic heating. The high temperature beta phase grains will undergo continuous dynamic recrystallization as they are stirred together. These refined beta grains, left behind in the deposited material, then cool and form a lamellar microstructure,

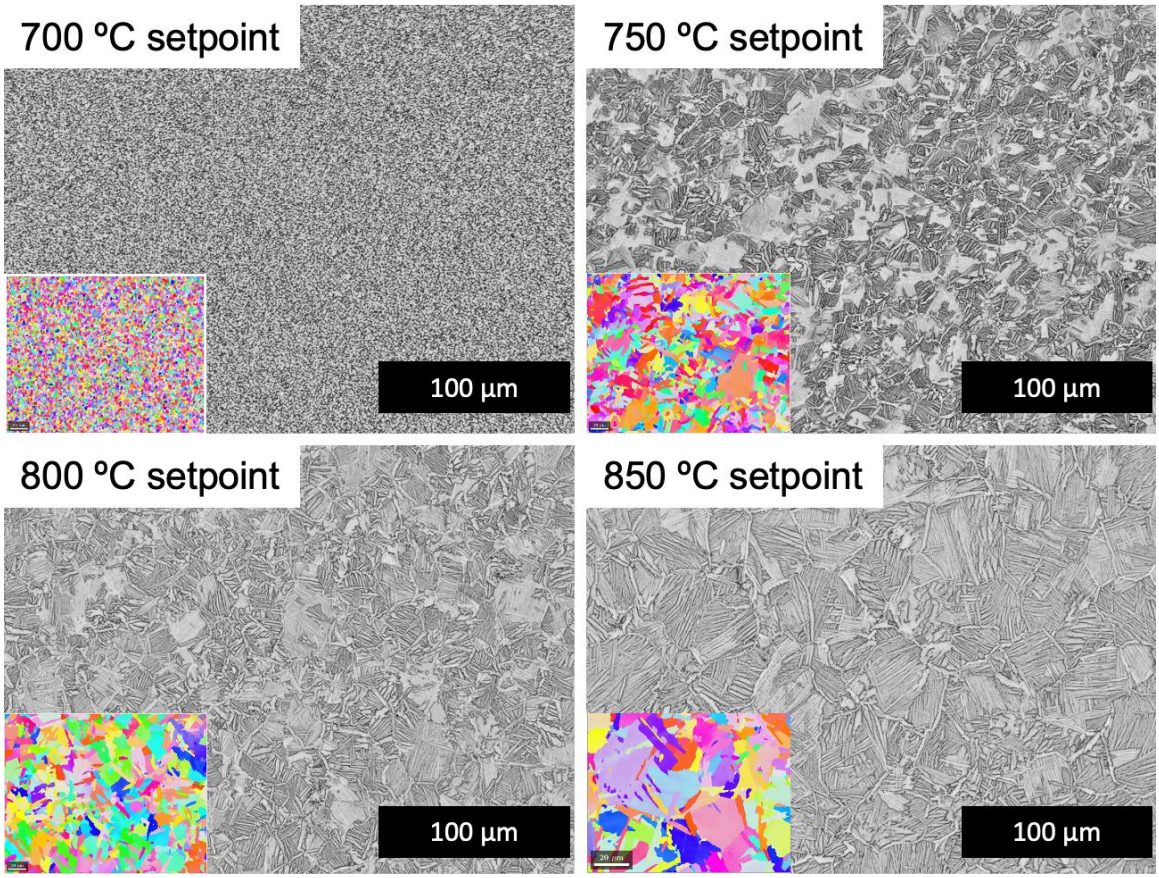


Figure 70: Etched microstructure and alpha Ti IPF for each temperature setpoint

where the lamellar alpha grain structures form via nucleation and growth upon cooling from the higher temperature beta phase. The nucleation and growth step occurs after the tool has passed meaning there should be no further deformation of the material. This should result in relatively stain free grains.

For the 750 ºC and 800 ºC temperature setpoint builds, the presence of both equiaxed alpha and lamellar microstructures indicate that multiple recrystallization mechanisms were active during the AFSD process at this temperature setpoint. This indicates that processing occurred near, but below the beta transus temperature in the alpha + beta phase field, where the microstructure partially, but incompletely, transformed to the high temperature beta phase during processing.

The equiaxed alpha microstructure morphology observed in the 700 ºC temperature setpoint case is characteristic of continuous dynamic recrystallization during deposition below the beta transus temperature. Because processing already took place in the alpha + beta phase field, no further phase transformations take place.

The trend of increasing alpha phase microstrain with increasing deposition temperature, however, seems paradoxical. For the 850 ºC temperature setpoint case, it can be seen from optical images of grain boundary alpha infilled with alpha laths that the stir zone temperature exceeded the beta transus temperature. Upon cooling in the absence of deformation, it should be expected that the new strain-free alpha grains should nucleate and grow into the prior beta grains. The presence of significant microstrain in the alpha phase implies that there may be deformation after the allotropic phase transformation from the high temperature beta phase to the lower temperature alpha

phase. Alternatively, the higher temperature deposits may allow for an annealing effect creating some residual stress relief as compared to the lower temperature setpoints.

Interestingly there are significant differences in the as-printed textures for the different temperature setpoint conditions as seen in **Figure 71**. With an increase in temperature setpoint, the material becomes increasingly textured. For the 700 ºC temperature setpoint, the texture is virtually random. This result can be explained by the AFSD deposition process below the beta transus temperature, where massive plastic deformation introduces dislocations into the microstructure. These dislocations form into subgrain networks and later grain boundaries as more and more dislocations are absorbed into the grain boundaries, increasing the grain misorientation. The result is a highly misoriented microstructure.

For the 850 ºC temperature setpoint, the deformation takes place in the high temperature beta phase. It has been previously noted that FSW/FSP of titanium allows above the beta transus temperature results in a D_1 bcc simple shear texture (182). This shear texture is preserved through the phase change to the low temperature alpha phase through the Burgers orientation relationship.

In the case of the 750 ºC and 800 ºC temperature setpoints, there is a combination of the above mechanisms, resulting in a transition from a minimally textured in the case of the 700 ºC temperature setpoint to highly textured in the case of the 850 ºC temperature setpoint.

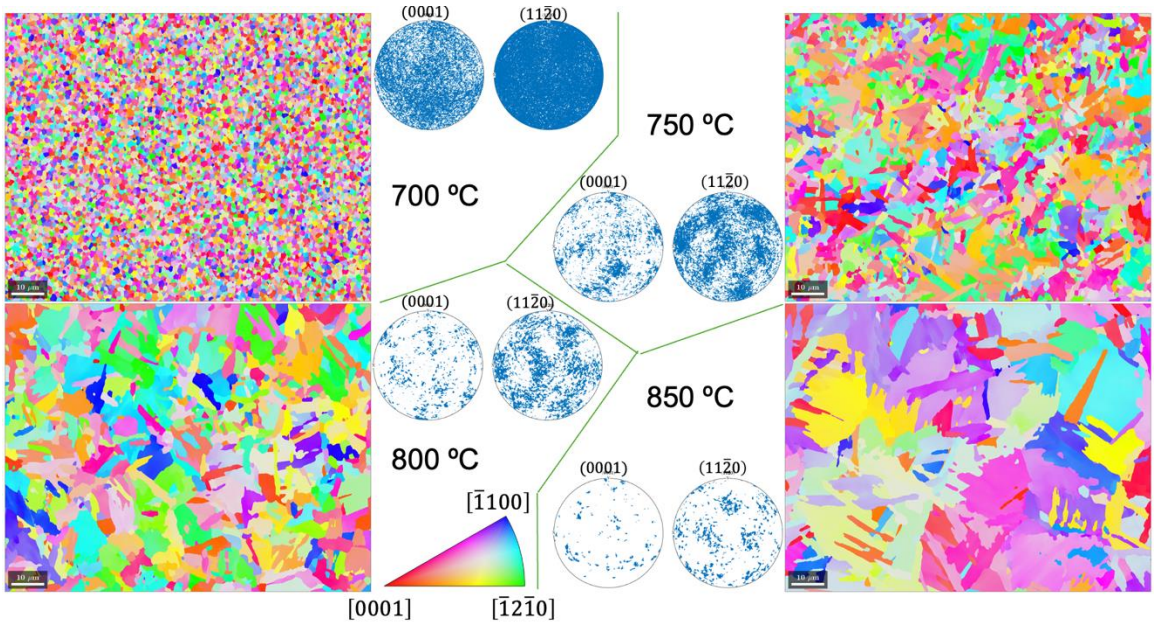


Figure 71: Alpha Ti IPFs and alpha textures for each temperature setpoint

Heterogenous Microstructure Development

In FSW Ti-6Al-4V, it has been reported that there is little difference between the advancing and retreating SZ microstructures (30). Similarly, there is little observed differences between the advancing and retreating sides in this study of AFSD Ti-6Al-4V. It should be noted, however, that in this present study, a back-and-forth raster build pattern was used. There remains the potential that advancing/retreating side differences may be apparent in a single direction multi-layer AFSD build.

The different deposition temperatures give distinct top layer stir zone microstructures. Below the stir zone, however, the etched micrographs reveal heterogenous microstructure development, as shown in **Figure 72** for the 850 ºC temperature setpoint. On a closer inspection of the etched microstructures, the light etching regions correspond to a lamellar microstructure while the dark etching regions correspond to an equiaxed alpha microstructure. Between the dark and light etching regions lies a mixed microstructure consisting of some fraction of both lamellar and equiaxed microstructure morphologies.

In addition to heterogenous microstructures, microhardness testing reveals heterogenous hardness through a transverse section of the tested samples. The microhardness was previously noted to vary on the order of the commanded layer height during deposition. Therefore, it is hypothesized that the small-scale layer banding directly results from the commanded layer height. Similarly, based on the observation that there were four discreetly deposited bars of material, it is hypothesized that the hardness

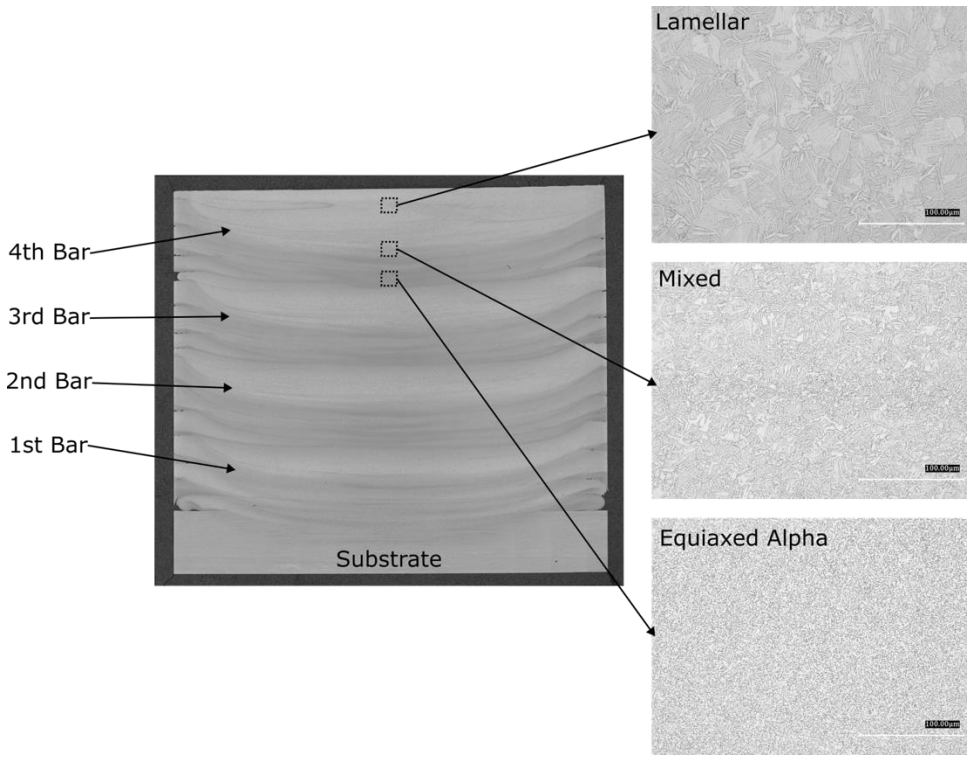


Figure 72: Microstructure heterogeneity in the 850 ºC sample

banding on the order of 5 mm is related to the process stoppages inherent to the discreet feed additive friction stir deposition machine used. The observed hardness banding was analyzed using a Fast Fourier Transform (FFT) based technique.

Fourier analysis using FFTs is commonly used to transform data into the frequency domain. In this technique, the 2D microhardness plot data is read into a Python program that performs a 2D FFT on the spatially varying hardness data. The zero-frequency component of the hardness data is filtered, effectively subtracting the mean hardness values to normalize the data. The microhardness plots, 2D FFT results, and a 1D vertical slice of the FFT data are then plotted.

The results of the technique are given in **Figure 73**. In the reciprocal space plots, there is virtually no hardness frequencies in the transverse axis of the sample. All the frequency information is in the vertical axis of the plots, corresponding to the normal direction of the build. The dotted line represents the commanded layer height of 1.02 mm (0.040 in). The dashed line represents the reload frequency of six times the commanded layer height. In the 700 ºC, 750 ºC, and 800 ºC FFT hardness data, there is higher frequency data in the reciprocal plots, while there is little higher frequency data in the 850 ºC sample. This higher frequency data can be seen to correlate with the layer height, with multiples of the layer height showing up as well at slightly lower frequencies.

Lower frequency data is visible in the FFT analysis is visible as well. It can be observed that the every-six-layer reload frequency is readily apparent in all the tested build conditions and matches exactly in the FFT data. The large peaks in the 1D FFT at

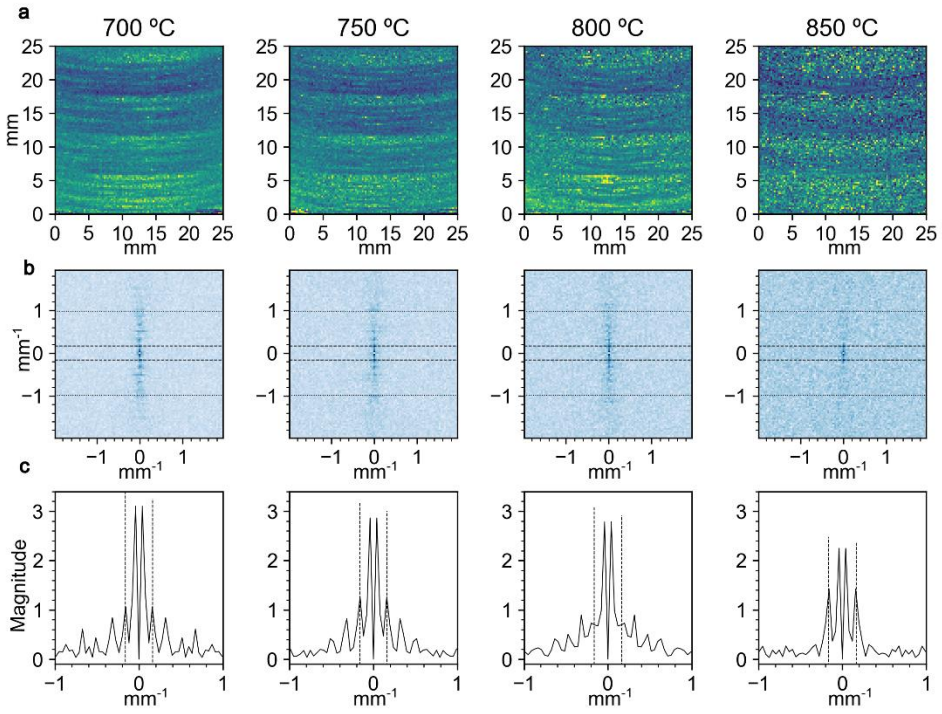


Figure 73: FFT analysis results: (a) microhardness plots, (b) FFT results in reciprocal space, (c) 1D vertical slice of the FFT data

the lowest frequencies correspond to the 24 total layers in the build. It is of note that there is little to no higher frequency data in the 850 ºC. The lack of mechanical heterogeneity on a scale other than the reload frequency can be explained by the microstructure development as discussed earlier.

For the 850 ºC case, the material is completely above the beta transus temperature during the AFSD process. After the tool passes and massive plastic deformation ceases, the deposited material cools and transforms from the high temperature beta phase to the low temperature alpha phase through nucleation and growth, creating new strain free grains. If the volume below the tool that is above the beta transus temperature is larger than the stir zone, the microstructure that develops after the phase transformation will not show layer-scale mechanical heterogeneities that arise if the stir zone is below the beta transus temperature. If the build stays at high temperature throughout the build, either because only a single bar is deposited in a discrete feed machine or because there are no pauses in deposition with a discreet feed machine, this finding can explain how previous publications such as Farabi et al. (8) and Yoder et al. (9) describe a uniform microstructure after AFSD of Ti-6Al-4V.

Below the beta transus temperature, some of the deformation is taking place in the alpha phase, where dynamic continuous recrystallization is instead the operant mechanism. For this case of processing below the beta transus temperature, there is not further transformation after deposition, leaving small, finely distributed equiaxed grains.

Differences Compared to Traditional FSW/FSP

Both the AFSD and FSW/FSP processes rely on using frictional heating to soften a material and allow for solid-state bonding to occur, there are some significant differences between the two processes.

The FSW process is dominated by shear. The AFSD process, however, also has a deformation component resulting from feed material pushed through the hollow tool. In this present study, the material feed actuator exerted a force ranging from 11.4 kN to 15 kN. Assuming that this force is applied solely to the 9.5 mm by 9.5 mm cross-sectional area of the feedstock, this corresponds to 126 MPa to 162 MPa. These stress values give an idea of the stress in the material as it begins to deform and exit the tool. This material feed component has previously been reported to results in the formation of a concave down shaped interface between the deposit material and the substrate in a study on the AFSD of aluminum (90).

Another significant difference between FSW and AFSD is that the FSW process is typically only a single pass. A single welding pass means that the material will undergo only a single thermo-mechanical cycle. AFSD, by its additive nature, will undergo multiple thermo-mechanical cycles. FSP may consist of multiple passes, however, the effects of this thermomechanical cycling have not been significantly reported on in literature. It is hypothesized that this thermomechanical cycling leads to the heterogenous microstructures observed in this study.

Mechanical Properties

Temperature Setpoint and Mechanical Properties

Due to the use of a subsize tensile specimen, there may be an effect on resulting measured tensile properties. Gussev et al. (183) found that scale factor had a weak effect resulting in only a small effect on accurate measurement of yield stress, ultimate tensile stress, and uniform elongation, with the caveat that systematic differences between different scales should be considered in interpreting results. Additionally, they reported that techniques such as digital image correlation can reduce the effects of scale factor and improve resulting measurements. Based on internal testing of the effects of scale factor for wrought Ti-6Al-4V comparing 3.05 mm (0.12 in) thick ASTM E8 subsize tensile specimens and the subscale tensile geometry used in the present study, it was shown that the smaller tensile specimens measured on the order of 10% lower in yield strength, ultimate tensile strength, and elongation than ASTM E8 subsize tensile specimens (unpublished).

Another potential source of error is from the surface finish after EDM machining. It has been reported in literature that EDM machining of titanium can result in decreased fatigue properties due to the formation of a brittle recast layer (184). Despite the EDM surface finish, tensile properties were overall good for all tested parameters and surface cracking was not observed. The mean YS and UTS averaged for all tested orientations as a function of deposition temperature is given in **Figure 74**. Mean elongations are similarly plotted in **Figure 75**.

The strain hardening exponent as a function of temperature setpoint and tensile bar orientation is given in **Figure 76**. For all tensile bar orientations, there was an

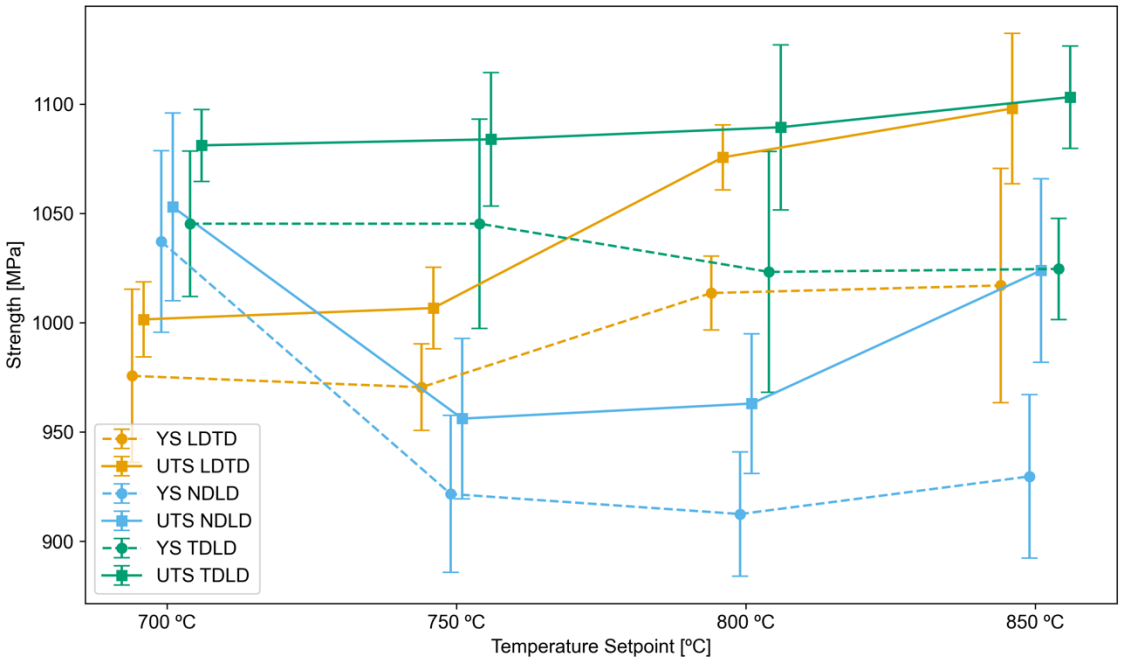


Figure 74: Mean tensile properties as a function of temperature setpoint

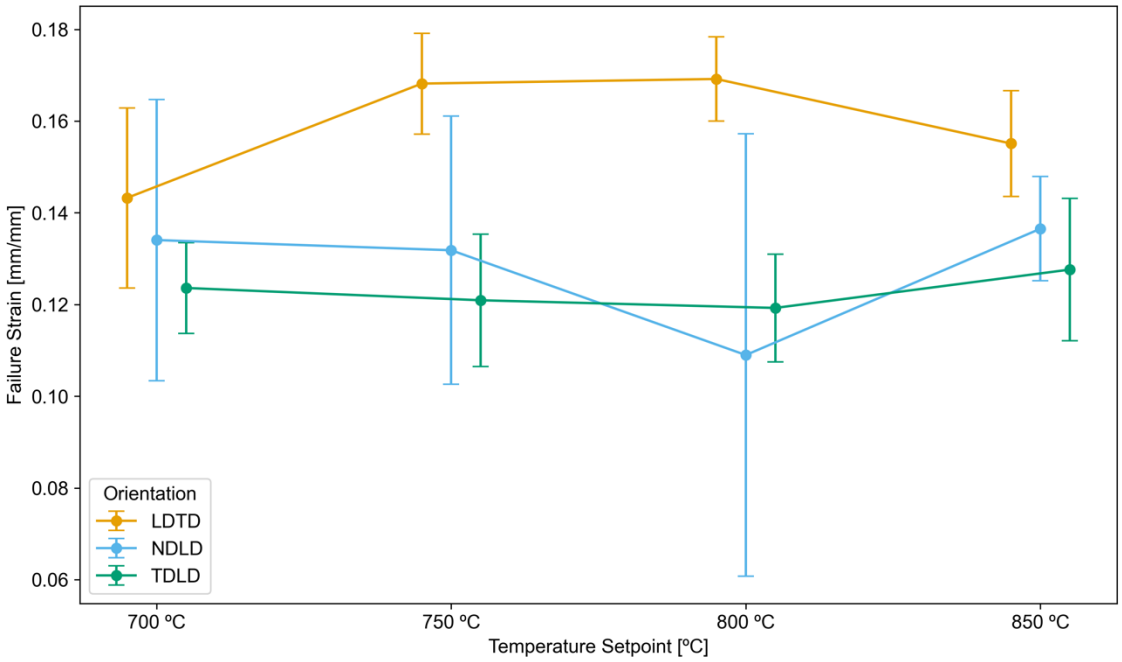


Figure 75: Mean elongations as a function of temperature setpoint

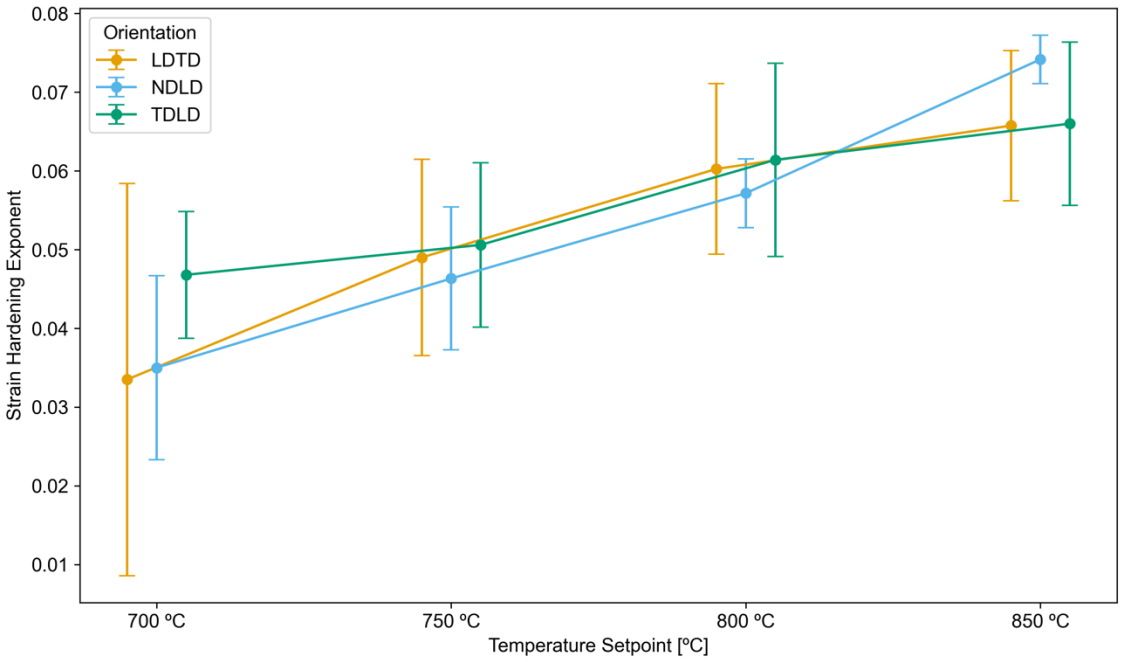


Figure 76: Strain hardening exponent as a function of temperature setpoint and tensile bar orientation

increasing trend work hardening as a function of temperature setpoint. It is worth noting that the XRD microstrain measurements for the alpha phase also display an increasing trend with temperature setpoint (**Figure 33**). While peak broadening in X-ray diffraction can result from a multitude of sources in addition to dislocations (178), this indicates that the lower deposition temperature conditions will broadly contain a lower dislocation density than the higher deposition temperatures. Since strain hardening results from the interaction of dislocations with other dislocations and other barriers to dislocation motion (14), this may indicate that, for increasing deposition temperatures, there is more dislocation pile up with preexisting dislocations, resulting in an increasing trend in strain hardening exponent with increasing deposition temperature.

Microstructure and Mechanical Properties

To better elucidate the relation between microstructure and mechanical properties, a series of ND-LD tensile bars were polished and etched before being characterized and mechanically tested. All the tested polished and etched samples exhibit at least some amount of initial yielding in the lamellar microstructure regions, even if the eventual failure later occurred in an equiaxed region. Samples 700S13 and 750S13 show initial yielding in lamellar regions before failure occurred in an equiaxed region. While not tested to failure, sample 800S13 shows yielding in its lamellar regions with significant necking in the uppermost lamellar region. Sample 850S13 also shows significant deformation and necking in multiple lamellar regions with the eventual failure being in the uppermost lamellar region.

The observation of this multiple yielding behavior showing that some regions initially yield without eventually becoming the failure location suggests that there may be

some texture effects on the resulting mechanical properties of AFSD Ti-6Al-4V. From traditional FSW literature, it is known that FSW/FSP can impart a deformation texture on processed titanium (20,182,185–187). Additionally, it is known from this study that AFSD Ti-6Al-4V exhibits increasingly textured microstructures as a function of temperature setpoint.

It is hypothesized that the more strongly textured lamellar regions exhibit initial yielding due texture effects. This could potentially originate from preferential yielding of the $\{0\ 0\ 0\ 1\}_{\alpha}$ titanium directions as has been previously observed in AFSD Ti-6Al-4V (10). The deformation may then potentially result in the rotation of the crystal structure to favor a greater alignment of the stronger alpha titanium c-axis, limiting further plasticity. Considering not enough texture information has been gathered in the present study to prove this hypothesis, a more thorough investigation of the effects of AFSD processing on resulting texture of titanium and its effects on resulting mechanical properties is merited.

Defects in AFSD Ti-6Al-4V

Oxygen/Nitrogen Pickup

Since oxidation in titanium can reduce ductility and lead to embrittlement (11), it is critical that a high-quality inert environment must be maintained during high temperature processing of titanium. While the samples in the present study were built in an argon inert environment, it was not a perfectly inert. The mean oxygen content and standard deviation in the inert enclosure are given in **Table 4**. While there was some variation in the oxygen content during the builds, the mean oxygen content during the AFSD processing of all the samples was 0.6%. Because there was only one oxygen

sensor, however, it not known how uniform the oxygen content was inside the inert enclosure. Nitrogen pickup can also be a concern; however, the nitrogen content inside the enclosure during deposition is not known.

In a study on the effects of oxygen content in the inert enclosure during WAAM of Ti-6Al-4V by Halisch et al., it was found that, even with oxygen contents of up to 0.6% in the enclosure, the resulting printed samples still met aerospace requirements during tensile testing (188). While the material met the required tensile properties, the measured oxygen content in the samples did exceed the 0.20 wt. % maximum. In the present study, oxygen content in the inert enclosure matched the highest oxygen concentration from the Halisch et al. publication. The temperatures of the titanium during deposition, however, are significantly lower than the melting temperature of the material: on the order of 0.5 $T_{max}/T_{melting}$ for the present study. Therefore, it can be inferred that the amount of oxygen absorbed during the AFSD process will be lower than during the WAAM process.

From the bulk chemical analysis measurements, it was found that the oxygen content in the AFSD samples did not exceed the 0.20% maximum requirement for Ti-6Al-4V. While it was hypothesized that lower deposition temperatures may limit the uptake of oxygen into the as-deposited samples as compared to the higher temperature samples, there was no measured difference in oxygen content in any of the deposition temperatures. All the AFSD temperature setpoint conditions picked up approximately 0.01 wt. % oxygen during processing. Because of the reactivity of titanium, however, it may be preferrable to begin with a lower oxygen content feedstock to give more of a buffer to maintain the material specifications for oxygen content.

Equiaxed Alpha Banding

Darkly etching bands of equiaxed alpha were visible in some of the etched samples. An example of this banding is shown in **Figure 77**. The presence of equiaxed alpha bands that can be traced to the flash regions, indicating that the banding is linked to the interlayer regions of the deposits. This may additionally indicate that there may be a local pickup of oxygen at the surface of each printed layer, like the formation of an alpha case during fusion welding in an oxygen contaminated environment. Upon subsequent printed layers, this potentially oxygen enriched region could be pushed down and into the printed material. While equiaxed alpha banding in the closed-loop temperature-controlled AFSD samples did not seem to significantly affect tensile testing, it nonetheless could be considered a defect if the cause can be definitively attributed to oxygen contamination. Alpha case is well known in titanium literature to decrease ductility and contribute to premature failure of components (11). A Ti-O phase diagram is given in **Figure 78**.

Observations of the microstructure at the darkly etching layer interfaces, paradoxically reveals the presence of an equiaxed alpha microstructure. Tungsten particles can also be observed. The presence of equiaxed alpha is unexpected because tungsten is a beta phase stabilizer. Therefore, it was hypothesized that oxygen contamination during the build may have introduced an alpha case on the previously deposited layer that was then encased into the build by subsequently printed layers. EMPA analysis was conducted to analyze the possibility that the equiaxed alpha microstructures were caused by local oxygen contamination. EMPA analysis has previously been used to investigate alpha case in titanium (189). For this study, EMPA

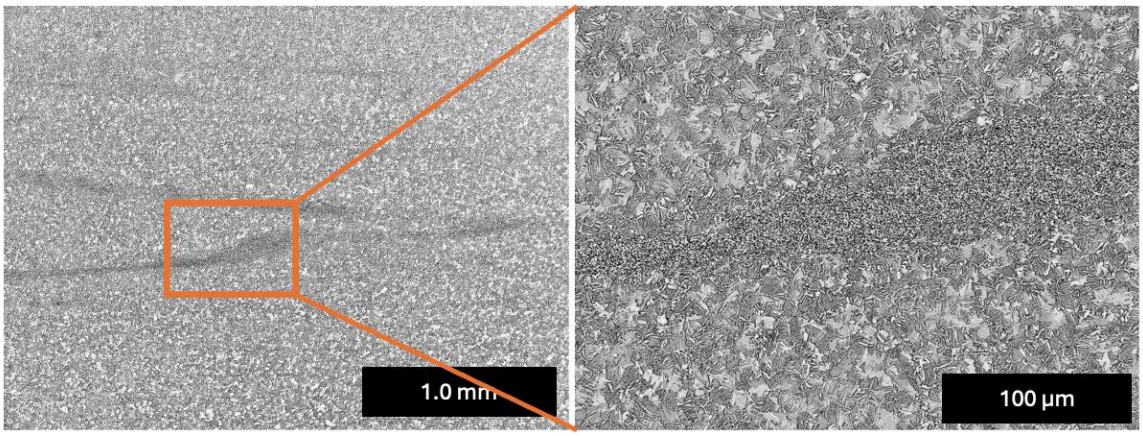


Figure 77: Etching Band of Equiaxed Alpha in the 850 ºC Sample

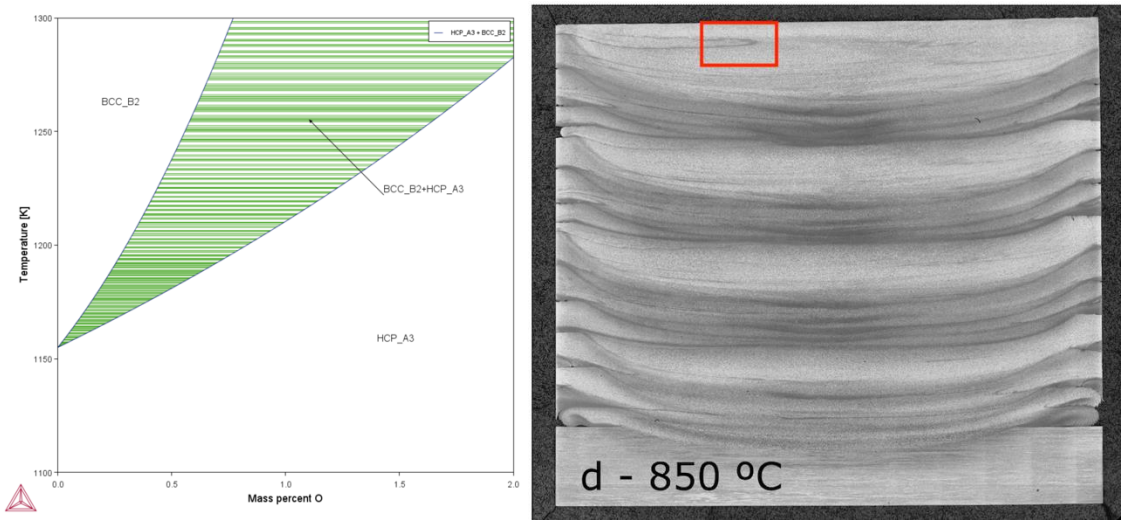


Figure 78: a) Ti-O Phase Diagram and b) WDS Location for Electron Microprobe Analysis

analysis was conducted across a tungsten band in the microstructure. The tungsten banding indicating a previous layer interface in the printed material. The analysis, however, did not reveal any spikes in the oxygen content at the layer interface. It instead measured a consistent ~ 2 wt. % oxygen content for the entire 200 μm line scan. It is not known if this oxygen content is the effect of surface oxidation on the sample, or simply oxygen in the sample that has diffused along a longer length scale than the 200 μm line scan.

While no peaks in the oxygen content were observed, a peak of the nitrogen content corresponding to the location of the tungsten banding can be seen in the EMPA data. Nitrogen is also known to be a strong alpha stabilizer, as seen in **Figure 79**. With the EMPA data indicating some nitrogen pickup in the equiaxed banding, it is likely that there is also oxygen pickup as well due to the higher reactivity of titanium and oxygen. This finding provides evidence that the hypothesized oxygen contamination may be below the noise floor created by surface contamination resulting from the polished surface reacting with atmospheric oxygen. While nitrogen was positively observed, it was not possible to confirm the presence of oxygen contamination aside from surface contamination. Atom probe tomography could potentially be used to definitively prove if oxygen contamination is present in the equiaxed banding regions.

There may be an additional explanation for the existence of the equiaxed alpha banding observed in the same areas as tungsten contamination. Fine, sub-micron scale tungsten particles have already been observed to locally increase the hardness (**Figure 38**). Tungsten particles can be seen to be in the same areas as equiaxed alpha

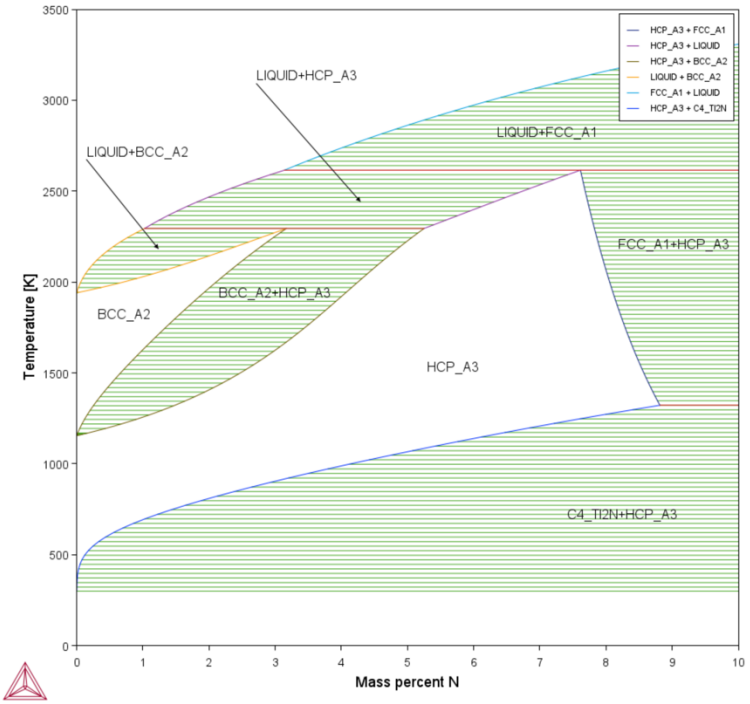


Figure 79: Ti-N phase diagram

morphologies in **Figure 80**. The size of these particles is given in **Figure 81** indicating that most of the particles are smaller than 0.1 μm in equivalent diameter based on their measured areas. Upon heating from the low temperature alpha phase to the high temperature beta phase. these finely dispersed hard particles may locally inhibit recrystallization by pinning the grain boundaries (19). With a sluggish phase transformation, there is not enough time for the tungsten contaminated area to transform to the high temperature beta phase, as so the deformation takes place in the alpha phase, leading to an equiaxed alpha microstructure. Of note, the vanadium enriched beta phase areas are enlarged in the tungsten contaminated equiaxed alpha regions as compared to the uncontaminated lamellar regions, indicating that more partitioning of vanadium into the beta and corresponding partitioning of aluminum out of the beta took place in the contaminated equiaxed alpha regions. This can be seen in **Figure 82** and **Figure 83**. There may be additional partitioning of tungsten into the beta as well or even a combination of the two mentioned processes. Potential partitioning of tungsten was investigated further via BSE images and EDS.

Upon closer examination of the tungsten contaminated regions, there does not appear to be any diffusion of tungsten from the particles into the titanium matrix as apparent in BSE images, as seen in **Figure 82** and **Figure 83**. A more thorough investigation into the question of if W is diffusing into the Ti matrix was performed using quantitative EDS. A quantitative EDS line scan was taken over one of the tungsten particles in the W contaminated equiaxed alpha region.

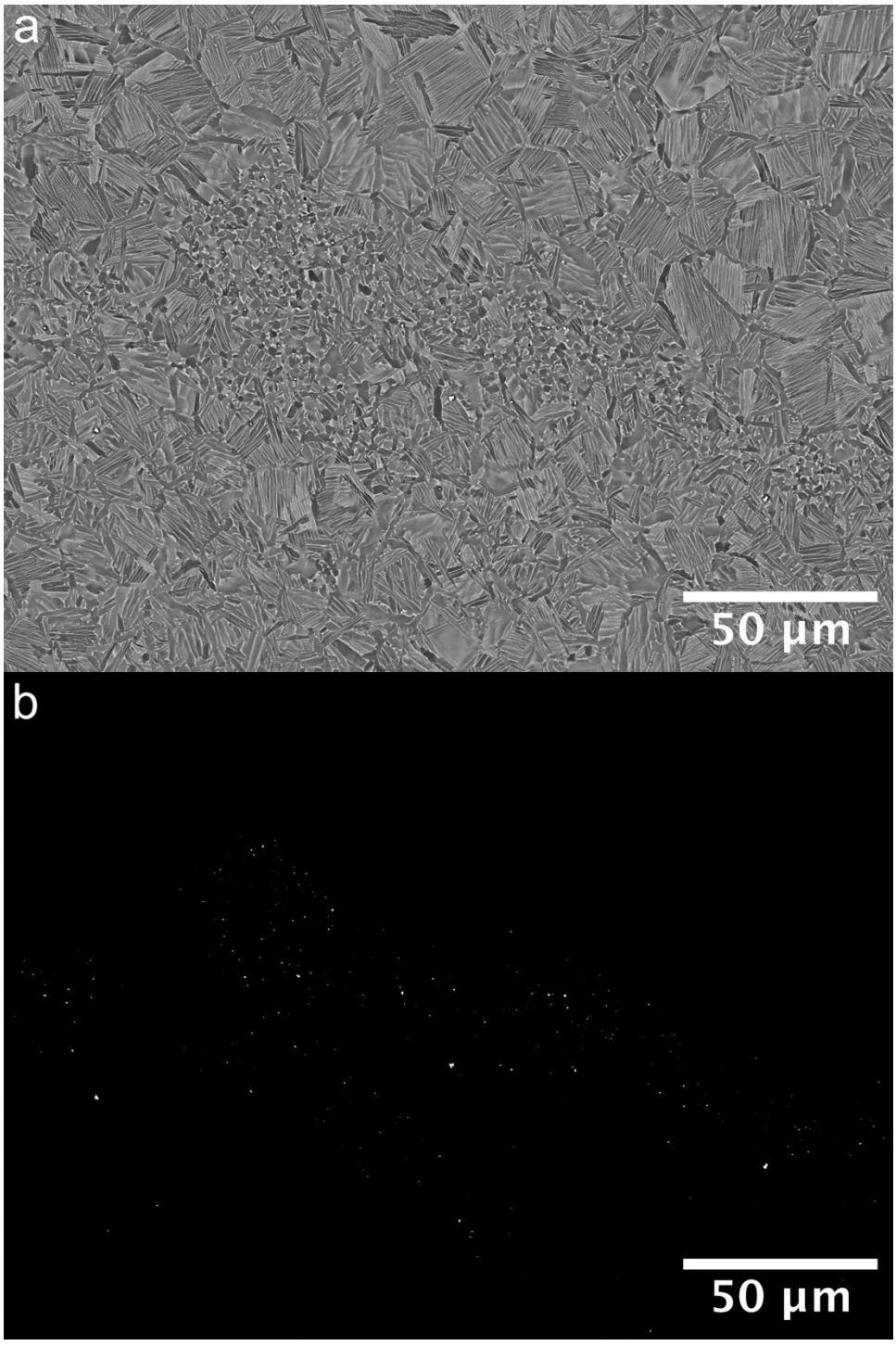


Figure 80: Equiaxed alpha banding in tungsten contaminated region surrounded by lamellar alpha (a) CLAHE filtered BSE image and (b) W particle spatial distribution

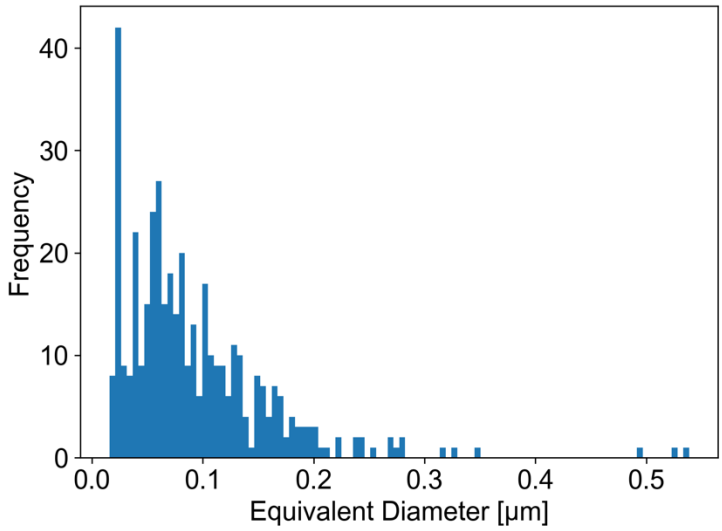


Figure 81: Histogram of W particle size from Figure 80 (b)

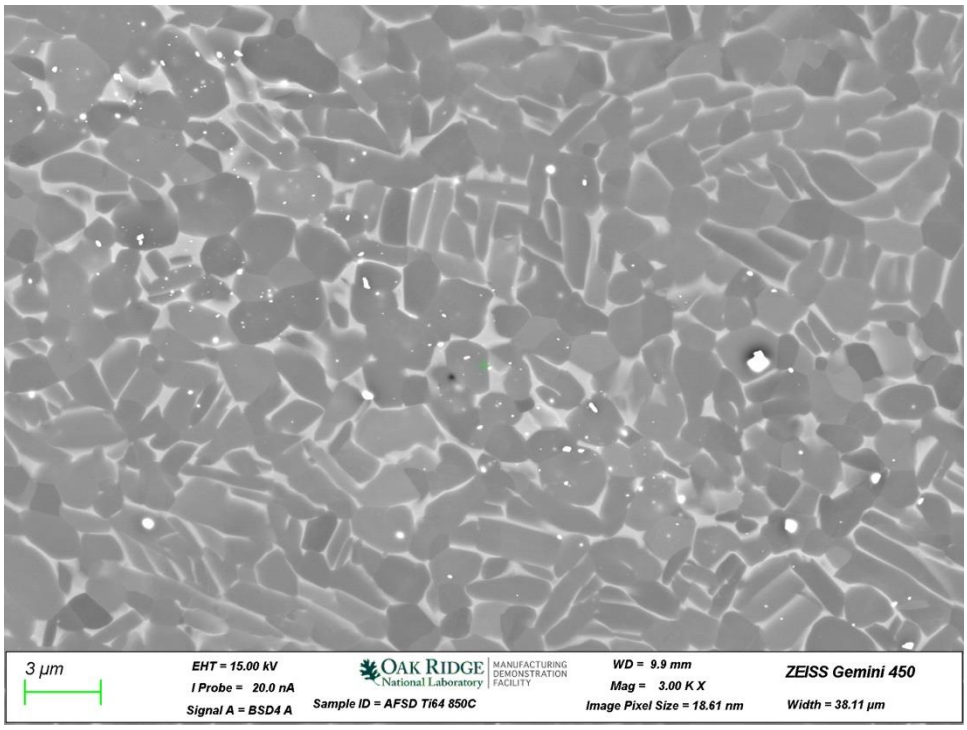


Figure 82: BSE image of W contaminated equiaxed region at 3k magnification

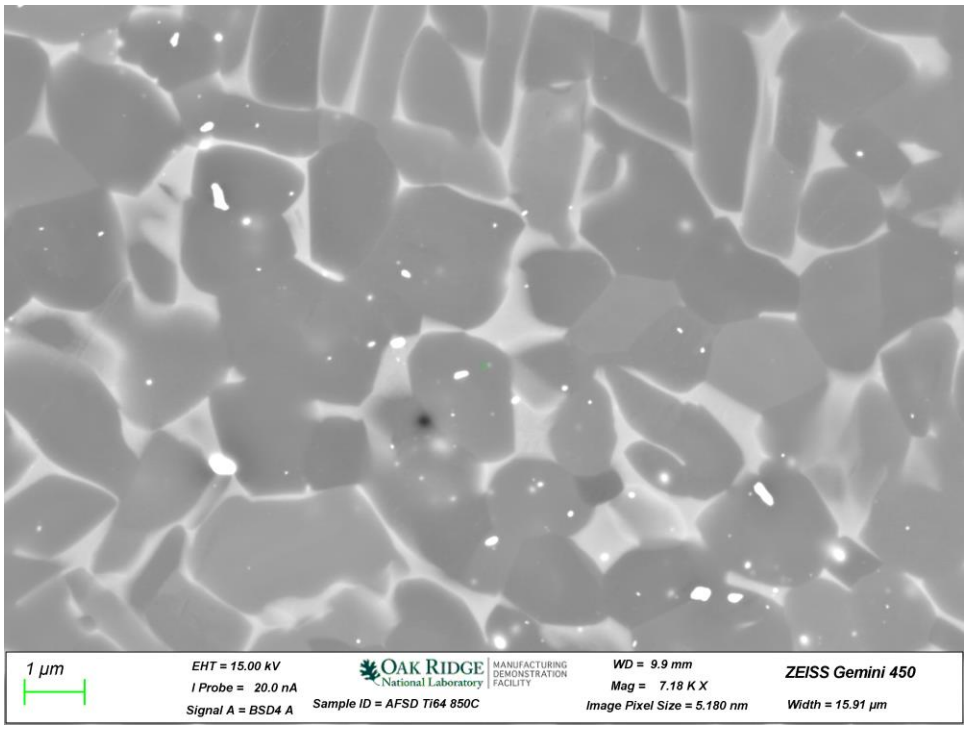


Figure 83: BSE image of W contaminated equiaxed region at 7.18k magnification

The location of the line scan is shown in **Figure 84** and **Figure 85**. It was observed that the elemental mapping was offset from the BSE image; however, this offset was observed to be consistent for the entire map. As this discrepancy was observed for Al and V in addition to W, the offset may be related to the relatively high magnification (3k x) used for the collection of this data as well as due to the offset EDS detector positioning as compared to that of the BSE detector. There could also be an issue relating to the image registration calibration showing up as an imperfect alignment between the BSE and EDS data. The results of the quantitative EDS line scan across the tungsten particle are given in **Figure 86**.

Tungsten Inclusions

In a study of FSW of titanium, it was found that tool debris did not seem to impact mechanical properties including low cycle fatigue and tensile testing (120). Nonetheless, it is desirable that tool inclusions be eliminated from welds. Farabi et al. noted that tungsten contamination was not observed with the use of a lanthanated tungsten tool (8). However, despite the similar use of a lanthanated tungsten tool material, tungsten contamination was present in all process conditions in this current study. The scale of the tungsten inclusions observed in this study ranged from sub-micron scale (**Figure 38**) to tens of microns (**Figure 88**) to more than 1.5 mm in length (**Figure 89**). Based on traditional FSW literature, tool wear can be abrasive or adhesive (also known as diffusive or chemical) in nature. For all temperature setpoints in the present study, tungsten inclusions appear to be in the form of distinct particles. There is no significant dissolution of tungsten into the titanium matrix as has been previously observed an AFSD Ti-6Al-4V deposition shown in **Figure 87**. This means that the tool

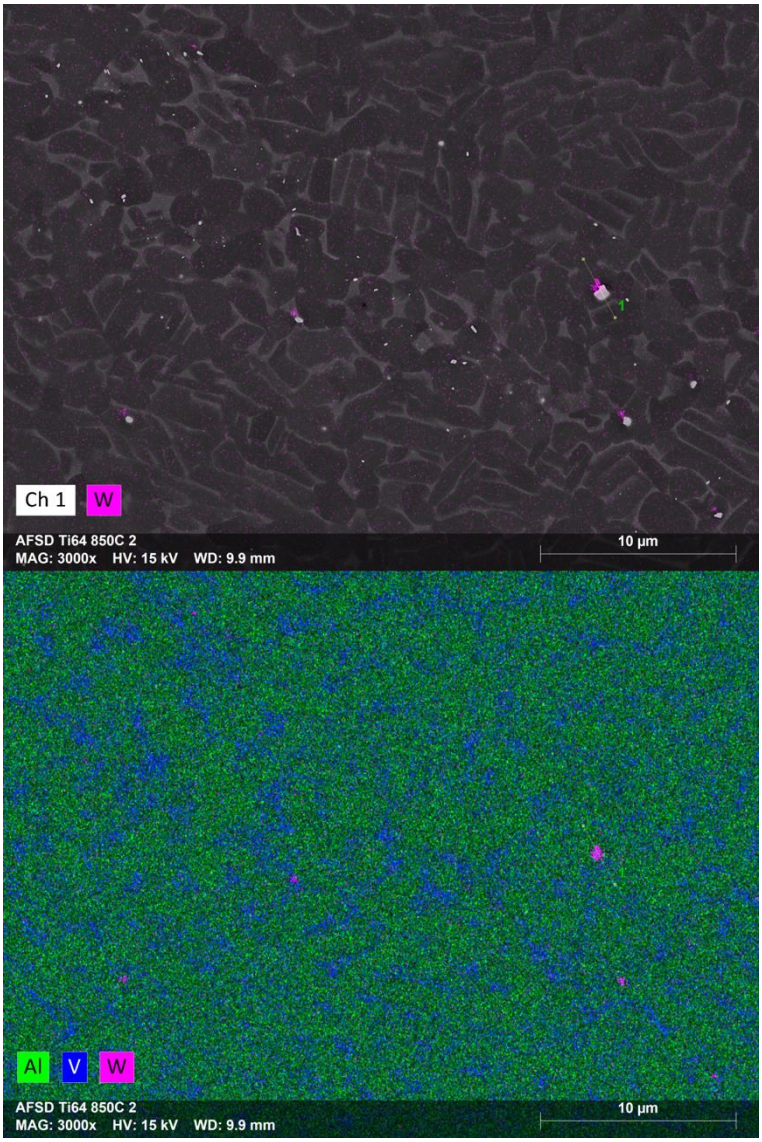


Figure 84: Quantitative EDS line scan location and elemental map

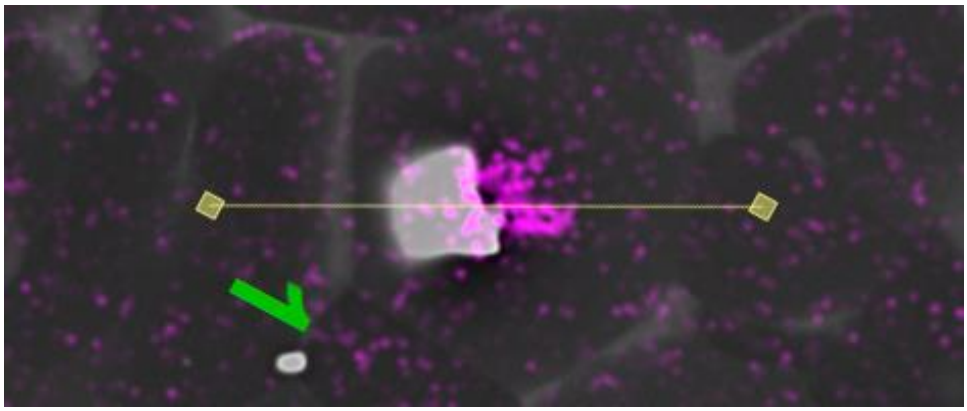


Figure 85: Quantitative EDS line scan location

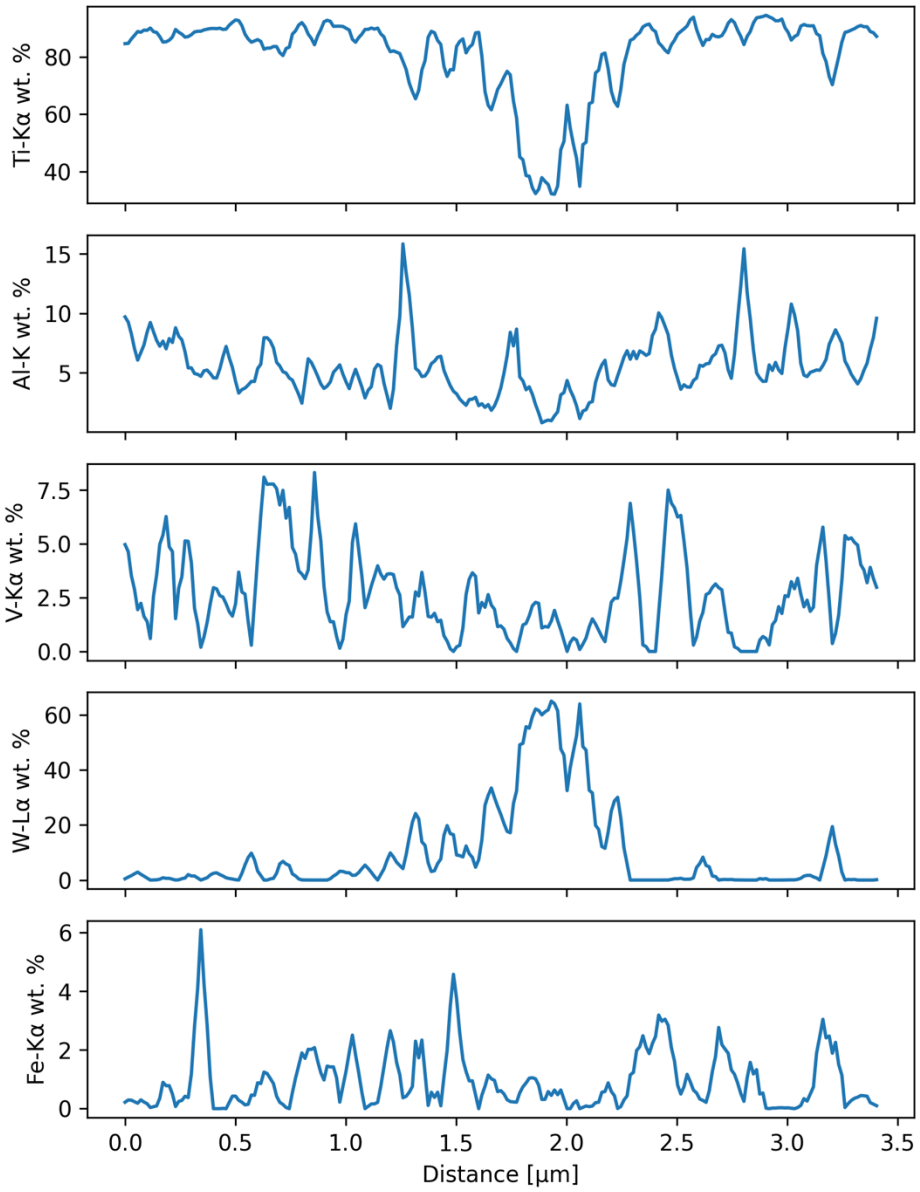


Figure 86: Quantitative EDS line scan wt. % results

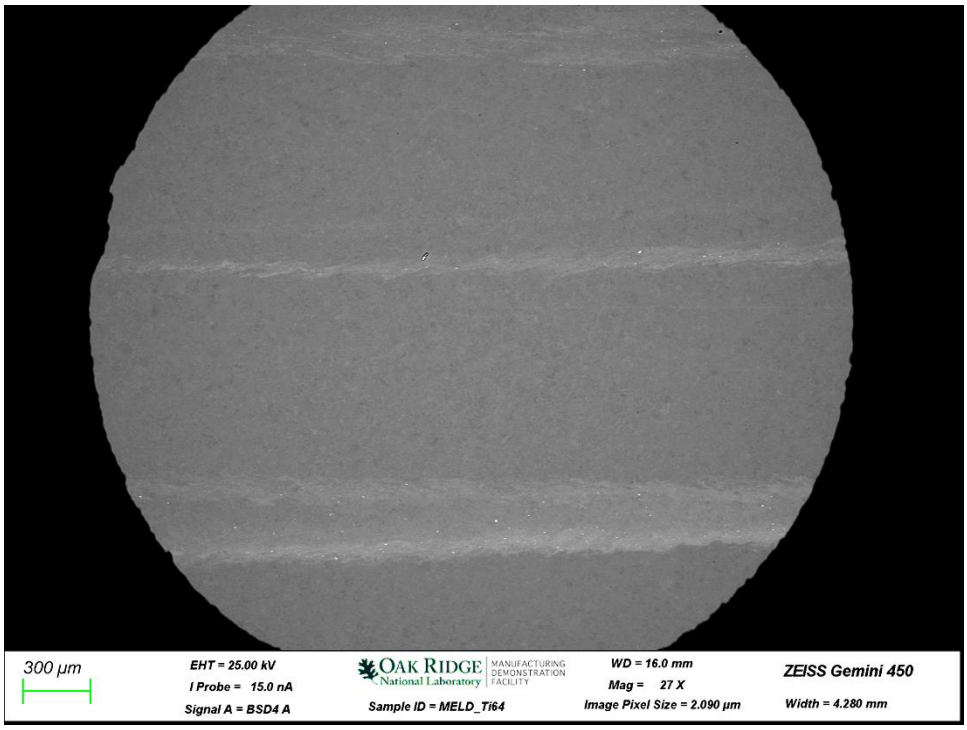


Figure 87: Diffusive tungsten tool wear in an AFSD Ti-6Al-4V build (process parameters unknown)

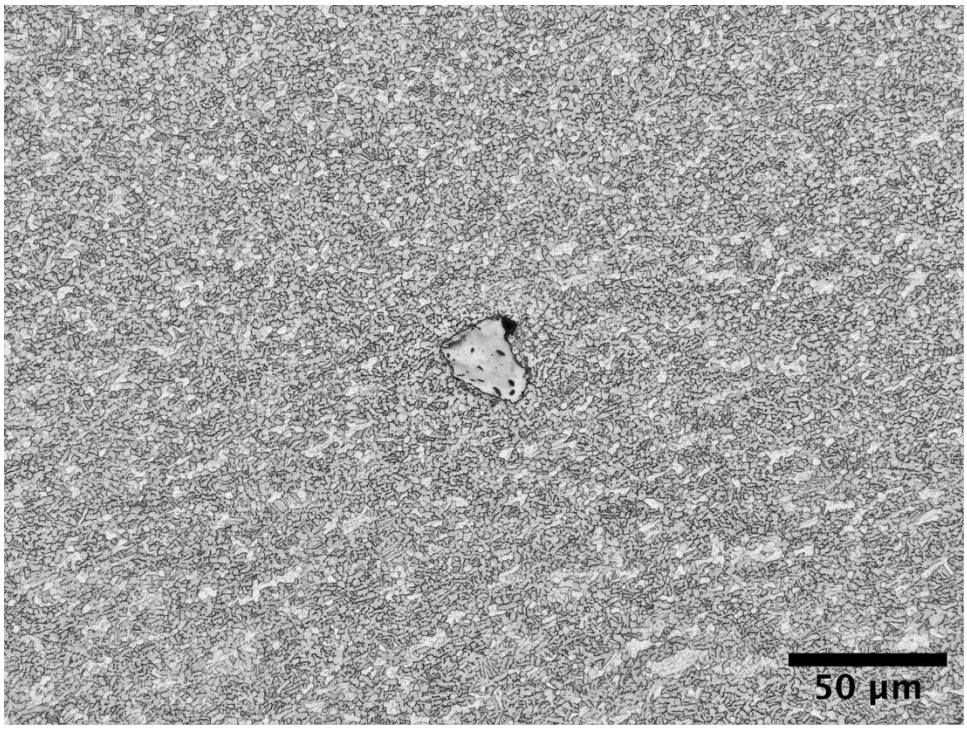


Figure 88: A large tungsten inclusion in the 800 ºC AFSD sample

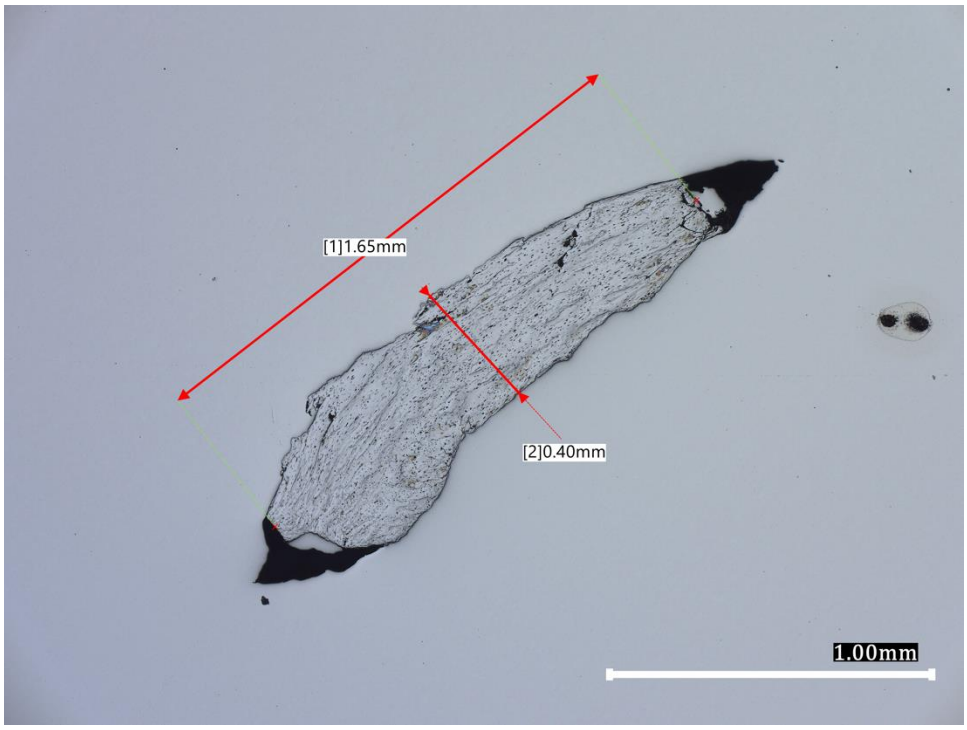


Figure 89: A very large tungsten inclusion in the 850 ºC temperature setpoint build

wear observed in this study is abrasive in nature. It is hypothesized that temperatures at the tool-material interface remained cool enough to prevent adhesive wear.Agrawal observed tool wear for AFSD of Ti-6Al-4V using compacted bars of machining chips, noting that tool wear was more pronounced during cooler AFSD depositions (7). A comparison of **Figure 90** (a) vs (b) comparing tungsten contamination in the 700 ºC vs 850 ºC builds appears to corroborate this claim. It appears that there is increased tool wear, as apparent in the BSE images, in the lower temperature 700 ºC temperature setpoint build. There also appears to be increased tool wear than can be traced back to the first layers printed for each bar reload in the 850 ºC temperature setpoint.

On the topic of the effects of tool wear on mechanical properties, tungsten inclusions were visible in most of the observed fracture surfaces. Of the imaged fracture surfaces, only ND-LD 850S14 did not have any apparent tungsten inclusions in the fracture surface. Sample ND-LD 800S14 exhibited decreased ductility compared to the other build direction samples in the center of the deposit. Upon examination of the high magnification BSE SEM fracture surface images, a large fraction of small tungsten inclusions were visible. These tungsten inclusions may have contributed to the lower ductility observed in this sample. While the presence of tungsten is linked to this early failure, further study of tool wear in AFSD of Ti-6Al-4V is merited to more affirmatively link the effects of tungsten contamination to potential effects on mechanical properties.

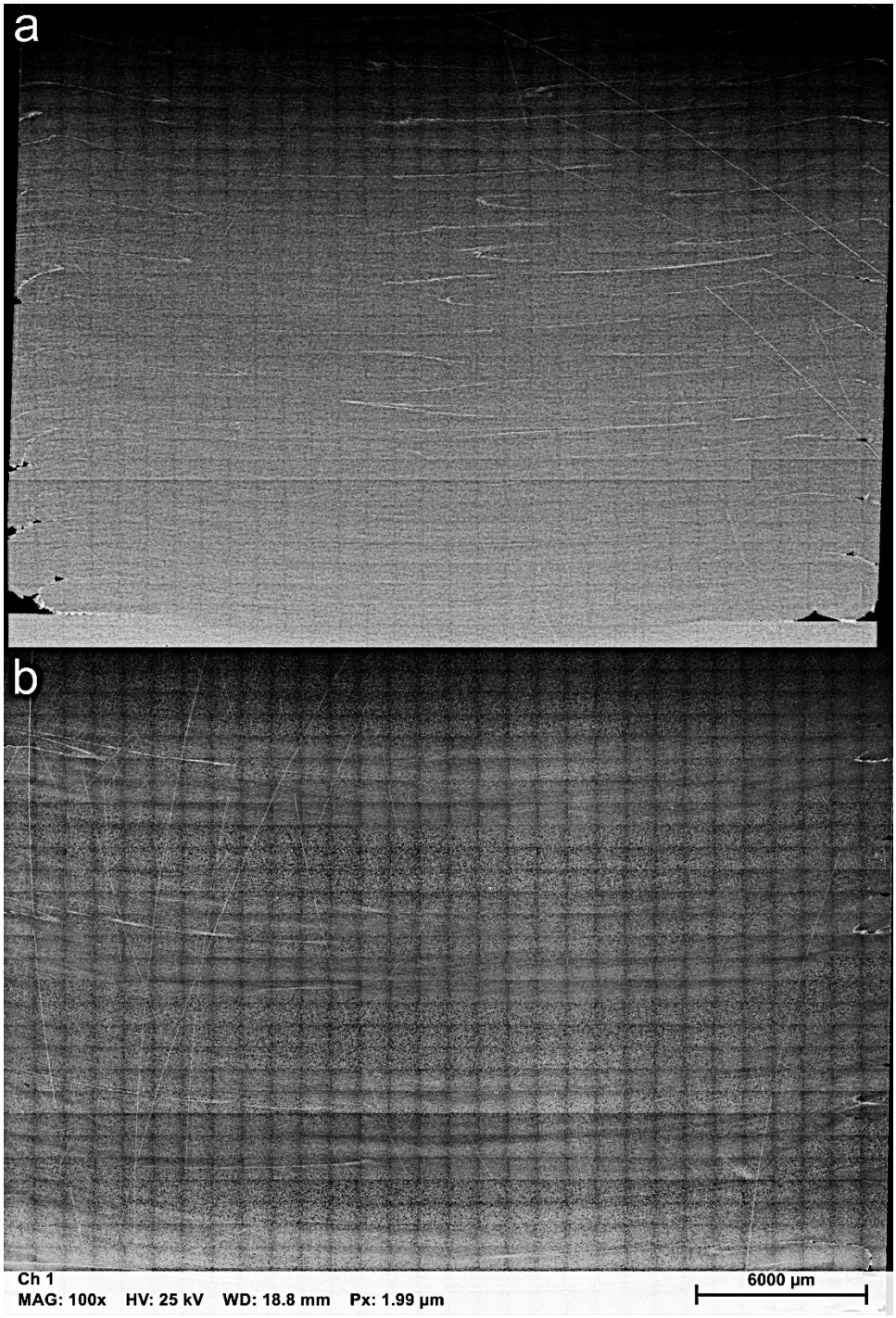


Figure 90: BSE montage image of tungsten inclusions in (a) 700 ºC and (b) 850 ºC temperature setpoint builds

Flash/Kissing Bonds

As has been previously noted in AFSD, the process results in incomplete bonding at the periphery of the deposits (9). While these areas are typically machined away, the present study elected to keep a portion of the flash regions at the sides of the deposits. The flash regions at the side of the deposit can be seen to extend into the deposited material in a way that is analogous to kissing bonds as observed in friction stir welding, where the preexisting oxide layer on the material is not sufficiently broken up to allow metallic bonding. An example of this type of defect is given in **Figure 91**.

The number of tensile bars extracted in the ND-LD direction can help yield insight into the fraction of material with inadequate bonding at the edges due to flash. The average number of tensile bars extracted in the build direction from each build was 26. Considering the cutting kerf of approximately 0.38 mm (0.015 in), this means that only approximately 25.4 mm (1 in) width of material was deposited with some amount of bonding despite the printed walls nominally being 38 mm (1.5 in) in width. The early failure of some ND-LD S26 samples indicates that flash defects extend further into the material even if the material is somewhat bonded. It was observed that flash regions may sometimes exhibit partial bonding, as shown in Figure 92. It is possible that this poor bonding may be visible in one of the fracture surfaces as well. From an observation of the fracture surface of ND-LD 750S22, shown in Figure 61, it appears that there is an onion skin type pattern such as that typically visible on the top surface of traditional FSW and AFSD processed materials. Additionally, there is a large amount of tungsten debris in the fracture surface shown in Figure 62, confirming that the material was previously in

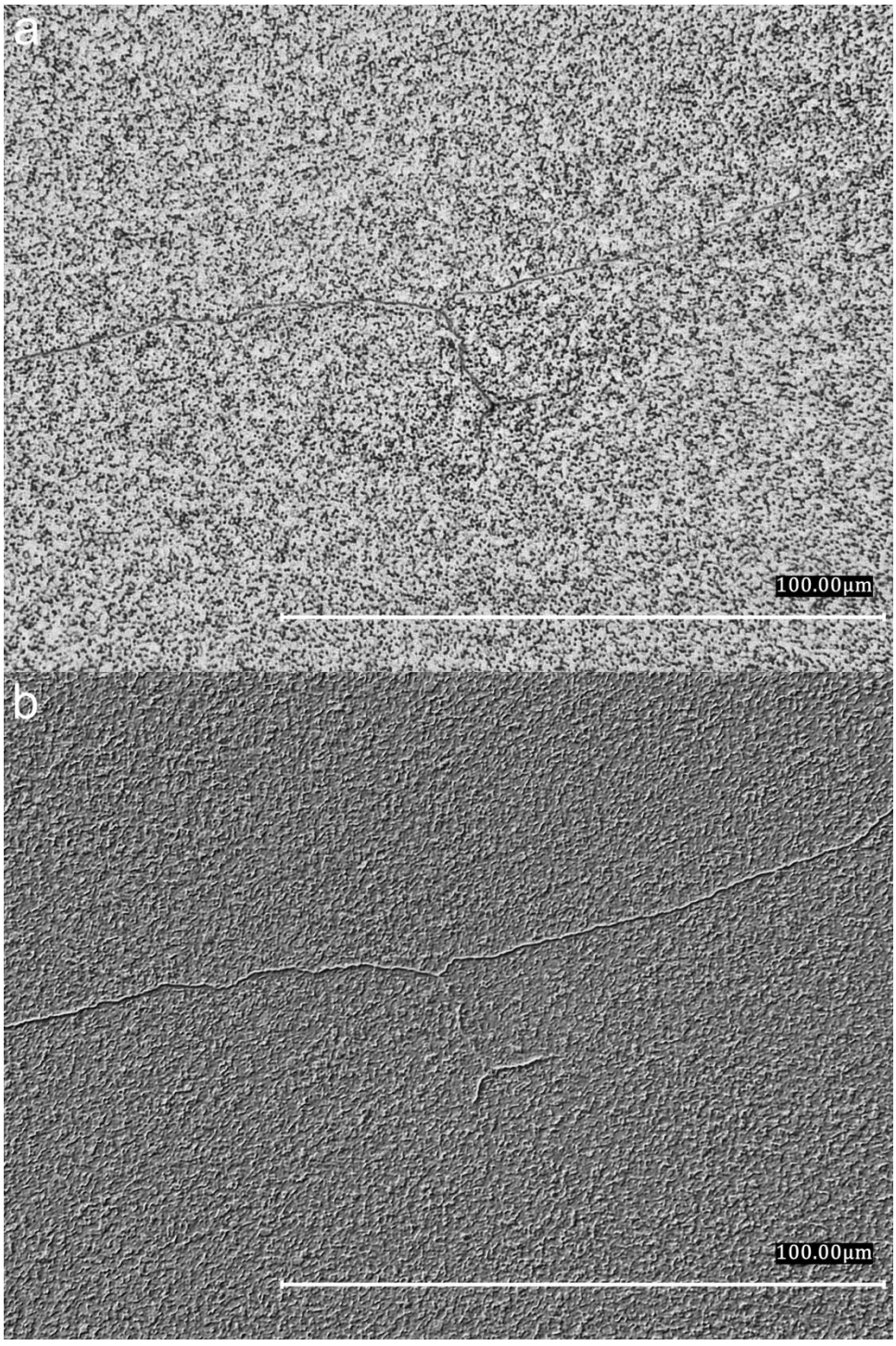


Figure 91: Apparent kissing bond in the 700 ºC sample originating at the flash (a) optical (b) Keyence Optical Shadow Effect Mode

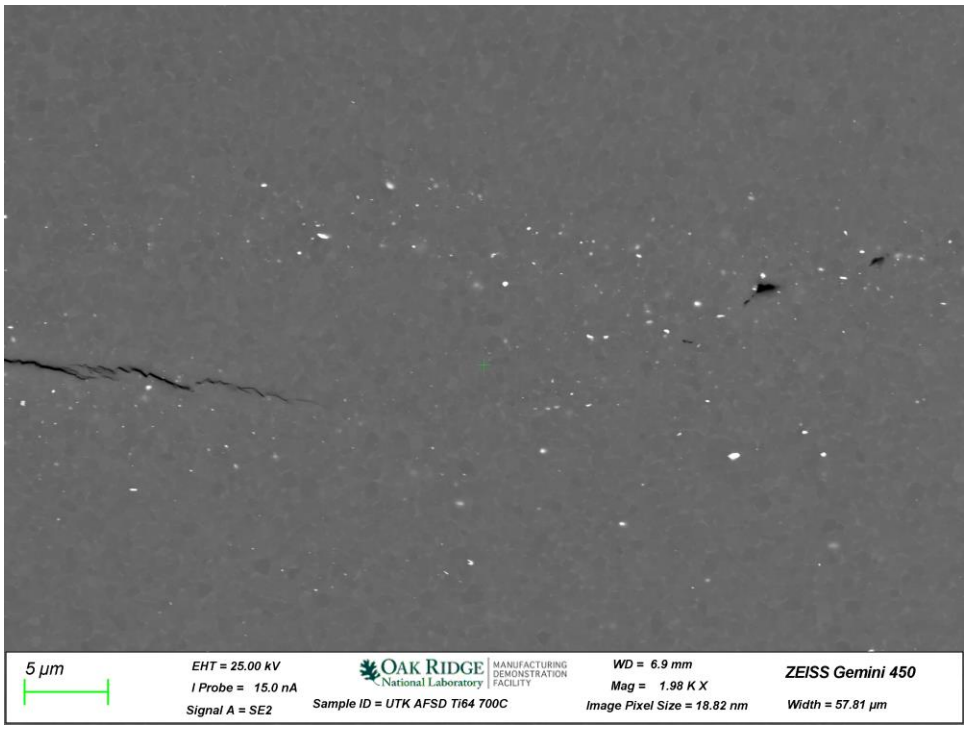


Figure 92: Flash region of 700 ºC temperature setpoint exhibiting partial bonding

contact with the tool. It is hypothesized that the visible onion skin surface indicates incomplete bonding.

CHAPTER 6

FUTURE WORK

Texture Development and Effect on Mechanical Properties

With yielding seen in multiple areas, it is hypothesized that texture effects may play a large role in the observed yielding behavior of the tested tensile samples. While the effects of FSW/FSP on texture development have been extensively studied (20,182,185–187), there are no studies to date that investigate the texture development of AFSD titanium. Future study should be undertaken to determine the effects of deposition of multiple layers and thermal cycling on texture development of AFSD titanium. Additionally, it is hypothesized in the present study that texture effects may contribute the non-uniform yielding behavior observed in the polished and etched ND-LD samples. Future texture study via EBSD or XRD could help explain the relationship between texture and mechanical properties observed in AFSD Ti-6Al-4V.

Fatigue Testing

Due to the incredibly harsh environmental conditions of plastically flowing titanium, tool wear is a significant concern. Due to the beta stabilizing effects of Tungsten, tool wear contamination could potentially negatively impact fatigue properties due to the lower modulus of the beta titanium phase. While tool debris has not been noted to limit low cycle fatigue life in FSW titanium (120), more thorough investigation is needed for AFSD. Fatigue testing will be needed to determine the fatigue response of AFSD Ti-6Al-4V.

Tool Development

To mitigate the issues with tool wear, future work can investigate the effects of different tool designs and materials. Iridium-based tools have previously been observed to have an optimal combination of properties for the FSW of high temperature materials and may present an opportunity for the development of more durable AFSD tools despite the high cost of iridium alloys (104–106).

Another method may be to revisit ceramic based tooling. The key issue to be solved, however, is the issue that AFSD tooling experiences tensile stresses (76). Metal 3D printing of refractory alloys is becoming more mature. A solution may be to first produce a refractory alloy lattice matrix using metal additive manufacturing that is then infilled with a sintered ceramic to create a solid hybrid material tool. The refractory alloy matrix may better bear the tensile loads of the process while the ceramic can provide higher wear resistance. A similar technique has been previously used to create titanium-ceramic hybrid materials for armor applications(190).

Residual Stress

The investigation of residual stress in AFSD Ti-6Al-4V also presents an interesting path forward for research. While some literature has noted that residual stress from the AFSD process is small (191), other literature indicated that it may be higher than initially thought(84). Based on visual inspection, the titanium build plates in the as-built condition exhibited noticeable warping. From the results of the current study, it is not known if the build plate warping resulted from the AFSD process or preexisting residual stresses in the rolled build plate.

Process Monitoring / PID Tuning

For this series of builds, untuned PID coefficients were chosen, resulting in ringing characteristic of an underdamped system. Future work could be undertaken to find PID coefficients that lead to a critically damped system for each of the potential temperature setpoints.

In-Situ Process Modification

In traditional FSP of both CP titanium and Ti-6Al-4V, a nitrogen atmosphere was used to produce surface nitriding and, below the surface, a dispersion of nitrides, creating an in-situ metal matrix composite like material (192,193). This shows that in-situ process modification using a nitrogen build environment may be a route to the production of titanium metal matrix composites. The composition of the build environment could be controlled to fine tune the reaction between titanium and nitrogen, perhaps at different layers to create a functionally graded material.

Increase Deposition Rates Using Hydrogen

Hydrogen is a potent beta stabilizer with the potential to decrease the beta transus temperature to a eutectoid temperature of 300 ºC (11). It has been found in friction stir welding literature that hydrogenated titanium exhibits reduced flow stress (194), greater thermo-plasticity (195), and can reduce initial tool plunging forces and stabilize spindle torque during welding (196). A hydrogenation/dehydrogenation process where the feedstock is infused with hydrogen, the hydrogenated titanium is deposited, then the hydrogen is baked out of the material through vacuum annealing, may allow for several benefits. The process, after dehydrogenation, has been found to result in a very fine equiaxed alpha microstructure (197). It could also increase material deposition rates by

decreasing the flow stress of the material. Higher deposition rates could be highly beneficial, particularly for non-aerospace applications where hydrogen content in the material may not be as much of a concern.

Hydrogenated titanium may also hold the potential to allow for deposition of titanium without an enclosed, fully inert environment. Below 550 ºC, oxygen diffusion rates through the outer oxide layer are low enough to prevent significant oxygen ingress into the bulk material (11). If deposition can be successfully achieved near or below 550 ºC, this may significantly ease some of the difficulties in depositing titanium, by allowing only local shielding at the deposit. Lower deposition temperatures and forces may also enhance tool life and limit tool wear (195).

AFSD Modeling

AFSD modeling of titanium deposition could better inform process parameters and help increase understanding of the effects of process stoppages on resulting microstructures and mechanical properties. While modeling has been pursued for AFSD of aluminum alloys, literature on modeling AFSD titanium is limited. Robust simulation methods could also help provide insights into the complex material flow that exists during AFSD of titanium. With a better understanding of the material flow and shear directions during deposition, modeling could provide insights into the texture development of AFSD titanium.

CHAPTER 7

SUMMARY AND CONCLUSIONS

Summary

Closed-loop temperature controlled additive friction stir deposition of Ti-6Al-4V was performed to deposit single track walls at a series of temperature setpoints ranging from 700 ºC to 850 ºC in 50 ºC increments via the use of a tool embedded thermocouple. The builds were monitored using thermocouples embedded in the build plates and IR thermography from the side. The resulting depositions were sectioned normal to the tool travel direction and analyzed using optical micrography, backscattered electron imaging, and electron backscatter diffraction. Chemical analysis was performed via the inert gas fusion technique, energy dispersive X-ray spectroscopy, and wavelength dispersive X-ray spectroscopy. The crystal structure of the deposits was analyzed using X-ray diffraction. Mechanical properties were investigated using microhardness testing on a polished cross section. Additionally, quasi-static tensile testing was conducted on a subscale tensile specimen geometry with strain measured using 3D digital image correlation.

It was found that the 700 ºC temperature setpoint resulted in an equiaxed alpha microstructure in the stir zone. The 850 ºC temperature setpoint resulted in a lamellar microstructure. The 750 ºC and 800 ºC intermediate temperature setpoints produced a mixed microstructure of equiaxed and lamellar morphologies. EBSD results indicate that the 700 ºC exhibits a mostly random texture. The microstructures become increasingly textured with increasing deposition temperatures.

There was tungsten tool wear visible in all process conditions. The mechanism appeared to be abrasive wear as evidenced by the limited diffusion of tungsten into the titanium matrix. Oxygen ingress into the material was limited for all process conditions, and all deposited material met material requirements for oxygen content. XRD revealed comparable phase fractions for all deposition conditions, but also revealed some differences in cell volume and microstrain.

Under quasi-static tensile testing, the AFSD Ti-6Al-4V average tensile properties for all temperature setpoints exceeded the ASTM B381 minimum forging standards of 828 MPa yield strength, 895 MPa ultimate tensile strength, and 10% elongation at failure. Some tensile failures were attributable to incomplete bonding at the flash interface.

Conclusions

- AFSD of Ti-6Al-4V was successfully conducted at PID temperature controlled setpoints of 700 ºC, 750 ºC, 800 ºC, and 850 ºC as measured by a thermocouple embedded in the tool near the tool face. The 700 ºC temperature setpoint produced an equiaxed alpha microstructure characteristic of processing in the alpha + beta phase field below the beta transus temperature. The equiaxed alpha grains are on the order of 1-micron in size. The 850 ºC temperature setpoint resulted in a lamellar microstructure resulting from nucleation and growth upon cooling from the high temperature beta phase after the tool had passed. The prior beta grains for the 850 ºC temperature setpoint were on the order of 20 μm to 50 μm. The alpha lath spacing was on the order of 1 μm. The intermediate temperature setpoints of 750 ºC and 800 ºC had mixed microstructures consisting of varying proportions of equiaxed alpha and lamellar microstructures resulting

from processing near, but below, the beta transus temperature. For the 750 ºC and 800 ºC temperature setpoints, the prior beta grains appeared to be on the order of 10 μm to 20 μm, where it was apparent. The lath spacing was on the order of 0.5 μm to 0.75 μm within chunkier grain boundary alpha on the order of 1.25 μm to 1.5 μm.

- Tensile properties for AFSD Ti-6Al-4V as tested on a sub-scale tensile geometry were overall good, exceeding ASTM B381 requirements for forged titanium, though it should be noted that the results in the present study used a non-ASTM subsize tensile geometry. The measured tensile properties were 994 MPa YS, 1045 MPa UTS, and 17% elongation in-plane in the weld direction and 1035 MPa YS, 1089 MPa UTS, and 13% elongation in-plane in the transverse direction. The out-of-plane tensile properties were measured at 950 MPa YS, 999 MPa UTS, and 14% elongation. Some samples in the ND-TD and LD-TD orientation near the printed deposits periphery failed prematurely. The cause was attributed incomplete bonding in the flash regions of the deposit.
- While all deposition temperatures exceed minimum standards, there are some differences in the tensile testing results. The LD-TD samples, extracted from the periphery of the deposited material exhibit an increasing YS and UTS with deposition temperature and an inversely correlated decrease in elongation. The TD-LD had the highest UTS for all tested conditions, though there was an increasing spread between the YS and UTS for increasing temperature deposition conditions. Elongation was relatively consistent. The ND-LD samples have a relatively higher YS and UTS at the 700 ºC temperature setpoint, before

decreasing for the intermediate temperature deposition conditions, and then rise slightly again for the 850 ºC temperature condition. Elongation for the out-of-plane samples more inconsistent than the in-plane samples.

- Build direction tensile samples exhibited non-uniform yielding behavior, initially yielding in lamellar microstructure regions even if the eventual failure occurred in equiaxed regions. It was hypothesized that this may be related to texture effects in the lamellar regions.
- The present work is the first demonstration of AFSD of Ti-6Al-4V below the beta transus temperature. Due to the differences in flow stress between the high temperature BCC beta phase and the low temperature HCP alpha phase, build parameters needed to be adjusted lower to accommodate the increased forces and power input needed for AFSD below the beta transus temperature.
- The pseudo-heat index as first applied to AFSD of the single-phase materials aluminum and copper by Garcia et al. (63) and later applied to AFSD of Ti-6Al-4V above the beta transus temperature by Yoder et al. (9) does not model heat generation in AFSD of Ti-6Al-4V near the beta transus temperature. The alpha/beta phase change in Ti-6Al-4V and resulting differences in flow stress result in more complicated heat generation as compared to single phase materials.
- Oxygen pickup during AFSD deposition of Ti-6Al-4V was relatively low, going from 0.19 wt. % in the feedstock to 0.20 wt. % in the finished deposits for all temperature setpoints. There was no measured differences in oxygen pickup for any of the different temperature setpoints, despite the oxygen content in the inert enclosure during printing being 0.6 %. All printed materials met the chemistry

requirements for O and N content for aerospace titanium and did not exceed the 0.20 wt. % oxygen limit for Ti-6Al-4V. There does not appear to be localized oxygen pickup at the layer interfaces, however, more investigation may yield more insights into the formation of equiaxed alpha in those areas.

- Tool wear exists in all process conditions despite the use of a lanthanated tungsten tool. This tool wear led to defects including tungsten inclusions at different scales. Submicron tungsten wear particles resulting from abrasive wear of the tool locally increased the hardness for a single hardness indent. One large tungsten inclusion was greater than 1.5mm in length. Overall, because tungsten is a beta phase stabilizer, caution should be taken if heat treating AFSD Ti-6Al-4V parts due to the potential of tungsten dissolution modifying the local chemistry and resulting microstructure.
- There are hardness variations through the build with two characteristic length scales: one resulting from the layer-by-layer printing process and another resulting from process stoppages due to material reloads. The layer scale hardness variation was on the order of the layer height of 1 mm. The longer-range hardness variation was on the order of the number of printed layers before each process stoppage (~ 6 mm). Despite the hardness variation, the mean hardness for all temperature conditions was virtually the same.
- X-ray diffraction reveals some similarities and some differences for the different temperature setpoint processing conditions. Like the Yoder et al. study (9), alpha/beta phase fractions were comparable for all printed conditions, even with processing below the beta transus temperature. There was, however, a difference

in the phase fraction between the feedstock and the printed material. Microstrain broadening between the two phases showed an inverse relationship with increasing temperature processing conditions. This may suggest differences in plasticity and recovery under different processing conditions, however, interpretation of XRD results can be complicated by differences in microstructure. When measured over multiple layers worth of material, the printed material was less textured than the originating feedstock. Tungsten and oxide trace phases were not observed through XRD.

Significance of Current Work

This current work aims to more fully describe the AFSD process with respect to the closed-loop temperature-controlled deposition of Ti-6Al-4V, particularly through an analysis of the effects of deposition temperature on microstructure and mechanical properties. An analysis of the effects of processing on the resulting microstructure is given. The effects of the microstructure, including morphology and heterogeneity, are then tested via hardness testing and quasi-static tensile testing to determine their effects on mechanical properties.

While friction stir welding of Ti-6Al-4V below the beta transus temperature has previously been demonstrated, this work is the first demonstration of AFSD of Ti-6Al-4 below the beta transus temperature. This unlocks a new category of microstructure morphology that can be deposited. Importantly, the resulting equiaxed microstructure from sub-beta transus AFSD is impossible to achieve solely through any melting-based process such as L-PBF or WAAM, which typically result in large columnar grains. AFSD of Ti-6Al-4V yields small grains for all processing conditions, which help enhance

mechanical properties in the Z-direction. Although there was some variation in the mechanical properties as a function of the location and deposition temperature which resulted indifferences in microstructure, all the samples from all the deposition conditions exceeded ASTM B381 forging standards in for all tested orientations, despite microstructural heterogeneity, hardness variations, and the presence of tungsten contamination in all conditions.

Ti-6Al-4V is an important material in the context of many industrial uses. It is hoped that this study has increased an understanding of the complex interplay between processing, microstructure, and resulting mechanical properties for a variety of deposition temperatures. It is hoped that this research will contribute to future parameter selection for both research and commercial production of Ti-6Al-4V components using AFSD.

REFERENCES

1. Yu HZ, Jones ME, Brady GW, Griffiths RJ, Garcia D, Rauch HA, et al. Non-beam-based metal additive manufacturing enabled by additive friction stir deposition. Scr Mater. 2018 Aug 1;153:122–30.
2. Khodabakhshi F, Gerlich AP. Potentials and strategies of solid-state additive friction-stir manufacturing technology: A critical review. Vol. 36, Journal of Manufacturing Processes. Elsevier Ltd; 2018. p. 77–92.
3. Yu HZ, Mishra RS. Additive friction stir deposition: a deformation processing route to metal additive manufacturing. Mater Res Lett. 2021 Feb 1;9(2):71–83.
4. Gopan V, Leo Dev Wins K, Surendran A. Innovative potential of additive friction stir deposition among current laser based metal additive manufacturing processes: A review. Vol. 32, CIRP Journal of Manufacturing Science and Technology. Elsevier Ltd; 2021. p. 228–48.
5. Raihan GA. Thermo-Mechanical Process Modeling of Friction Stir Deposition of Ti6Al4V Alloy [Internet]. [New Orleans]: University of New Orleans; 2022. Available from: https://scholarworks.uno.edu/td
6. Miller MO. AS-DEPOSITED MICROSTRUCTURE AND TENSILE BEHAVIOR OF SOLID-STATE ADDITIVE MANUFACTURED TI-6AL-4V. [Tuscaloosa]: The University of Alabama; 2019.
7. Agrawal P, Haridas RS, Yadav S, Thapliyal S, Gaddam S, Verma R, et al. Processing-structure-property correlation in additive friction stir deposited Ti-6Al-4V alloy from recycled metal chips. Addit Manuf [Internet].

2021;47(May):102259. Available from: https://doi.org/10.1016/j.addma.2021.102259

8. Farabi E, Babaniaris S, Barnett MR, Fabijanic DM. Microstructure and mechanical properties of Ti6Al4V alloys fabricated by additive friction stir deposition. Additive Manufacturing Letters. 2022 Apr 1;2.
9. Yoder JK, Erb DJ, Henderson R, Yu HZ. Closed-loop temperature controlled solid-state additive manufacturing of Ti-6Al-4V with forging standard out-of-plane tensile properties. J Mater Process Technol. 2023 Dec 1;322.
10. Metz PC, Arwood Z, Franz C, Heikkenen E, Chawla V, Babu SS, et al. Non-uniform plastic deformation in additive friction stir deposited Ti-6Al-4V. Materialia (Oxf). 2023 Aug 1;30.
11. Lutjering G, Williams JC. Titanium. 2nd ed. 2007.
12. Majumdar P, Singh SB, Chakraborty M. Elastic modulus of biomedical titanium alloys by nano-indentation and ultrasonic techniques-A comparative study. Materials Science and Engineering A. 2008;489(1–2):419–25.
13. Larson F, Zarkades A. Properties of Textured Titanium Alloys. 1974.
14. Dieter GE. Mechanical Metallurgy. McGraw-Hill Book Company; 1988.
15. Bhadeshia HKDH. Geometry of Crystals, Polycrystals, and Phase Transformations. Boca Raton, FL: CRC Press; 2018.
16. Burgers WG. On the Process of Transition of the Cubic-Body-Centered Modification into the Hexagonal-Close-Packed Modification of Zirconium. 1934;

17. Doherty RD, Hughes DA, Humphreys FJ, Jonas JJ, Jensen DJ, Kassner ME, et al. Current issues in recrystallization: a review. Vol. 238, Materials Science and Engineering. 1997.

18. Humphreys FJ. A UNIFIED THEORY OF RECOVERY, RECRYSTALLIZATION AND GRAIN GROWTH, BASED ON THE STABILITY AND GROWTH OF CELLULAR MICROSTRUCTURES - I. THE BASIC MODEL. Acta Metallurgica. 1997;45(10):4231–40.

19. Humphreys FJ. A UNIFIED THEORY OF RECOVERY, RECRYSTALLIZATION AND GRAIN GROWTH, BASED ON THE STABILITY AND GROWTH OF CELLULAR MICROSTRUCTURES - II. THE EFFECT OF SECOND-PHASE PARTICLES. Acta Metallurgica. 1997;45(12):5031–9.

20. Pilchak AL, Williams JC. Microstructure and texture evolution during friction stir processing of fully lamellar Ti-6Al-4V. In: Metallurgical and Materials Transactions A: Physical Metallurgy and Materials Science. 2011. p. 773–94.

21. Thomas WM, Nicholas ED, Needham JC, Murch MG, Temple-Smith P, Dawes CJ. Hot shear butt welding. United Kingdom; GB9125978D0, 1991.

22. Kitamura K, Fujii H, Iwata Y, Sun YS, Morisada Y. Flexible control of the microstructure and mechanical properties of friction stir welded Ti-6Al-4V joints. Mater Des. 2013 Apr;46:348–54.

23. Edwards P, Ramulu M. Peak temperatures during friction stir welding of Ti-6Al-4V. Science and Technology of Welding and Joining. 2010 Aug 1;15(6):468–72.

24. Esmaily M, Nooshin Mortazavi S, Todehfalah P, Rashidi M. Microstructural characterization and formation of α' martensite phase in Ti-6Al-4V alloy butt joints produced by friction stir and gas tungsten arc welding processes. Mater Des. 2013;47:143–50.

25. Zhou L, Liu HJ, Liu QW. Effect of process parameters on stir zone microstructure in Ti-6Al-4V friction stir welds. J Mater Sci. 2010 Jan;45(1):39–45.

26. Li B, Shen Y, Hu W, Luo L. Surface modification of Ti-6Al-4V alloy via friction-stir processing: Microstructure evolution and dry sliding wear performance. Surf Coat Technol. 2014 Jan 25;239:160–70.

27. Chatterjee S, Wang HS, Yang JR, Bhadeshia HKDH. Mechanical stabilisation of austenite. Materials Science and Technology. 2006 Jun;22(6):641–4.

28. Kumar S, Kamath R, Nandwana P, Chen Y, Babu S. Dynamic phase transformations in additively manufactured Ti-6Al-4V during thermo-mechanical gyrations. Materialia (Oxf) [Internet]. 2020;14(August):100883. Available from: https://doi.org/10.1016/j.mtla.2020.100883

29. Koike J, Shimoyama Y, Ohnuma I, Okamura T, Kainuma R, Ishida K, et al. STRESS-INDUCED PHASE TRANSFORMATION DURING SUPERPLASTIC DEFORMATION IN TWO-PHASE Ti-Al-Fe ALLOY. Acta Mater [Internet]. 200AD;48:2059–69. Available from: www.elsevier.com/locate/actamat

30. Lippold JC, Livingston JJ. Microstructure evolution during friction stir processing and hot torsion simulation of Ti-6Al-4V. Metall Mater Trans A Phys Metall Mater Sci. 2013 Aug;44(8):3815–25.

31. Knipling KE, Fonda RW. Microstructural evolution in Ti-5111 friction stir welds. Metall Mater Trans A Phys Metall Mater Sci. 2011 Aug;42(8):2312–22.

32. Zhou L, Liu HJ, Liu QW. Effect of rotation speed on microstructure and mechanical properties of Ti-6Al-4V friction stir welded joints. Mater Des. 2010 May;31(5):2631–6.

33. Lee WB, Lee CY, Chang WS, Yeon YM, Jung SB. Microstructural investigation of friction stir welded pure titanium. Mater Lett. 2005 Nov;59(26):3315–8.

34. Zhang Y, Sato YS, Kokawa H, Park SHC, Hirano S. Stir zone microstructure of commercial purity titanium friction stir welded using pcBN tool. Materials Science and Engineering: A. 2008 Aug 15;488(1–2):25–30.

35. Pilchak AL, Broderick TF. Evidence of a massive transformation in a Ti-6Al-4V solid-state weld? JOM. 2013 May;65(5):636–42.

36. Mishra RS, Mahoney MW. Friction Stir Welding and Processing. Materials Park, OH: ASM International; 2007.

37. Pilchak AL, Tang W, Sahiner H, Reynolds AP, Williams JC. Microstructure evolution during friction stir welding of mill-annealed Ti-6Al-4V. In: Metallurgical and Materials Transactions A: Physical Metallurgy and Materials Science. 2011. p. 745–62.

38. Ma ZY, Pilchak AL, Juhas MC, Williams JC. Microstructural refinement and property enhancement of cast light alloys via friction stir processing. Scr Mater. 2008 Mar;58(5):361–6.

39. Pilchak AL, Norfleet DM, Juhas MC, Williams JC. Friction stir processing of investment-cast Ti-6Al-4V: Microstructure and properties. Metall Mater Trans A Phys Metall Mater Sci. 2008 Jul;39(7):1519–24.

40. Boivineau M, Cagran C, Doytier D, Eyraud V, Nadal MH, Wilthan B, et al. Thermophysical Properties of Solid and Liquid Ti-6Al-4V (TA6V) Alloy. Int J Thermophys. 2006 Mar;27(2):507–29.

41. Milošević N, Aleksić I. Thermophysical properties of solid phase Ti-6Al-4V alloy over a wide temperature range. International Journal of Materials Research. 2012;6(103):707–14.

42. Palanivel S, Nelaturu P, Glass B, Mishra RS. Friction stir additive manufacturing for high structural performance through microstructural control in an Mg based WE43 alloy. Mater Des. 2015 Jan 1;65:934–52.

43. Ardalanniya A, Nourouzi S, Jamshidi Aval H. Effects of Multipass Additive Friction Stir Processing on Microstructure and Mechanical Properties of Al-Zn-Cup/Al-Zn Laminated Composites. JOM. 2021 Oct 1;73(10):2844–58.

44. Yuqing M, Liming K, Chunping H, Fencheng L, Qiang L. Formation characteristic, microstructure, and mechanical performances of aluminum-based components by friction stir additive manufacturing. International Journal of Advanced Manufacturing Technology. 2016 Apr 1;83(9–12):1637–47.

45. Roodgari MR, Jamaati R, Jamshidi Aval H. Fabrication of a 2-layer laminated steel composite by friction stir additive manufacturing. J Manuf Process. 2020 Mar 1;51:110–21.

46. Rodelas J, Lippold J. Characterization of Engineered Nickel-Base Alloy Surface Layers Produced by Additive Friction Stir Processing. Metallography, Microstructure, and Analysis. 2013 Feb 1;2(1):1–12.

47. Mukhopadhyay A, Saha P. Mechanical and microstructural characterization of aluminium powder deposit made by friction stir based additive manufacturing. J Mater Process Technol. 2020 Jul 1;281.

48. Gotawala N, Kumar Mishra N, Shrivastava A. Solid-state depositions of multilayer SS304 by friction stir metal deposition. Mater Lett. 2022 May 1;314.

49. Hanke S, Staron P, Fischer T, Fitseva V, dos Santos JF. A method for the in-situ study of solid-state joining techniques using synchrotron radiation - observation of phase transformations in Ti-6Al-4V after friction surfacing. Surf Coat Technol. 2018 Feb 15;335:355–67.

50. Khalid Rafi H, Phanikumar G, Prasad Rao K. Material flow visualization during friction surfacing. Metall Mater Trans A Phys Metall Mater Sci. 2011 Apr;42(4):937–9.

51. Gandra J, Krohn H, Miranda RM, Vilaça P, Quintino L, Dos Santos JF. Friction surfacing - A review. Vol. 214, Journal of Materials Processing Technology. Elsevier Ltd; 2014. p. 1062–93.

52. Xie R, Chen X, Shi Y, Yang C, Chen S, Liu H. Printing high-strength high-elongation aluminum alloy using commercial ER2319 welding wires through deformation-based additive manufacturing. Materials Science and Engineering: A. 2023 Mar 14;868.

53. Xie R, Shi Y, Liu H, Chen S. A novel friction and rolling based solid-state additive manufacturing method: Microstructure and mechanical properties evaluation. Mater Today Commun. 2021 Dec 1;29.

54. Blindheim J, Grong Ø, Aakenes UR, Welo T, Steinert M. Hybrid Metal Extrusion & Bonding (HYB) - A new technology for solid-state additive manufacturing of aluminium components. In: Procedia Manufacturing; NAMRC 46. Elsevier B.V.; 2018. p. 782–9.

55. Bor T, Leede M de, Deunk F, Lind J, Lievestro W, Smit HJ, et al. Friction screw extrusion additive manufacturing of an Al-Mg-Si alloy. Addit Manuf. 2023 Jun 25;72.

56. Haridas RS, Gumaste A, Varshney P, Manu BR, Kandasamy K, Kumar N, et al. SolidStir Additive Manufacturing: A Novel Deformation-Based Additive Manufacturing Using Friction Stir Technology. JOM. 2023 Oct 1;75(10):4231–41.

57. Chen H, Meng X, Chen J, Xie Y, Wang J, Sun S, et al. Wire-based friction stir additive manufacturing. Addit Manuf. 2023 May 25;70.

58. Zhang Z, Wan L, Meng X, Xie Y, Tian H, Mao D, et al. Robotic wire-based friction stir additive manufacturing. Addit Manuf. 2024 May 25;88.

59. Liu F, Dong P, Khan AS, Zhang Y, Cheng R, Taub A, et al. 3D printing of fine-grained aluminum alloys through extrusion-based additive manufacturing: Microstructure and property characterization. J Mater Sci Technol. 2023 Mar 10;139:126–36.

60. Creehan K, Schultz JP. SYSTEM FOR CONTINUOUS FEEDING OF FILLER MATERIAL FOR FRICTION STIR WELDING, PROCESSING AND FABRICATION. Vol. 792. 2012.

61. Phillips BJ, Avery DZ, Liu T, Rodriguez OL, Mason CJT, Jordon JB, et al. Microstructure-deformation relationship of additive friction stir-deposition Al–Mg–Si. Materialia (Oxf) [Internet]. 2019;7(April):100387. Available from: https://doi.org/10.1016/j.mtla.2019.100387

62. Alzahrani B, Seleman MMES, Ahmed MMZ, Elfishawy E, Ahmed AMZ, Touileb K, et al. The applicability of die cast a356 alloy to additive friction stir deposition at various feeding speeds. Materials. 2021 Oct 1;14(20).

63. Garcia D, Hartley WD, Rauch HA, Griffiths RJ, Wang R, Kong ZJ, et al. In situ investigation into temperature evolution and heat generation during additive friction stir deposition: A comparative study of Cu and Al-Mg-Si. Addit Manuf. 2020;34(June).

64. Joshi SS, Patil SM, Mazumder S, Sharma S, Riley DA, Dowden S, et al. Additive friction stir deposition of AZ31B magnesium alloy. Journal of Magnesium and Alloys. 2022 Sep 1;10(9):2404–20.

65. Williams MB, Robinson TW, Williamson CJ, Kinser RP, Ashmore NA, Allison PG, et al. Elucidating the effect of additive friction stir deposition on the resulting microstructure and mechanical properties of magnesium alloy we43. Metals (Basel). 2021 Nov 1;11(11).

66. Sharma S, Mani Krishna K V., Radhakrishnan M, Pantawane M V., Patil SM, Joshi SS, et al. A pseudo thermo-mechanical model linking process parameters to

microstructural evolution in multilayer additive friction stir deposition of magnesium alloy. Mater Des. 2022 Dec 1;224.

67. Griffiths RJ, Garcia D, Song J, Vasudevan VK, Steiner MA, Cai W, et al. Solid-state additive manufacturing of aluminum and copper using additive friction stir deposition: Process-microstructure linkages. Materialia (Oxf) [Internet]. 2021;15(August 2020):100967. Available from: https://doi.org/10.1016/j.mtla.2020.100967

68. Priedeman JL, Phillips BJ, Lopez JJ, Tucker Roper BE, Hornbuckle BC, Darling KA, et al. Microstructure Development in Additive Friction Stir-Deposited Cu. Metals (Basel). 2020 Nov 19;10(11):1538.

69. Agrawal P, Haridas RS, Yadav S, Thapliyal S, Dhal A, Mishra RS. Additive friction stir deposition of SS316: Effect of process parameters on microstructure evolution. Mater Charact. 2023 Jan 1;195.

70. Beladi H, Farabi E, Hodgson PD, Barnett MR, Rohrer GS, Fabijanic D. Microstructure evolution of 316L stainless steel during solid-state additive friction stir deposition. Philosophical Magazine. 2022;102(7):618–33.

71. Gottwald RB, Gotawala N, Erb DJ, Yu HZ. An exploratory study on miniaturized additive friction stir deposition. J Manuf Process. 2024 Sep 30;126:154–64.

72. Rivera OG, Allison PG, Jordon JB, Rodriguez OL, Brewer LN, McClelland Z, et al. Microstructures and mechanical behavior of Inconel 625 fabricated by solid-state additive manufacturing. Materials Science and Engineering A. 2017;694(October 2016):1–9.

73. Patil SM, Krishna KVM, Sharma S, Joshi SS, Radhakrishnan M, Banerjee R, et al. Thermo-mechanical process variables driven microstructure evolution during additive friction stir deposition of IN625. Addit Manuf. 2024 Jan 25;80.

74. K VMK, Patil SM, Sharma S, Joshi SS, Jin Y, Radhakrishnan M, et al. Additive friction stir deposition of Al 6061-B4C composites: Process parameters, microstructure and property correlation. Materials Science and Engineering: A. 2024 Sep 1;910.

75. Agrawal P, Haridas RS, Agrawal P, Mishra RS. Deformation based additive manufacturing of a metastable high entropy alloy via Additive friction stir deposition. Addit Manuf. 2022 Dec 1;60.

76. Griffiths RJ, Wilson-Heid AE, Linne MA, Garza E V., Wright A, Martin AA. Additive Friction Stir Deposition of a Tantalum–Tungsten Refractory Alloy. Journal of Manufacturing and Materials Processing. 2024 Aug 1;8(4).

77. Joey Griffiths R, Petersen DT, Garcia D, Yu HZ. Additive friction stir-enabled solid-state additive manufacturing for the repair of 7075 aluminum alloy. Applied Sciences (Switzerland). 2019 Sep 1;9(17).

78. Avery DZ, Cleek CE, Phillips BJ, Rekha MY, Kinser RP, Rao HM, et al. Evaluation of Microstructure and Mechanical Properties of Al-Zn-Mg-Cu Alloy Repaired via Additive Friction Stir Deposition. J Eng Mater Technol. 2022 Jul 1;144(3).

79. Martin LP, Luccitti A, Walluk M. Evaluation of Additive Friction Stir Deposition for the Repair of Cast Al-1.4Si-1.1Cu-1.5Mg-2.1Zn. Journal of Manufacturing Science and Engineering, Transactions of the ASME. 2022 Jun 1;144(6).

80. Hartley WD, Garcia D, Yoder JK, Poczatek E, Forsmark JH, Luckey SG, et al. Solid-state cladding on thin automotive sheet metals enabled by additive friction stir deposition. J Mater Process Technol. 2021 May 1;291.

81. Ahmed MMZ, El-Sayed Seleman MM, Elfishawy E, Alzahrani B, Touileb K, Habba MIA. The effect of temper condition and feeding speed on the additive manufacturing of AA2011 parts using friction stir deposition. Materials. 2021 Nov 1;14(21).

82. Ghadimi H, Talachian M, Ding H, Emanet S, Guo S. The Effects of Layer Thickness on the Mechanical Properties of Additive Friction Stir Deposition-Fabricated Aluminum Alloy 6061 Parts. Metals (Basel). 2024 Jan 1;14(1).

83. Anderson-Wedge K, Avery DZ, Daniewicz SR, Sowards JW, Allison PG, Jordon JB, et al. Characterization of the fatigue behavior of additive friction stir-deposition AA2219. Int J Fatigue. 2021 Jan 1;142.

84. Zhu N, Avery DZ, Chen Y, An K, Jordon JB, Allison PG, et al. Residual Stress Distributions in AA6061 Material Produced by Additive Friction Stir Deposition. J Mater Eng Perform. 2023 Jun 1;32(12):5535–44.

85. Stubblefield G, Fraser KA, Phillips BJ, Jordon JB. Smoothed Particle Hydrodynamic Modeling of Additive Friction Stir Deposition Manufacturing of Aluminum Alloy 6061 [Internet]. 2018. Available from: https://www.researchgate.net/publication/327848250

86. Stubblefield GG, Fraser K, Phillips BJ, Jordon JB, Allison PG. A meshfree computational framework for the numerical simulation of the solid-state additive

manufacturing process, additive friction stir-deposition (AFS-D). Mater Des. 2021;202.

87. Kincaid KC, MacPhee DW, Stubblefield GG, Jordon JB, Rushing TW, Allison PG. A Finite Volume Framework for the Simulation of Additive Friction Stir Deposition. J Eng Mater Technol. 2023 Jul 1;145(3).

88. Stubblefield GG, Fraser KA, Van Iderstine D, Mujahid S, Rhee H, Jordon JB, et al. Elucidating the influence of temperature and strain rate on the mechanics of AFS-D through a combined experimental and computational approach. J Mater Process Technol. 2022 Jul 1;305.

89. Merritt GR, Williams MB, Allison PG, Jordon JB, Rushing TW, Cousin CA. Closed-Loop Temperature and Force Control of Additive Friction Stir Deposition. Journal of Manufacturing and Materials Processing. 2022 Oct 1;6(5).

90. Perry MEJ, Griffiths RJ, Garcia D, Sietins JM, Zhu Y, Yu HZ. Morphological and microstructural investigation of the non-planar interface formed in solid-state metal additive manufacturing by additive friction stir deposition. Addit Manuf. 2020 Oct 1;35.

91. ASTM Standard. B381-21: Standard Specification for Titanium and Titanium Alloy Forgings. ASTM International [Internet]. 2021;1–8. Available from: www.astm.org.

92. Rai R, De A, Bhadeshia HKDH, DebRoy T. Review: Friction stir welding tools. Science and Technology of Welding and Joining. 2011;16(4):325–42.

93. Wu LH, Wang D, Xiao BL, Ma ZY. Tool wear and its effect on microstructure and properties of friction stir processed Ti-6Al-4V. Mater Chem Phys. 2014 Aug 14;146(3):512–22.

94. Amirov A, Chumaevskii A, Savchenko N, Gurianov D, Nikolaeva A, Krasnoveykin V, et al. Features of Permanent Joints of Titanium (α+β)-Alloys Obtained by Friction Stir Welding Using a Nickel Superalloy Tool. Metals (Basel). 2023 Feb 1;13(2).

95. Tarasov S, Amirov A, Chumaevskiy A, Savchenko N, Rubtsov VE, Ivanov A, et al. Friction Stir Welding of Ti-6Al-4V Using a Liquid-Cooled Nickel Superalloy Tool. Technologies (Basel). 2022 Dec 1;10(6).

96. Amirov A, Eliseev A, Kolubaev E, Filippov A, Rubtsov V. Wear of ZhS6U nickel superalloy tool in friction stir processing on commercially pure titanium. Metals (Basel). 2020 Jun 1;10(6):1–15.

97. Du S, Liu H, Jiang M, Zhou L, Li D, Gao Y. Effects of tool wear on the microstructure evolution and mechanical properties of friction stir welded TA5 alloy. International Journal of Advanced Manufacturing Technology. 2022 Mar 1;119(1–2):1109–21.

98. Ambrosio D, Wagner V, Vivas J, Dessein G, Aldanondo E, Cahuc O. Advances in friction stir welding of Ti6Al4V alloy complex geometries: T-butt joint with complete penetration. Archives of Civil and Mechanical Engineering. 2023 Aug 1;23(3).

99. Nasresfahani AR, Soltanipur AR, Farmanesh K, Ghasemi A. Effects of tool wear on friction stir welded joints of Ti–6Al–4V alloy. Materials Science and Technology (United Kingdom). 2017 Mar 24;33(5):583–91.

100. Buffa G, Fratini L, Micari F, Settineri L. On the Choice of Tool Material in Friction Stir Welding of Titanium Alloys. In: Proceedings of NAMRI/SME, Vol 40. 2012.

101. Fall A, Fesharaki MH, Khodabandeh AR, Jahazi M. Tool wear characteristics and effect on microstructure in Ti-6Al-4V friction stir welded joints. Metals (Basel). 2016 Nov 1;6(11).

102. Farias A, Batalha GF, Prados EF, Magnabosco R, Delijaicov S. Tool wear evaluations in friction stir processing of commercial titanium Ti-6Al-4V. Wear. 2013 Apr;302(1–2):1327–33.

103. Wang J, Su J, Mishra RS, Xu R, Baumann JA. Tool wear mechanisms in friction stir welding of Ti-6Al-4V alloy. Wear. 2014 Dec 1;321:25–32.

104. Tanaka K, Nakazawa T, Sakairi K, Sato Y, Kokawa H, Omori T, et al. Feasibility of Iridium Containing Nickel Based Superalloy Tool to Friction Stir Spot Welding of High Strength Steel. In: Minerals, Metals and Materials Series. Springer International Publishing; 2017. p. 29–35.

105. Miyazawa T, Iwamoto Y, Maruko T, Fujii H. Development of high strength Ir based alloy tool for friction stir welding. Science and Technology of Welding and Joining. 2012 Apr 3;17(3):213–8.

106. Miyazawa T, Iwamoto Y, Maruko T, Fujii H. Development of Ir based tool for friction stir welding of high temperature materials. Science and Technology of Welding and Joining. 2011 Feb;16(2):188–92.

107. David SA, Feng Z. Friction Stir Welding of Advanced Materials: Challenges. 2004.

108. Ragu Nathan S, Balasubramanian V, Malarvizhi S, Rao AG. An investigation on metallurgical characteristics of tungsten based tool materials used in friction stir welding of naval grade high strength low alloy steels. Int J Refract Metals Hard Mater. 2016 Apr 1;56:18–26.

109. Thompson BT, Babu SS, Lolla T. Application of Diffusion Models to Predict FSW Tool Wear. In: International Offshore and Polar Engineering Conference. International Society of Offshore and Polar Engineers; 2011. p. 520–6.

110. Michael Eff Graduate Program in Welding Engineering B, Suresh Babu S, David Phillips A. The Effects of Tool Texture on Tool Wear in Friction Stir Welding of X-70 Steel.

111. Pilchak AL, Juhas MC, Williams JC. Observations of tool-workpiece interactions during friction stir processing of Ti-6Al-4V. Metall Mater Trans A Phys Metall Mater Sci. 2007 Feb;38(2):435–7.

112. Zhang YN, Cao X, Larose S, Wanjara P. Review of tools for friction stir welding and processing. Canadian Metallurgical Quarterly. 2012;51(3):250–61.

113. Nathan SR, Malarvizhi S, Balasubramanian V, Rao AG. Failure analysis of tungsten based tool materials used in friction stir welding of high strength low alloy steels. Eng Fail Anal. 2016 Aug 1;66:88–98.

114. Mashinini PM, Dinaharan I, David Raja Selvam J, Hattingh DG. Microstructure evolution and mechanical characterization of friction stir welded titanium alloy Ti–6Al–4V using lanthanated tungsten tool. Mater Charact. 2018 May 1;139:328–36.

115. Thompson BT. Tool Degradation Characterization in the Friction Stir Welding of Hard Metals. The Ohio State University; 2010.

116. Thompson B, Babu SS. Tool Degradation Characterization in the Friction Stir Welding of Hard Metals. Weld J. 2010 Dec;Vol. 89:256–61.

117. Pilchak AL, Juhas MC, Williams JC. Observations of tool-workpiece interactions during friction stir processing of Ti-6Al-4V. Metall Mater Trans A Phys Metall Mater Sci. 2007 Feb;38(2):435–7.

118. Mohanty PP. Wear of friction stir tools considering qualitative and quantitative aspects: a review. Vol. 43, International Journal of Ambient Energy. Taylor and Francis Ltd.; 2022. p. 5535–53.

119. Mishra RS, Mahoney MW, editors. Friction Stir Welding and Processing. Materials Park, OH: ASM International; 2007.

120. Trapp T, Helder E, Subramanian PR. FSW of titanium alloys for aircraft engine components. In: Friction stir welding and processing II. San Diego California: TMS; 2003. p. 173–8.

121. Schwartz AJ, Kumar M, Adams BL, editors. Electron Backscatter Diffraction in Materials Science. Electron Backscatter Diffraction in Materials Science. Springer US; 2000.

122. Wright SI, Nowell MM. EBSD image quality mapping. Microscopy and Microanalysis. 2006 Feb;12(1):72–84.

123. Rui SS, Han QN, Wang X, Li S, Ma X, Su Y, et al. Correlations between two EBSD-based metrics Kernel Average Misorientation and Image Quality on indicating dislocations of near-failure low alloy steels induced by tensile and cyclic deformations. Mater Today Commun. 2021 Jun 1;27.

124. Wang F, Stinville JC, Charpagne M, Echlin MP, Agnew SR, Pollock TM, et al. Dislocation cells in additively manufactured metallic alloys characterized by electron backscatter diffraction pattern sharpness. Mater Charact. 2023 Mar 1;197.

125. Germain L, Gey N, Humbert M. Reliability of reconstructed β-orientation maps in titanium alloys. Ultramicroscopy. 2007 Nov;107(12):1129–35.

126. Tiley JS, Shiveley AR, Pilchak AL, Shade PA, Groeber MA. 3D reconstruction of prior β grains in friction stir-processed Ti-6Al-4V. J Microsc. 2014;255(2):71–7.

127. Niessen F, Nyyssönen T, Gazder AA, Hielscher R. Parent grain reconstruction from partially or fully transformed microstructures in MTEX. J Appl Crystallogr. 2022 Feb 1;55:180–94.

128. Glavicic MG, Kobryn PA, Bieler TR, Semiatin SL. A method to determine the orientation of the high-temperature beta phase from measured EBSD data for the low-temperature alpha phase in Ti-6Al-4V. Materials Science and Engineering A [Internet]. 2003;50–9. Available from: www.elsevier.com/locate/msea

129. Glavicic MG, Kobryn PA, Bieler TR, Semiatin SL. An automated method to determine the orientation of the high-temperature beta phase from measured EBSD data for the low-temperature alpha-phase in Ti-6Al-4V. Materials Science and Engineering A [Internet]. 2003;258–64. Available from: www.elsevier.com/locate/msea

130. Glavicic MG, Kobryn PA, Semiatin SL. Validation of an automated EBSD method to deduce the β-phase texture in Ti-6Al-4V with a colony-α microstructure. Materials Science and Engineering A. 2004 Nov 15;385(1–2):372–6.

131. Makiewicz KT. Development of simultaneous transformation kinetics microstructure model with application to laser metal deposited Ti-6Al-4V and alloy 718 [Internet]. Thesis. Ohio State University. 2013. Available from: http://rave.ohiolink.edu/etdc/view?acc_num=osu1366023857%5Cnhttps://drive.google.com/open?id=0B0fTxDBXtHZMWjVpQXdEVzgxRG8

132. Makiewicz K, Babu SS. Microstructure Evolution During Laser Additive Manufacturing of Ti6Al4V Alloys. In 2012. Available from: https://www.researchgate.net/publication/267902949

133. Tiley JS. MODELING OF MICROSTRUCTURE PROPERTY RELATIONSHIPS IN Ti-6Al-4V. The Ohio State University; 2002.

134. ASTM Standard. E562-19: Standard Test Method for Determining Volume Fraction by Systematic Manual Point Count. ASTM International [Internet]. 2019; Available from: www.astm.org,

135. Kelly SM. Thermal and Microstructure Modeling of Metal Deposition Processes with Application to Ti-6Al-4V [Internet]. Materials Science and Engineering. 2004. Available from: http://scholar.google.com/scholar?q=Thermal and microstructure modeling of metal deposition processes with application to Ti-6Al-4V&btnG=&hl=en&num=20&as_sdt=0%2C22

136. Ducato A, Fratini L, Cascia M La, Mazzola G. An Automated Visual Inspection System for the Classification of the Phases of Ti-6Al-4V Titanium Alloy. In: Computer Analysis of Images and Patterns. 2013. p. 362–9.

137. Sosa JM, Huber DE, Welk B, Fraser HL. Development and application of MIPAR^{TM}: a novel software package for two- and three-dimensional microstructural characterization. Integr Mater Manuf Innov. 2014 Dec 1;3(1):123–40.

138. Bhadeshia HKDH. Neural Networks in Materials Science. ISIJ International. 1999;39(10):966–79.

139. Plotkowski A, Ferguson J, Stump B, Halsey W, Paquit V, Joslin C, et al. A stochastic scan strategy for grain structure control in complex geometries using electron beam powder bed fusion. Addit Manuf. 2021;46:102092.

140. Raghavan N, Simunovic S, Dehoff R, Plotkowski A, Turner J, Kirka M, et al. Localized melt-scan strategy for site specific control of grain size and primary dendrite arm spacing in electron beam additive manufacturing. Acta Mater [Internet]. 2017;140:375–87. Available from: https://doi.org/10.1016/j.actamat.2017.08.038

141. Kelly SM, Kampe SL. Microstructural Evolution in Laser-Deposited Multilayer Ti-6Al-4V Builds: Part I. Microstructural Characterization. Metallurgical and Materials Transactions A. 2004;35A(June 2004):1861–7.

142. Sames WJ, List FA, Pannala S, Dehoff RR, Babu SS. The metallurgy and processing science of metal additive manufacturing. International Materials

Reviews [Internet]. 2016;61(5):315–60. Available from: http://www.tandfonline.com/doi/full/10.1080/09506608.2015.1116649

143. Kumar S, Vijayan SR, Nandwana P, Poplawsky JD, Yan C, Babu SS. Role of thermo-mechanical gyrations on the α/β interface stability in a Ti6Al4V AM alloy. Scr Mater. 2021 Nov 1;204.

144. Kelly SM, Kampe SL. Microstructural Evolution in Laser-Deposited Multilayer Ti-6Al-4V Builds: Part II. Thermal Modeling. Metallurgical and Materials Transactions A. 2004;35A(June 2004):1869–79.

145. Raplee J, Plotkowski A, Kirka MM, Dinwiddie R, Okello A, Dehoff RR, et al. Thermographic Microstructure Monitoring in Electron Beam Additive Manufacturing. Sci Rep [Internet]. 2017;7(March). Available from: http://dx.doi.org/10.1038/srep43554

146. Yoder S, Morgan S, Kinzy C, Barnes E, Kirka M, Paquit V, et al. Characterization of topology optimized Ti-6Al-4V components using electron beam powder bed fusion. Addit Manuf [Internet]. 2018;19:184–96. Available from: http://dx.doi.org/10.1016/j.addma.2017.12.001

147. Plotkowski A, Kirka MM, Babu SS. Verification and validation of a rapid heat transfer calculation methodology for transient melt pool solidification conditions in powder bed metal additive manufacturing. Addit Manuf. 2017;18:256–68.

148. Stump B, Fergusonli JS, Plotkowski AJ, Sisco KD. 3DThesis (3D THErmal Simulation Software). Oak Ridge, TN: Oak Ridge National Lab (ORNL); 2018.

149. Malik V, Kailas S V. Plasticine modeling of material mixing in friction stir welding. J Mater Process Technol. 2018 Aug 1;258:80–8.

150. Liechty BC, Webb BW. The use of plasticine as an analog to explore material flow in friction stir welding. J Mater Process Technol. 2007 Apr 12;184(1–3):240–50.

151. Tamadon A, Pons DJ, Clucas D. Analogue Modelling of Flow Patterns in Bobbin Friction Stir Welding by the Dark-Field/Bright-Field Illumination Method. Advances in Materials Science. 2020 Mar 1;20(1):56–70.

152. Babu SS, Livingston J, Lippold JC. Physical simulation of deformation and microstructure evolution during friction stir processing of Ti-6Al-4V alloy. Metall Mater Trans A Phys Metall Mater Sci. 2013;44(8):3577–91.

153. Arora A, Debroy T, Bhadeshia HKDH. Back-of-the-envelope calculations in friction stir welding - Velocities, peak temperature, torque, and hardness. Acta Mater. 2011 Mar;59(5):2020–8.

154. Roth A, Hake T, Zaeh MF. An analytical approach of modelling friction stir welding. In: Procedia CIRP. Elsevier B.V.; 2014. p. 197–202.

155. Stephen Leon J, Jayakumar V. An investigation of analytical modelling of friction stir welding. International Journal of Mechanical and Production Engineering Research and Development. 2019 Jan 3;9(1):179–90.

156. Schmidt H, Hattel J, Wert J. An analytical model for the heat generation in friction stir welding. Model Simul Mat Sci Eng. 2004 Jan;12(1):143–57.

157. Gadakh VS, Kumar A, Vikhe Patil GJ. Analytical Modeling of the Friction Stir Welding Process Using Different Pin Profiles. Weld J. 2015;94:115–24.

158. Essa ARS, Ahmed MMZ, Mohamed AKYA, El-Nikhaily AE. An analytical model of heat generation for eccentric cylindrical pin in friction stir welding. Journal of Materials Research and Technology. 2016 Jul 1;5(3):234–40.

159. Zhang S, Chen G, Liu Q, Li H, Zhang G, Wang G, et al. Numerical analysis and analytical modeling of the spatial distribution of heat flux during friction stir welding. J Manuf Process. 2018 Jun 1;33:245–55.

160. Haghpanahi M, Salimi S, Bahemmat P, Sima S. 3-D transient analytical solution based on Green's function to temperature field in friction stir welding. Appl Math Model. 2013 Dec 15;37(24):9865–84.

161. S.R. R, Bang HS, Chang WS, Kim HJ, Bang HS, Oh CI, et al. Numerical determination of residual stress in friction stir weld using 3D-analytical model of stir zone. J Mater Process Technol. 2007 Jun 12;187–188:224–6.

162. Qian J, Li J, Sun F, Xiong J, Zhang F, Lin X. An analytical model to optimize rotation speed and travel speed of friction stir welding for defect-free joints. Scr Mater. 2013 Feb;68(3–4):175–8.

163. Kincaid KC, Allison PG. PROCESS MODELING FOR ADDITIVE FRICTION STIR DEPOSITION VIA THE FINITE VOLUME METHOD FOR TERRESTRIAL AND NON-TERRESTRIAL APPLICATIONS. 2022.

164. Gotawala N, Yu HZ. Material flow path and extreme thermomechanical processing history during additive friction stir deposition. J Manuf Process. 2023 Sep 8;101:114–27.

165. Buffa G, Fratini L, Micari F. Mechanical and microstructural properties prediction by artificial neural networks in FSW processes of dual phase titanium alloys. J Manuf Process. 2012 Aug;14(3):289–96.

166. Maleki E. Artificial neural networks application for modeling of friction stir welding effects on mechanical properties of 7075-T6 aluminum alloy. IOP Conf Ser Mater Sci Eng. 2015;103(1).

167. Shi T, Wu J, Ma M, Charles E, Schmitz T. AFSD-Nets: A Physics-Informed Machine Learning Model for Predicting the Temperature Evolution During Additive Friction Stir Deposition. J Manuf Sci Eng. 2024 Aug 1;146(8).

168. Hunter JD. Matplotlib: A 2D Graphics Environment. Comput Sci Eng. 2007;9(3):90–5.

169. ASTM Standard. E407-23: Standard Practice for Microetching Metals and Alloys [Internet]. ASTM International. 2023. p. 1–22. Available from: https://iris.epa.gov/ChemicalLanding/&substance_nmbr=144

170. Schindelin J, Arganda-Carreras I, Frise E, Kaynig V, Longair M, Pietzsch T, et al. Fiji: An open-source platform for biological-image analysis. Vol. 9, Nature Methods. 2012. p. 676–82.

171. Preibisch S, Saalfeld S, Tomancak P. Globally optimal stitching of tiled 3D microscopic image acquisitions. Bioinformatics. 2009 Jun;25(11):1463–5.

172. Johnson KA, Hagen GM. Artifact-free whole-slide imaging with structured illumination microscopy and Bayesian image reconstruction. Gigascience. 2021;9(4).

173. Pedregosa F, Varoquaux G, Gramfort A, Michel V, Thirion B, Grisel O, et al. Scikit-learn: Machine Learning in Python. Journal of Machine Learning Research [Internet]. 2011;12:2825–30. Available from: http://scikit-learn.sourceforge.net.

174. Lenthe WC, Singh S, Graef M De. A spherical harmonic transform approach to the indexing of electron back-scattered diffraction patterns. Ultramicroscopy. 2019 Dec 1;207.

175. ASTM Standard. E384-22: Standard Test Method for Microindentation Hardness of Materials. ASTM International [Internet]. 2022;1–40. Available from: www.astm.org.

176. ASTM Standard. E8/E8M-24: Standard Test Methods for Tension Testing of Metallic Materials. ASTM International [Internet]. 2024;1–35. Available from: www.astm.org,

177. ASTM Standard. E1409-13: Standard Test Method for Determination of Oxygen and Nitrogen in Titanium and Titanium Alloys by Inert Gas Fusion. ASTM International [Internet]. 2021; Available from: www.astm.org.

178. Ungár T. Microstructural parameters from X-ray diffraction peak broadening. Scr Mater. 2004;51(8 SPEC. ISS.):777–81.

179. Mironov S, Sato YS, Kokawa H. Friction-stir welding and processing of Ti-6Al-4V titanium alloy: A review. J Mater Sci Technol. 2018 Jan 1;34(1):58–72.

180. Zhao R, Chen C, Wang W, Cao T, Shuai S, Xu S, et al. On the role of volumetric energy density in the microstructure and mechanical properties of laser powder bed fusion Ti-6Al-4V alloy. Addit Manuf. 2022 Mar 1;51.

181. Bertoli US, Wolfer AJ, Matthews MJ, Delplanque JPR, Schoenung JM. On the limitations of Volumetric Energy Density as a design parameter for Selective Laser Melting. Mater Des [Internet]. 2017;113:331–40. Available from: http://dx.doi.org/10.1016/j.matdes.2016.10.037

182. Fonda RW, Knipling KE. Texture development in friction stir welds. Science and Technology of Welding and Joining. 2011 May;16(4):288–94.

183. Gussev MN, Busby JT, Field KG, Sokolov MA, Gray SE. Role of Scale Factor During Tensile Testing of Small Specimens. Small Specimen Test Techniques: 6th Volume. 2014;1:1–19.

184. Mower TM. Degradation of titanium 6Al-4V fatigue strength due to electrical discharge machining. Int J Fatigue. 2014;64:84–96.

185. Knipling KE, Fonda RW. Texture development in the stir zone of near-α titanium friction stir welds. Scr Mater. 2009 Jun;60(12):1097–100.

186. Yoon S, Ueji R, Fujii H. Effect of rotation rate on microstructure and texture evolution during friction stir welding of Ti-6Al-4V plates. Mater Charact. 2015 Aug 1;106:352–8.

187. Huang W, Jiang L, Liu C, Chen C, Guo Y, Guo F. The Microstructure Morphology and Texture Evolution of α-Ti in Ti-6Al-4V Alloy During Friction Stir Processing With Low Rotation Speed and Traverse Speed. Adv Eng Mater. 2019 Aug 1;21(8).

188. Halisch C, Milcke B, Radel T, Rentsch R, Seefeld T. Influence of oxygen content in the shielding gas chamber on mechanical properties and macroscopic structure of Ti-6Al-4V during wire arc additive manufacturing. International Journal of Advanced Manufacturing Technology. 2023 Jan 1;124(3–4):1065–76.

189. Tiley J, Shaffer J, Shiveley A, Pilchak A, Salem A. The effect of lath orientations on oxygen ingress in titanium alloys. Metall Mater Trans A Phys Metall Mater Sci. 2014 Feb;45(2):1041–8.

190. Nunn SD, Dehoff RR, Simunovic S. Functionally Graded and Geometrically Ordered Titanium Composite Armor Materials [Internet]. ORNL. 2013 [cited 2024 Oct 1]. Available from: https://thyme.ornl.gov/Armor/home/home.cgi

191. Yu HZ. Additive Friction Stir Deposition. Elsevier; 2022.

192. Li B, Shen Y, Hu W. Surface nitriding on Ti-6Al-4V alloy via friction stir processing method under nitrogen atmosphere. Appl Surf Sci. 2013 Jun 1;274:356–64.

193. Shamsipur A, Kashani-Bozorg SF, Zarei-Hanzaki A. Production of in-situ hard Ti/TiN composite surface layers on CP-TI using reactive friction stir processing under nitrogen environment. Surf Coat Technol. 2013;218(1):62–70.

194. Wu LH, Jia CL, Han SC, Li N, Ni DR, Xiao BL, et al. Superplastic deformation behavior of lamellar microstructure in a hydrogenated friction stir welded Ti-6Al-4V joint. J Alloys Compd. 2019 May 30;787:1320–6.

195. Zhou L, Liu HJ. Effect of 0.3 wt% hydrogen addition on the friction stir welding characteristics of Ti-6Al-4V alloy and mechanism of hydrogen-induced effect. Int J Hydrogen Energy. 2010 Aug;35(16):8733–41.

196. Hovanski Y. Temporarily Alloying Titanium to Facilitate Friction Stir Welding [Internet]. Washington State University; 2009. Available from: http://www.ntis.gov/ordering.htm

197. Zhou L, Liu HJ. Effect of 0.5 wt.% hydrogen addition on microstructural evolution of Ti-6Al-4V alloy in the friction stir welding and post-weld dehydrogenation process. Mater Charact. 2011 Nov;62(11):1036–41.

APPENDIX

Table 13: LD-TD 700 ºC Tensile Testing Data

Sample ID	Modulus (GPa)	Yield Strength (MPa)	Ult Strength (MPa)	Ext Strain @ UTS (mm/mm)	Yield Strain (mm/mm)	Ext Strain @Rupture (mm/mm)	Strain Hardening Exponent
700S2	108	979	1000	0.028	0.011	0.20	0.031
700S6	108	924	979	0.065	0.011	0.15	0.058
700S10	-	-	-	-	-	-	-
700S14	114	979	1007	0.063	0.011	0.17	0.045
700S18	112	1020	1020	0.010	0.011	0.19	0.000
Average	111	976	1001	0.0415	0.0109	0.176	0.0335
Std Dev	3	40	17.2	0.0270	0.0003	0.02	0.025
Max	114	1020	1020	0.065	0.0112	0.197	0.058
Min	108	924	979	0.01	0.0106	0.147	0
CV (%)	3.0	4.1	1.7	65.1	2.9	13.3	74.3
Range	6.9	97	41	0.055	0.0006	0.05	0.058

Table 14: LD-TD 750 ºC Tensile Testing Data

Sample ID	Modulus (GPa)	Yield Strength (GPa)	Ult Strength (GPa)	Ext Strain @ UTS (mm/mm)	Yield Strain (mm/mm)	Ext Strain @Rupture (mm/mm)	Strain Hardening Exponent
750S2	-	-	-	-	-	-	-
750S6	119	965	979	0.057	0.010	0.17	0.039
750S10	119	1000	1014	0.052	0.011	0.16	0.038
750S14	120	958	1020	0.074	0.010	0.18	0.063
750S18	121	958	1014	0.059	0.010	0.16	0.056
Average	120	970	1007	0.0605	0.0102	0.168	0.049
Std Dev	1	20	18.7	0.0095	0.0002	0.01	0.012
Max	121	1000	1020	0.074	0.0105	0.183	0.063
Min	119	958	979	0.052	0.0101	0.157	0.038
CV (%)	0.7	2.0	1.9	15.7	1.9	6.6	25.4
Range	2.1	41	41	0.022	0.0004	0.026	0.025

Table 15: LD-TD 800 ºC Tensile Testing Data

Sample ID	Modulus (GPa)	Yield Strength (MPa)	Ult Strength (MPa)	Ext Strain @ UTS (mm/mm)	Yield Strain (mm/mm)	Ext Strain @Rupture (mm/mm)	Strain Hardening Exponent
800S2	119	993	1083	0.062	0.010	0.18	0.066
800S6	-	-	-	-	-	-	-
800S10	118	1034	1055	0.061	0.011	0.17	0.044
800S14	115	1014	1076	0.079	0.011	0.17	0.065
800S18	108	1014	1089	0.069	0.012	0.16	0.066
Average	115	1014	1076	0.06775	0.0109	0.169	0.06025
Std Dev	5	17	14.9	0.0083	0.0005	0.01	0.011
Max	119	1034	1089	0.079	0.0115	0.179	0.066
Min	108	993	1055	0.061	0.0104	0.158	0.044
CV (%)	4.3	1.7	1.4	12.3	4.2	5.2	18.0
Range	11.0	41	34	0.018	0.0011	0.021	0.022

Table 16: LD-TD 850 ºC Tensile Testing Data

Sample ID	Modulus (GPa)	Yield Strength (MPa)	Ult Strength (MPa)	Ext Strain @ UTS (mm/mm)	Yield Strain (mm/mm)	Ext Strain @Rupture (mm/mm)	Strain Hardening Exponent
850S2	119	938	1048	0.053	0.010	0.14	0.077
850S6	122	1041	1117	0.070	0.011	0.16	0.064
850S10	119	1055	1103	0.074	0.011	0.15	0.054
850S14	123	1034	1124	0.079	0.011	0.17	0.068
850S18	-	-	-	-	-	-	-
Average	120	1017	1098	0.069	0.0105	0.155	0.06575
Std Dev	2	54	34.4	0.0113	0.0004	0.01	0.010
Max	123	1055	1124	0.079	0.0109	0.169	0.077
Min	119	938	1048	0.053	0.01	0.141	0.054
CV (%)	1.8	5.3	3.1	16.4	3.6	7.4	14.5
Range	4.1	117	76	0.026	0.0009	0.028	0.023

Table 17: TD-LD 700 ºC Tensile Testing Data

Sample ID	Modulus (GPa)	Yield Strength (MPa)	Ult Strength (MPa)	Ext Strain @ UTS (mm/mm)	Yield Strain (mm/mm)	Ext Strain @Rupture (mm/mm)	Strain Hardening Exponent
700S2	114	1034	1076	0.056	0.011	0.12	0.048
700S6	118	993	1055	0.059	0.011	0.11	0.059
700S10	118	1076	1089	0.061	0.011	0.13	0.040
700S14	119	1055	1096	0.052	0.011	0.12	0.048
700S18	116	1069	1089	0.050	0.011	0.13	0.039
Average	117	1045	1081	0.0556	0.0111	0.123	0.0468
Std Dev	2	33	16.5	0.0046	0.0003	0.01	0.008
Max	119	1076	1096	0.061	0.0114	0.133	0.059
Min	114	993	1055	0.05	0.0105	0.11	0.039
CV (%)	1.8	3.2	1.5	8.3	3.1	8.2	17.2
Range	5.5	83	41	0.011	0.0009	0.023	0.02

Table 18: TD-LD 750 ºC Tensile Testing Data

Sample ID	Modulus (GPa)	Yield Strength (MPa)	Ult Strength (MPa)	Ext Strain @ UTS (mm/mm)	Yield Strain (mm/mm)	Ext Strain @Rupture (mm/mm)	Strain Hardening Exponent
750S2	108	986	1062	0.055	0.011	0.11	0.067
750S6	110	1007	1055	0.054	0.011	0.11	0.055
750S10	118	1062	1076	0.062	0.011	0.18	0.042
750S14	117	1103	1131	0.056	0.012	0.11	0.044
750S18	121	1069	1096	0.060	0.011	0.14	0.045
Average	114	1045	1084	0.0574	0.0112	0.132	0.0506
Std Dev	6	48	30.6	0.0034	0.0002	0.03	0.010
Max	121	1103	1131	0.062	0.0115	0.184	0.067
Min	108	986	1055	0.054	0.011	0.11	0.042
CV (%)	4.9	4.6	2.8	6.0	1.7	24.4	20.7
Range	13.1	117	76	0.008	0.0005	0.074	0.025

Table 19: TD-LD 800 ºC Tensile Testing Data

Sample ID	Modulus (GPa)	Yield Strength (MPa)	Ult Strength (MPa)	Ext Strain @ UTS (mm/mm)	Yield Strain (mm/mm)	Ext Strain @Rupture (mm/mm)	Strain Hardening Exponent
800S2	110	931	1027	0.053	0.011	0.10	0.076
800S6	117	1027	1110	0.063	0.011	0.13	0.069
800S10	118	1027	1083	0.057	0.011	0.13	0.056
800S14	121	1069	1103	0.050	0.011	0.12	0.044
800S18	119	1062	1124	0.060	0.011	0.12	0.062
Average	117	1023	1089	0.0566	0.0109	0.119	0.0614
Std Dev	4	55	37.8	0.0052	0.0002	0.01	0.012
Max	121	1069	1124	0.063	0.0111	0.133	0.076
Min	110	931	1027	0.05	0.0106	0.103	0.044
CV (%)	3.7	5.4	3.5	9.2	1.8	9.9	20.0
Range	11.7	138	97	0.013	0.0005	0.03	0.032

Table 20: TD-LD 850 ºC Tensile Testing Data

Sample ID	Modulus (GPa)	Yield Strength (MPa)	Ult Strength (MPa)	Ext Strain @ UTS (mm/mm)	Yield Strain (mm/mm)	Ext Strain @Rupture (mm/mm)	Strain Hardening Exponent
850S2	120	1020	1131	0.053	0.011	0.11	0.080
850S6	123	1055	1103	0.062	0.011	0.13	0.052
850S10	123	1007	1096	0.061	0.010	0.12	0.071
850S14	121	1041	1117	0.056	0.011	0.15	0.063
850S18	121	1000	1069	0.063	0.010	0.13	0.064
Average	122	1025	1103	0.059	0.0105	0.128	0.066
Std Dev	2	23	23.4	0.0043	0.0002	0.02	0.010
Max	123	1055	1131	0.063	0.0107	0.147	0.08
Min	120	1000	1069	0.053	0.0103	0.109	0.052
CV (%)	1.4	2.3	2.1	7.3	1.8	12.1	15.7
Range	3.4	55	62	0.01	0.0004	0.038	0.028

Table 21: ND-LD 700 ºC Tensile Testing Data

Sample ID	Modulus (GPa)	Yield Strength (MPa)	Ult Strength (MPa)	Ext Strain @ UTS (mm/mm)	Yield Strain (mm/mm)	Ext Strain @Rupture (mm/mm)	Strain Hardening Exponent
700S2	110	979	986	0.013	0.011	0.07	0.042
700S6	110	1007	1020	0.043	0.011	0.01	0.031
700S10	111	1041	1069	0.061	0.012	0.16	0.042
700S14	107	1014	1041	0.060	0.012	0.16	0.040
700S18	118	1069	1096	0.053	0.011	0.15	0.038
700S22	110	1103	1110	0.013	0.012	0.14	0.042
700S26	107	1048	1048	0.012	0.012	0.13	0.010
Average	110	1037	1053	0.036	0.012	0.117	0.035
Std Dev	4	42	43	0.023	0.0004	0.056	0.012
Max	118	1103	1110	0.061	0.012	0.162	0.042
Min	107	979	986	0.012	0.011	0.011	0.010
CV (%)	3.4	4.0	4.1	63.1	3.6	47.7	33.4
Range	11.0	124.1	124.1	0.049	0.001	0.151	0.032

Table 22: ND-LD 750 ºC Tensile Testing Data

Sample ID	Modulus (GPa)	Yield Strength (MPa)	Ult Strength (MPa)	Ext Strain @ UTS (mm/mm)	Yield Strain (mm/mm)	Ext Strain @Rupture (mm/mm)	Strain Hardening Exponent
750S2	104	924	931	0.030	0.011	0.08	0.028
750S6	91	986	1020	0.064	0.013	0.19	0.050
750S10	99	889	931	0.066	0.011	0.26	0.050
750S14	104	931	979	0.067	0.011	0.26	0.048
750S18	98	889	931	0.058	0.011	0.14	0.050
750S22	-	-	-	-	-	-	-
750S26	92	910	945	0.063	0.012	0.13	0.052
Average	98	922	956	0.058	0.012	0.177	0.046
Std Dev	6	36	37	0.014	0.0008	0.074	0.009
Max	104	986	1020	0.067	0.013	0.264	0.052
Min	91	889	931	0.030	0.011	0.077	0.028
CV (%)	5.8	3.9	3.8	24.3	6.7	41.7	19.6
Range	13.1	96.5	89.6	0.037	0.002	0.187	0.024

Table 23: ND-LD 800 ºC Tensile Testing Data

Sample ID	Modulus (GPa)	Yield Strength (MPa)	Ult Strength (MPa)	Ext Strain @ UTS (mm/mm)	Yield Strain (mm/mm)	Ext Strain @Rupture (mm/mm)	Strain Hardening Exponent
800S2	94	903	931	0.023	0.012	0.02	0.050
800S6	103	896	952	0.053	0.011	0.14	0.061
800S10	106	917	972	0.067	0.011	0.13	0.056
800S14	91	883	931	0.060	0.012	0.08	0.055
800S18	92	910	979	0.063	0.012	0.15	0.060
800S22	88	965	1014	0.070	0.013	0.13	0.061
800S26	-	-	-	-	-	-	-
Average	96	912	963	0.056	0.012	0.109	0.057
Std Dev	7	28	32	0.017	0.0009	0.048	0.004
Max	106	965	1014	0.070	0.013	0.147	0.061
Min	88	883	931	0.023	0.011	0.024	0.050
CV (%)	7.6	3.1	3.3	30.7	7.3	44.3	7.6
Range	18.6	82.7	82.7	0.047	0.002	0.123	0.011

Table 24: ND-LD 850 ºC Tensile Testing Data

Sample ID	Modulus (GPa)	Yield Strength (MPa)	Ult Strength (MPa)	Ext Strain @ UTS (mm/mm)	Yield Strain (mm/mm)	Ext Strain @Rupture (mm/mm)	Strain Hardening Exponent
850S2	105	952	1041	0.083	0.011	0.19	0.071
850S6	99	903	993	0.073	0.011	0.14	0.073
850S10	92	869	958	0.070	0.012	0.15	0.078
850S14	107	931	1027	0.074	0.011	0.13	0.072
850S18	108	958	1048	0.061	0.011	0.13	0.073
850S22	112	965	1076	0.065	0.011	0.12	0.078
850S26	-	-	-	-	-	-	-
Average	104	930	1024	0.071	0.011	0.144	0.074
Std Dev	7	37	42	0.008	0.0003	0.025	0.003
Max	112	965	1076	0.083	0.012	0.192	0.078
Min	92	869	958	0.061	0.011	0.124	0.071
CV (%)	6.8	4.0	4.1	10.8	2.6	17.7	4.1
Range	20.0	96.5	117.2	0.022	0.001	0.068	0.007

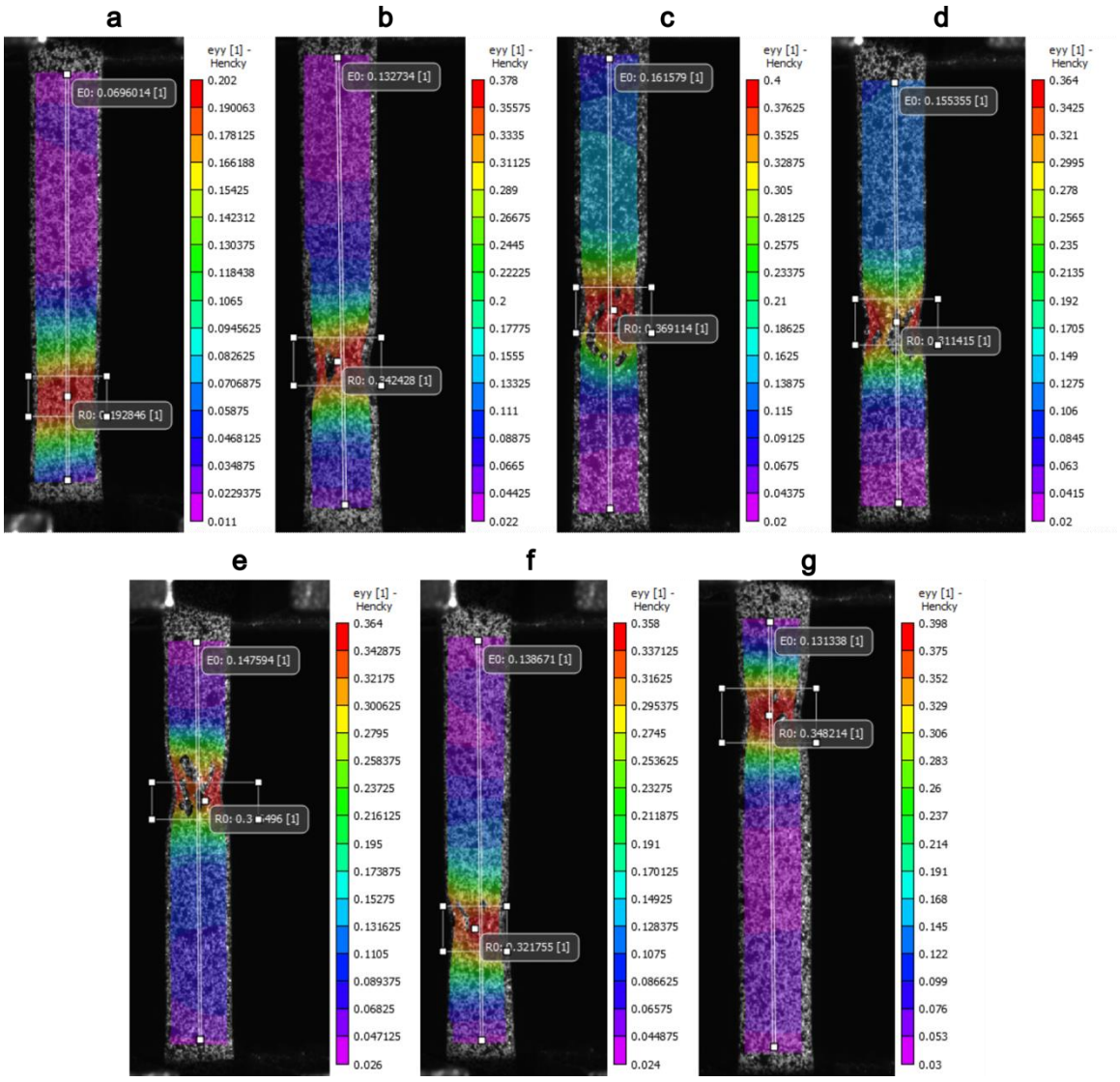


Figure 93: ND-LD 700ºC Tensile Specimens at Failure (a) s2, (b) s6, (c) s10, (d) s14, (e) s18, (f) s22, (g) s26

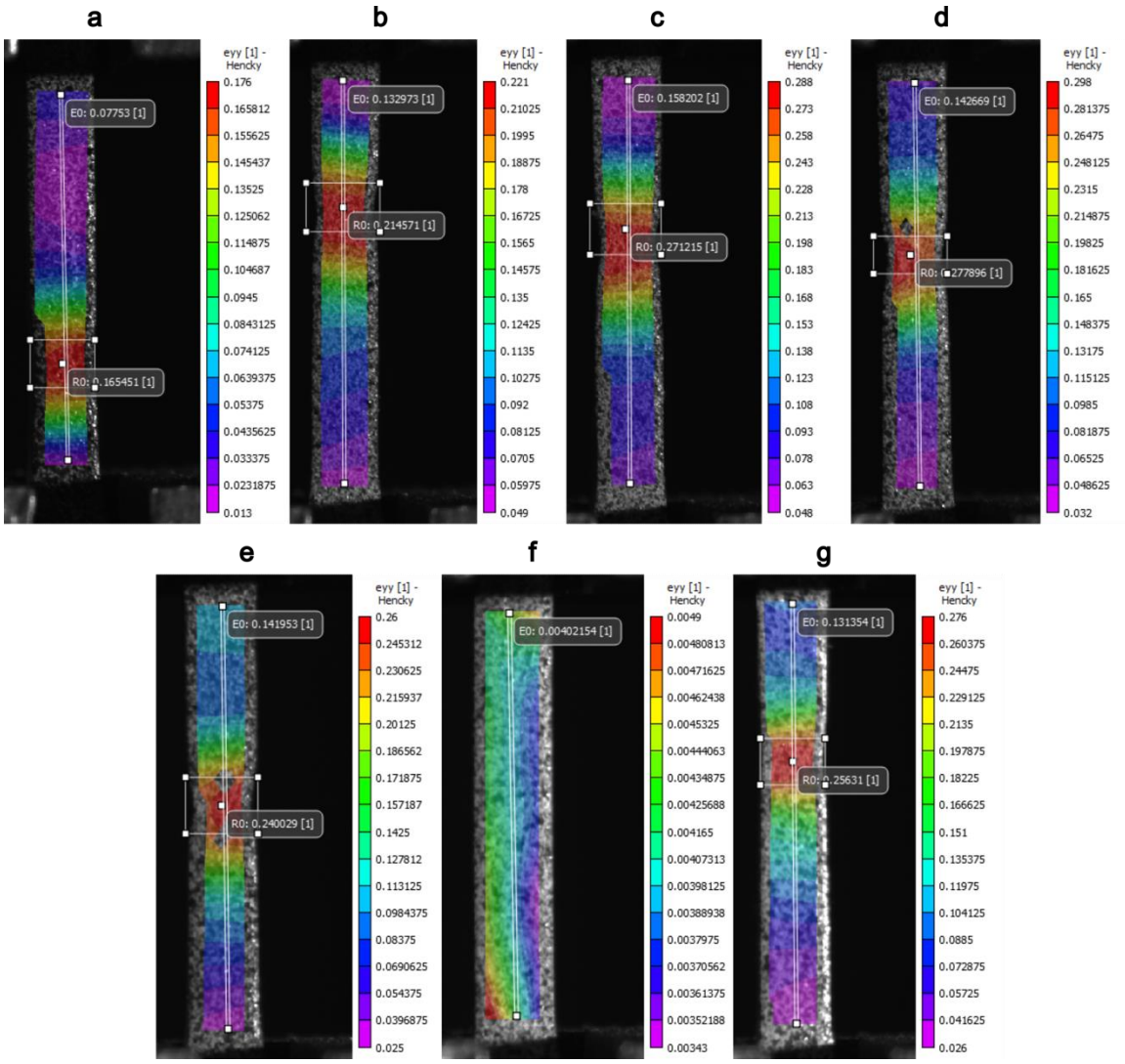


Figure 94: ND-LD 750ºC Tensile Specimens at Failure (a) s2, (b) s6, (c) s10, (d) s14, (e) s18, (f) s22, (g) s26

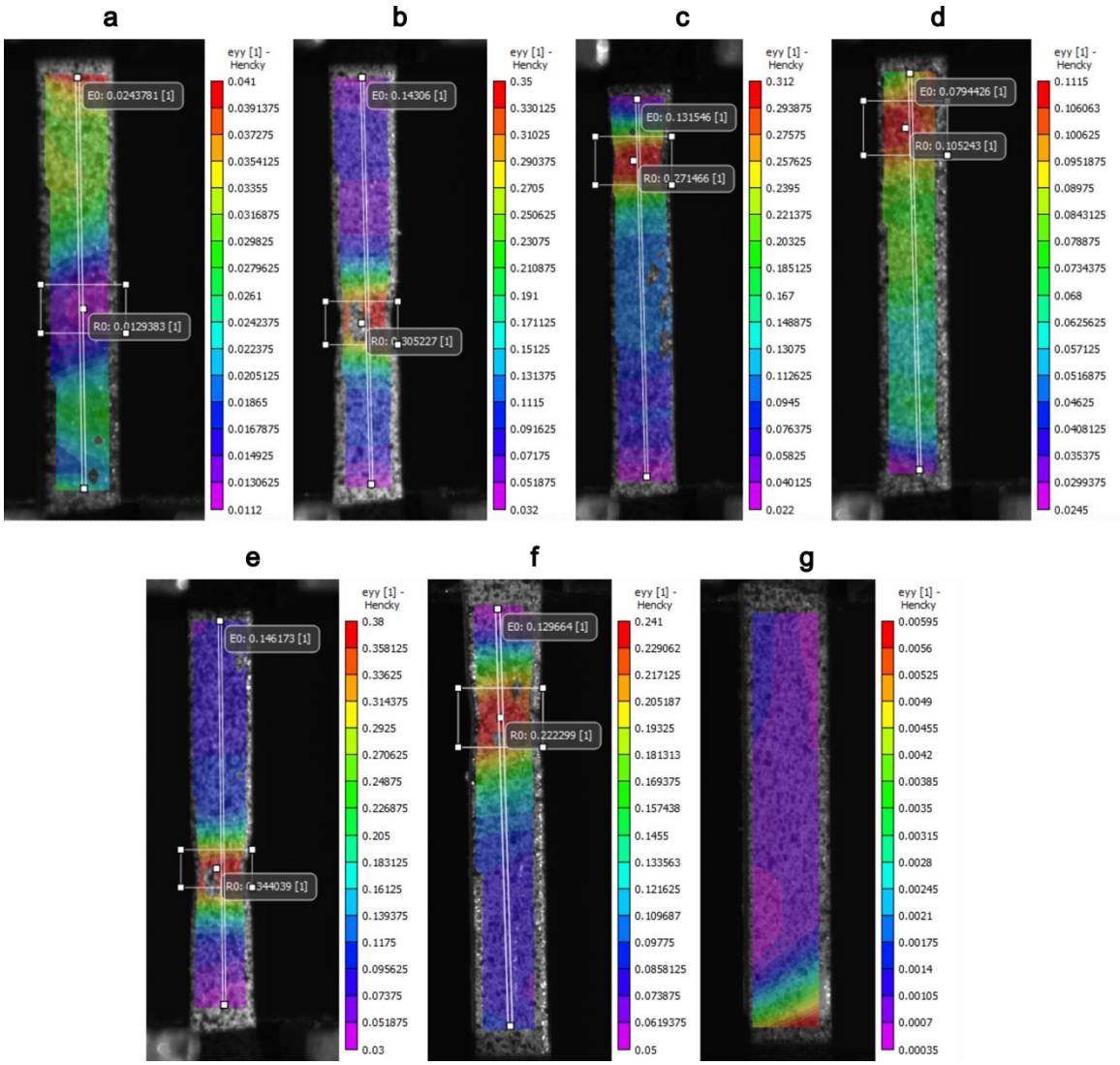


Figure 95: ND-LD 800ºC Tensile Specimens at Failure (a) s2, (b) s6, (c) s10, (d) s14, (e) s18, (f) s22, (g) s26

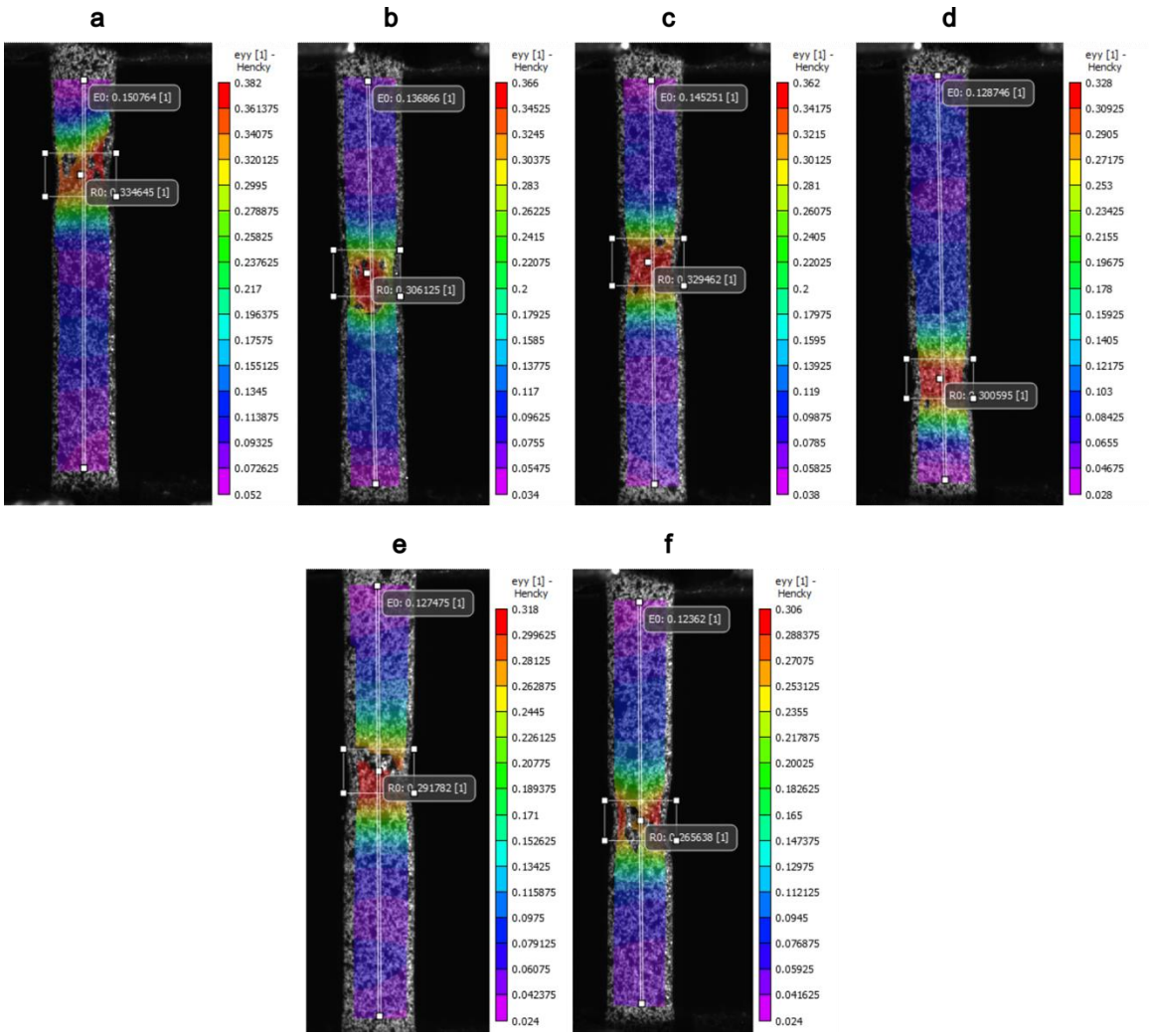


Figure 96: ND-LD 850ºC Tensile Specimens at Failure (a) s2, (b) s6, (c) s10, (d) s14, (e) s18, (f) s22

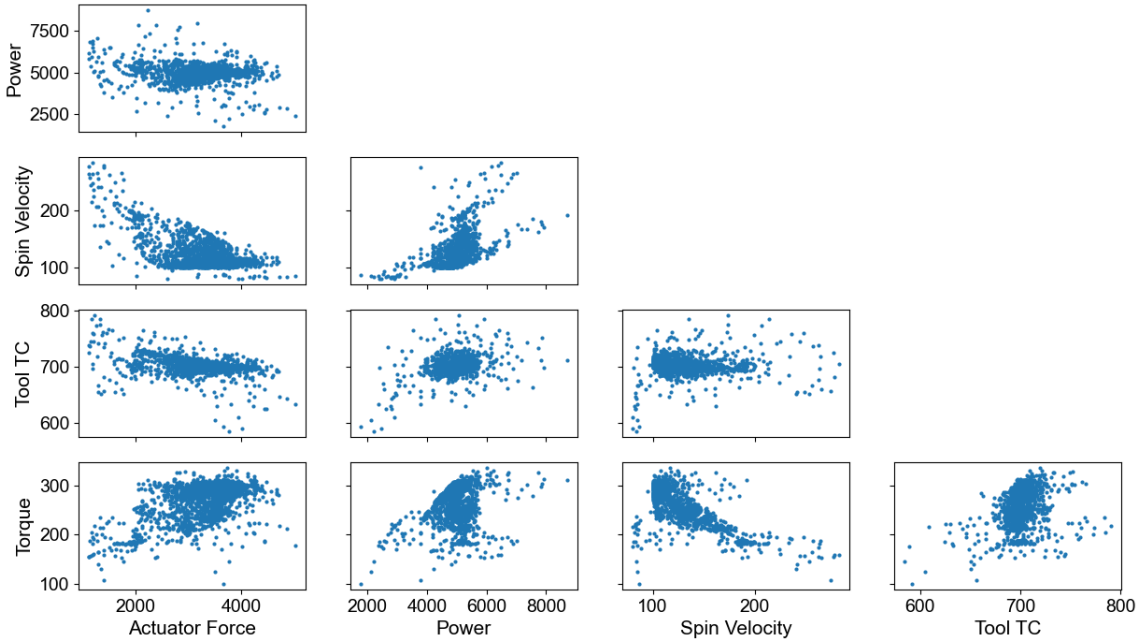


Figure 97: 700 ºC pair plot

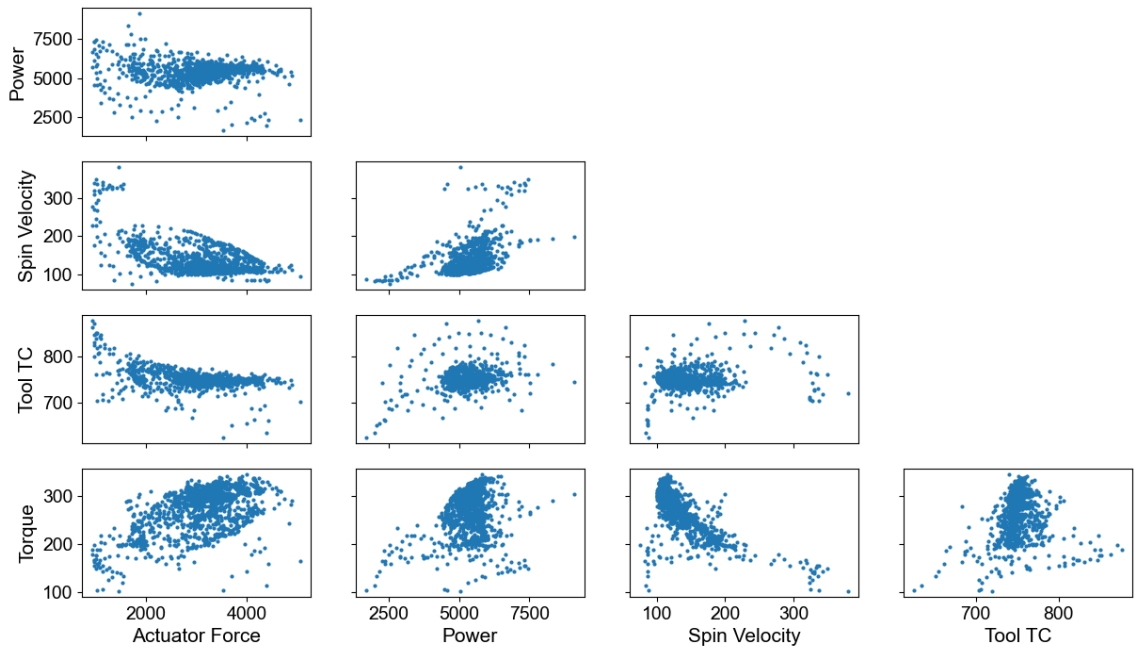


Figure 98: 750 ºC pair plot

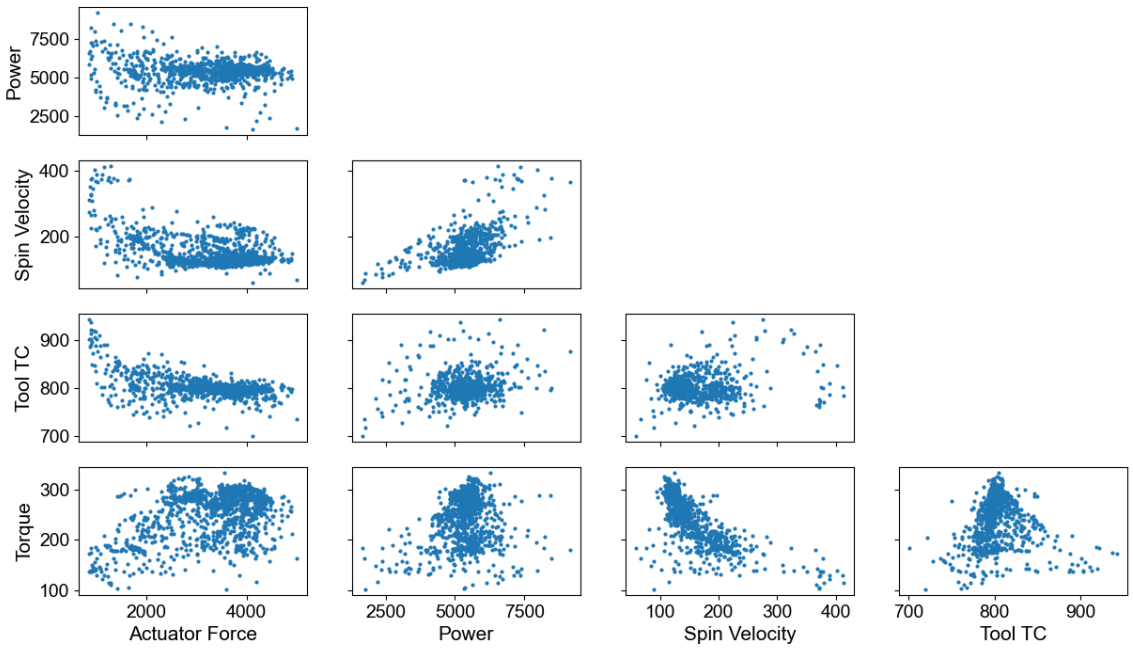


Figure 99: 800 ºC pair plot

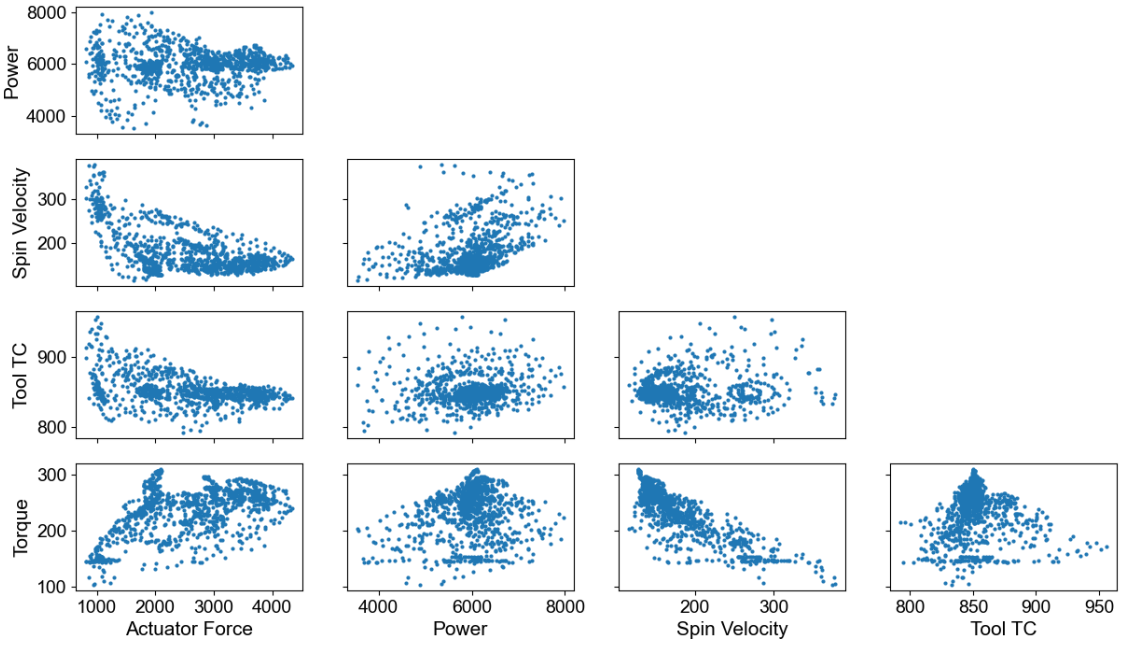


Figure 100: 850 ºC pair plot

VITA

Eric Heikkenen was born in Ft. Worth, Texas, on April 14th, 1994. He graduated from Baylor High School in 2013 and earned a bachelor's degree in mechanical engineering from The University of Tennessee, Knoxville in 2017. Following his undergraduate studies, he pursued a master's degree in mechanical engineering at The University of Tennessee, Knoxville completing it in early 2024.

For his time at the University of Tennessee, Knoxville, Eric studied various metal additive manufacturing process and materials, ranging from EB-PBF of titanium and nickel alloys to L-PBF and L-DED of aluminum, steel, nickel, and cobalt alloys.
For the topic of his PhD, Eric focused on Additive Friction Stir Deposition of titanium.
He is grateful to Dr. Suresh Babu and Dr. Tony Schmitz for abundant mentoring, as well as the University of Tennessee and Oak Ridge National Lab for providing an incredible environment for learning and growth.